Earth-Science Reviews 222 (2021) 103812

Contents lists available at ScienceDirect

Earth-Science Reviews

journal homepage: www.elsevier.com/locate/earscirev

Fold geometry and folding – a review

Seyed Tohid Nabavi [a,*], Haakon Fossen [b]

[a] Faculty of Earth Sciences, Department of Geology, Shahid Beheshti University, Tehran, Iran
[b] Museum of Natural History/Department of Earth Science, University of Bergen, Postboks 7803, N-5020 Bergen, Norway

ARTICLE INFO

Keywords:
Folding
Geometry
Kinematics
Mechanics
Fold style
Fold classification
Crustal deformation

ABSTRACT

Our understanding of folds and folding builds on detailed geometrical analysis. Proper description of folds and their relation to other structures such as fractures, cleavage and lineations form, together with physical and numerical modelling, the foundation for linking folds to stress, strain, kinematics, mechanics, and underlying tectonic processes. A large number of classification schemes and approaches have accumulated over the past century or so, and this overview critically considers a substantial portion of these schemes together with models for fold formation. We find folds and folding to be sensitive to many different factors, including material properties, layer thickness, mechanical anisotropy, boundary conditions, initial layer orientation, structural interaction between propagating folds or adjacent layers, inherited fracture and fault structures, deformation mechanisms, temperature, and confining pressure. However, there is no strong relationship between fold geometry and depth of formation, since microscale deformation mechanisms are of limited importance in this regard. For this reason, the geometric relations explored in clay/sandbox experiments are directly applicable to folds formed under metamorphic conditions by crystal-plastic mechanisms. The most fundamental distinction of folds is probably that of passive versus active folding. Passive folding, where viscosity contrasts are small or neglectable, is well understood and simple to model. Active folding, where fold nucleation and amplification is controlled by contrasts in viscosity or strength, is more complicated, and future work should focus on experimental and numerical modelling of well-defined examples of active fold geometries observed in rocks. In addition, the concept of bending, which can include both passive and active elements, is useful to maintain. Active and passive folding reflect rheology and strain, but do not directly relate to tectonic regime. Information about tectonic regime must come from other sources of information, but when known, fold analysis can be applied to characterize and quantify the deformation in that regime. Future work should focus on integrating field-based observations, sub-surface data sets, and 3D numerical modelling of folds in different model configurations (number of layers, layer thicknesses, type of perturbation and its amplitude in the layer interface, type of contact between interacting layers such as free-slip and or no-slip interfaces), different geological and tectonic settings (i.e., the type of applied boundary conditions and also in the form of displacement-based and strain-rate-based boundaries), and different mechanical properties or stratigraphy.

1. Introduction

Folds are extremely common deformation structures (Fig. 1) in any tectonic regime, including: 1) orogens, fold-and-thrust belts, and accretionary prisms (Fig. 2a, b) (e.g., van der Pluijm and Marshak, 2004; Fossen, 2016); 2) strike-slip systems (Fig. 2c) (e.g., Wilcox et al., 1973; Sylvester, 1988), 3) transpression (Fig. 2d) and transtension zones (Fig. 2e) (e.g., Venkat-Raman and Tikoff, 2002; Fossen et al., 2013; Ghosh et al., 2014; Frehner, 2016; Nabavi et al., 2017a, 2018a,b, 2019); 4) shear zones (Fig. 2f) (e.g., Ramsay, 1980; Carreras et al., 2005; Fossen and Cavalcante, 2017; Dutta and Mukherjee, 2019); 5) regional extension in the form of continental rifting or orogenic collapse (Fig. 2g) (Fossen and Holst, 1995; Harris et al., 2002; Coleman et al., 2019); 6) salt diapirs as drape of the sedimentary roof over rising or advancing salt (Fig. 2h) (e.g., Jackson and Hudec, 2017); 7) soft-sediment deformation related to gravity driven slumps and sediment mass transport (Fig. 2i) (e.g., Hudleston, 1977; Alsop et al., 2020); 8) sediments and rocks shortened in front of and under advancing glaciers (glaciotectonics) (Fig. 2j) (e.g., Phillips, 2018). Their geometric features and occurrence bear important information on strain, kinematics and rheology. Folds of

* Corresponding author.
E-mail address: T_nabavi@sbu.ac.ir (S.T. Nabavi).

https://doi.org/10.1016/j.earscirev.2021.103812
Received 19 April 2021; Received in revised form 13 August 2021; Accepted 15 September 2021
Available online 26 September 2021

different size, shape, style and geometry form from an interplay between forces, boundary conditions and rheology. As for deformation in general, they can be analysed with respect to geometry (e.g., structural orientation, attitude, size and morphology or shape), kinematics (involving position, displacement, velocity and acceleration of as many points as possible and thus progressive deformation) and dynamics (the relationship between forces or stress and kinematics). Analysis of fold structures as observed in the field or from remote sensing data forms the foundation for understanding and quantifying fold-related deformation at various scales (microscopic, mesoscopic and macroscopic), strongly supported by physical and numerical modelling.

More specifically, folds are curviplanar structures that form by transformation of any tectonic or primary foliation into curved geometries through a non-linear transformation (for completion, we note that already existing folds may in rare cases unfold during folding). Furthermore, a fold is the result of a folding history dominated by growth dominated by permanent ductile deformation, during which material continuity and cohesion is largely maintained at the scale of observation. However, discontinuities can occur in the form of associated veins and fracture, typically seen in the outer arc of competent layers, and also along week layers or bedding planes during flexural slip. At the microscale, folding can be associated with both crystal-plastic and/or brittle deformation mechanisms. For example, a folding in medium- and high-grade metamorphic rocks typically involves dislocation creep and dynamic recrystallization, whereas soft-sediment folding occurs by frictional grain-boundary sliding, grain comminution and grain rotation. Folding of limestones, on the other hand, is typically accommodated by pressure solution and precipitation processes. The fundamental terminology used to describe the resulting folds is presented in many textbooks (e.g., Ramsay, 1967; Ramsay and Huber, 1987; Price and Cosgrove, 1990; van der Pluijm and Marshak, 2004; Twiss and Moores, 2007; Fossen, 2016), and key terms used in this contribution are shown schematically in Fig. 1.

Variations in fold shape, especially in multilayer examples, reflect differences in their mechanical response to stress and strain due to differences in layer thickness, viscosity, matrix-layer viscosity (or competence) contrast, mechanical anisotropy and inherited fracture and fault structures. Fold shape also relates to the key factors controlling strain

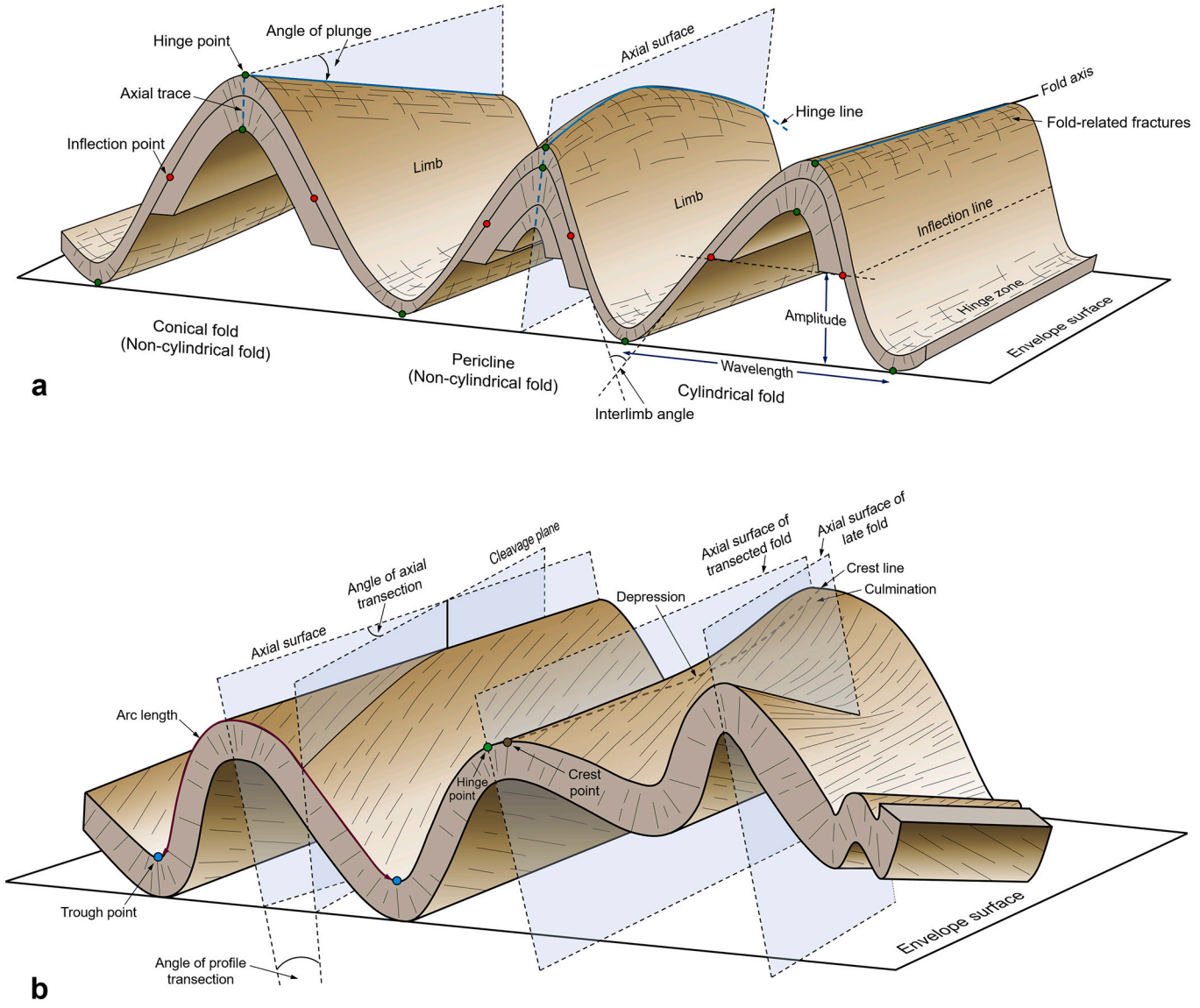

Fig. 1. a) Geometric parameters of cylindrical and non-cylindrical folds (based on Fossen, 2016). b) The relationship between cleavage plane, axial surface, and enveloping surface in folds with transected cleavage and transected fold. Note the obliquity of the bedding-cleavage intersection lineation to the hinge line.

localisation in ductile deformation, notably strain-dependent rheology, strain intensity, deformation path, and the influence of layer irregularities (e.g., Ramberg, 1964; Lan and Hudleston, 1995; Schmalholz and Podladchikov, 2001; Toimil and Griera, 2007; Hudleston and Treagus, 2010; Fitz-Díaz et al., 2012; Eckert et al., 2014, 2016; Schmalholz and Mancktelow, 2016). These parameters have been shown to correlate with geometrical parameters such as fold wavelength (twice the distance between inflection points), fold arc-length, amplitude (the distance between the line joining two inflection points and the line tangential to the hinge and or, more practically, half the height measured from crest to

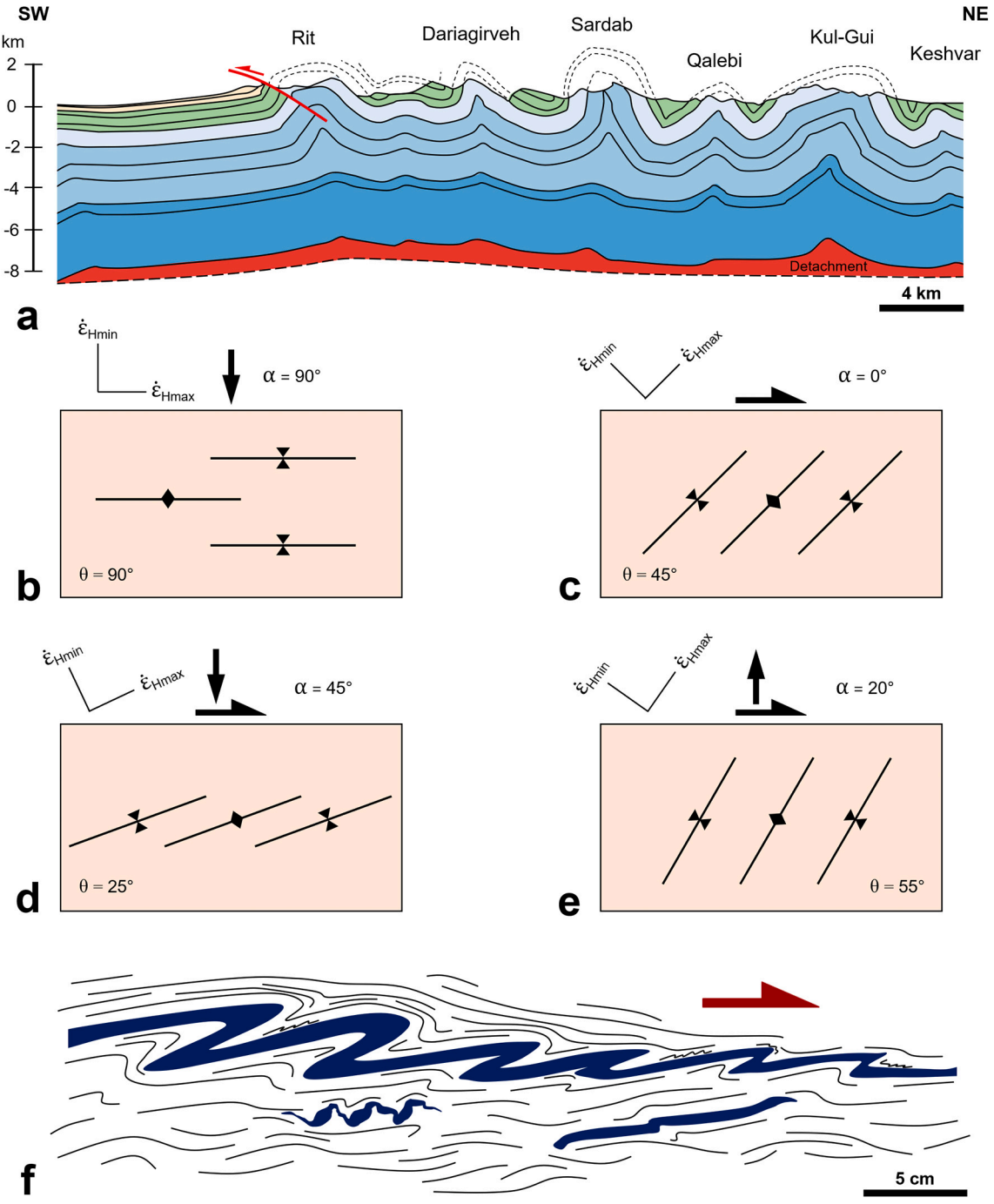

Fig. 2. Development of folds in various environments: a) Folds developed in the upper part show much tighter upright anticlines and synclines. NW Zagros belt (modified after Vergés et al., 2011). Fold orientation can be used to discriminate between pure contraction (b), pure strike-slip (c), transpression (d), and transtension zones (e). f) Asymmetrical folds in a shear zone, indicating sense of shear. g) Example of extensional fold developed in the hangingwall to a 10 km displacement fault in the North Sea rift basin. The fold is related to the non-planar fault geometry. Differential compaction above the hangingwall also produce a very gently fold seen at the base of the post-rift sequence. h) Sketch of Hormuz salt extrusion, Zagros, with the first-order recumbent anticline characteristic of a spreading salt sheet above rigid bedrock, and also second-order recumbent flow folds. The geometry is one of upward-facing parasitic folds in the upper limb, downward-facing parasitic folds in the inverted lower limb, and a recumbent tank-tread fold at the outer margin of the salt glacier (modified after Talbot et al., 2009). i) The main geometries and styles of folding during soft-sediment deformation of competent layers (brown) above a basal detachment (generalized sketch modified from Alsop et al., 2020). j) Folding and shearing sediments above a basal detachment below and ahead of advancing ice sheet (modified after Benediktsson et al., 2010). (For interpretation of the references to colour in this figure legend, the reader is referred to the web version of this article.)

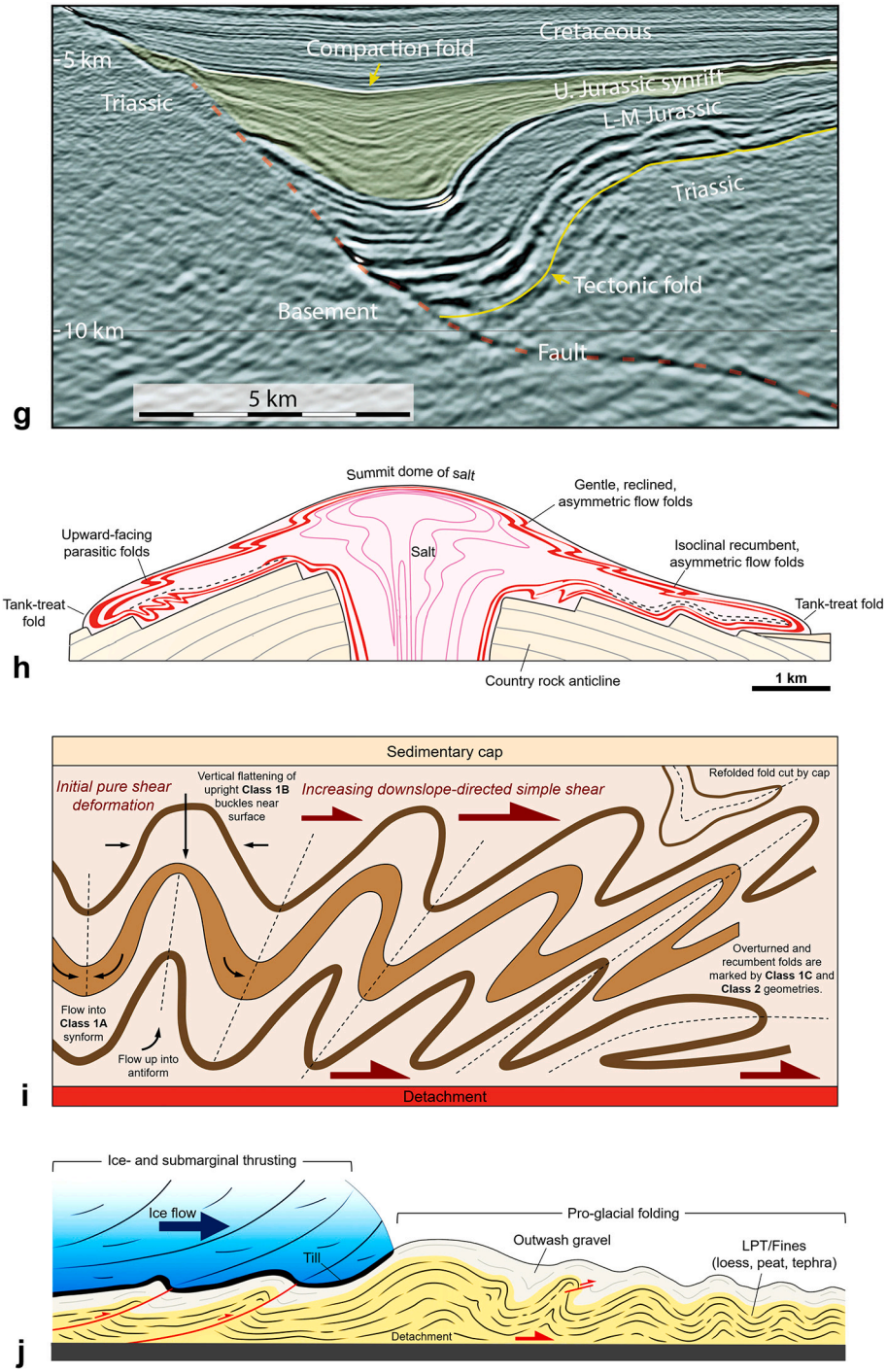

Fig. 2. (*continued*).

trough) (Fig. 1), hinge bluntness, and layer thickness. For instance, where viscosity contrast is low, folding is unlikely to develop during layer-parallel shortening. Multilayers of high viscosity contrasts favour concentric folding, while shorter wavelengths are developed in thinner layers. Where there are layers of different thickness, the geometry of the resultant fold train will be controlled by the thickest layer(s), for a constant viscosity contrast (e.g., Price and Cosgrove, 1990; Frehner and Schmalholz, 2006; Frehner and Schmid, 2016). The geometric parameters of folds are of primary importance, as they can be used to estimate finite strain and rheological properties during deformation (e.g., Hudleston and Lan, 1993; Lan and Hudleston, 1995).

In general, geometric interpretation of three-dimensional fold and fault structures is imperative for proper tectonic analysis. To discuss the geometry of fold structures, it is necessary to establish a frame of reference. Several questions about folds should be raised to identify, analyse and interpret of fold structure, including the following. What is the best approach for geometric analysis? What geometric classification scheme is appropriate? Which parameters exert the greatest control on the observed fold geometry and folding mechanism? Which parameters need to be analysed? What are the dominant fold geometries and folding mechanisms at different crustal depths and in different tectonic settings? How can fold analysis provide an estimate of strain? How did the fold evolve? What is needed to improve the mapping, analysis and understanding of folds and folding in the future?

Answering such questions requires careful analysis and description of the fold structure.

In the following sections, we will focus on geometric descriptions of fold structures and to a lesser extent on the kinematics of folding mechanisms, the patterns of strain distribution in folded single- and multilayers and how their structural complexities can be interpreted using suitable classification schemes. The literature on fold geometry is vast because these geological structures (i) can develop in any tectonic setting, (ii) occur at any scale from micro- to map-scale, (iii) can be analysed using a variety of geometric classification schemes, (iv) were studied for different bulk deformation geometries such as pure shear and simple shear, (v) can be studied for single- and multilayer configurations, (vi) can be studied in two- and three-dimensions, (vii) can be studied for isotropic and anisotropic materials, and (viii) were studied using analytical, analogue and numerical models. A vast body of literature exists that focuses mainly on the kinematics (strain-oriented) and dynamics (stress-oriented) aspects of folding, whereas less work is published on numerical modelling. In this regard, Hudleston and Treagus (2010) and Schmalholz and Mancktelow (2016) reviewed the progress in understanding the kinematics and mechanical dynamics of single and multilayer folding. Following kinematic and mechanical aspects, however, geometrical analyses of folds is an important tool to help understand deformation.

The present review has two main aims. The first is to summarize and review existing geometrical classification schemes for folds, to discuss for which geometric problem each of these classification schemes might be justified, and to discuss their advantages, their applications to natural examples, and potential problems and limitations of the different schemes. For simplicity, we will focus on the geometry of fold structures generated by progressive shortening and their kinematic evolution. The second aim is to provide a discussion of and new insights into the geometrical interpretation of folds using modern and accurate classification schemes as well as fundamental concepts. This paper will not repeat all of the basic concepts covered in structural geology textbooks, but rather focus on the link between fold geometry and kinematics. We acknowledge that it is still difficult to extract kinematic and mechanical information from geological structures, especially folds, since their geometries in rocks are highly variable and depend on several parameters. The many parameters influencing the occurrence and style of folds make prediction of such structures difficult in detail. However, geometry is of fundamental importance for fold classification and for understanding folding mechanisms. The most important distinction between the ways folds form probably lies in whether the layering responds actively or passively to the imposed strain field.

In this review we will, after a note on the importance of folds and a historical review, discuss the geometry and geometric description of folds. This section applies to all kinds of folds, unless otherwise noted. Kinematic and mechanical aspects of folding will then be covered by considering buckle (active) folding, where the competence or viscosity contrast between the folding layer and its host rock is important. We will then deal with passive folding, where layers are simply passive markers with no rheological influence, followed by a treatment of bending, where forces are applied across the layering. Finally, following the advantages, limitations, and modifications of the current schemes, we conclude with a section discussing applied aspects of folds geometry and folding, and how interpretation depends on the geometry of the geological structure with an outlook on future research on fold geometry.

2. Why are folds and folding important?

The fact that folds are extremely common structures in many different geological settings makes them one of the most important structures in rocks and sediments. Large folds can influence landscape evolution during erosion, typically with ridges along steep limbs and valleys along synforms (e.g., the Valley and Ridge region or the flatirons of Laramide monoclines of the Colorado Plateau), or with resistant cores creating positive topographic landforms (e.g., Sheep Mountains, Montana and San Rafael Swell, Utah). Folds and folding furthermore influence the evolution of the Earth's surface as they form, controlling patterns of erosion, sediment routing and depocenters. These processes cause rapid stratigraphic thickness variations that relate to the growth history of the folds (e.g., Darnault et al., 2016; Jackson and Hudec, 2017).

These points are particularly relevant to petroleum geology, as folding can generate hydrocarbon traps and influence sedimentary depositional patterns and variations in sedimentary facies and reservoir properties. Classical hydrocarbon and CO_2 traps are formed by domes or uprights folds in both extensional, transcurrent and contractional settings (e.g., Morley et al., 2013). Folding is often associated with small-scale structures such as fractures, stylolites and deformation bands that are unevenly distributed within folded layers. Such structures tend to affect fluid flow, and as they are impossible to detect from geophysical data, their prediction must be based on fold geometry and a good understanding of the folding mechanisms (e.g., Zuluaga et al., 2016). Folding also makes mining operations and the prediction of ore bodies at depth more complicated. Complexly folded ore bodies in orogenic belts, including banded iron formations, are examples of this. Furthermore, fold structures may also affect the distribution of stress in rock masses and ore bodies, causing stability problems and influencing the size, orientation and location of seismic events generated by mining operations.

Fold systems also reflect local strain and kinematics, although any rotation of fold structures during or after their evolution must be accounted for. The relative or absolute ages of folds, for example from stratigraphy, intrusions or overprinting relations, are also important for understanding the evolution of orogenic belts. Folds are particularly useful when conducting tectonic investigations in orogens, to: *(i)* determine tectonic shortening directions, *(ii)* calculate the amount of tectonic shortening, *(iii)* interpret the geometry of larger-scale structures, and *(iv)* investigate the rheological properties of the folded rocks. They are also important for interpreting deeper structures, for example the prediction of deep faults from fault-propagation folds or salt structures from dome-shaped folds.

Fold structures can also control the stability and behaviour of natural and engineered rock slopes depending on their orientations, geometry and structural complexity with respect to a given slope face (e.g., Stead and Wolter, 2015). This summary shows that folds are not only relevant to the academic field of structural geology, but are also highly pertinent to a wide range of practical and economic geoscience topics.

3. Historical background

Folds in rocks are eye-catching structures that have been explored and discussed for centuries, for instance by Leonardo da Vinci (1452–1519) and Nicholas Steno (1669) (Vai et al., 1986; Vai, 2003). Folds were recognized and described in more detail in Wales and the European Alps around Lake Uri in Switzerland by Luigi F. Marsili and Johann J. Scheuchzer in 1705 (Fig. 3a) (Ellenberger, 1995). From the late 1700s, understanding of fold structures and their origins was one of several great problems in structural geology. Studies show that De Saussure (1796) was the first to attribute folding to horizontal compression (lateral push or *refoulement horizontaux/latéral*) as the agent of shortening and folding, during his attempts at a structural synthesis of the European Alps. Although he did not speculate specifically on their causes, he writes (De Saussure, 1796):

> "*We are still ignorant by what cause these rocks have been tilted. But it is already an important step among the prodigious quantity of vertical strata in the Alps to have found certain examples which we can be perfectly certain were formed in a horizontal position*".

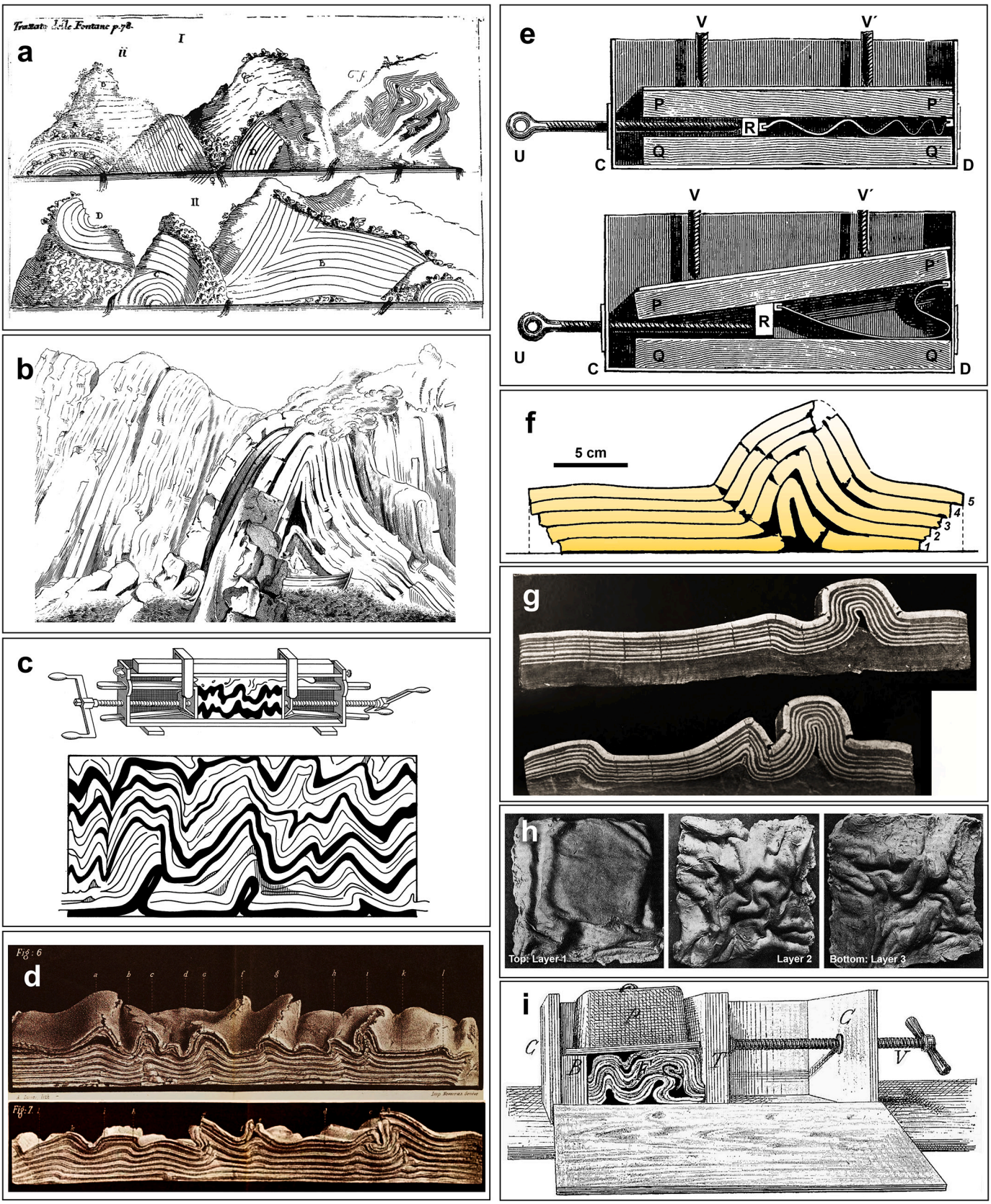

Fig. 3. a) Field observations in the European Alps around Lake Uri, Switzerland. The panel shows a part of a larger sketch of Johann Scheuchzer, published by Antonio Vallisneri (1715) (from Ellenberger, 1995). b) Field observations of folding in slate near St. Abb's Head, Berwckishire (after Hall, 1815). c) Top: device for scale model of folding by lateral compression, presented by James Hall to the Royal Society of Edinburg in 1812. Bottom: Original sketch of James Hall's (1815) folding experiment (after Hall, 1815). d) Original photographs of Favre's (1878) folding experiments where deformation was applied by releasing a stretched basal rubber film overlain by clay layers (after Favre, 1878). e) Daubrée's (1879) device and experimental model investigating fold formation under confining pressure (after Daubrée, 1879). f) Reade's (1886) clay folds investigating flexural slip (after Reade, 1886). g) Original photograph of Willis's (1894) folding experiments using

wax, plaster, and oil mixtures (after Willis, 1894). h) Avebury's (1903) experimental results on the 3D evolution of folds with depth (after Avebury, 1903). i) Meunier's (1904) experimental model investigating fold asymmetry and confining pressure relationships. j) Folds developed under pure shear and simple shear conditions (after Mead, 1920). k) Folds, faults, and fault-related folds developed in multi-layered models made of dampened clay and sand mixtures in different contractional and extensional settings (from Forchheimer, 1883). l) Fault-related folding resulting from horizontal shortening of a sand and clay multilayer sequence (from Schardt, 1884). m) Cadell (1889) simulating folds and thrusts with his experimental 'squeeze box' surrounded by the materials and devices used to conduct the experiments (after Cadell (1889). Cadell's watercolour illustrations summarizing the evolution (right to left) of folds and thrusts (Image courtesy the British Geological Survey). Bottom: Redrawn sketch of Cadell's (1889) folding and faulting experiments (from Cadell, 1889). n) Folds and fault-related folds developed in multi-layered models made of dampened sand, clay, and plaster (gypsum) mixtures under horizontal shortening conditions (from Paulcke, 1912). o) Folds and faults developed in multi-layered models that show the relationship between rheology and deformation pattern (from Lohest, 1913). p) Illustration of how parasitic folds develop in limbs of the major parallel fold (from Hall, 1815). q) Illustration of mechanical analysis of buckling with the formation of cleavage surface and sliding in the interface between different layers (from Smoluchowski, 1909). r) Experimental buckling of single layer (1–3) and multilayer (4–9) that show effects of thickness and spacing on fold geometry (from Currie et al., 1962). s) Formation of similar folds according to Carey (1962). t) Distribution of computed shear viscosities during 25 to 90% shortening (from Parrish, 1973). u) Stages in the development of the finite strain patterns for the fold with a viscosity ratio of 42.1. The lines are oriented in the directions of the principal strains and their lengths are proportional to the quadratic extension (from Casey, 1976). v) Logarithmic viscosity distribution of linear-viscous finite element models of single layer folding under pure and simple shear (from Llorens, 2019). w) Finite element modelling showing the distribution of the maximum shear strain after 28% of bulk shortening and investigate the control of overburden, thickness, and detachment layers on the style of deformation and fold geometries (from Humair et al. (2020)).

Playfair (1802) also reached this conclusion, although he considered the primary fold-forming force to be vertical. Experimental modelling has now been used in the study of folds and folding for more than 200 years, building upon the approach first applied by Sir James Hall in 1815 (Fig. 3b, c), who has been called "the Father of Experimental Geology".

James Hall was also probably the first to use the word *fold* in connection with geological structures (Hall, 1815, p. 86), where he wrote:

> "*The consequence was, that the extremities were bought nearer to each other, the heavy door was gradually raised, and the strata were constrained to assume folds, bent up and down, which very much resembled the convoluted beds of killas, as exhibited in the craggs of Fast Castle, …*".

Hall (1815), a few years after De Saussure's death, insisted that the cause of folds was to be found in great tangential pressure in the Earth's crust. He had examined the belt of deformed Silurian clastic rocks that run in an approximately ENE direction across the southern Uplands of Scotland from Galloway to Berwickshire (Hall, 1815). His schematic cross-section to illustrate the hypothetical continuation of the strata where they had been removed by erosion or were covered by plants and debris is shown in Fig. 3b. In order to demonstrate that such forces could produce the results observed, he made his famous analogue models, where during shortening the layers and rocks buckled (Fig. 3c). Favre (1878) developed another experimental setup based on the progressive release of an initially stretched basal rubber film onto which a homogeneous potter clay layer was deposited. In this way, Favre was able to produce a series of anticlines and synclines (Fig. 3d). Daubrée (1879), who for over forty years devoted himself untiringly to the pursuit of experimental geology and whose great work entitled "Études synthétiques de Géologie Expérimentale", studied the influence of layer properties (thickness and rheology) and pressures performed on the geometry of a single layer fold. He demonstrated that fold wavelength depends on the layer thickness and rheology, whereas the fold symmetry depends on the confining pressure (Fig. 3e). Reade (1886) also developed several experimental models investigating layer-parallel sliding or flexural slip and the influence of layer thickness on folding (Fig. 3f).

Reade (1886, p. 216–217) was also probably the first to use the geometric term *Chevron fold*, where he wrote in a figure caption (Fig. 4a):

> "*A to B represents a series of horizontal sedimentary beds, and B to C the same set of beds folded into zigzags, which I call chevron-folds, from their likeness to the Norman ornament of that name*".

Among the early experimental studies on folding are the outstanding contributions of Willis (1894) in his study of Appalachian folding. Willis used brittle-viscous material made of a mixture of beeswax and plaster to investigate the influence of confining pressure, layer thickness, and layer plasticity (competence) on folding (Fig. 3g). Hence, he explored the concepts of "active" and "passive" roles of layering in folding. Willis (1894) also introduced the concept that "initial dips" play a significant role in determining where folds will initiate.

As studies on folds and folding progressed, experimental modellers also started investigating features like 3D evolution of folding with depth (Avebury, 1903, 1905) (Fig. 3h), the relationship between fold asymmetry and confining pressure (Meunier, 1904) (Fig. 3i), fold axis orientation as a function of kinematics (Mead, 1920) (Fig. 3j), the growth of en-échelon folds (Link, 1928), and according to the fact that faults and folds could be associated with each other, the relationship between folding and thrusting in multi-layered models made of dampened clay and sand mixtures under varying boundary condition (extension, horizontal and vertical shortening) (Forchheimer, 1883) (Fig. 3k), the effect of layer rheology on fold and fault-related fold geometry (Schardt, 1884) (Fig. 3l), and the evolution of fault-related folds, thrust sequences, nappe tectonics and wedge dynamics (Fig. 3m-o) (e.g., Cadell, 1889, 1896; Paulcke, 1912; Koenigsberger and Morath, 1913; Lohest, 1913; Chamberlin and Shepard, 1923; Chamberlin, 1925; Terada and Miyabe, 1929; Kuenen and de Sitter, 1938). Among the early studies on experimental modelling of folds, there are some pioneering works on the geometric relationships between folds, cleavages and lineations (e.g., Sharpe, 1847; Sorby, 1849; Fisher, 1884; Harker, 1885; Becker, 1893, 1896). The seminal work of Hubbert (1937) introduced the concept of "scaled models" to the geological community, a concept already well known at the time in civil engineering, as well as in hydro- and aerodynamics. A properly scaled model can not only reproduce natural geometries and structures, but also allows inferring physical quantities.

The earliest attempts to classify folds were made by De Margerie and Heim (1888), p. 49–63), who introduced and classified "simple folds" into six types: upright, asymmetric, overturned, recumbent, isoclinal, fan-shaped folds, as well as "composite folds" (Fig. 4b), and then Van Hise (1896a, 1896b), who, in addition to the definition of composite and complex folds, observed that many geological folds either show a relatively constant orthogonal layer thickness (now usually termed "parallel" or "concentric folds") (Fig. 4c) or limb thickness reduction (now usually known as "similar folds") (Fig. 4d). Van Hise (1896a, 1896b) also was concerned with the asymmetry of folds. He deduced that asymmetry can be a result of interactions of folds with different wavelength. In this regard, he also recognized that the "abnormal folds" (now called "parasitic folds"), are a result of layer-parallel slip associated with the larger fold (Fig. 3p). The identification of structural and fabric symmetry was also an important topic, as considered in several works, for example, the very term *déjeté* and or *régard d'un pli* used by French researchers (e.g., Thurmann, 1853, quoted by De Margerie and Heim, 1888, p. 110; Favre, 1878, p. 205; Schardt, 1884, p. 153), which applied to an asymmetrical fold and suggests movement or tilting in a certain direction and toward the steeper side. Many older structural geology

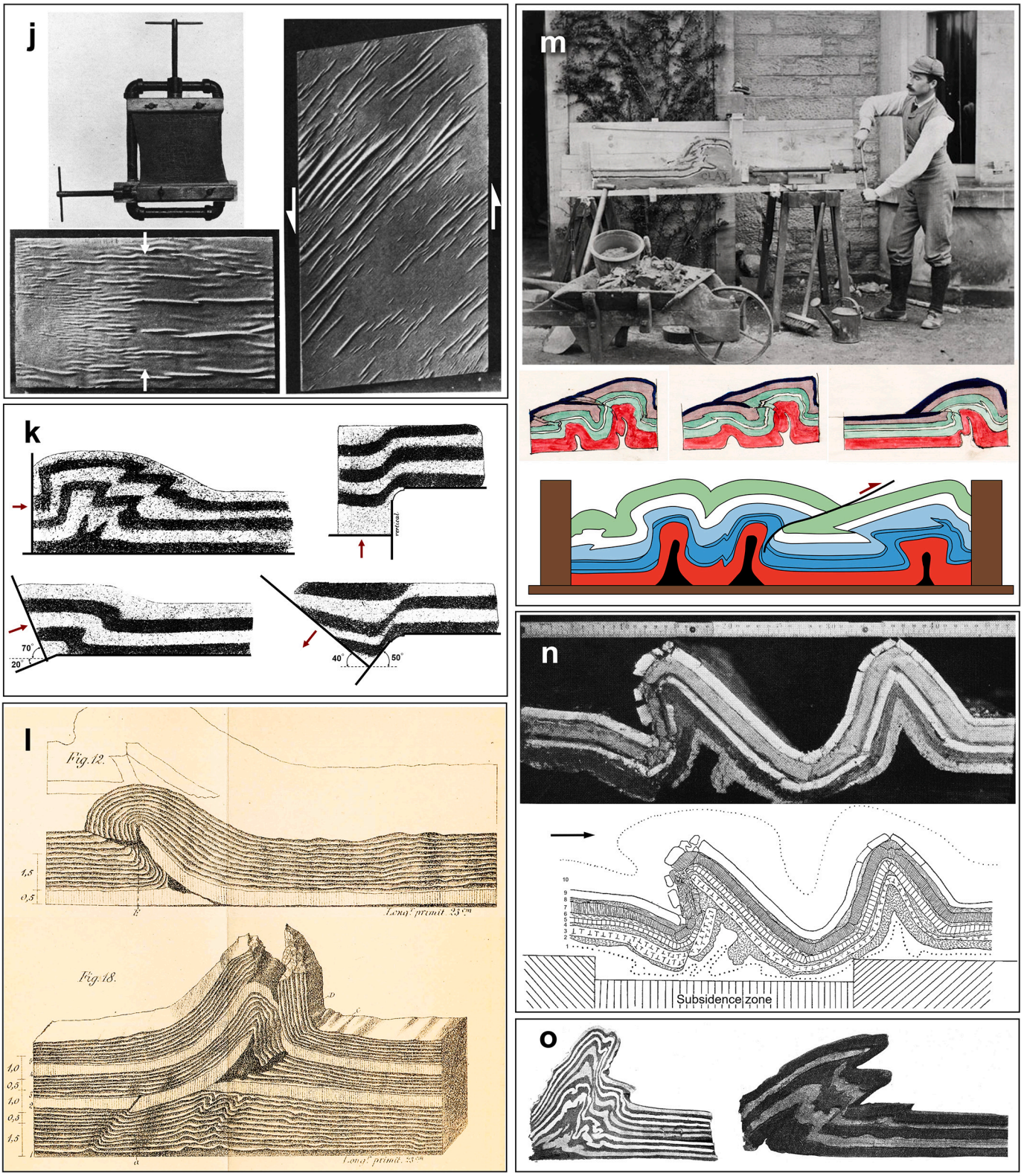

Fig. 3. (*continued*).

text books (e.g., Geikie, 1908; Leith, 1913; Willis, 1923; Nevin, 1931; Willis and Willis, 1934; Billings, 1946; Hills, 1963; de Sitter, 1964) provided detailed considerations and analyses of folds and other structures based on fold geometry, kinematics and, to a lesser extent, mechanics.

The first mechanical analysis of folding as a buckling problem was studied by Smoluchowski (1909), who computed the shape of waves in an elastic layer on a dense, inviscid, fluid substratum, and also noted that the formation of cleavage surfaces and sliding in the interface between different layers (Fig. 3q). The geological problem that interested Smoluchowski (1909) was the deformation of the Earth's crust on a soft mantle. However, from the late 1950s onwards, mathematical

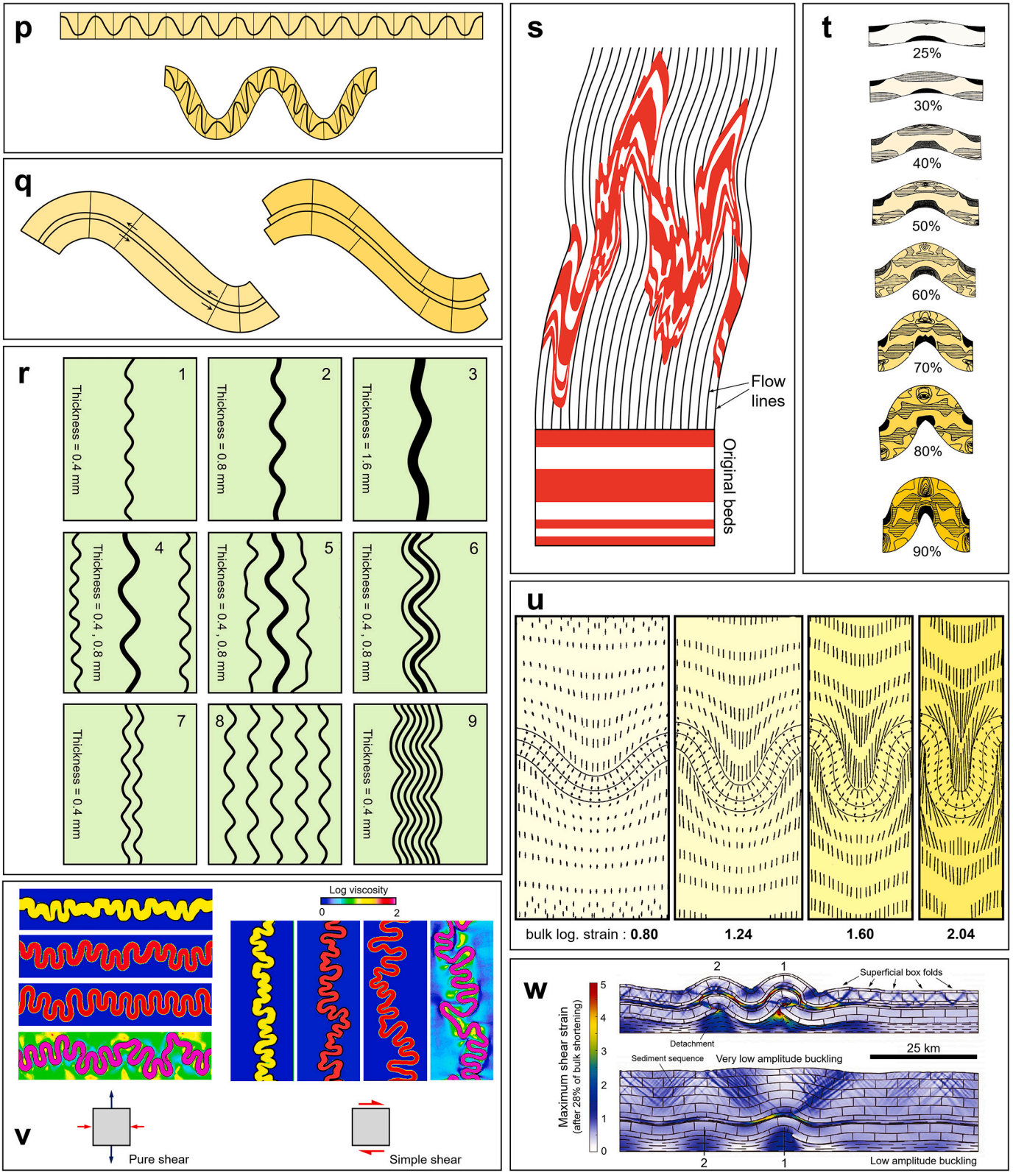

Fig. 3. (*continued*).

expressions were introduced to the structural geology community to explain folds and folding based on geometry, kinematic and continuum mechanic fashions. In this regard, Maurice Biot (1957, 1961) entered the field of geological folding theory with a paper in 1957 that had a huge impact on the geological community until the present day. Biot also produced several other benchmark papers (e.g., Biot, 1959, 1961, 1964, 1965) that presented some ideas on the mechanisms of folding, especially the role of *instability*, arguing that rock deformation and fold shapes are governed by viscosity (a belief that is still held by some researchers to the present day). However, the basic fold shape in his theories is sinusoidal for low-amplitude folds in an infinite medium with initial imperfections that are consistent with some observations.

Ramberg (1959, 1961) arrived at the same equations as Biot (1957, 1961) for the *dominant wavelength* for folding of viscous layers, although using different techniques and assumptions. Biot et al. (1961) rederived his earlier result and assumed perfect slip whereas Ramberg (1959, 1961) assumed perfect cohesion between the layers. There were also some researchers who continued to develop the earlier single-layer elastic models. Carey (1962) considered passive similar folds, which had termed "*rheid folds*" by Carey (1953), formed by heterogeneous simple shear along the axial surface or "*flow lines*", with no shortening normal to the shear flow direction (Fig. 3s), although he did not clearly name his mechanism. However, according to Flinn (1962), the classical concept of rheid folding is mechanically unrealistic. Flinn (1962) considered the movement of planes and lines in progressive homogeneous strain and showed that during homogeneous strain, no folds and boudins can be generated. Hence, he concluded that folds are a result of a process of buckling and strong flattening. Furthermore, Flinn (1962) emphasized that fold orientation is largely controlled by orientation of the finite strain axes and the pre-existing fabrics in a progressive bulk coaxial strain field of various strain symmetries, so that layer-parallel shortening of a horizontal layer gives upright folds with horizontal

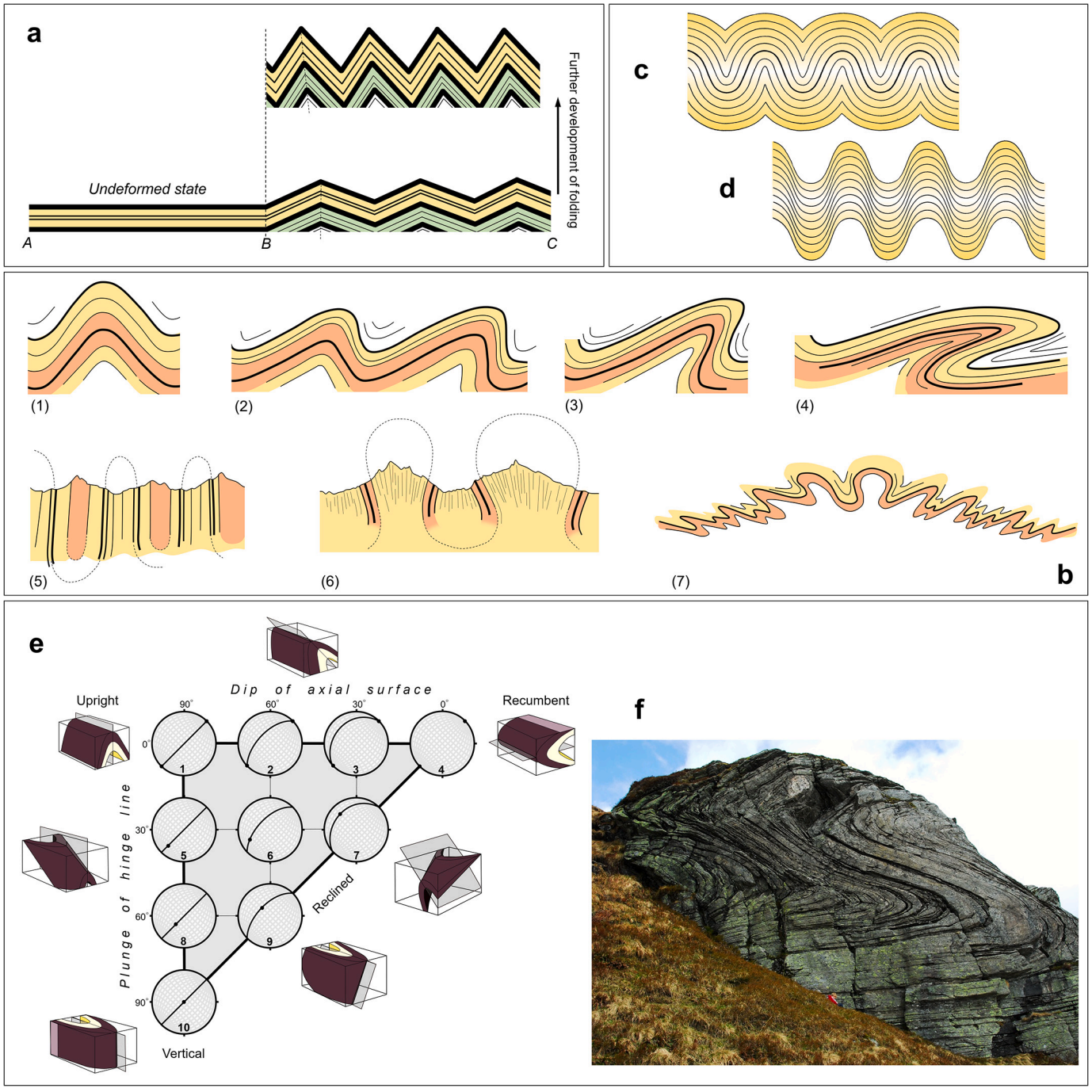

Fig. 4. a) Redrawn sketch of chevron folds identified and introduced by Reade (1886). b) Redrawn sketches of simple and composite folds classified by De Margerie and Heim (1888): 1) simple upright, symmetric fold, 2) simple asymmetric or inclined fold, 3) simple overturned fold, 4) simple recumbent fold, 5) simple isoclinal fold, 6) simple fan-shaped fold, 7) ideal composed fan fold. c) Parallel, and d) similar folds (after Van Hise, 1896a). e) Fleuty's (1964) diagram used for describing the orientation and classification of folds based on the geometric parameters of axial surface and hinge line (modified after Fleuty, 1964). f) Recumbent folds related to backsliding of Caledonian nappes, SW Norway.

fold axes, dipping layers give plunging folds, and vertical layers give vertical fold axes (Fig. 4e). Moreover, a folded layer can be lengthened and unfolded when rotated into the extensional field during progressive deformation. In addition, hinge orientation typically varies in layers oblique to the principal strain axes, which results in complex structural relationships, including non-cylindrical fold geometries.

Currie et al. (1962) presented an elastic model concerning the mechanics of rock folding, in particular looking at the folding of sedimentary rocks under tangential loads using stiff layers of rubber of varying thickness in softer photoelastic gelatine, and extended previous models to a multilayer formulation by considering layers of equal thickness, as well as neglecting friction between the layers and assuming the bending energy of each layer would be the same as its neighbour's (Fig. 3r). Following studies on structural analysis of geological structures and spatial and temporal relations of different structures and fabrics, the term *tectonic style* was introduced through an unpublished statement by M. Lugeon in 1948. This term refers to the total character of a group of related mesoscopic structures that distinguishes it from a group of comparable structures of another place or age to describe of all tectonic structures including folds (Turner and Weiss, 1963, p. 78–79). Hence, a tectonic style embraces all the morphological features that characterize a given structure. Fleuty (1964) proposed terms to define fold attitude (hinge and axial surface orientation) and tightness (interlimb angle), and these parameters became the basis for practical geometric classification of folds (Fig. 4e, f). Fleuty's classification and terminology, which also helped link fold shape with strain, was quickly accepted and rigorously applied by the structural geology community. However, folding (and also refolding) of rock layers into a large range of different patterns was still rather enigmatic to structural geologists when John Graham Ramsay (1931–2021) began working out the details of fold geometry, classification, mechanisms in relation to stress and strain in a relevant mathematical framework, which lead to his landmark textbook "*Folding and fracturing of rocks*" (Ramsay, 1967).

The use of numerical models, especially finite difference and finite element methods, since the late 1960s has greatly extended knowledge and quantitative understanding of the mechanical evolution of folding. Chapple (1964, 1968) was the first to publish computer simulations of buckle folding of a viscous layer embedded in a matrix of lower viscosity, where the layer was initially in the form of a low-amplitude sine wave, and extended the infinitesimal analysis of Biot's theory using finite difference equations and calculating strain rates and finite strains. After that, the first fully two-dimensional finite element simulation of viscous buckle folding was performed by Dieterich and Carter (1969) and Dieterich (1970) with geometry predicted by Euler's method, who calculated the stress evolution (magnitude and orientation) in amplifying single layer folds in a uniform isotropic plate, as well as the role of relative viscosity of the layer and media on the shape of high-amplitude folds. Hudleston and Stephansson (1973) obtained the same general results using the finite element method, but changed the amount of layer-parallel shortening during amplification and in order to compare the resulting fold shapes to natural folds. Parrish (1973) used the finite element method to study high-amplitude folding of power-law (non-Newtonian) material and obtained the same previous general results as Hudleston and Stephansson (1973) (Fig. 3t). Casey (1976) and Cobbold (1976, 1977) repeated some of the earlier works (e.g., Dieterich and Carter, 1969), using a more accurate and comprehensive method of numerically integrating the displacement rate solutions with the geometry predicted by Biot's theory of internal instability for successive stages in the amplification of a sinusoidal single layer buckle fold (viscous layer and matrix) and also patterns of cleavages around fold hinges (Fig. 3u). Since this pioneering time of computational structural geology and tectonics, an increasing number of more sophisticated numerical models have been published (Fig. 3v, w) (e.g., Hobbs et al., 2011; Llorens et al., 2013a, 2013b; Schmalholz and Mancktelow, 2016; Llorens, 2019 and references therein).

4. 2D geometric classification of folds

Most descriptions of fold shapes focus on 2D fold profiles perpendicular to the fold hinge. Several graphical methods aim to do this: the Busk method deals with parallel folds; and the Higgins (1962) method uses concentric arcs. The following discussion uses the usual definition of the term 'fold hinge' as the row of points of maximum local curvature between two adjacent inflection points (i.e., points for which the curvature equals to zero) on the profile of a folded surface. Fold hinges and inflection points are usually selected by visual inspection. In order to reduce and eliminate the errors, Srivastava and Rastogi (2010) developed HingeInflex, a numerical program developed in MATLAB® to accurately determine inflection and hinge points. This method calculates the curvature at different points along a curved profile, but can only analyse fold shapes described by a single-value function. Fold profiles may be analysed geometrically as either: (1) a set of layers with variable thickness defined by some geometrical attribute such as dip isogons, or (2) the form of a set of single boundary surfaces described as a geometric function (Whitten, 1966; Ramsay, 1967; Hudleston, 1973b, 1973c; Stowe, 1988). Geometrical descriptions of folds and fold complexes go beyond basic descriptions of limb dip, hinge-line plunge etc., but such descriptions usually form the foundation of a structural description that is independent of any geodynamic concept.

4.1. Classification of profiles of individual folded surfaces

4.1.1. Classifications based on the use of non-functional parameters

4.1.1.1. Interlimb angle. For geometrical fold analysis, it is necessary to choose a fold parameter and select a reference system with two lines: one tangential to the fold profile curve at the hinge point (x-axis) and an orthogonal y-axis. In 2D analysis, the fold attitude can be described by simply specifying the plunge of the axial trace (Fig. 1a) in the fold profile plane. A fold profile is a two-dimensional projection of the fold onto a plane perpendicular to the fold hinge (Ramsay, 1967). As the hinge is the point of local extreme curvature between two inflection points (Fig. 1a) on the limbs, this definition fails for concentric folds with their limbs of constant curvature. To solve this problem, Adamuszek et al. (2011) described fold geometry using a fold geometry toolbox. This toolbox positions the fold so that all points in curvature-arc-length space between inflection points are fitted to a second-order polynomial. The local extreme in this polynomial represents the fold hinge (Fig. 1a). The topographically highest and lowest points of a fold, respectively, are called crest point and trough point (Fig. 1b), and these points do not necessarily coincide with fold hinge lines which are commonly found to be curved. Fold arc-length is the distance measured over the folded surface and twice the arc-length between two inflection points (Fig. 1b) (Hudleston, 1986).

A variety of parameters have been used to describe fold geometry. Fleuty (1964) defined the term fold limb (Fig. 1a) as the part of the folded surface between adjacent fold hinges on the same surface. He used the interlimb angle (θ) (Fig. 1a) to describe fold tightness (Fleuty, 1964, p. 470–471, Fleuty, 1987) as the minimum angle between the limbs as measured in the profile perpendicular to the fold axis, or the angle between the lines drawn tangential to the fold surface at the inflection points (Fleuty, 1964). Fleuty (1964) then used interlimb angle to describe fold tightness and differentiate between the following types of folds (Fig. 5): gentle ($180^\circ > \theta > 120^\circ$), open ($120^\circ \geq \theta > 70^\circ$), close ($70^\circ \geq \theta > 30^\circ$), tight ($30^\circ \geq \theta > 0^\circ$), isoclinal ($\theta \approx 0^\circ$) (Tremlett, 1976) and elasticas or mushroom ($\theta < 0^\circ$ or less than -3°). Measurements of interlimb angle can be obtained from images of fold profiles, by direct measurement in the field, or by plotting fold limbs on an equal-area net. For layer-parallel shortening, this angle is related to the amount of shortening perpendicular to the fold axial surface, and there are three main fold shapes for a particular limb dip: circular, sinusoid and chevron

folds (Currie et al., 1962; Treagus, 1997; Ghassemi et al., 2010). The arc-length of different fold shapes is expressed as mathematical functions by Ghassemi et al. (2010) for similar folding, and the evolution of the amplitude – half wavelength aspect ratio with respect to the maximum limb dip at inflection point, is introduced for each individual fold shape (Fig. 6). For chevron folds, this aspect ratio increases faster during fold tightening than for other fold shapes, even though slip often takes place and rotates the chevron fold limbs. From the sinusoidal shape, the amplitude – half wavelength aspect ratio decreases as limb rotation progresses, following the parabola, double hinge and ellipsoidal curves (Fig. 6).

A quantitative description of fold shape based on statistical techniques is proposed by Loudon (1964). He applied statistical moments to poles to bedding, expressed as direction cosines and considered each moment as a measure of any particular fold. The first two moments are:

$$m_1 = \frac{\sum_{i=1}^{N}\theta_i}{N}, \text{a measure of attitude} \quad (1)$$

$$m_2 = \frac{\sum_{i=1}^{N} cos^2\theta_i}{N}, \text{a measure of tightness} \quad (2)$$

where θ_i is the angle between the line joining inflection points and a bedding pole and N is the number of equi-spaced readings of θ_i. Other moments or combinations of moments can be used as measures of asymmetry, shape, skewness and kurtosis (the "tailedness" of the probability distribution of a real-valued random variable in probability theory and statics, or the sharpness of the peak of a frequency-distribution curve). These moments are a series of scalar quantities, with potential use for classification purposes and for regional analysis of folds. Whitten (1966) has also applied a more general version of Loudon's method to folds but was unable to calculate the statistical moments for individual folds, as most natural folds are non-cylindrical. The main disadvantage of this method is related to its application of statistical moments. In addition, Grose et al. (2017, 2019) adapted the technique so that the fold profiles and fold axis fields can be derived from structural measurements using spatially adapted statistical methods to the "fold coordinate system" that includes uncertainty characterization and sampling of the model space.

Folds with equal interlimb angle can differ in tightness due to the variations in curvature along their profiles. For buckle folds, the shape of the fold in sections perpendicular to its axis (Fig. 1a) is related to the rheological behaviour of the folded multilayer sequence, which continuously controls the attitude of layers at increasing distance from the fold hinge. Ramsay (1967, pp. 349–351), suggested that the simplest way of defining the limits of the hinge zone is by comparing its curvature with that of a circular arc drawn with i_1 i_2 (inflection points of folded surface) as diameter. In this regard, that part where the fold curvature exceeds that of the circular arc can be defined as the hinge zone and the parts of the fold on either side of it where the curvature is less than that of the circular arc are defined as the fold limb (Ramsay, 1967; Price and Cosgrove, 1990). This definition is useful, but one of its limitations becomes apparent when applied to those folds where the amplitude to half-wavelength ratios (or curvature) are $\leq$1.

Alternatively, the hinge zone is defined by two parameters P_1 and P_2 to describe fold profiles. P_1 is the ratio of the fold limbs lengths to the width of the hinge zone. P_1 is then defined as the ratio of the length of projection of limbs on the line joining the inflection points to the length of the projection of hinge zone on the same line. Moreover, P_2 is obtained by expressing the maximum curvature of the folded surface as a ratio of the unit curvature of the circle drawn with two inflection points as a diameter. A limitation of this definition is that the values of both P_1 and P_2 approach infinity as the hinge zone is reduced to a point as in a perfect chevron fold. Thus, Hudleston and Lan (1994) focused on the curvature of the fold hinge to evaluate the power-law exponent of viscous layers involved in buckle folds. They calculated the curvature, $k(x)$, by fitting low-degree polynomials to the x-y coordinates used to represent shapes and evaluate Eq. 3 for a best-fit polynomial:

$$k(x) = \frac{d^2y/dx^2}{\left[1 + (dy/dx)^2\right]^{3/2}} \quad (3)$$

Increasingly angular hinges imply more localised and therefore higher hinge strains, and thus a higher power-law exponent.

4.1.1.2. The classification suggested by Twiss (1988). Twiss (1988) and Twiss and Moores (2007), based on Fleuty's (1964) work, proposed three classifying parameters of fold style by comparison with the shapes of cylindrical surfaces. These parameters were: the aspect ratio P of the amplitude to the half-wavelength, the relative limb rotation or folding angle ϕ (= 180° – interlimb angle; this relation is valid for gentle to isoclinal folds) (Fig. 7a), and a measure of the relative curvature at the fold closure (the bluntness, b). The term *fold style* was used specifically about the set of geometric and morphologic features that describe the form of folds, notably cylindricity, tightness, symmetry, aspect ratio P, and bluntness (angularity). Fold style involves any geometrical feature that is common to a group or generation of folds, particularly in an orogenic belt or in a single lithological unit.

In Twiss' (1988) fold classification, (a) the folding angle (Fig. 7a) in the range of 0–360° defines the three major types: Acute ($0° < \phi < 180°$), Isoclinal ($\phi \approx 180°$), and Obtuse ($180° < \phi \leq 360°$) and six subtypes (gentle, open, close, tight, fan and involute), (b) if the aspect ratio, folding angle and bluntness fall within the range of $0.1 \leq P \leq 10$ (or $-1 \leq \log P \leq 1$) which defines five categories of folds as (Fig. 7b): wide, broad, equant, short and tall, and (c) if the bluntness falls within the range $0.0 \leq b \leq 2$ it defines six fold types as sharp, angular, subangular, subrounded, rounded and blunt (Fig. 7c) (Twiss and Moores, 2007, p. 284–287). The bluntness in perfect chevron and circular folds is equal to 0 and 1, respectively.

A challenge with Twiss' (1988) fold classification is that the results of its application cannot be fully represented on a two-dimensional diagram so that natural folds will plot in the "impossible geometries" domain of the trapezoidal diagram shown in Fig. 7d. Moreover, data from complex multilayer buckle folds and macro-scale to regional folds as plotted on this diagram will show large errors. Twiss' (1988) diagram (Fig. 7d) has to our knowledge never been applied in published research. Furthermore, the classification of asymmetric folds is complicated by requiring six parameters (aspect ratio, folding angle, bluntness of closure, two inclination angles and the hinge tangent angle). In general, the simplest classification of asymmetry is the ratio between the short and long limbs, which is very easy to use.

4.1.2. Mathematical classification of fold profile

4.1.2.1. Classification using Fourier series. Several authors (Chapple, 1968; Stabler, 1968; Hudleston, 1973a; Ramsay and Huber, 1987, p. 314–316; Stowe, 1988; Singh and Gairola, 1992; Bastida et al., 1999, 2005) have used Fourier series to describe single fold shapes, assuming that folds are naturally periodic. The Fourier coefficients were optimized using least squares fitting of the coefficients for a known wavelength. The advantage of this method is that a limb is approximated by a mathematical function, which is useful for further analysis of folding mechanism.

The most commonly used Fourier transformation for folds was suggested by Hudleston (1969, 1973a, pp. 15–26), who used only the two coefficients b_1 and b_3 of a sine series to classify the profile shapes of folded surfaces through a graphical representation of b_1 vs. b_3. In this regard, if $f(x)$ is a periodic function with period 2π and integrable between $-\pi$ and π, the form of the Fourier transformation useful to geologists is (Fossen, 2016):

$$f(x) = b_1 sinx + b_3 sin3x + b_5 sin5x \ldots \quad (4)$$

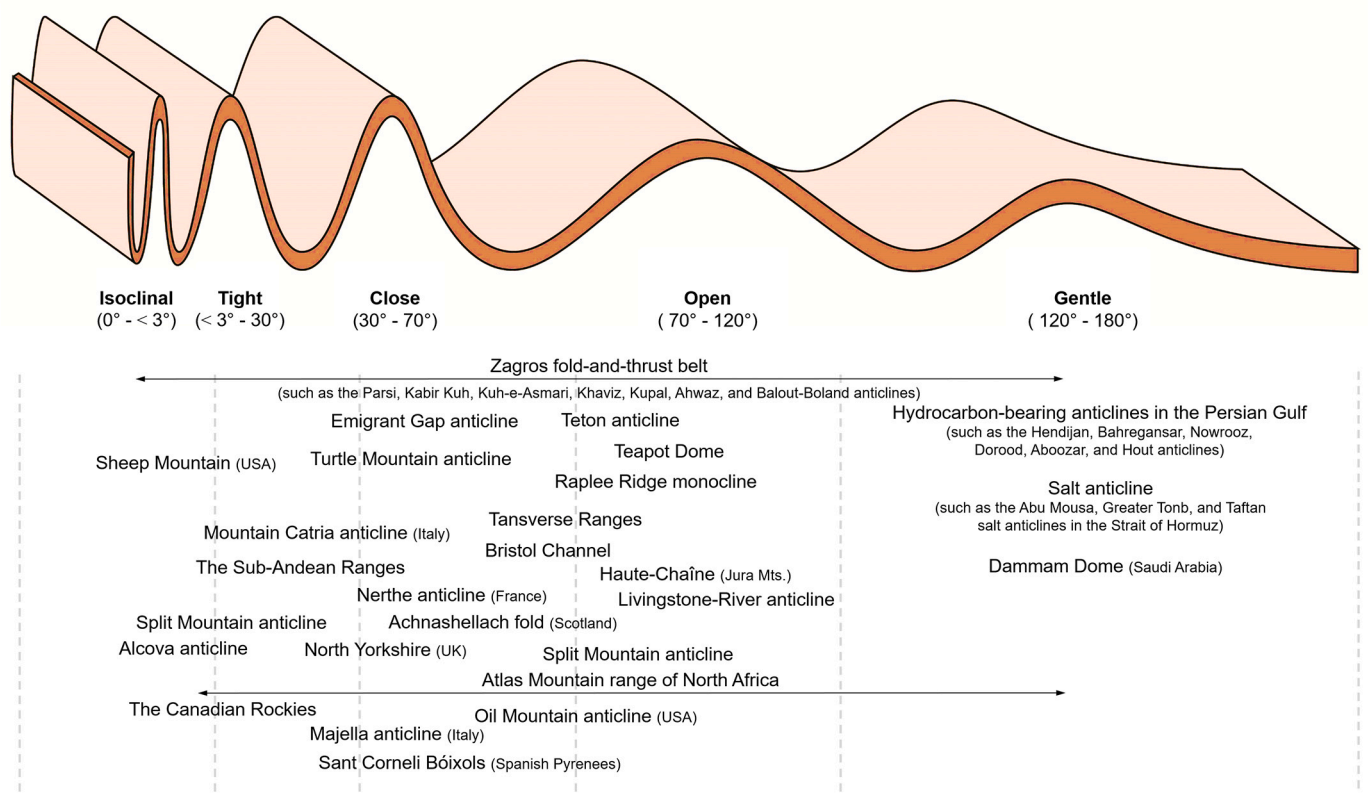

Fig. 5. Geometrical fold classification based on interlimb angle (modified after Fleuty, 1964) with the following examples of folds: From the Zagros fold-and-thrust belt, the Parsi, Kabir Kuh, Kuh-e-Asmari, Kuh-e-Pahn, Khaviz, Sim, and Meymand anticlines; From the USA, the Teton anticline, Sheep Mountain, Teapot dome, Emigrant Gap anticline, Grand Hogback monocline, Raplee Ridge monocline, and the Transverse Ranges; From the United Kingdom, Bristol Channel and North Yorkshire; From Europe, Sant Corneli Bóixols in the Spanish Pyrenees, Mt. Catria and Majella anticlines in Italy, and Nerthe anticline in France; as well as examples from the Persian Gulf, the Strait of Hormuz, Canadian Rockies, the sub-Andean Ranges, the North Sea, North Africa, and eastern Arabia.

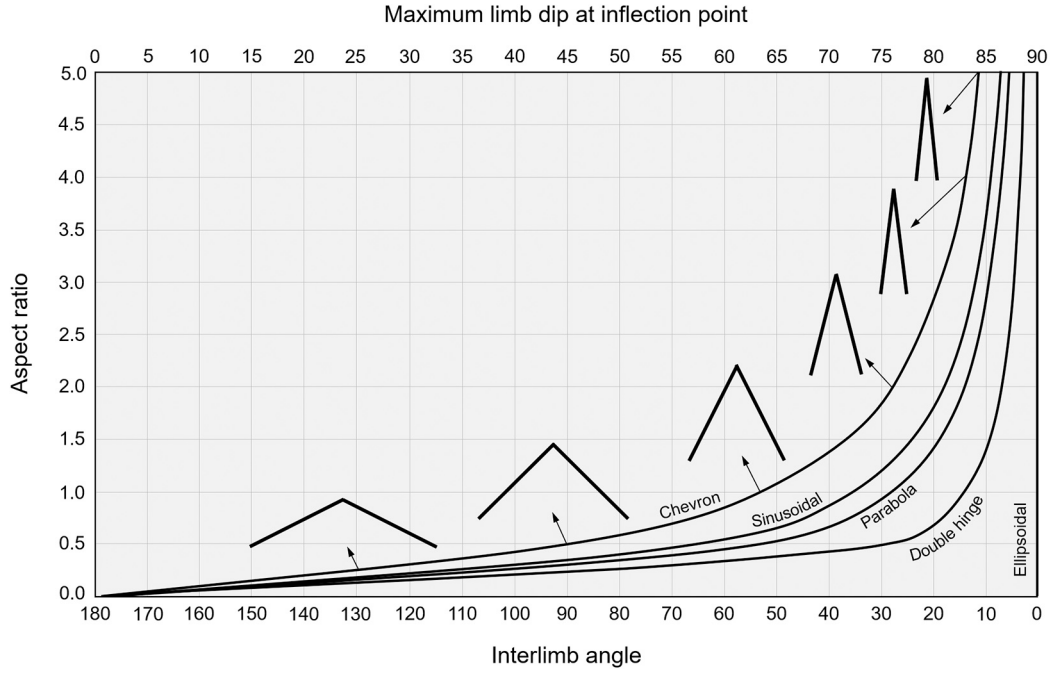

Fig. 6. Diagram of interlimb angle and maximum limb dip of different fold shaped versus the aspect ratio (i.e. ratio of fold amplitude to half the wavelength) of the folds (modified after Ghassemi et al., 2010).

where b_1 and b_3 are called the Fourier Coefficients, which are considered as significant inputs into the description of fold shapes and are unique to each waveform. Hudleston (1973a) dropped the b_5 components from this classification because it has little effect on the fold shapes and amplitudes. To apply this classification to natural folds, first select a sector of the complete layer between an inflection point and a hinge point. The coordinate y-axis is chosen so that it passes through the inflection point and is parallel to the axial surface of the fold. The x-axis of the coordinate system passes through inflection point perpendicular to the y-axis so that the origin is the inflection point. With this coordinate frame all the a-type Fourier coefficients become zero; only the b-type Fourier coefficients can be represented in the function. The values of these components can be obtained by finding coordinate values of any points on the original layer (Stabler, 1968):

$$y_1 = b_1 sinx_1 + b_3 sin3x_1 \tag{5}$$

$$y_2 = b_1 sinx_2 + b_3 sin3x_2 \tag{6}$$

$$y_3 = b_1 sinx_3 + b_3 sin3x_3 \tag{7}$$

By dividing the quarter wavelength fold sector into three equal parts, four determinants become very simple algebraic expressions and three ordinate measurements can be made to give the values (Stabler, 1968):

$$b_1 = \left(y_1 + \sqrt{3}\, y_2 + y_3\right) \Big/ 3 \tag{8}$$

$$b_3 = (2y_1 - y_3)/3 \tag{9}$$

Fourier transformation or harmonic analysis distinguishes folds into six standard shapes, from A (box folds) to F (chevron folds) (Fig. 8a), with five standard amplitudes (from 1 to 5) (Fig. 8b). For example: 2-4E to 2-3F fold classes are tight-to-open angular, chevron folds, with narrow hinge zones and quite straight limbs. Folds are classified by their general style or may be given a definitive letter and number classification to denote more exactly the amplitude-wavelength relationships. Hudleston's (1973a) scheme distinguishes 30 idealized fold profiles (Fig. 8b).

Stabler (1968) and Hudleston (1973a) both used the sine terms of a Fourier series to characterize single-surface fold shape, and Fletcher (1979), Johnson and Pfaff (1989) and Cruikshank and Johnson (1993) have used the cosine terms to analyse fold shape (layer and surface) and its changes during fold growth from low to moderate amplitudes. However, it should be noted that the single layer fold profiles we see in natural examples are solutions to the Swift-Hohenberg equation (Swift and Hohenberg, 1977; Ord and Hobbs, 2019):

$$\frac{\partial w}{\partial t} = \alpha \frac{\partial^4 w}{\partial x^4} + \beta \frac{\partial^2 w}{\partial x^2} + f(w) \tag{10}$$

where $w(x,t)$ is the deflection of a layer during folding measured as the displacement normal to the layer from its initial condition, x is a distance measured along the layer, t is time, and α, β are constants. In this equation, $f(w)$ is a function that expresses the resistance in the matrix to the deflection of the layer. This expression was solved assuming $f(w)$ to be a linear function of w (Biot, 1965), whereas in principle, the resultant fold profile could be quite irregular so that the solution is a localised fold rather than a sinusoidal fold train.

The Fourier approach is particularly useful for sinusoidal fold shapes whereby a limb can be approximated by a single mathematical function. One the negative side, it cannot be applied to chevron, elliptical or box folds. Upon inspection of the shapes of Hudleston (1973a) fold classes, we find that certain fold classes are defined by the ratio b_3/b_1, while the others involve variable ranges of b_3/b_1 values. The ratio b_3/b_1, or the slope on a graph of b_3 against b_1, is a sensitive indicator of shape, and varies from negative values for straight-limbed folds, through zero for sinusoidal shapes, to positive values for folds with rounded hinges and short limbs (Hudleston and Lan, 1994). Another limitation is that two Fourier coefficients can give only a rough approximation of the functions that describe fold morphologies (Stowe, 1988). Singh and Gairola (1992) reduced the ranges by adding eight more classes to Hudleston (1973b) classification. The ranges could be reduced still further by introducing more new classes. However, this would probably only increase the confusion in the nomenclature of fold shapes.

Schemes based on Fourier analyses do not describe fold asymmetry. Hence, Tripathi and Gairola (1999) proposed a classification of folds based on a concept of 'degree of symmetry' (D_A). D_A is deduced from the Fourier coefficients that define the shape and size of the two limbs of the fold. The degree of asymmetry of a folded surface, from one inflection point to another, is thus a function of the distance between the two points, which represents two limbs of an asymmetric fold, on the b_3 vs b_1 graph from the origin. In this regard, the degree of asymmetry is the sum of the differences in the aspect ratio (or size component) (Δ_{size}) and the shape component (Δ_{shape}) of the two limbs of an asymmetric fold (Tripathi and Gairola, 1999). A problem with this method is that the degree of symmetry does not express the extent to which the asymmetry is due to differences in shape or amplitude. Profiles of symmetric folds are characterized by a mirror plane of symmetry that passes through the closure and is normal to, and bisects, the median line segment between adjacent inflection points. Asymmetric folds have a shorter and steeper limb called a forelimb and a longer and gentler limb called a backlimb (Fig. 9). In order to represent the fold asymmetry on a 2D coordinate graph, it is necessary to describe this geometrical feature using only two parameters, but such a description is not complete. Bastida et al. (2005) improve this classification scheme by defining the degree of asymmetry as the ratio of "shape asymmetry" $S_a = A_b/A_f$ and "size asymmetry" $A_a = y_{0b}/y_{0f}$, where A_b and A_f are, respectively, normalised area of the backlimb and forelimb. The normalised area is the ratio of the area between the limb area and the rectangular area that bounds the limbs (Fig. 9). Also, y_{0b} and y_{0f} are the y_0 parameters of the backlimb and forelimb, respectively (Fig. 9). The plot of these parameters in a diagram of S_a against A_a for all folds of a specific set allows visualization of the variation in asymmetry of these folds.

Schemes based on Fourier analyses do not describe the degree of harmony of multilayer folds. This problem was partly solved by Srivastava and Gairola (1997) who proposed classifying multi-layered folds using an 'Index of Non-Harmony' (INH), that describes the degree of variation in shape of different fold surfaces. In this classification, $INH = 1000\,\sigma_n$, and:

$$\sigma_n = \sqrt{\frac{(\sum x^2) - (\sum x)^2/n}{n}} \tag{11}$$

where n is number of fold surfaces and $x = b_3/b_1$. Values of INH of multilayered folds are classified as 'Strictly Harmonic' (INH = 0), 'Periharmonic' ($0 < INH \leq 15$), 'Subharmonic' ($15 < INH \leq 30$), 'Subnonharmonic' ($30 < INH \leq 45$), 'Nonharmonic' ($45 < INH \leq 75$) and 'Strongly Nonharmonic' ($INH > 75$) (Srivastava and Gairola, 1997). This classification is limited, for example by being based on the b_3/b_1 ratio and not on the actual geometry of the fold surfaces. This implies, theoretically, that disharmonic multilayer buckle folds sharing the same shape but with different wavelengths and amplitudes (e.g., concentric semi-circular folds) may offer a 'strictly harmonic' fold class because the constitutive surfaces share the same b_3/b_1 ratio.

A harmonic fold is simply defined as being continuous along its axial surface for many multiples of the half wavelength, whereas a disharmonic fold dies out within a couple of half wavelengths (Twiss and Moores, 2007, p. 289; Fossen, 2016, p. 259). Multilayer folds formed by active folding die out in both directions along the axial surface trace, unless the fold ends at a discontinuity. In this regard, the half wavelength may be approximated by the spacing of adjacent axial surfaces (S) (Twiss and Moores, 2007, p. 290; Alsop et al., 2020), and the continuity of the axial surface (D) (or the depth of folding; see Twiss and Moores, 2007, p. 289–290) may be directly measured to produce a scale-

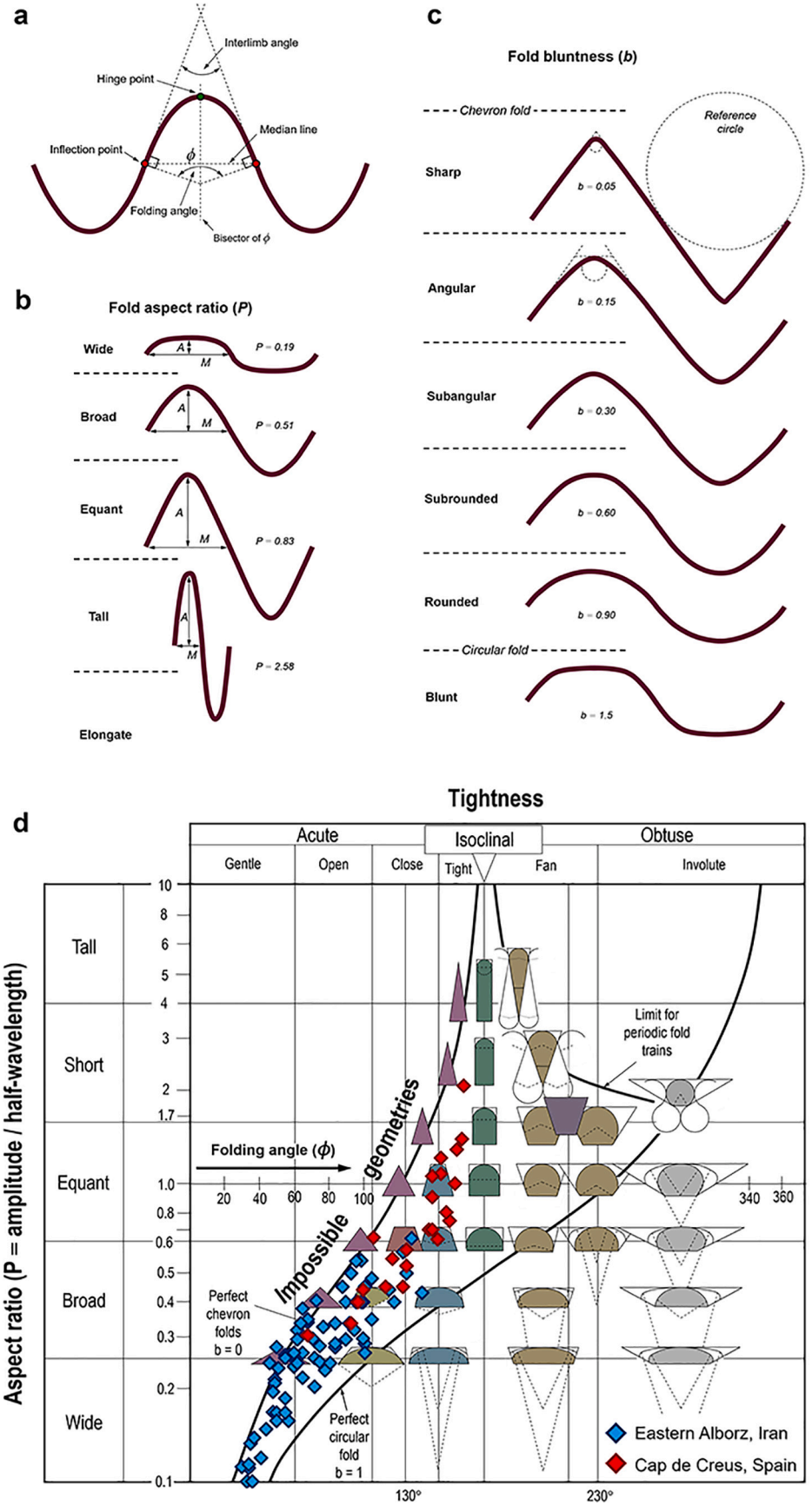

Fig. 7. a) The folding angle, interlimb angle, and symmetry of the folded surface. The folding angle ϕ is the angle between the normal to the folded surface constructed at the inflection points. b) Geometries of symmetric folds with various values of aspect ratio *P*. c) Geometries of symmetric folds with various values of bluntness *b* (a-c after Twiss and Moores, 2007). d) Plots of natural data sets on the trapezoidal system (logarithm of aspect ratio versus tightness) of Twiss's (1988) fold classification. For a given trapezoid, differences in fold style are defined by the bluntness. Modified after Twiss (1988).

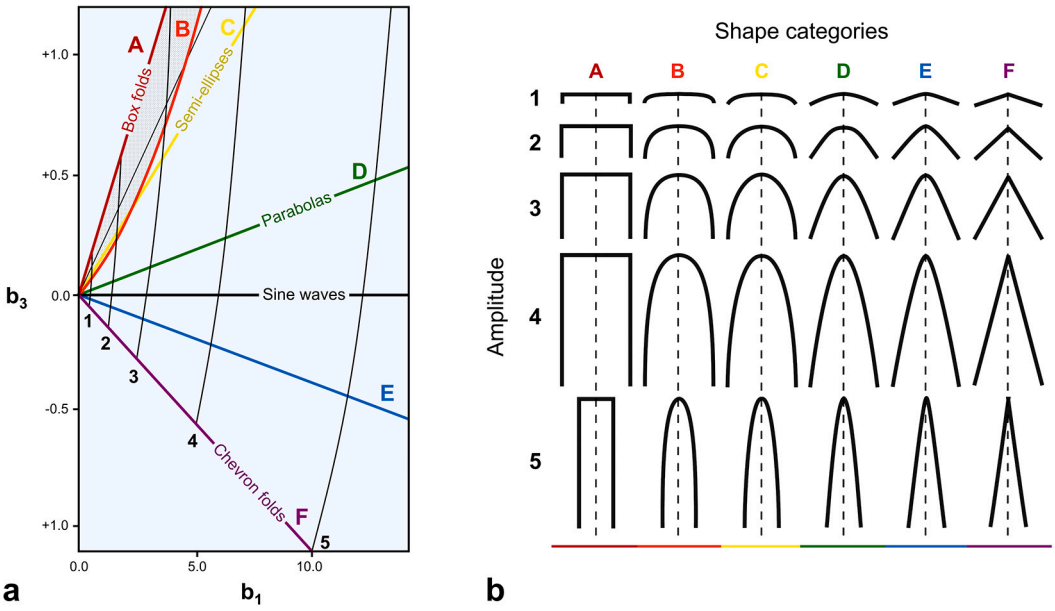

Fig. 8. a) Graphic method of plotting fold shape using Fourier coefficients (modified after Hudleston, 1969, 1973a). The stippled area is where double hinged folds occur. The letters A to F describe overall fold shape, and the numbers 1 to 5 relate to the amplitude number, which used for visual harmonic analysis and 30 ideal fold form defined between inflection and hinge points (b). Modified after Hudleston (1969, 1973a).

independent measure of the harmony (H) which is equivalent to the ratio D/S. Fig. 10 shows three examples of upright to asymmetric disharmonic folds. In general, plots on the D – S graph show that the distance (D) that individual meso-scale folds can be traced along their axial surfaces increases as the maximum spacing (S) between adjacent axial surfaces becomes greater (Fig. 10). In addition, the ratio H ranges 25 to 4, and is shown to reduce in a non-linear way as S increases (Fig. 10). In some cases, individual folds may form en-échelon arrays within the folded multilayer sequence. These folds do not geometrically interlink and do not therefore create refold patterns.

4.1.2.2. Classification using power function and conical curves. Bastida et al. (1999) proposed classifying fold shapes using a power function to characterize single limbs of fold profiles. They describe how to convert the shape parameter obtained from a given classification to the corresponding shape parameter for another scheme:

$$y = y_0 \left(\frac{|x|}{x_0} \right)^n \tag{12}$$

where n characterizes the fold shape, x_0 and y_0 are the coordinates of the inflection point, and y and x are the parallel to the vertical fold axial surface and horizontal coordinates, respectively within the interval $[-x_0 \ , \ x_0]$. In order to avoid the fold size effect, a normalised area, defined as the ratio between the area under the fold and the area under chevron fold with the same aspect ratio (or $2A/x_0y_0$) is used (Fig. 11a). Using these functions, a fold limb can be described by two parameters: (1) the exponent (n) of the corresponding power function describing the limb shape ($n = \frac{A}{x_0 y_0 - A}$), and (2) the aspect ratio or normalised amplitude, y_0/x_0, which is the ratio between the height and the width of the limb (Fig. 11a) (Bastida et al., 1999, 2005; Lisle et al., 2006). The amplitude and wavelength depend on layer thickness and viscosity contrast, so that the wavelength increases and the amplitude decreases with increasing layer thickness and viscosity contrast.

The following n values characterize some distinctive fold shapes (Fig. 11b): (1) $n < 1$ for cuspate folds; (2) $n = 1$ for chevron folds; (3) $n = 2/(\pi - 2) \approx 1.75$ for sinusoidal folds; (4) $n = 2$ for parabolic folds; (5) $n > 2$ for double hinge folds, and (6) $n \rightarrow \infty$ for box folds. Cuspate-lobate folds are trains of low-amplitude short wavelength folds with narrow sharp hinges in one direction and broad rounded hinges in the opposite direction. They are characteristic of compressed interfaces separating layers of strongly differing mechanical competence, so that the lobate folds are cored by the more competent and cuspate folds by the less competent material (i.e., cusps always point into the material with higher viscosity) (Ramsay and Huber, 1987, p. 394; Fossen, 2016). Cuspate-lobate folds formed in competent layers tend toward a perfect circular (concentric) shape (subclass 1B, see Subsection 4.2.1) with a maximum layer-parallel shortening of 36% (de Sitter, 1964; Ramsay, 1967), and a wavelength close to twice the layer thickness. Cuspate-lobate folds formed in an incompetent layer of thickness t enclosed in a more competent medium tend to form class 3 folds (Zagorčev, 1993). The power functions approximate well the geometry of folded surface profiles with interlimb angle >0°. The system chosen by Bastida et al. (1999) is formed by the tangent to the profile at its hinge point (x-axis) and its normal through this point (y-axis). This selection may cause practical problems of accurately determining the hinge and inflection point, a problem discussed by Aller et al. (2004).

Conic sections, as the method of mathematical function to description the geometry of folded surface profiles, have been used as a convenient way to characterize non-cylindrical folds or parts of folds (e.g., Dahlstrom, 1954; Twiss and Moores, 2007, p. 278; Davis et al., 2011, p. 365), even though it represents a simplification of most natural non-cylindrical fold shapes (Welker et al., 2019). Conic curves correspond to planar sections through a circular cone at different angles (Fig. 11). The shape of the conic depends on the orientation of the section, and lies in a spectrum of shapes ranging from closed ellipses with different aspect ratios, to parabola, and then through to hyperbolas with different aspect ratios (Fig. 11c). This progression in shape is expressed by an increase in the eccentricity, e (the amount a conic section deviates from being perfectly circular); this is the distance from a general point on the conical curve to a fixed focus divided by the distance from the general point to a fixed straight line. When $0 \leq e < 1$, the result is an ellipse, while $e = 1$ defines a parabola, and ($e > 1$) a hyperbola. The aspect ratios of the limbs h, defined as the ratio between their height and width of the limb considered (Aller et al., 2004) suggest that natural folds show a variety of shapes and amplitudes similar to the range exhibited by parts of conic sections with different eccentricities and axial ratios. However, Aller et al. (2004) point out a drawback in using eccentricity as a

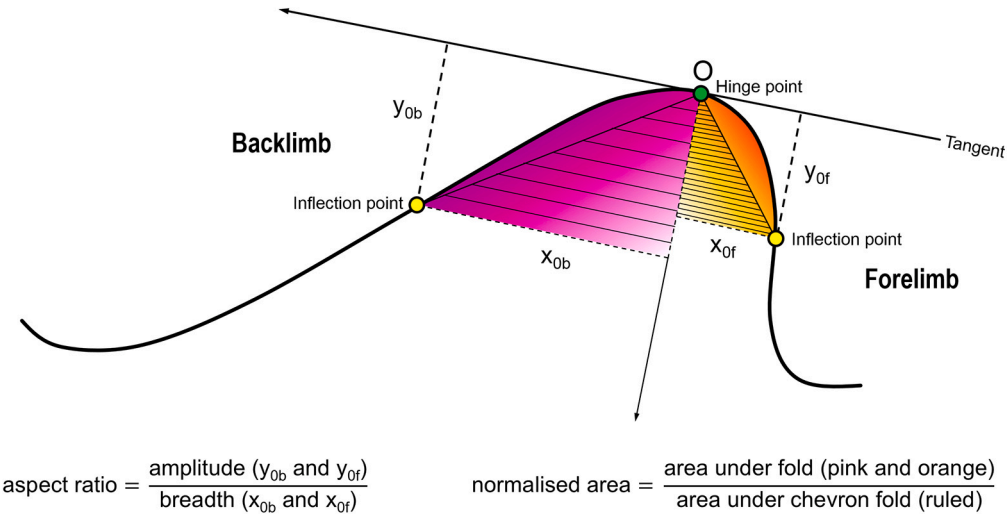

Fig. 9. Definition of breadth, amplitude, aspect ratio and normalised area of a forelimb and backlimb in an asymmetric folded surface. Modified after Lisle et al. (2006).

classification parameter, which is that the admissible range of e for conics depends on their aspect ratio. Instead, they preferred to use the normalised area (as defined by Bastida et al., 1999 and Lisle et al., 2006), which is a fundamental variable for a two-dimensional description of folds. A classification scheme of folds with a set of conic standard shapes to facilitate the classification of natural fold profiles by visual comparison is shown in Fig. 11d. This scheme shows a range from chevron to elliptical folds, similar to the Hudleston (1973a) fold classification (Fig. 8b). Cuspate folds and isoclinal folds, except those approaching a quarter of an ellipse, cannot be fitted by a cone. However, isoclinal folds can be fitted by a function composed of a quarter of an ellipse and a line segment of length *c* that is a prolongation of the ellipse arc, so that c/y_0 ratio allows us to extend the range of fold shapes with a possible fit as far as the box fold (Fig. 11) (Aller et al., 2004; Bastida et al., 2005).

4.1.2.3. Classification using Bézier curves. A Bézier curve (Bézier, 1966, 1967) is a cubic equation that can be used to simulate many natural fold shapes. It consists of one or more polynomial segments concatenated in daisy-chain fashion (Srivastava and Rastogi, 2010; Gogoi and Mukherjee, 2019). Each segment of such a curve is uniquely defined by the position of four points (two end points and two control points) labelled P_j, where $j = 0, 1, 2, 3, \ldots$ to classify fold profiles (De Paor, 1996; Srivastava and Lisle, 2004;Srivastava et al., 2010; Srivastava and Rastogi, 2010). It always follows end point interpolation property, i.e., it passes through the first and last control points. Bézier curves are always tangent to the control polygon at the endpoints. Through this property, sequential Bézier curves are joined easily at their end control points, which ensures that complicated shapes can be drawn with elegance. Using Bézier curves, the process of designing shapes can be quickly mastered by just moving the control points. Most 2D graphic drawing software packages use Bézier curves. Srivastava and Lisle (2004) used computer-aided Bézier curve analysis by three points: P_0 (0, R), P_1 (L, R) and $P_2 = P_3$ (1,0) to describe fold shapes (Fig. 12a). The distance *L* between P_0 and P_1 determines the fold shape (or shape of the curve), whose simplified parametric equations, with relation to the reference frame shown in Fig. 12b are:

$$x(t) = 3(1-t)^2 tL + 3(1-t)t^2 + t^3 \quad (13)$$

$$y(t) = R\{(1-t)^3 + 3(1-t)^2 t\} \quad (14)$$

The parameter t marks progress along the Bézier curve from the start point (P_0), where $t = 0$, toward the end point (P_2), where $t = 1$. The parameter R is the aspect ratio (= A/B), where *A* is amplitude and *B* is base length (Fig. 12b). Note that only two parameters, *L* and *R*, are needed to define the fold shape. *L* is here related to the distribution of curvature on a single fold limb between the hinge and inflection points, while *R* relates to the amplitude/wavelength ratio. The effect of varying *L* and *R* on fold shapes modelled as Bézier curves is shown in an *L* – *R* graph (Fig. 12c, d). On the *L* – *R* graph, L = 0, corresponds to chevron folds with straight limbs and curvature concentrated at the hinge. L = 0.44, 0.55 and 1 correspond to cosine curves, parabolic folds and elliptical folds (by ductile flow), respectively (Fig. 12c, d) (Srivastava and Lisle, 2004; Lisle et al., 2006). Slight variations in amplitude, interlimb angle and frequency of folding indicate that folds can develop parasitically on the rear of a macroscopic fold (Ramsay and Huber, 1987, pp. 320, 454).

Lisle et al. (2006) offered a MATLAB® code for classifying profiles of folded surfaces with a versatile program called FOLD PROFILER that incorporates four existing methods: cubic Bézier curves, conic sections, power functions and super-ellipses. Classification by FOLD PROFILER compares natural fold profiles with curves representing mathematical functions (Fig. 12c, d). This allows for rapid implementation of the four methods above for the analysis of fold shapes, but has the disadvantage that the results are sensitive to the user's selection of the position of the fold hinge point and where to measure the tangent to the limb slope. The main advantage of this method is that the theoretical curves are repeatedly remodeled during the fitting procedure, giving an immediate appreciation of the effect and sensitivity of changes in these parameters. Liu et al. (2009) also developed the program 'Bézier Fold Profiler' and determined a classification of folds based on two parameters: the axial lift-up ratio of the central part of a fold ($=l_{FD}/l_{AD}$) (Fig. 12c) to describe the distribution of curvature between the hinge point and the inflection point, and the interlimb angle. This approach generates folds with a broad spectrum of forms ranging from box folds to chevron folds. Natural folds are rarely isolated structures so, in order to simulate complex natural folds, three more parameters are used; the angle through which the axial surface is deflected, the increment of thickness of the hinge zone, and the limb elongation (Liu et al., 2009).

4.2. Classification of profiles through folded layers

4.2.1. Ramsay's dip isogon classification

Ramsay (1967) recognized that the issues of fold curvature and layer thickness in describing fold shape could not be adequately covered by just having parallel and similar folds. Thus, he considered the many

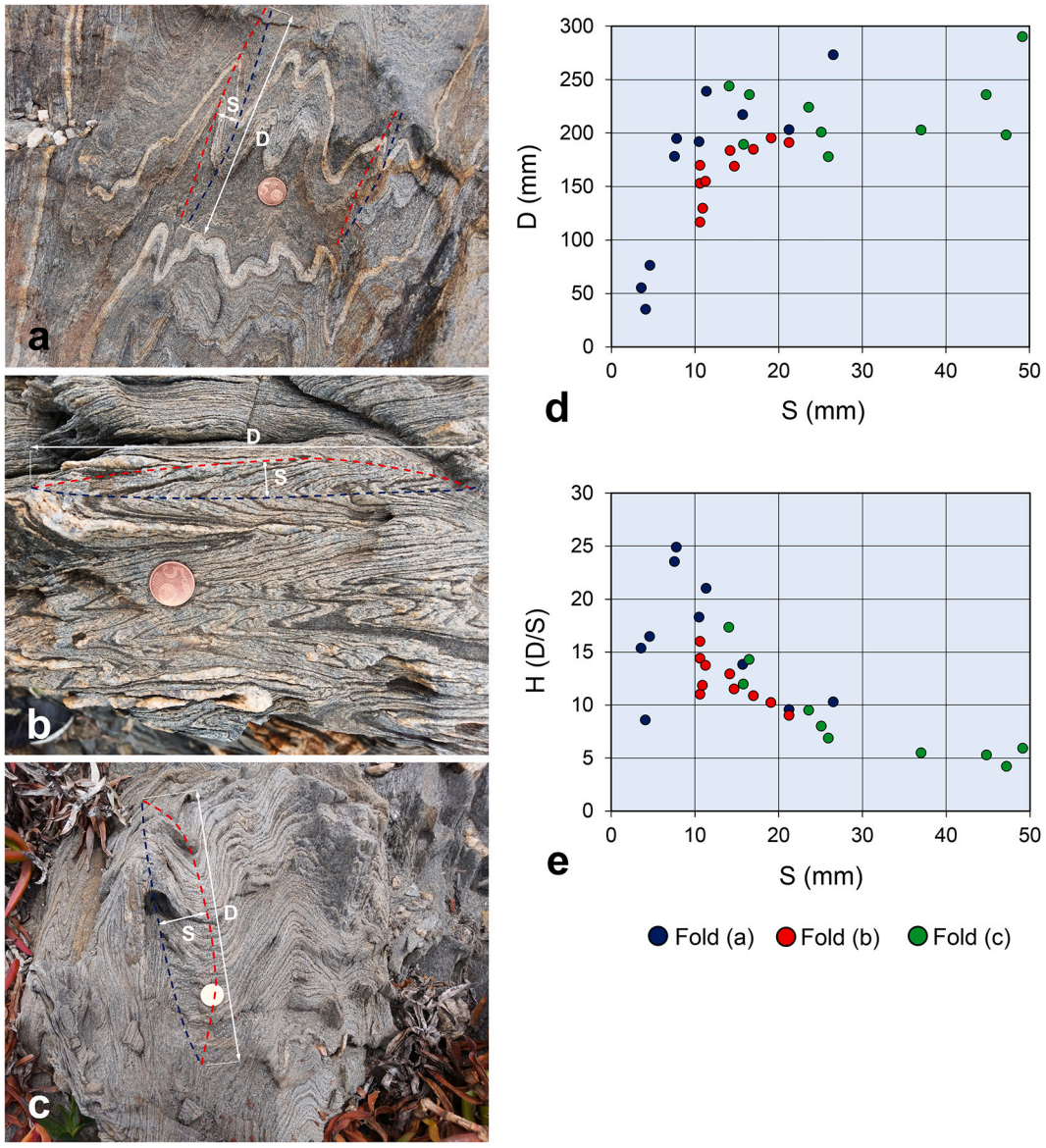

Fig. 10. Harmonic and disharmonic fold analysis in three natural examples from Cap de Creus, Spain. The half wavelength of folds is approximated by the spacing (S) of adjacent axial surfaces (shown in red and blue), while the continuity of the axial surface may be measured directly (D) to produce a ratio (H) that is equivalent to D/S (see Twiss and Moores, 2007, p. 289–290). (For interpretation of the references to colour in this figure legend, the reader is referred to the web version of this article.)

variations between these two kinds of folds such as changes in layer thickness through the fold and also changes in curvature in successive layers within a multilayer fold. His geometrical classification of folded layers is based on patterns of dip isogons, orthogonal thickness (t_α) and the thickness parallel to the axial surface (T_α). He also advocated measuring the variation of orthogonal thickness with distance along the bedding plane in fold profiles, and the variation of layer thickness parallel to the axial surface with the distance to the axial surface (Fig. 13). Such classifications were very influential and have long played an important role in the study of fold morphology and in elucidating the principal folding mechanisms (Ramsay, 1967; Hudleston, 1973a). Note that the axial surface of the fold is determined from the axial trace and the fold axis. The axial trace drawn through the points of maximum curvature of the bedding planes and defines the strike of the axial surface. The axial trace can also come from intersection of the axial lane and any other plane (e.g., erosional or folded surfaces). The axial surface of a cylindrical fold can be found by connecting the centres of ellipses (elliptical outcrop pattern of cylinder on a plane topographic surface) drawn tangential to several folded surfaces in their hinge zones (Stauffer, 1973). This technique may also be applied to asymmetric cylindrical folds. The axial surface contains both the strike line and the fold axis. The orientation of a fold axis controls the attitude of folded layers in a direction parallel to the fold axis.

Ramsay (1967) uses the concept of curvature, measured on cross-sections through cylindrical folds, to establish a classification scheme for the relationship between adjacent folded surfaces. In cylindrical folds, every surface can be defined by a straight geometric line parallel to the hinge line known as the fold axis. Elliott (1965) introduced the useful concept of 'dip isogon' as the lines (or curves) joining top and bottom points of equal dip (α) of a layer in the fold profiles or on adjacent folded layers (Figs. 13a and 14a, b). Constructing several dip isogons on the fold profile exhibit one of three patterns: divergent, parallel or convergent isogons from outer arc and inwards. Often, isogons are drawn at 10° intervals for each surface (Peña, 2001), but the choice is dictated by the actual form of the fold. Ickes (1923), in determining the geometry of parallel, similar and neutral-surface

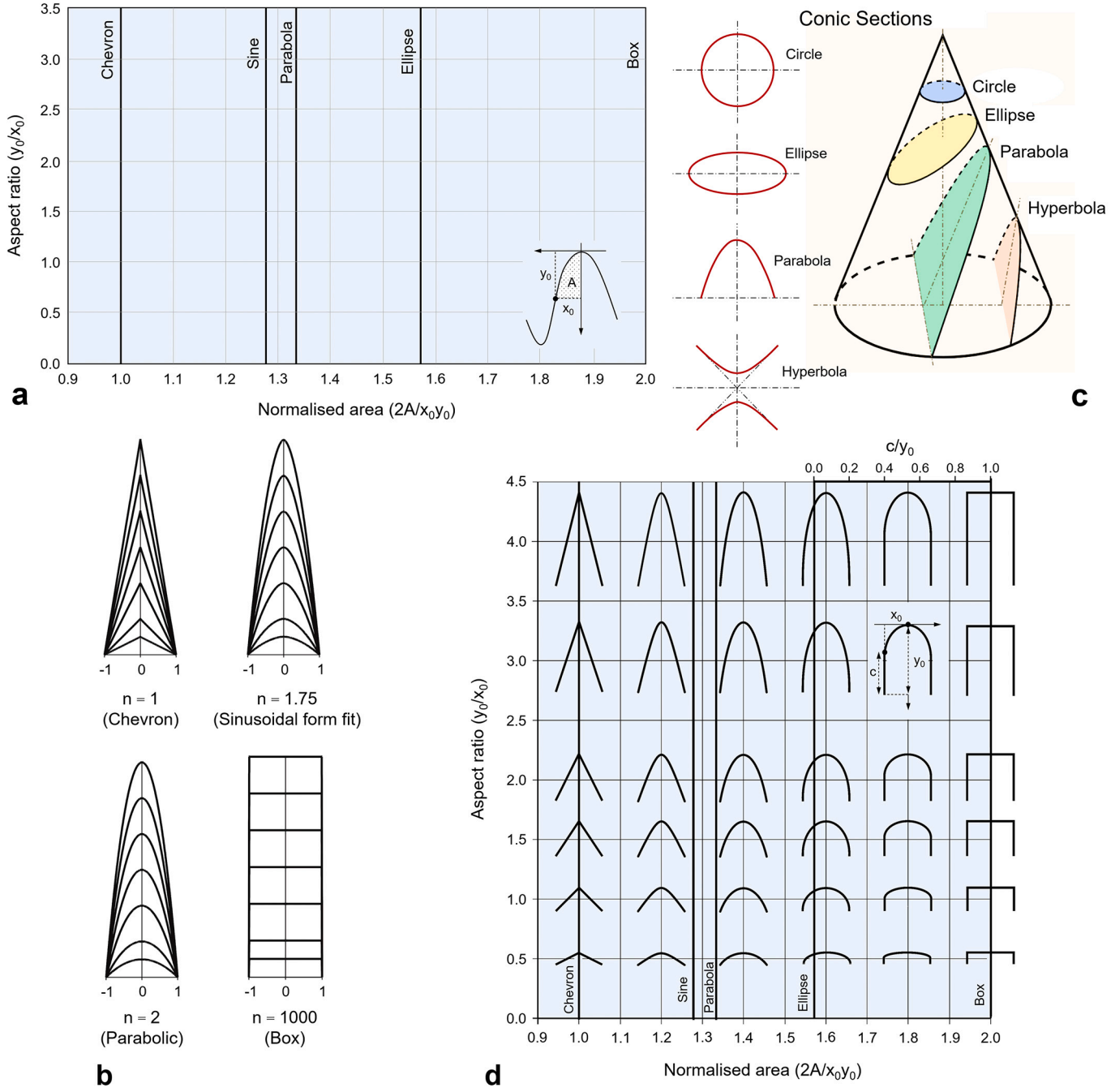

Fig. 11. a) Classification of shapes of the folded surface based on the diagram of aspect ratio versus normalised area (modified after Bastida et al., 1999, 2005; Lisle et al., 2006). b) Some of the main fold morphologies obtained from monomial functions with several values of exponent n and normalised amplitude (after Bastida et al., 1999, 2005). c) Main types of conic sections resulting from the intersection of a right circular cone and a plane. d) Chart of conic standard shapes that can be used in the classification of natural fold profiles by visual comparison. c is a prolongation of the ellipse arc, and c/y_0 is the normalised length (after Aller et al., 2004).

folding used isogons in the same way as described here, although he did not use the term isogon. The zero-degree isogon can be taken as a reference isogon for such analysis. Ramsay (1967) used patterns of isogons, together with folded layer thicknesses to separate folds into three classes, where Class 1 has convergent isogons, Class 2 has isogons parallel to the axial surface (similar folds), and Class 3 has divergent isogons (Fig. 13b). There are three subclasses for Class 1: 1A, 1B (parallel folds) and 1C (Fig. 13b). Convergent isogons imply that the curvature of the inner arc is greater than that of the outer arc, and this case is reversed for divergent isogons. Note that the degree of convergence of isogons reduce from subclass 1A toward 1C, and generally from Class 1 - Class 3. Subclass 1A was first recognized by Nevin (1931) as supratenuous folds (where layer thickness decreases in the hinge zone), and were, together with parallel and similar folds, included in a rarely used three-fold classification (Willis and Willis, 1934, pp. 34–38). If curvatures are compared for both interfaces of the same layer, then the curvature class for the waves of the layer can be expressed by two numbers e.g., 1,3 or 2,2 etc. (Chadwick, 1976). Perfect concentric and kink folds are examples of parallel folds, and perfect chevron and box folds exemplify similar folds. Similar folds are most common structures in orogenic hinterlands and are often assumed to have been flattened buckles in upper crustal rocks deformed at low metamorphic grades (Ramsay and Wood, 1973). They are also common in sheared rocks with little or no rheological layering, such as marbles and quartzites. In some folds called

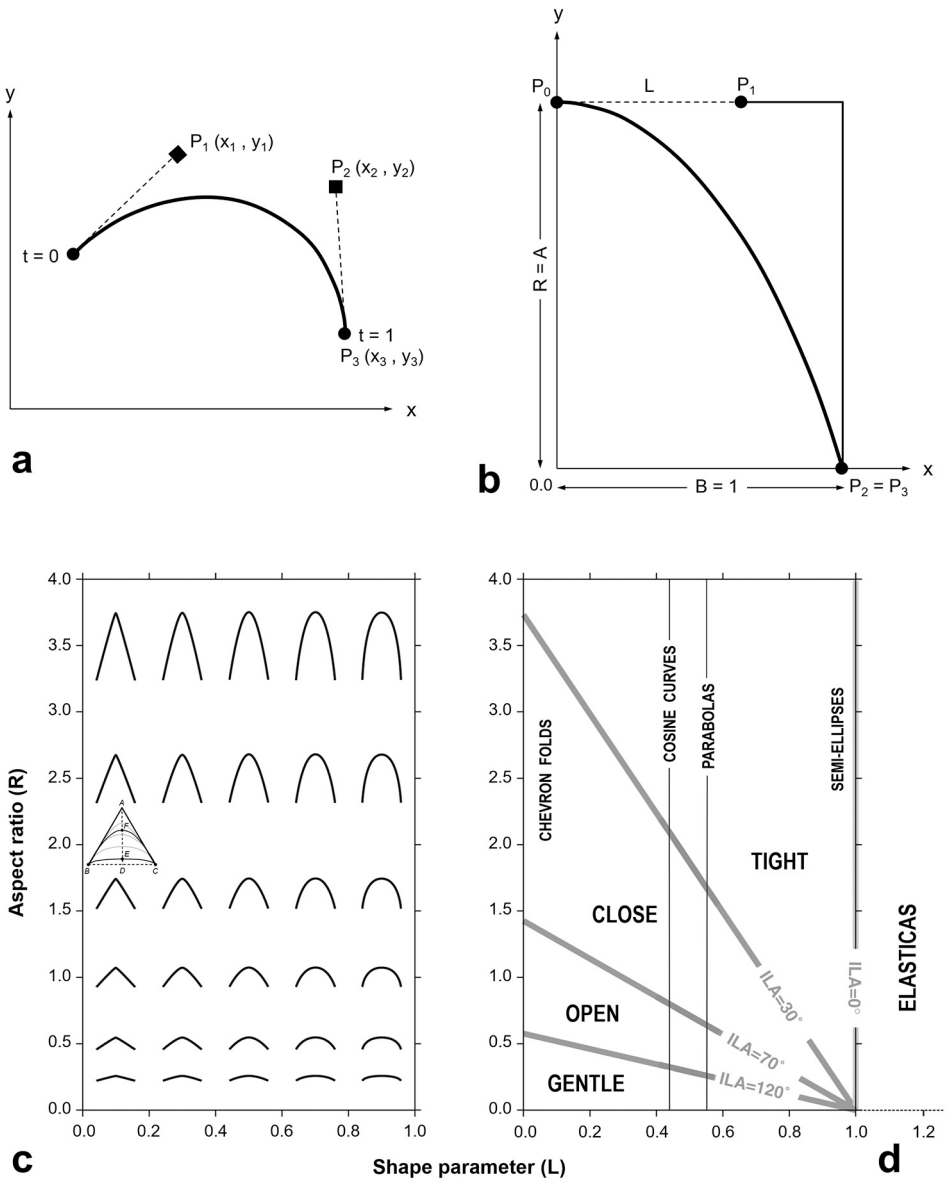

Fig. 12. a) A cubic Bézier curve defined by four control point, P_0-P_3. The parameter t describes progress of a moving point along Bézier curve. b) Reference frame and geometric elements of the simplified cubic Bézier curve used to fit and classify folded surface profiles (after Srivastava and Lisle, 2004; Srivastava and Rastogi 2010). Fold classification based on Bézier curve method (after Srivastava and Lisle, 2004): c) Classification scheme based on aspect ratio and shape. Lift-up ratio (==l_{FD}/l_{AD}) is used to describe the distribution of curvature between the hinge point and the inflection point, where l_{FD} and l_{AD} represent the length of the line segments FD and AD in which B, F and C are the three control points of the bottom layer (after Liu et al., 2009). d) relation of classification scheme to standard mathematical function. ILA is interlimb angle.

"constrained fold", both the normal and vertical thickness are variable, and their amplitudes die out systematically toward boundaries (Ramsay, 1962, 1967; Johnson and Pfaff, 1989). Ramsay (1967) used also the normalised orthogonal thickness t_α' (= t_α/t_0), the normalised axial surface thickness, T_α' (= T_α/T_0), and the limb dips (α) for graphically classifying natural folds. He suggested plotting these two derivatives of thickness against limb dips as the fold class depends on how the dip relates to the tangent of the curve t_α' (Figs. 13b and 14c, d). It may be possible to measure specimens of mesoscopic folds directly, but not on larger or smaller scale folds. Ramsay's (1967) dip isogon classification of folds is applied in Fig. 14 to a meso-scale fold profile in the Rabassers quartzite layers (Cap de Creus, Spain) perpendicular to the fold hinge.

Four morphological types of similar folds were proposed by Yakovlev (2008) based on the ratio of the competent layer thickness to the total thickness of rock sequence. They are (Fig. 15): (1) 'Single viscous layer folds' (Fig. 15a) if the ratio of the competent layer thickness to the total thickness of rock sequence is smaller than ~0.1, larger folds have more gentle shapes with hinges wider than 10–100 the layer thickness and relatively short limbs. However, the higher-order single viscous layer folds are mainly formed in the hinge space of larger folds. (2) 'Multilayer folds', forming when the competent layer thickness is ~0.3–0.7 of the total thickness of the folded rock sequence (Fig. 15b). They have widths narrower than ~10 times the total thickness of rock sequence and relatively long limbs. If slates and sandstones develop a cleavage, the cleavage fan opens upward in competent layers in anticlines and opens down in incompetent layers. The switch from a convergent fan in the inner arc to a divergent fan in the outer arc can be associated with the migration of the neutral line from the outer toward the inner arc with increasing shortening (Frehner and Exner, 2014; Bobillo-Ares et al., 2017). (3) 'Chevron-type folds' form where the competent layers comprise more than ~0.8–0.9 of the total thickness of rock sequence incorporating a high viscosity contrast (Fig. 15c). The mechanical interaction between layers during folding can influence the development of chevron folds, as explained by Johnson and Ellen (1974), Johnson and Honea (1975), and Ramberg and Johnson (1976). Fowler and Winsor (1996), chevron folds often form in the cores of concentric folds. Various terms have been proposed to apply to the space problems than often develop in chevron and parallel-type folds. Examples are fold-accommodation faults, bulbous hinges, hinge collapse (inner-arc collapse with volume loss), the filling of hinge voids by crystallizing minerals (i.e., saddle reef; Ramsay, 1974; or fold-related veins, Druguet, 2019), outer arc stretching, flow of incompetent material from the limbs

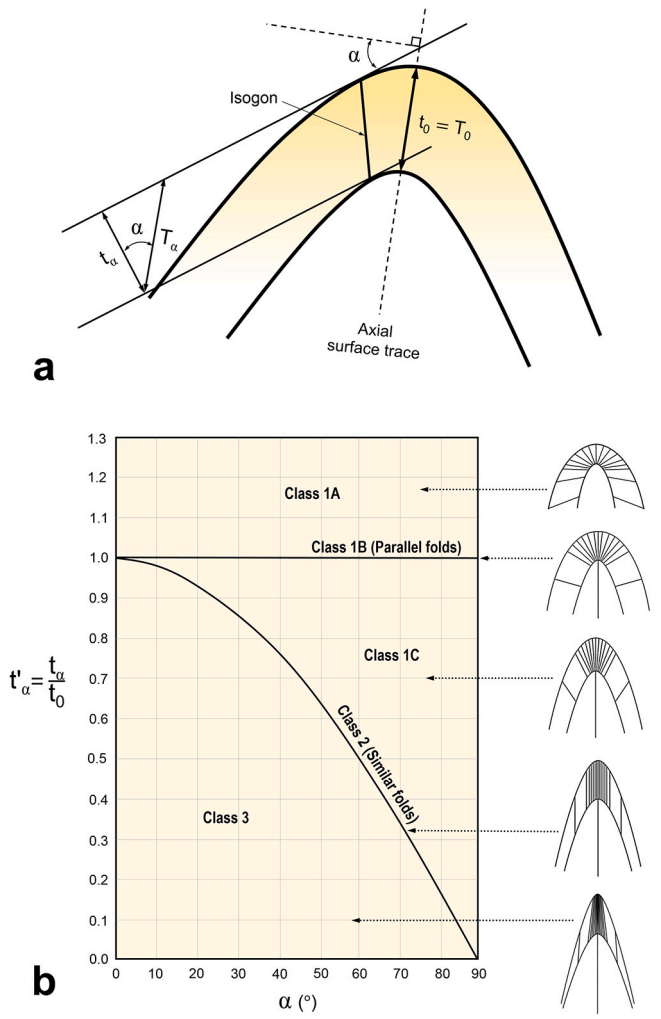

Fig. 13. a) Definition of layer inclination (α), dip isogon, orthogonal thickness (t_α) and thickness parallel to axial surface (T_α) of a folded surface (modified after Ramsay, 1967; Ramsay and Huber, 1987). b) Fold types defined on the $t'_\alpha - \alpha$ diagram (modified after Ramsay, 1967; Ramsay and Huber, 1987).

to hinges and flowage of interbedded competent and incompetent material that might include welding, and S-C structures that thin the limb (e.g., Ramberg, 1963a, 1964; Ramsay, 1974; Boyer, 1986; Mitra, 2002; Hudleston, 1986; Hudleston and Tabor, 1988; Ormand and Hudleston, 2003; Jeng and Huang, 2008; Bastida et al., 2007; Deng et al., 2013; Torremans et al., 2014). A common situation is where diagenetic cracks in a competent layer are perpendicular to bedding, the cleavage of slates may be used for measuring a shortening value, and (4) 'Stack folds' or 'Counter thrust folds' form if slates and sandstones have no cleavage, and the viscosity contrast of layers is low (~ 2 and smaller) due to numerous hinge wedge thrusts on the opposite limbs of the folds (Fig. 15d). The folds have sharp hinges where neighbouring thrusts have long limbs and are ~1–2 layer thicknesses apart. The necessary increase in thickness of layering in the hinge (similar h/H ratio, Class 2) exists due to doubling of inter-thrust units. Because almost pure buckling (rotation of limbs) is active, the dip angle of limbs relative to vertical axial surfaces relates to their percentage shortening value. In general, the main geometrical characteristics of ideal similar folds can be explained as the result of the heterogeneous rotation shear (Bobillo-Ares et al., 2018).

Ramsay's (1967) classification of folds is often used because it is non-genetic and easy to apply. This classification has two bases: (1) a lateral basis, that compares the curvatures of the inner to the outer arcs across one folded layer; and (2) a transverse basis, which is based on the angle though which the layer interfaces are deflected. Different deflection angles result in asymmetric (V-type), antisymmetric (W-type) and symmetric (X-type) fold classes (Chadwick, 1976). Ramsay (1967) also related fold geometry to mechanism, suggesting that single layer folds that fall into Class 1A and Class 3 signal that their evolution involved differential shortening across their axial surfaces, while a combination of Class 1B and Class 1C geometries signals by flexural slip. Fold mechanism can often be explored by evidence of (1) slip and slip sense from striae and slickenfibres, (2) hinge dilation, (3) boudinage with bedding-perpendicular veining, (4) or complex arrays of extension veins, shear fractures or stylolites near fold hinges, and (5) flexural slip developed only in the latest stage of folding (Dubey, 1980; Behzadi and Dubey, 1980; Dubey and Behzadi, 1981; Tanner, 1989; Jacques et al., 2014). Class 2 suggest shear folding or a mechanism involving slip or flow (e.g., Ramsay, 1967). Shear folds are Class 2 folds formed by heterogenous simple shear, where the shear plane parallels the axial plane of the fold. A transition from Class1B to Class 1C folds in competent layers is indicative of the migration of material from the fold limbs to the fold hinges. This migration could be related to either volume-loss or a superimposed homogeneous flattening (Jacques et al., 2014). Hence, a unit circle of Class 1B fold obtained by the "Inverse Thickness Method" of Lisle (1992b) changing to an ellipse, so that the axial ratio of this ellipse gives the finite flattening strain ratio.

A refinement of fold classifications was made by Donath and Parker (1964), where their classification is a generic-mechanical scheme based on *mean ductility* and *ductility contrast* (or absence of such) within the folded sequence. Although this scheme contrast with the descriptive classifications, it has long been employed by geologists because it can be used in the field. Donath and Parker (1964) classified folds into three main groups based on mechanism: (1) flexural folds, (2) passive folds, and (3) quasi-flexural (disharmonic) folds (e.g., Davis, 2014). The overall combination of buckling, flexural-slip, and tectonically driven pressure solution fashioned the quasi-flexural folds. Note that flexural flow in this classification (the thickening of the hinges during buckling) differs from flexural flow as used by Ramsay (1967) who used it for a combination of buckling and homogeneous flattening. Friction between layers is an essential factor in flexural-slip folding, where low and high friction favours the development of concentric and kink folds, respectively (Honea and Johnson, 1976; Tanner, 1989; Hudleston et al., 1996; Damasceno et al., 2017; Wu et al., 2019). 2D visco-elastic, plane strain FE-models (Damasceno et al., 2017; Wu et al., 2019) indicate that flexural-slip does not occur continuously during buckling. Overall, the temperature and pressure at which flexural-slip occurs are generally low. Instead, each frictional interface is activated and deactivated in a hierarchical sequence during folding. Moreover, the ratio of incompetent to competent layer thickness is a crucial parameter in the development of multilayer chevron folds.

The spacing between individual layers in a multilayer package also plays an important role in the behaviour of the mechanism of folding and the harmony of the fold geometry. If the spacing is sufficiently large, each individual layer folds as an active single layer independently of the others, forming disharmonic folds (Ramberg, 1962, 1964). In multilayers composed of alternate incompetent and competent layers, the competent units develop Class 1B or Class 1C folds and the incompetent layers develop Class 3 folds (Ramsay, 1967). Material model experiments by Hudleston (1973b) demonstrate that simultaneous buckling and flattening is also an efficient mechanism for developing Class 1C folds, particularly in situations where the initial wavelength of folds is much larger than the wavelength predicted by buckling equations and the viscosity contrast is very low. Folds in this category must either change their styles from layer to layer, or some structural discontinuity must develop in the folded sequence. Thus, it can be said that the geometries of folds of a multi-layered sequence are also a function of the number of layers as well as their mechanical properties.

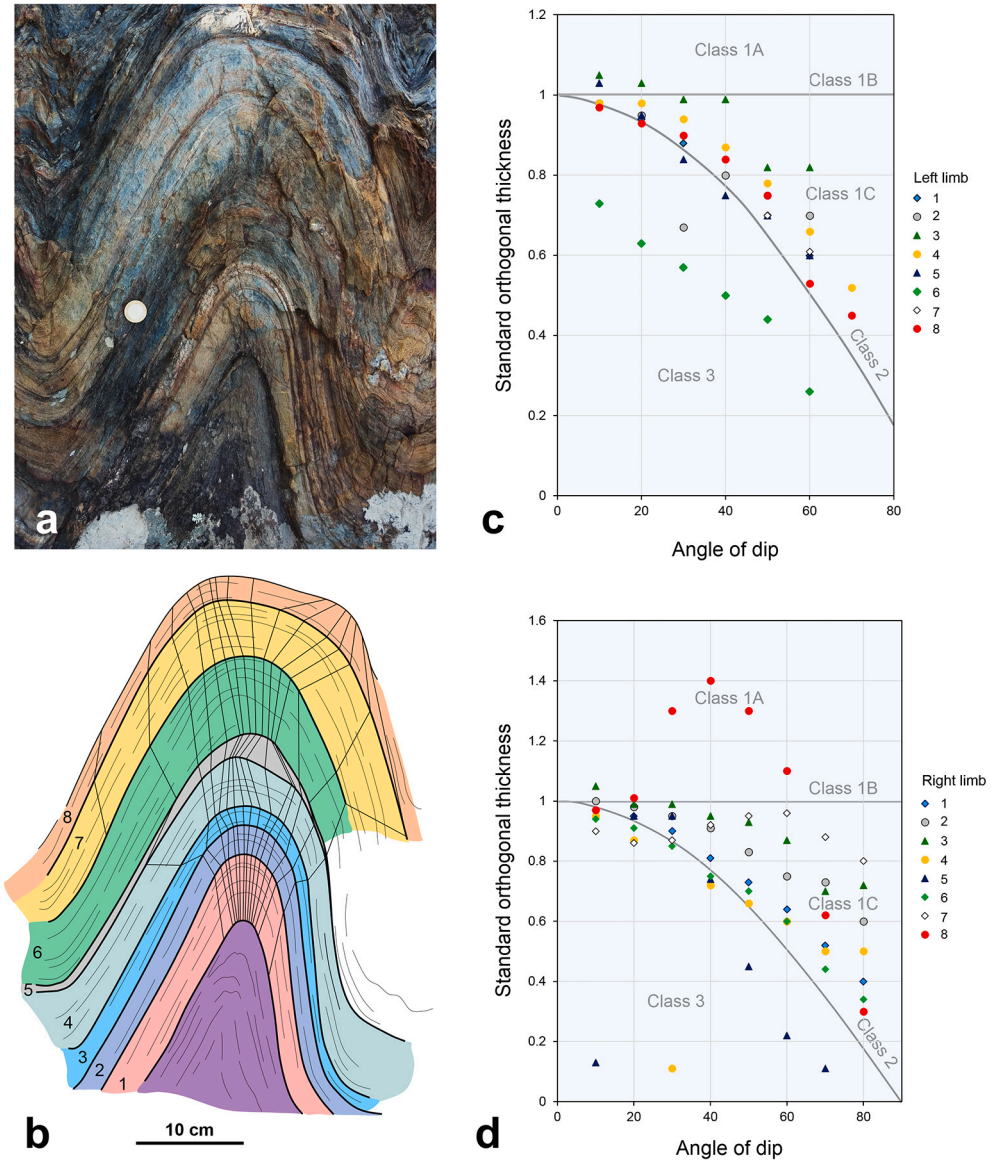

Fig. 14. Ramsay's (1967) fold classification and construction of dip isogon applied on a natural sub-vertical section through a multilayer fold in quartzite layers from Cap de Creus, Spain. Photograph is rotated 90° clockwise.

4.2.2. Problems with Ramsay's dip isogon classification

Fold thickness is a standard measurement for geometrical analysis and classification of folds. Ramsay's (1967) dip isogon classification has a rigorous mathematical basis, but it is difficult to measure the required data accurately if photographs of axial profiles are not available. This classification scheme does not also include folds such as chevron, kink and box folds whose profiles contain straight limbs and sharp hinges. Moreover, where dip is small, it is difficult to determine the exact tangent point to measure. Any inaccuracies will introduce errors in the classification. To ease this problem, Ramón-Lluch et al. (1989) provide a computer program aimed at eliminating the usual subjectivity in this type of measurement, making them easier and faster to use. The Applesoft BASIC program is called RAFOLD and automatically calculates the dips of different parts of a large fold. Ramsay (1967) defined the fold thickness as the distance between two parallel lines tangent to the upper and lower fold interface and measured thickness parallel to the axial surface or perpendicular to the tangents. Alternatively, Sherwin and Chapple (1968) defined thickness as the distance between folded interfaces as measured perpendicular to one interface. When discussing the definition above Adamuszek et al. (2011) mentioned that the thickness between the upper and lower interface is an imprecise definition of the axial surface and not applicable to generic fold shapes with complex geometries. However, the average thickness of a fold train can be defined by dividing it into discrete folds based on the solution of Laplace's equation and then using the FE-method solver code MILAMIN that divides folds based on the location of inflection points on their upper and lower interfaces (Dabrowski et al., 2008). Other problems with Ramsay's (1967) classification include: (i) it treats each layer separately rather than taking a multilayer fold as a single unit – a problem partially solved by Srivastava and Gairola (1999) (see subsection 4.2.3)., and (ii) the difficulty of positioning a hinge zone (Roder, 1978), and identifying the reference thickness (t_0) to determine t_α'. Ramsay (1967, p. 369) acknowledged that even though most folds have properties that conform to his isogon-based $t' - \alpha$ fold classification, there remain complexly shaped folds with curved hinges and axial surfaces formed during progressive or multiphase heterogeneous deformation (Fossen et al., 2019; Carreras and Druguet, 2019) that do not easily fit into this classification. Another limitation of Ramsay's (1967) classification was discussed by Hudleston (1973a), who introduced the new parameter (ϕ_α) and designed a new graph $\alpha - \phi_a$ that uses positive

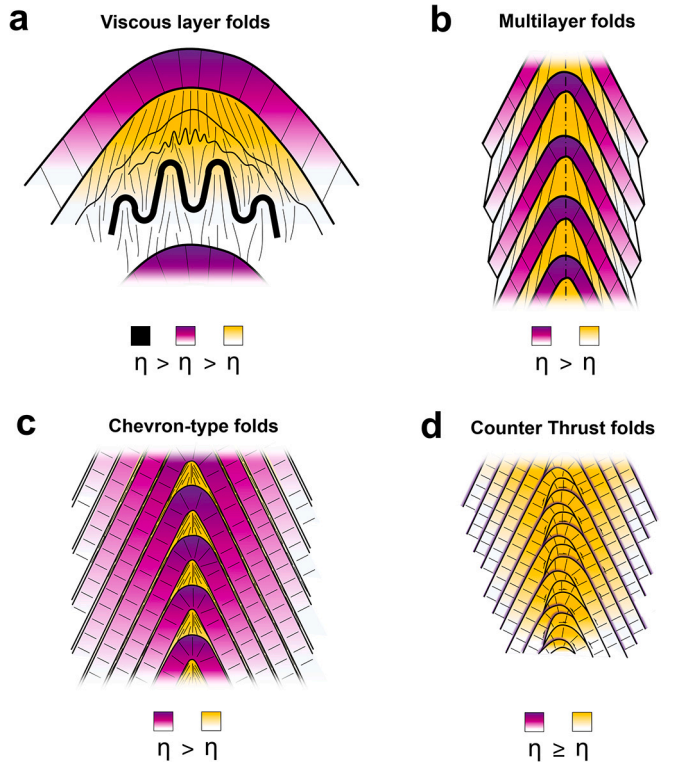

Fig. 15. Four types of similar folds distinguished by the ratio of the thickness of the competent and incompetent layers and by their viscosity contrast (modified after Yakovlev, 2008).

and negative signs (by convention) for the dip isogons. Hudleston (1973a) thereby distinguished three types of Class 1C folds to illustrate the scope and the limitations of the $t_\alpha' - \alpha$ and the $\phi - \alpha$ methods. Bastida (1993) first highlighted this problem and proposed to describe a fold limb by the ratio between the slopes of two segments of the curvilinear plot on the $t_\alpha' - \alpha$ graph. However, this method requires more measurements and calculations than the $t_\alpha' - \alpha$ graph (Fig. 13). Despite of the fact that the use of Ramsay's (1967) classification is laborious and unsuitable for the analysis of large data sets, the isogon approach is enduring and provides an excellent tool for analysing the geometry of single folds.

4.2.3. *Modifications of Ramsay's dip isogon classification*

Zagorčev (1974, 1993) modified Ramsay's (1967) dip isogon classification by further subdividing subclass 1A folds into three types 1A1, 1A2 and 1A3 using the straight line $\phi_\alpha = -\alpha$, symmetrical to $\phi_\alpha = \alpha$ in the Hudleston's diagram (1973) (Fig. 16). The line $\phi_\alpha = -\alpha$, equivalent to $t_\alpha' = \sec\alpha$ in the Ramsay diagram, divides fold type 1A2 into two separates fields: one for folds of the type 1A1 ($-\phi_\alpha > \alpha$), and other for folds of the type 1A3 ($-\phi_\alpha < \alpha$). Buckled layers usually form class 1B folds or folds close to 1B of 1A3 or 1C types. Zagorčev (1993) also subdivided class 3 folds into three subclasses: 3A, 3B and 3C. Folds of subclasses 3A and 3C can be defined as fold shapes complementary to subclasses 1C and 1A, respectively (Fig. 16). Nevertheless Zagorčev (1993) considered folds of types 1A1 and 3C to be rare in nature.

Lisle (1997) also suggested a different subdivision of Ramsay's fold classes by dividing class 3 folds into new classes 3A, 3B and 3C based on polar plots of the inverse of their layer thickness (Fig. 17). According to Lisle (1997), each fold can be characterized by a single number (their flattening index *F*). *F* describes the amount and direction of the flattening or the ellipse within each fold limb in terms of the semi-axis of the ellipse or the semi-axis of the hyperbola: $F = \pm b/a$, where the positive sign denotes an ellipse and the negative sign a hyperbola. This index describes the axial ratio of the elliptical pachymetric indicatrix on the inverse thickness polar diagram. For levels of layers and individual folds, the description of strain ellipse includes its shortening percentage perpendicular to the axial surface and hinge line of a fold as well as the orientation of the axial surface (the longest axis of the ellipsoid), which is perpendicular to the fold hinge line (Yakovlev, 2012a, 2012b). Folds with hinge lines subparallel to a stretching lineation or the axis of maximum elongation, may according to Lisle (1997) develop by: (a) superposition of a tectonic strain on a sedimentary compaction fabric, (b) superposition of two tectonic strains, and (3) progressive non-coaxial deformation. Such folds are common in high-strain shear zones, thrusts, mylonite belts, and transpression zones (e.g., Ramsay and Wood, 1973; Grujic and Mancktelow, 1995; Carosi and Montomoli, 1999; Morales et al., 2011; Bastida et al., 2014).

Class 1 folds are characterized by positive *F* values (0 to ∞) that measure the amount of homogeneous flattening perpendicular to the axial surface required to generate the fold shape from a parallel fold (Class 1C for $F > 1$, Class 1B for $F = 1$ and Class 1A for $0 < F < 1$) (Fig. 17). Class 3 folds are folds (or mullions) with strongly thinned of limbs, typically developed in incompetent single layers (Talbot and Sokoutis, 1992). These folds are characterized by negative *F* values (0 to -∞). According to Lisle (1997), Class 3A folds are generated by flattening of 3B folds normal to their axial surfaces and have *F* values ranging from −1 to -∞ (Fig. 17g). Class 3B folds ($F = -1$) have pure Class 3 fold geometries developed by the superposition of flattening strains. Class 3C folds ($-1 < F < 0$) are the result of flattening parallel to the axial surface and are relatively rare in nature. Srivastava (2003) presented a somewhat similar modification, but his method applies only to truly concentric folds. Variations in fold shapes can be due to variable rheological properties of the folded layers associated with physical conditions, and/or by non-steady flow during the folding processes.

Srivastava and Shah (2008) modified Ramsay's (1967) classification by introducing a character that they called an "isogon rosette" (Fig. 18a). Dip isogons drawn on fold profiles have two properties: (1) dip isogons in Class 1B folds are of equal length, and (2) the isogons behave as material lines during homogeneous flattening. These isogons can be arranged in a rosette by displacing the isogons without changing their orientation until their mid-points become the common intersection point. The outer ends of isogons in the rosette trace a characteristic curve that defines the fold geometry. This curve is a circle for parallel folds, an ellipse for flattened parallel folds, and it is reduced to a pair of points for similar folds (Fig. 18a). Since isogons behave as material lines during flattening, the characteristic curve, namely, the ellipse, directly represents the strain ellipse in flattened parallel folds. In this regard, the geometry of a given fold can be represented by a point on the $R_S - \theta$ graph (Fig. 18b), where R_S is the two-dimensional strain ratio and θ is the angle between the maximum principal strain and the fold axial trace. This method assumes that flattening occurs completely posterior to and not concomitant with the buckling stage. Most natural folds, however, occur as multi-layered sequences so that they may or may not demonstrate the simplicity of single layer folding schemes due to variations in the amount and direction of applied stress, composition, viscosity, porosity, shape and size of grains in different layers. In this regard, Srivastava and Gairola (1997, 1999, 2003) proposed a new classification scheme based on the degree of fluctuation in the geometry of different layers folded in multi-layered packages that may be represented by a single curve or line on a Cartesian plane in the $\sigma_n(t_\alpha')$ versus α or $\sigma_n(T_\alpha')$ versus α diagrams (Fig. 18c). Here, σ_n, t_α' and T_α' are standard deviation, orthogonal thickness and axial surface parallel thickness, respectively (Fig. 18c). They divided multi-layered folds into two major categories, namely 'isodeviatoric' and 'anisodeviatoric'. All plots in the diagram (Fig. 18c) will originate from the same origin but vary later. Thus, after $\alpha = 0°$ (say at 10°) if the fold plots parallel or along the abscissa, the fold is classified as 'isodeviatoric'. A special variety of isodeviatoric folds is 'analogous' folds (Fig. 18c) where all the layers have the same geometry. Analogous folds may be further categorized into 10 classes using

prefixes as 1A1-, 1A2-, 1A3, 1B-, 1C-, 2-, 3A-, 3B-, 3C- and composite- to analogous fold, depending upon the types of fold geometries in the folded package layers (Srivastava and Gairola, 1999). 'Anisodeviatoric' folds can be further divided into 'peri-analogous', 'sub-analogous', 'sub-nonanalogous', 'nonanalogous' and 'strongly nonanalogous fold' classes (Fig. 18c). This classification has three limitations. The first limitation relates to the use of the ratio of actual thickness (t_α) to axial surface thickness at dip isogon (T_0) zero degree, and the ratio of axial surface parallel thickness (T_α) to T_0. The actual thickness of the layer cannot be compared within a multi-layered fold or two or more of such folds, because similar ratios may apply to different combinations of layer thicknesses. Second, the classification does not convey the degree of harmony of the fold or folds. Thus, this classification is based on the degree of variation in the geometries of the layers rather than their actual geometries. This means that many different geometries within a multi-layered fold could be represented by the same one line or curve on the $\sigma_n(t_\alpha')$ versus α or $\sigma_n(T_\alpha')$ versus α diagrams. Third, results obtained from t_α' and T_α' will be the same as long as the relation between these two parameters is valid.

5. 3D fold classifications

Geometrical data obtained from natural folds are largely incomplete and often restricted to two dimensions. Also, strict fold trains are predicted by all 2D models as they must for a linear matrix, and geologists often approximate folds as cylindrical to simplify description and analysis. However, field-based observations, numerical as well as analogue modelling results show that fold geometry becomes complicated in 3D. Folds are inherently 3D structures and their geometries and processes also need to be studied in 3D. Hence, the attitude and geometry of folds in 3D help identify larger and regional-scale structures, their processes of growth and evolution, and also the distribution and pattern of fold-related fracture networks.

5.1. Classification of folds based on attitude

5.1.1. Fleuty's classification

Loudon (1964) and Whitten (1966) suggested the use of the four statistical moments of the orientation distribution of the normal to the fold profile to express the attitude, tightness, asymmetry, and shapes of folds. The attitude of a fold can be defined by the axial surface and hinge orientation, typically on spherical projections. Fleuty (1964, pp. 481–488) classified folds based on the dip of their axial surface and the plunge of their hinge line (Figs. 4e, 19). His simple and widely used diagram categorizes folds as overturned if both limbs dip in the same direction as the axial surface and the steep limb has an up-side-down

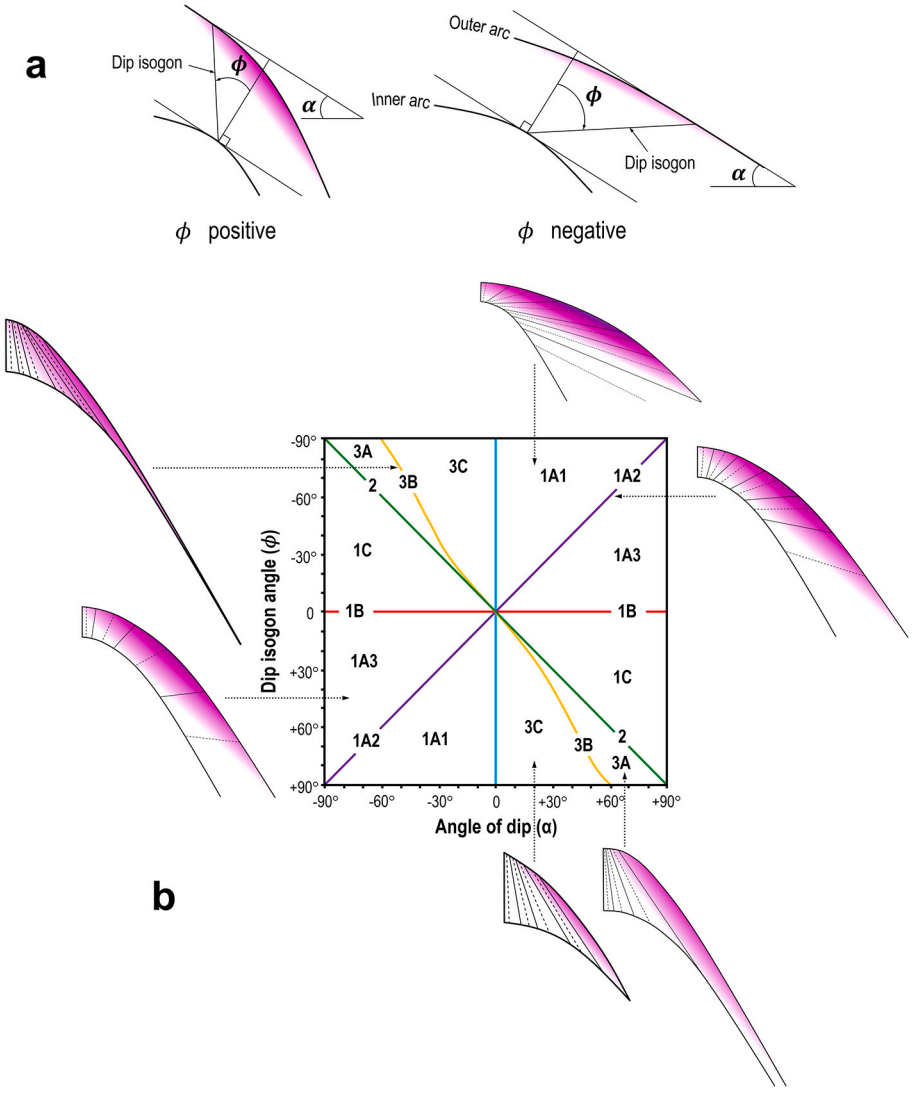

Fig. 16. a) Definition of angle ϕ_a for classification of folded layers and sign convention in the case of a positive dip angle (modified after Hudleston, 1973a). b) Classification diagram, modified from Hudleston (1973a) and Zagorčev (1993).

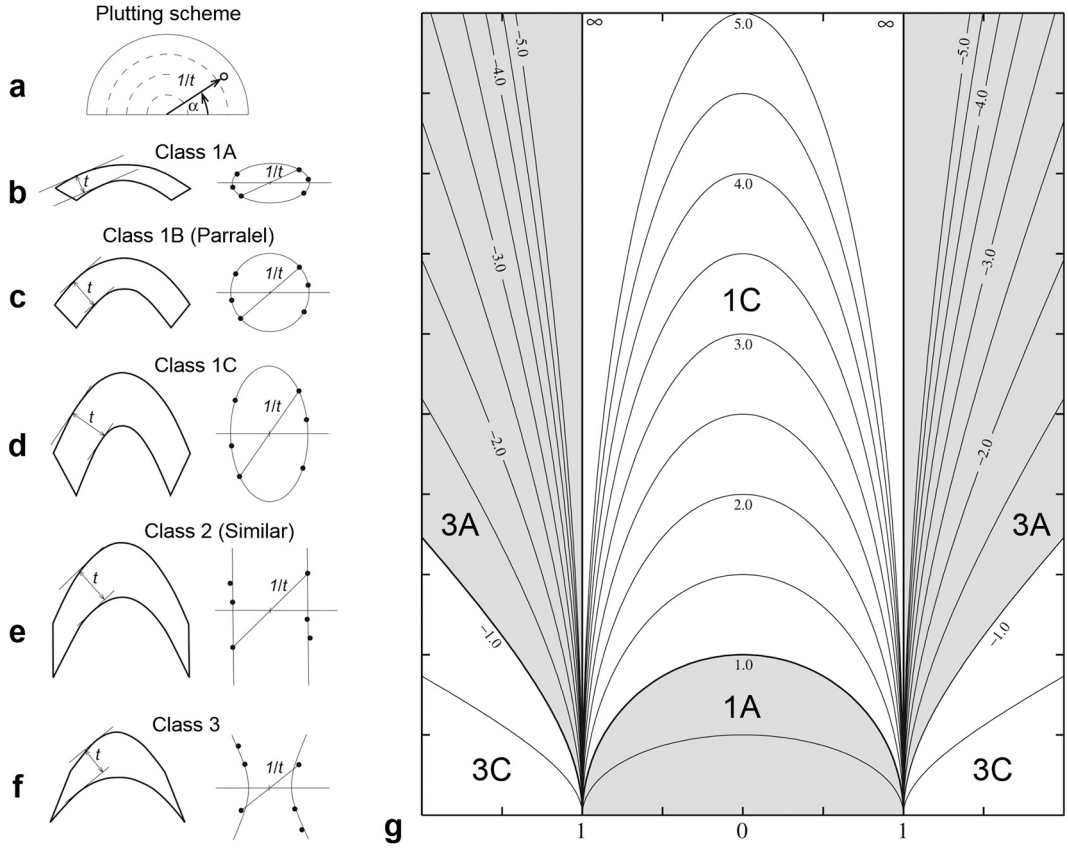

Fig. 17. a-f) Fold classes represented on the polar graph of inverse layer thickness (1/t) and orientation (α). g) Classification chart for folds plotted on polar graph of inverse normalize thickness (1/t) versus dip α. *F* is flattening index (after Lisle, 1997).

stratigraphy. Folds with subhorizontal axial surfaces or with maximum dip up to 10° are recumbent in Fleuty's (1964) classification.

Bastida et al. (2014) reviewed existing ideas on kinematic evolution, strain distribution, and significance of recumbent folds in orogens and their relationship with other structures. Large-scale recumbent folds can also form by flow of salt toward salt walls and in allochthonous salt and salt glaciers (Jackson and Hudec, 2017). Fold nappes are large recumbent folds with inverted limbs over several square kilometres in area and are common in high strain settings, for example, the Morcles fold nappe (Helvetic nappes of the Switzerland Alps) (Ramsay, 1981; France, 1987; Ramsay et al., 1983; Ramsay and Huber, 1987).

In many orogenic belts, spatial associations between overturned and tight to isoclinal recumbent and inclined to upright folds are common and classified in to two main types of transition. One type, from nappes in the internal zones of orogens to gentle to open upright folds in their foreland (Fig. 20), is displayed by the Pennine nappe pile stopping short of the upright folds of the Jura Mountains in front of the European Alps (Trumpy, 1960; Laubscher, 1978). The second type is where upright folds in the supra-structure overlie recumbent folds in the infra-structure (de Sitter and Zwart, 1960). The transition from upright to recumbent and vice versa first-generation folds has been discussed by Sanderson (1979) and Rattey and Sanderson (1982), who noted that as the axial surfaces rotate from upright to recumbent as the folds tighten, cleavage intensifies and the fold envelope steepens, with more and more rock layers becoming inverted. Upright folds (domes and basins) may also dominate orogenic core complexes, with recumbent folds being associated with the overlying detachment (Kruckenberg et al., 2011; Wiest et al., 2019).

When a time lag is assumed between the inception of folding and the development of cleavage, the cleavage may not be strictly axial planar. Consequently, the cleavage may cross one or both limbs and form transected folds (Fig. 1b). Transected folds form when there is a time difference between the onset of folding and cleavage formation; usually cleavage forms after a certain amount of folding (Borradaile, 1978; Johnson, 1991; Fossen et al., 2019). In transected folds, the cleavage can parallel the axial trace of the fold profile but cross the axial surface and also the fold hinge in three dimensions (Fig. 1b). A fold classification that relates the geometry of a fold to its cleavage was proposed by Treagus (1982). This classification is based on the angle β between the cleavage trace and the normal to the folded layer within the profile plane. Treagus' angle β (1982) is similar to Hudleston's angle ϕ_α (1973b), and uses the same sign convention. This angle is graphed against the normalised limb dip. This classification complements rather than replaces that of Ramsay (1967) and Hudleston (1973a). Numerical 2D modelling of folds can involve a variety of combinations of kinematic mechanisms. The MATHEMATICA™ program 'FoldModeler', developed by Bobillo-Ares et al. (2004, 2009) models how the fold profile accommodates progressive shortening as small successive increments are added during folding of an initially horizontal layer. 'FoldModeler' applies available information on cleavage orientation around the fold and makes the assumption that cleavage records the XY plane of the strain ellipsoid.

Fleuty's diagram (1964) can be very important for analysing transpressive deformation zones (e.g., Curtis et al., 2010; Debacker, 2012; Nabavi et al., 2017a). This means that, for originally horizontal layering, we can combine this diagram with the triangular strain diagram proposed by Jones et al. (2004). In this version of the Fleuty diagram (Fig. 19), recumbent, upright, and vertical folds relate to dip-slip, contraction and strike-slip movements. After plotting the attitude of all the folds of any stated generation in a particular area, the concentration of each dominant component becomes obvious in each part of the region. These concentrations divide the region into domains of non-

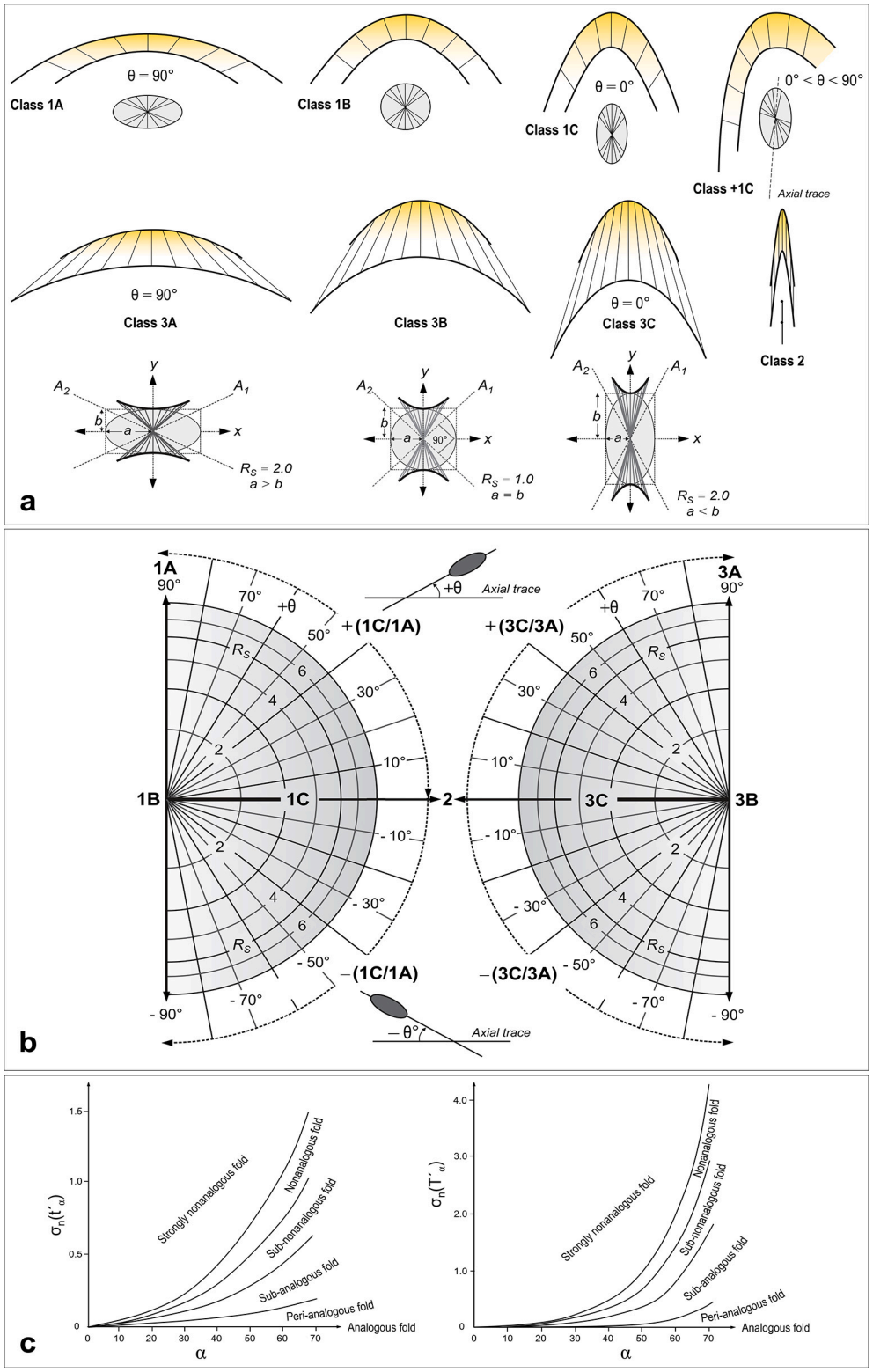

Fig. 18. a) Profile sections with isogon in different classes of folds with characteristic curves through end points of isogon rosettes (modified after Srivastava and Shah, 2008). The characteristic curve is a rectangular hyperbola, circle, ellipse, and hyperbolas. b) the geometry of a given fold can be represented and classified by a point on the $R_S - \theta$ graph, where R_S and θ are the two-dimensional strain ratio and the angle between the maximum principal strain and the fold axial trace, respectively (after Srivastava and Shah, 2008). The obliquity flattened folds with respect to the fold axial trace can be further classified into Class ±1A, Class ±1C, Class ±3A, and Class ±3C, depending upon whether the maximum principal strain is rotated counterclockwise or clockwise relative to the fold axial trace. c) $\sigma_n(t_\alpha')$ and $\sigma_n(T_\alpha')$ versus α diagram for multi-layered fold classification. The curves mark the limits of different fold classes. From Srivastava and Gairola (1999).

coaxial strain with axial surfaces from the oldest to the younger generations of folds with different tightness, symmetries, and rotations. The wide range of orientation of fold elements in the tectonic setting may be attributed to differences in orientation of pre-deformational foliations, later deformation events, progressive deformation, non-steady state deformation, flow heterogeneity, mechanical stratigraphy, and boundary conditions (in model setups). These factors not only cause a great diversity in the orientation of fold elements but also affected the cylindricity of folds. Little (1992) proposed a graph describing how the strikes of fold axial surfaces and interlimb angles vary for specific cases of simple shear, simple transpression and incremental transtension using the model assumptions of Sanderson and Marchini (1984). In general, we have a combination of strain components as heterogeneous deformations. In this regard, asymmetric distribution of fold attitudes data

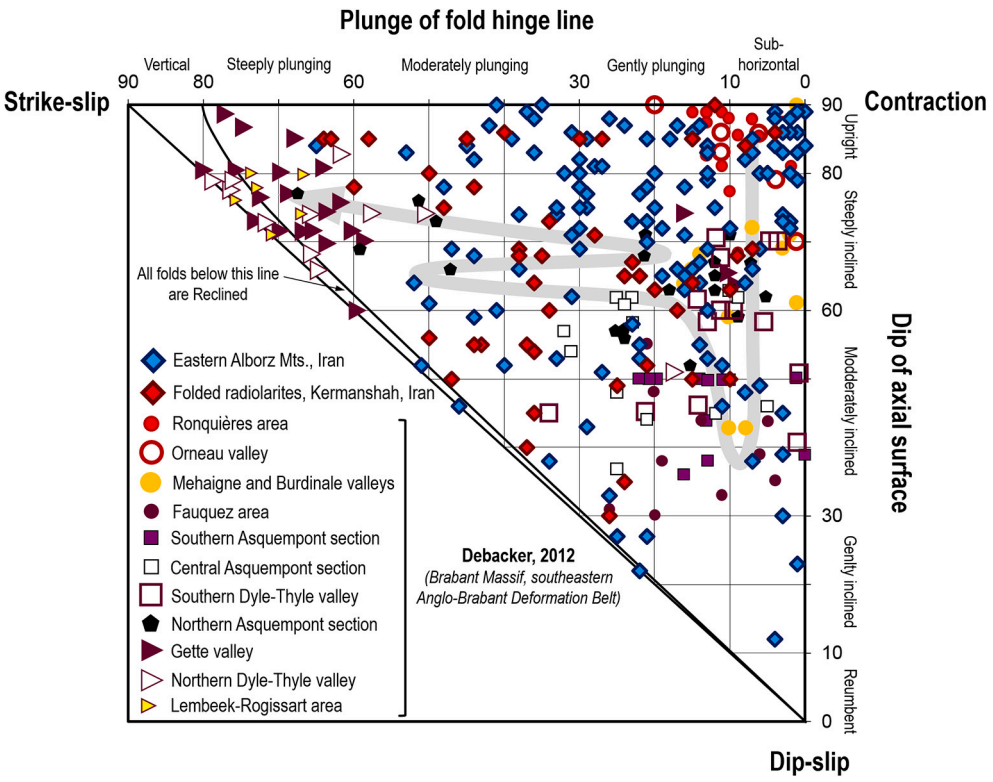

Fig. 19. Classification of folds based on the orientation of the hinge line and the axial surface (modified after Fleuty, 1964) combined with the strain triangle graph proposed by Jones et al. (2004). Gray curved arrow shows fold attitude transition zone and strain component. It should be noted that this only applies to transpression, not transtension, but we can make the lower left cornered Extension, and thereby also cover transtension.

sets (and also taking fold symmetry into consideration) on the Fleuty's (1964) diagram (Fig. 19) indicate a general curvilinear fold geometry within the transpressional zone. As a result, we can take Fleuty's (1964) diagram (Fig. 19) as showing the 'strain path of folding' and a relative estimation of strain partitioning through a systematic collection of fold data.

Rickard (1971) classified folds on the basis of three parameters: the dip of the axial plane, the plunge of the fold axis, and the pitch of the fold hinge in the form of a triangular diagram. He identified the following fields in which common fold types plot: (1) upright folds (with axial plane dipping 80° to 90°), (2) inclined folds (80° to 10°), (3) recumbent folds (10° to 0°), and (4) reclined folds (with pitches of fold hinge between 80° to 180° on the axial plane, thus plunging at the same angle as the dip of the axial plane) (Fig. 21). This is a special and comprehensive triangular diagram where the pitch of fold hinge is plotted with a variable scale along the lines representing constant dip of axial plane, while the plunge of fold axis varies from 0° along the base line to 90° at its zenith (Fig. 21). However, the plot is still restricted by the assumption of cylindricity.

5.1.2. *The attitudes of folds on the equal-area net*

When folds are too large or poorly exposed to be measured directly in the field there are a variety of methods available to characterize their geometries. One of these methods involves the use the equal-area or Schmidt net. Turner and Weiss (1963) provide abundant examples of how to describe large folds in metamorphic rocks using field measurements plotted on equal-area nets. Sediments accumulate as sub-horizontal layers so that, where undeformed, the pole to their bedding is everywhere sub-vertical and, plots near the centre of the net. After cylindrical folding, the poles to folded layers are distributed along a great circle, on what is called the π-diagram (Fig. 22). The pole of that great circle corresponds to the fold axis (or β-axis). Alternatively, the fold axis

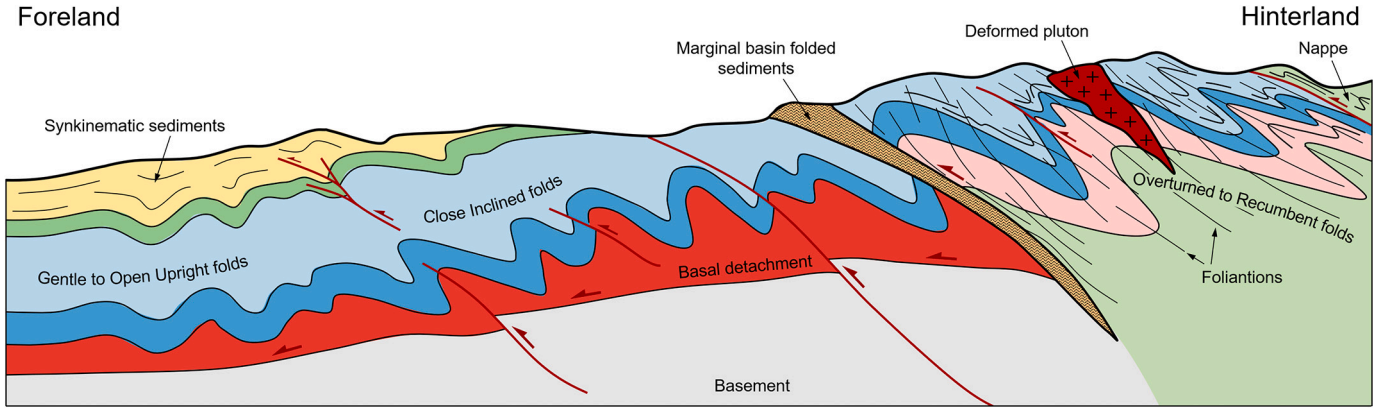

Fig. 20. Change in deformation and fold style in the orogenic belt, like the Zagros orogen, Iran.

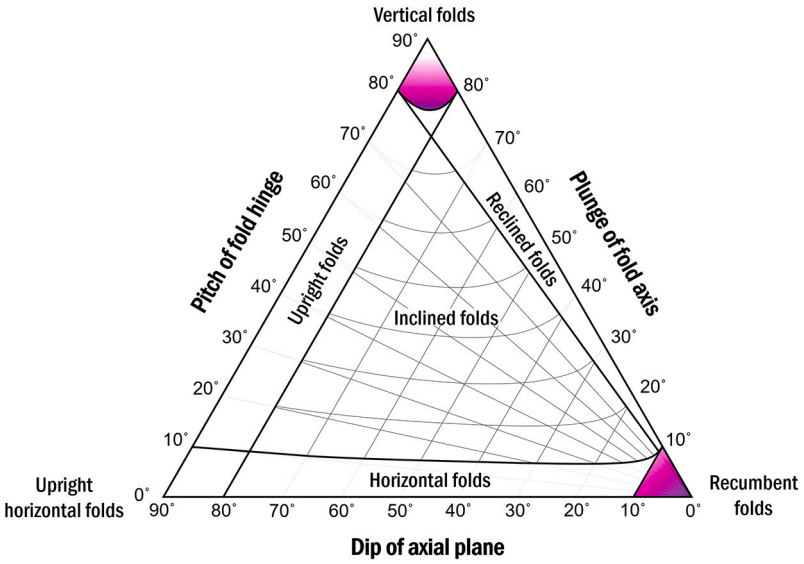

Fig. 21. Triangular graph of classifying fold attitude (modified after Rickard, 1971).

can be inferred from the intersection on a Schmidt net, of great circles, representing different orientations of the fold limbs on what is now known as the β-diagram on an equal area net or Schmidt net (Ramsay, 1964). Commonly, a π-diagram, which plots the poles of folded surfaces on the equal-area (Schmidt) net, is used to graphically show the orientation of such elements of fold geometry as the plunge of the fold axis, its fold symmetry, interlimb angle and the attitude of its axial surface (Ramsay, 1964).

Ramsay (1967) suggested two mathematical techniques for fold analysis. The first determined the unimodal pole distribution using vectors of directional cosines, and this technique is often called summing vectors. The second technique fixes the axes of cylindrical folds by determining the best-fit pole to their π-circles. Each pole to folded bedding is 90° from the axis of a perfectly cylindrical fold. In practice, the poles of any natural folds seldom lie exactly on a single great circle but define a zone around this circle (Fig. 22a-c) from which the great circle can be determined statistically. The attitude of a fold axial surface can be constrained if the orientation of its axial trace is known. If the fold is of parallel (or similar) type, its axial surface can be obtained by joining the bisector of interlimb angle with the fold axis, because the axial surface always bisects the interlimb angle of parallel folds.

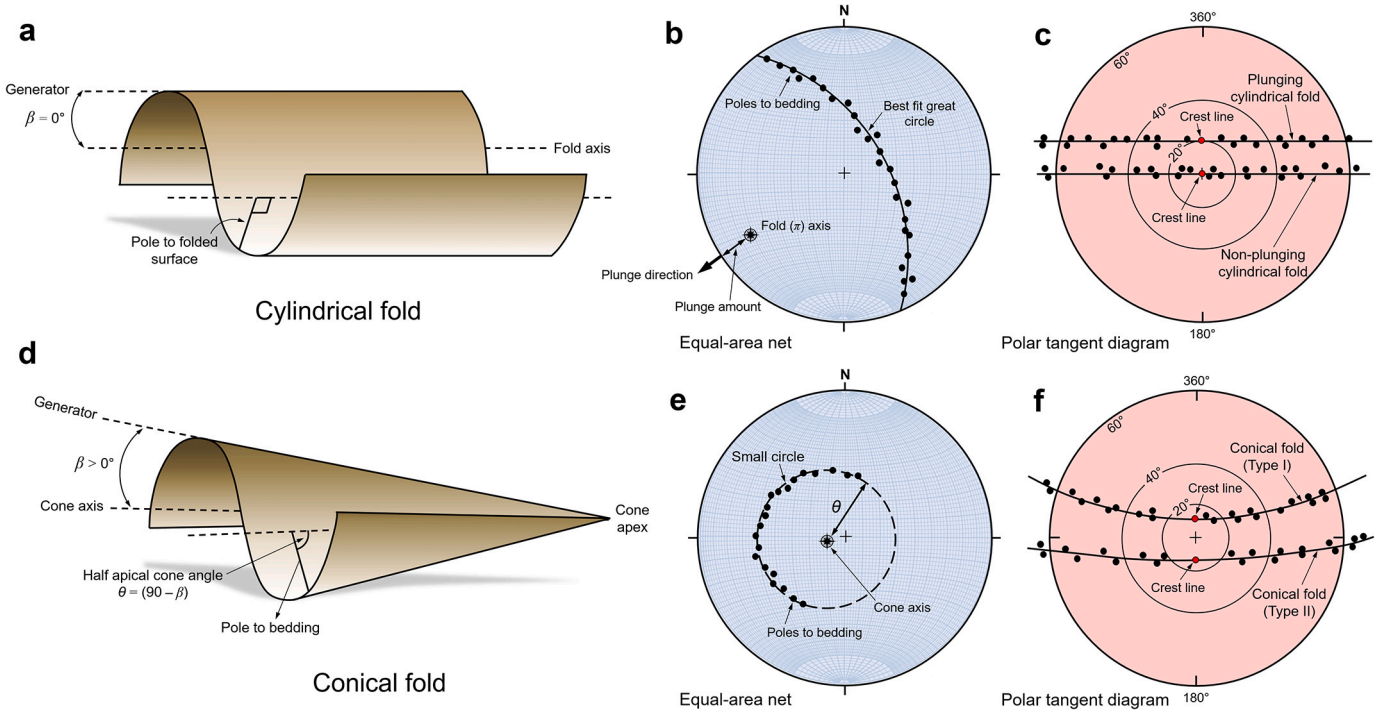

Fig. 22. Cylindrical fold geometry: a) 3D sketch of a cylindrically folded layer. b) Lower-hemisphere of Schmidt net for a cylindrical fold. c) Polar tangent diagram of layer attitude in non-plunging and plunging cylindrical folds (modified after Bengston, 1980). Conical fold geometry: d) 3D sketch of a conically folded layer. e) Lower-hemisphere Schmidt net projection of a conically folded surface. c) Polar tangent diagram of layer attitude in Type-I and Type-II conical folds (modified after Bengston, 1980).

A conical surface can be generated by rotating a line (the generator that is fixed at the apex of a cone) oblique to a defined rotation axis (Fig. 22d). This conical surface has a conical axis coinciding with the rotation axis, and the angle θ is equal to the angle between the pole to fold limbs and the rotation axis. Geometrically, a conical fold is characterized by the trend and plunge of fold axis, and by a semiapical angle β, which is the angle between the generator (where one end of the generator is fixed in the cone apex and the other end is free to move) of the conical surface and the fold axis (Fig. 22d, e). The semiapical angle is zero in perfect cylindrical folds (Fig. 22a). Folds with two hinge zones are conical if their hinges are not parallel to one another and the intersection of their axial surfaces is the axis of rotation (Stauffer, 1964, 1967; Gray et al., 1980; Stockmal and Spang, 1982; Nicol, 1993; Pueyo et al., 2003; Mandujano and Keppie, 2006; Pastor-Galán et al., 2012; Mulchrone et al., 2013). Overall, conical folds can be divided into circular conical, elliptical conical (symmetrical and asymmetrical) folds and combination of segments of different ellipses (e.g., Stauffer, 1967; Wilson, 1967; Venkitasubramanyan, 1971; Kelker and Langenberg, 1982, 1987, 1988). The simplest geometry of a conical fold is a circular conical fold, in which the angle between the generator and the cone axis is constant and equal to the semiapical angle. Furthermore, conical folds can be classified as Type-I and Type-II based on a hyperbola curve passing through bedding data and its curvature with respect to the origin on a polar tangent diagram (Bengston, 1980, 1981). The polar tangent diagram is a circular template that on it is perimeter azimuths are plotted in 2° increment clockwise from 0° to 360°. In addition, dips are plotted as a set of concentric circles, representing 5° intervals from the origin to the periphery (i.e., from 0° to 90°). Type-I conical fold is defined by a hyperbola concave toward the origin on the polar tangent diagram and the fold spreads out and flattens down plunge (Fig. 22f). In contrast, Type-II conical fold is defined by a hyperbola convex toward the origin on the polar tangent diagram and the fold comes to a point down plunge (Fig. 22f). The amount of curvature of the data locus reflects the magnitude of the apical angle of the conical fold. In this regard, as the apical angle increases, the amount of curvature increases (Bengston, 1980, 1981). Many authors have described the geometries and kinematics of conical folds and suggested several statistical methods capable of distinguishing between cylindrical, circular conical and elliptical conical folds among any data set. In the case of cylindrical folds, the most important features depend on its curvature (e.g., hinge and inflection lines and dependent features such as limb, interlimb angle, wavelength, etc.). The description of non-cylindrically folded layers requires the specification of additional parameters (Lisle and Robinson, 1995; Lisle, 2003). In general, curved orogens may be a likely location of large-scale conical folds when deformation is primarily due to differential rotation around a rotation axis affecting a population of geological surfaces with a variety of initial orientations.

It is useful to compare cylindrical and conical folds to understand these effects. If the axis of a cylindrical fold has been rotated to horizontal, then the strike of every single layer not only parallels all other layers, but also parallels the fold axis. In such folds, any folded layer will reach the pre-deformational position if the plunge of the axis is restored. But this does not happen in conical folds because the strike of the folded layer varies. A folded surface can be represented by the normal (pole) to the surface measured at several locations. When plotted on the net, the pattern of poles (or normal) determines the type of fold. Poles measured around a cylindrical fold are the easiest to fit (Cruden and Charlesworth, 1972; Kelker and Langenberg, 1976) because they lie on a great circle on the unit sphere. By contrast, poles to circular conical folds lie on small circles (Fig. 22e), and poles to elliptical conical folds lie in an ellipse projected onto the surface of the sphere. Parts of our knowledge concerning fold attitudes is achieved through the use of Schmidt net, and several digital applications can be used for such analysis, for example FieldMove Clino (Petroleum Experts), GEOrient (Holcombe software Holcombe, 2013), Stereo32 (Röller and Trepmann, 2008), OpenStereo (Grohmann and Campanha, 2010), Stereonet (Cardozo and Allmendinger, 2013) and StereonetMobile (https://www.rickallmendinger.net/).

5.2. Classification of folded surfaces

Turner and Weiss (1963) distinguished cylindrical from non-cylindrical folds based on the shape of the axial surface. They defined planar cylindrical folds (Figs. 23a and 24a), planar non-cylindrical fold (Figs. 23b and 24b), non-planar cylindrical fold (or polyclinal folds; Carreras and Druguet, 2019) (Fig. 23c), non-planar non-cylindrical fold with cylindrical (Fig. 23d), and non-cylindrical axial surface (Fig. 23e). Following this classification scheme, Williams and Chapman (1979) proposed a classification of non-cylindrical folds using a triangular PQR plot and based on measurements of two parameters: the interlimb angle (θ) and the hinge angle (β) (Fig. 25a). The end members of the resulting triangular plot are planes, cylindrical isoclines, and isoclinal domes. One

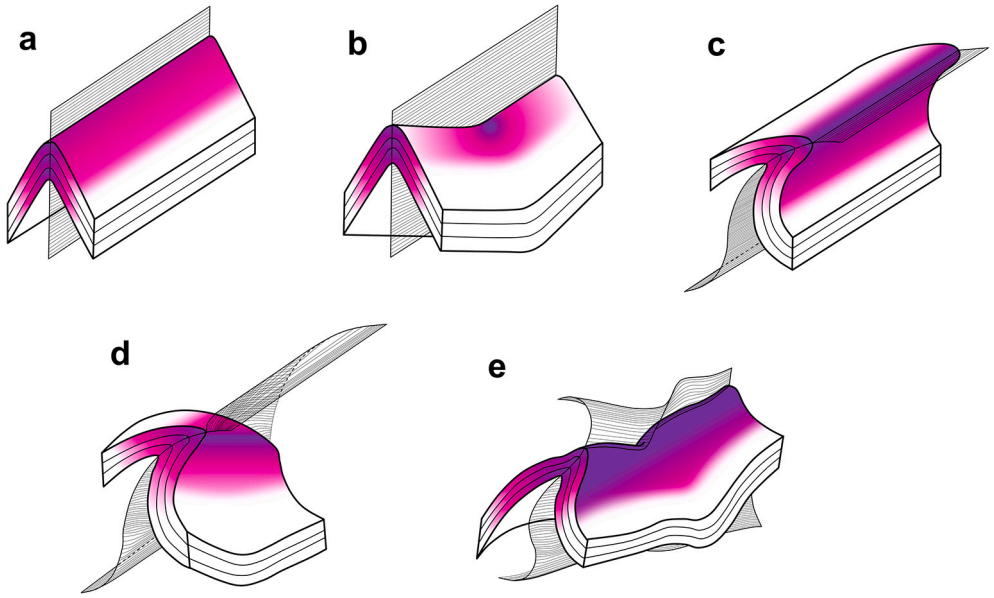

Fig. 23. a) Folds are described as plane and non-plane depending on the shape of the axial surface (after Turner and Weiss, 1963).

Fig. 24. a) A segment of gently inclined and plane cylindrical fold in the large-scale non-cylindrical folded turbiditic sequences at Almograve, Portugal. Photograph by Sigurd Fossen. b) Upright and non-plane non-cylindrical fold in turbiditic sequence at Makran, SE Iran. Photograph by Stefen M. Schmalholz.

of the conditions for the PQR diagram is that the hinge angle must be less than the interlimb angle. In this classification, there are also non-planar non-cylindrical folds (Fig. 24b) which use a parameter of axial surface angle (γ) (Fig. 25b). Fold shapes vary infinitely between the three end-members planes, cylindrical isoclines, and isoclinal domes based on degree of planarity ($P = \alpha/180$), degree of domicity ($Q = 180 - (\alpha + (180 - \beta))/180$), and degree of non-cylindrism ($R = (180 - \beta)/180$) (Fig. 25c) (Williams and Chapman, 1979). Each parameter varies between 0 and 1, while the relationship between all three parameters is: $P + Q + R = 1$. Therefore, if two of these values are known, the third can be determined. Furthermore, the degree of non-planarity of non-planar non-cylindrical folds could be represented by a parameter $S = (180 - \gamma)/180$), varying from 0 for plane folds to 1 for folds with isoclinally folded axial surfaces. It may be plotted on the triangular PQR diagram as a circle whose area is proportional to the size of S or by a proportional bar-scale or by writing in the axial surface angle γ (Fig. 25b) (Fig. 3 in Williams and Chapman, 1979).

The orientation of a conical fold is described by the trend and plunge of its axis and by the semi-apical angle between the fold axis and a straight line constructed on the conical surface, called a generatrix. Considering fold amplitude (A) versus fold width (W), three forms of conical folds for shape reference emerges: vertical elliptical conical folds ($A/(\lambda/2) = 2$), circular conical folds ($A/(\lambda/2) = 0.5$), and horizontal elliptical conical folds ($A/(\lambda/2) = 0.25$). These define linear trends of constant values for the ratio A/W with the terminus of the conical folds vanishing at the origin (Fig. 25d) (Welker et al., 2019).

Sheath folds (Fig. 26) are strongly non-cylindrical folds whose hinge lines curve more than 90°. They can form in zones of simple shear by gradual rotation of fold hinges toward the shear direction and by drag effect associated with rigid inclusions during non-coaxial deformation. In cross-section, sheath folds typically exhibit elliptical shapes (Fig. 26) (Carreras et al., 1977; Alsop and Carreras, 2007; Alsop and Holdsworth, 2012).

5.3. Fold classification based on curvature analysis

Recently developed surveying and remote sensing methods all offer some sort of mathematical framework for quantitative description. Differential classification of surfaces, introduced by Leonhard Euler (1707–1783), allows us to group surfaces according to curvature definition, as defined by Carl Friedrich Gauss (1777–1855). Curvature, in addition to dip magnitude, dip direction, coherence, energy gradients and reflector rotation, is one of the more popular geometric attributes. Curvature measures the lateral change in dip magnitude and dip direction. As the fold gets more open, the tangent circle and its radius get larger and larger until straight with an infinite radius with zero curvature. The normal curvature will reach maximum and minimum values in two orthogonal directions, and these values are the principal curvatures k_1 and k_2, respectively (Fig. 27a) (e.g., Bergbauer and Pollard, 2003; Mynatt et al., 2007; Pollard and Fletcher, 2005). The directions $\mathbf{k_1}$ and $\mathbf{k_2}$ corresponding to these principal curvatures are the principal directions. The principal curvatures and directions are a convenient way of describing surface curvature in the vicinity of a point on the surface. In this regard, the maximum principal curvature and its direction at every point can highlight the areas of tightest folding, and paired with the directions of minimum principal curvature can highlight the locations of fold hinges (Pearce et al., 2006). Other curvature parameters calculated from the principal curvatures (Gaussian, K_G, and mean curvatures, K_m) together provide a quantitative description of the shape of a surface (Mynatt et al., 2007; Lisle and Toimil, 2007; Zulauf et al., 2017). Other important curvatures are the most positive (k_{pos}), most negative (k_{neg}), dip (k_{dip}), and strike (k_{strike}) curvatures (Roberts, 2001). Various algorithms and software have been proposed for the calculation of principal curvatures of geological surfaces (e.g., Ozkaya, 2002a, 2002b; Bergbauer and Pollard, 2003; Bergbauer et al., 2003). Most of these deal with infinitesimal properties of the surfaces and their variation (Fernández-Martínez and Lisle, 2009).

The goal of curvature analysis is to describe how a surface changes its shape. Curvature analysis has been related to strain (e.g., Lisle, 1994) and has been applied to the exploration of fractured petroleum reservoirs to identify variations in subseismic fracture and deformation band density and its relation to porosity and permeability (e.g., Fischer and Wilkerson, 2000; Mandujano et al., 2005; Allwardt et al., 2007; Bergbauer, 2007; Stephenson et al., 2007; Pearce et al., 2011; Shaban et al., 2011). It has also been applied to subsidence-related risks, glaciated mountain landscapes, watersheds, mineral resource assessment, landslide, landform, and rivers (e.g., Stecchi et al., 2009; Romstad and Etzelmüller, 2012; Prasicek et al., 2014).

Roberts (2001) proposed a geologic curvature classification scheme for a point on a surface by using the Gaussian curvature (K_G): $K_G = K_{min}$. K_{max}, and mean curvature (K_M): $K_M = (K_{min} + K_{max})/2$ (Fig. 28). To mitigate the muting effect of K_M, Stewart and Podoloski (1998) proposed using the total curvature (K_T), where $K_T = k_1 + k_2$. The concept of Gaussian curvature was introduced in Gauss's landmark paper on the

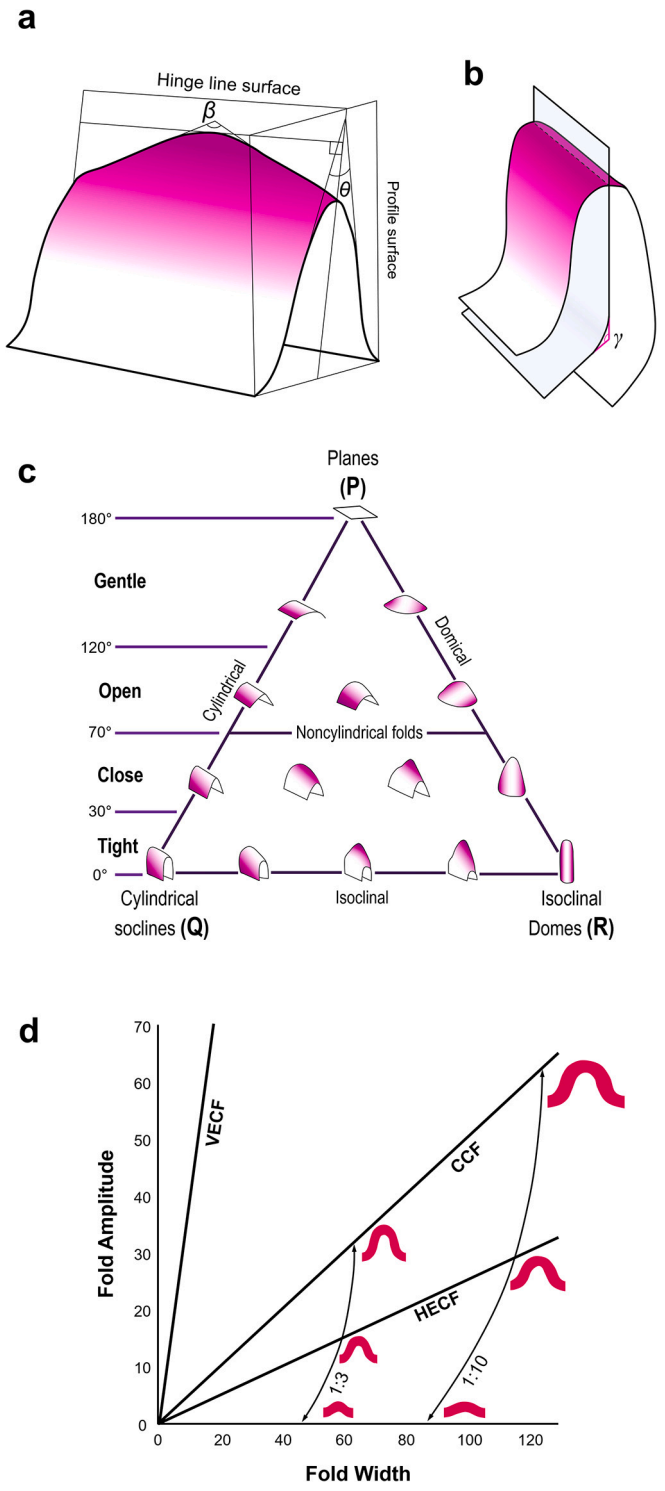

Fig. 25. a) Geometrical description of a noncylindrical plane fold, as θ, interlimb angle and β, hinge angle. b) hinge surface γ in the cylindrical, non-plane folded surface. c) The variety of fold shapes and their position on the PQR diagram (a-c modified after Williams and Chapman, 1979). d) Plot of fold amplitude (A) versus fold width (W). Three forms of conical folds for shape reference (modified after Welker et al., 2019): Vertical Elliptical Conical Folds (VECF) (amplitude/(λ/2) = 2), Circular Conical Folds (CCF) (amplitude/(λ/2) = 0.5), and Horizontal Elliptical Conical Folds (HECF) (amplitude/(λ/2) = 0.25) define linear trends of constant values for the ratio of A/W with the terminus of the conical folds vanishing at the origin. Profile sections along the crestal trend of the 1:3 and 1:10 periclines define curved trends for the ratio A/W that are highly discordant to conical fold trends and do not terminate at the origin (modified after Welker et al., 2019).

Theorema Egregium ("remarkable theorem"), considered by some to be the most important theorem within differential geometry. It is clear from the Gaussian curvature relation that the Gaussian curvature at a certain point vanishes as soon as one of the principal curvatures becomes zero, in which case the point is called a *parabolic* point (Fig. 27c). When the principal curvatures are both non-zero and positive, the Gaussian curvature is positive and the point is termed *elliptic* (Fig. 27b). Finally, when the principal curvatures are non-zero and of opposite signs (i.e., the surface curves upwards in one direction and downwards in the other), the Gaussian curvature is negative, which corresponds to a *hyperbolic* point (Fig. 27d). While both the mean and Gaussian curvatures could be defined in terms of the two principal curvatures k_1 and k_2, they represent a fundamentally different perspective on surface curvature. The mean curvature is an *extrinsic* measure of the surface curvature. This means that it depends on the way the surface is embedded in the surrounding 3D space. On the other hand, the Gaussian curvature is an *intrinsic* measure of the surface curvature, meaning that it is independent of the surrounding space within the space itself (Hyde et al., 1996; Weeks, 2001). We have stated that the Gaussian curvature is an intrinsic property of the surface, yet the classical definition that we have given above relies on extrinsic concepts, namely the principal curvatures. This is in fact the "remarkable" aspect in the Theorema Egregium of Gauss. However, Gauss showed that the Gaussian curvature could also be defined on the basis of angle and distance measurements within the surface itself (i.e., intrinsically). The distinction between the mean and Gaussian curvatures is important, as some surfaces might be extrinsically curved, yet remain intrinsically flat, for example, buckling a flat stratum into a sequence of symmetrical cylindrical folds gives the surface a non-zero mean curvature, even though the Gaussian curvature of the surface is still zero since one of the principal curvatures is zero. Consequently, a flat plane cannot be transferred into a spherical or saddle-shaped surface by buckling/bending deformations alone since these surfaces have non-zero intrinsic curvature.

Maps of total curvature describe the shape of surfaces better that mean curvature, where strain can vary over small areas and surface curvature changes rapidly (Dunham and Crider, 2012). Different combinations of ranges of these principal curvatures define structures such as saddle ($K_G < 0$), cylindrical folds (monoclastic or uniclastic surfaces) ($K_G = 0$), and domes and basins ($K_G > 0$). These can be further divided into synformal structures (including basins, $K_M < 0$) and antiformal structures (including domes, $K_M > 0$) (Fig. 28) (Fig. 2 of Mynatt et al., 2007; Florinsky, 2016; Zulauf et al., 2017). $K_M = 0$ indicates the surface is a flat plane (that is neither concave nor convex) or a surface where $K_{min} = -K_{max}$ what Lisle and Toimil (2007) refer to as 'perfect saddle'. Structures where $K_G = 0$ must have $K_{min} = 0$ and are therefore consistent with a plane strain deformation. Areas of extreme K_G are generally inferred to correspond to areas of high 3D strain. It is important to note that the principal curvatures cannot be uniquely determined in points where the normal curvatures are all equal. Such a point is called an *umbilical point* (Hyde et al., 1996). The plane and sphere are the only two surfaces that are entirely composed of umbilical points. Perfect fold types shown in Fig. 28 require at least one principal curvature to be zero even for the plane, saddle, and cylindrical folds, whereas these geometries rarely occur in natural folds and often associated with measurement errors, inherent irregularities, fold-accommodation faults/fractures, and penetrative strain.

Principal curvatures are useful to quantify the amount of folding and to identify fold axes and generalized hinge lines ((Mynatt et al., 2007); Lisle et al., 2010). Assuming that rocks layers deform according to thin plate theory, Bergbauer and Pollard (2003) have demonstrated show curvature analysis based on approximate mathematical descriptions of generalized fold geometries can lead to significant errors between the maximum curvature of a planar curve and the second partial derivative as a function of slip along the curved line when considering more complex areas of non-cylindrical folding. For further analysis of the folded surfaces, differential geometry is the appropriate tool for

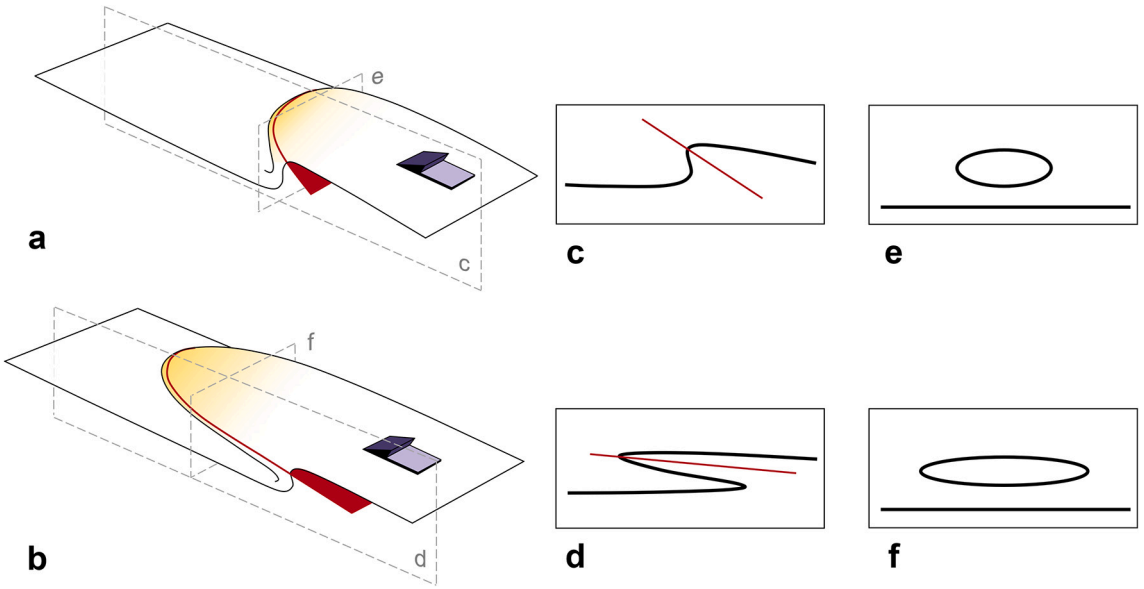

Fig. 26. a-b) illustration of progressive folding into a sheath fold during shearing in high strain zones. (c-d) and (e-f) show sections parallel and perpendicular to the transport direction (shear sense), respectively, as indicated by dashed lined in (a-b) (modified after Fossen et al., 2019).

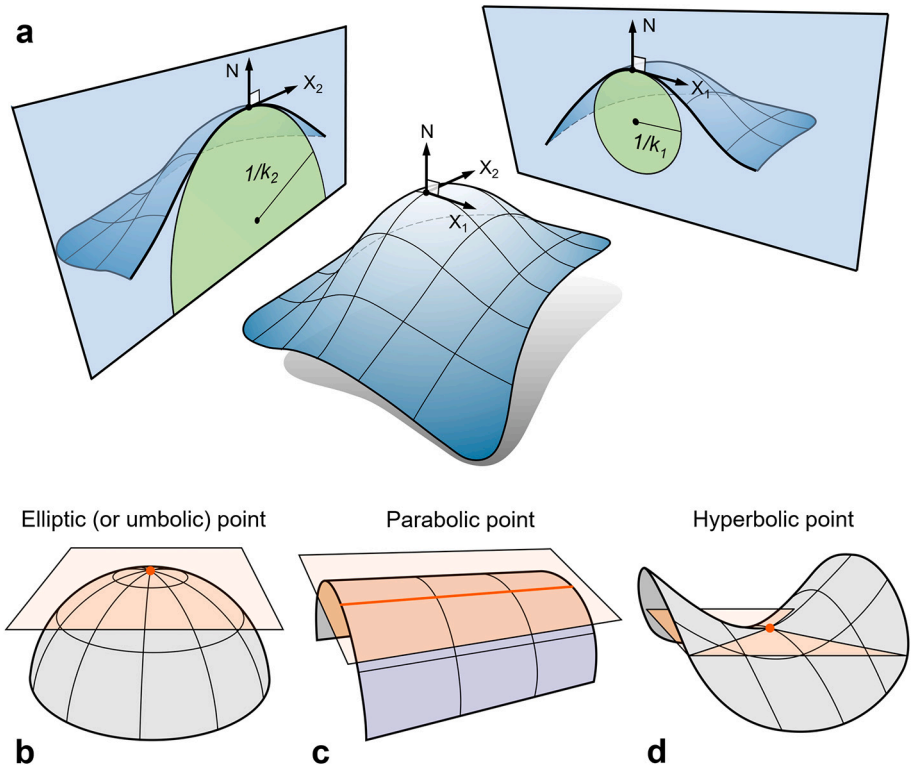

Fig. 27. a) 3D conceptual model of curvature of the surface. The unit vectors X_1 and X_2 along which we find the maximum and minimum normal curvatures k_1 and k_2 are called the principal directions, which are orthogonal; the curvatures k_i are called the principal curvatures. Surface categorization based on the sign of Gaussian curvature, a surface point is called: b) elliptic (or umbilic) point, if $K_G > 0$; c) parabolic point, if $K_G = 0$; d) hyperbolic point, if $K_G < 0$.

quantitative description of curved geological surfaces such as bedding, fractures, faults, plumose structures, foliations, sedimentary boundaries and unconformities. The geologic curvature classification combines the information from both the Gaussian curvature and the mean curvature and, thus, successfully divides geologic surfaces into areas of structural similarity (Lisle and Robinson, 1995; Ozkaya, 2002b; Schmid et al., 2008). The Gaussian curvature is sometimes referred to as the total curvature, which is a powerful tool to detect and analyse non-cylindrical

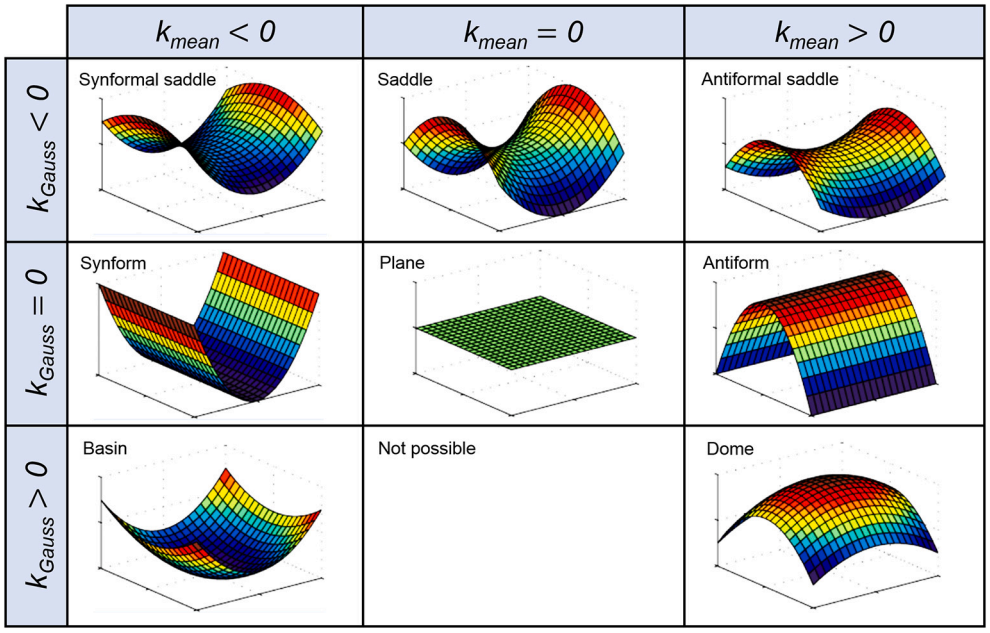

Fig. 28. Geologic curvature classification. The geologic curvature of a point on a surface can be determined from the Gaussian curvature (K_{gauss}) and mean curvature (K_{mean}) at the point (modified after Roberts, 2001; Bergbauer and Pollard, 2003; Bergbauer et al., 2003; Mynatt et al., 2007).

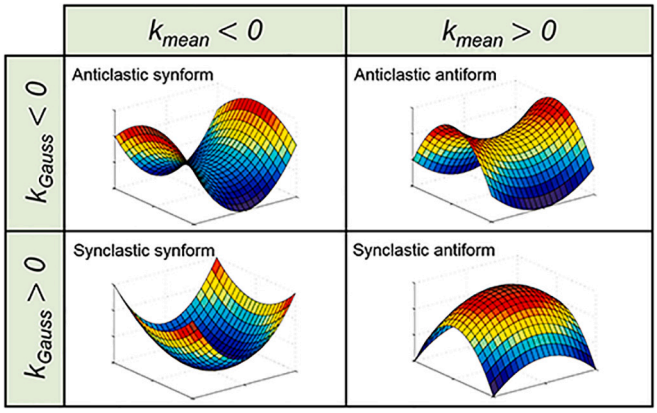

Fig. 29. Fold classification scheme based on the Gaussian curvature (K_{gauss}) and mean curvature (K_{mean}) (modified after Lisle and Toimil, 2007).

shapes and to predict fractures (Lisle, 1992a, 1994; Bergbauer, 2007; Shaban et al., 2011; Sou et al., 2012) in which the fracture patterns vary in terms of geometrical and topological relationships. However, because the Gaussian curvature is an intrinsic quantity, it is not adequate for distinguishing between differently aligned shapes in space. The difference between predominantly convex and predominantly concave situations can only be determined by the mean curvature. In geologic terms, the mean curvature separates antiformal from synformal shapes. Curvature-based predictions typically assume that folded layers behave like flexed elastic plates, and relate plate strain to the shape of a folded layer (Mynatt et al., 2007).

Lisle and Toimil (2007) suggested ways of analysing geological surfaces in terms of the number and characters of the folds present (Fig. 29). This method uses differential geometry to work out a generalized definition of folds as being composed of "adjacent points on a surface that share some common curvature characteristic". The sign of the value of principal curvature indicates the sense of curvature. According to definition, a (convex-upward) antiform is composed only of points with positive curvature, whereas a (concave-upward) synform is made up of negatively curved portions of the surface; the boundaries between adjacent folds of both types are marked by points of zero curvature. A positive Gaussian curvature implies that four classes of folds result from this definition (Fig. 29): 1) Synclastic antiforms ($M > 0$, $G > 0$) include domes and more elongate whale-back forms. 2) Anticlastic antiforms ($M > 0$, $G < 0$) resemble house roofs with a sagging ridge. 3) Anticlastic synforms ($M < 0$, $G < 0$) have the form of a shoehorn or a stick or rhubarb or celery. And 4) Synclastic synforms ($M < 0$, $G > 0$) are basins and more elongate canoe-shape folds.

Lisle (2003) described a periclinal fold as a kind of non-cylindrical fold that define elliptical and/or hyperbolic pattern on maps, for which the ratio of their principal curvature values is known as Dupin's indicatrix. In such folds, elliptical and hyperbolic patterns indicate dome-basin structures with synclastic curvature and saddle-like anticlastic curvature, respectively. Geological curvature is a combination of the mean curvature and the Gaussian curvature. This procedure allows us to identify and visualize the shape and orientation of areas on geological surface. Hence, the geological curvature classification is a powerful tool to subdivide surfaces into areas of structural similarity (e.g., Bergbauer and Pollard, 2003; Lisle and Toimil, 2007; (Mynatt et al., 2007); Burtscher et al., 2012). Together with a reasonable curvature threshold, k_t was introduced to extract geologically significant aspects of fold shapes by disregarding curvature magnitudes less than a certain value, quantifying to what extent a surface locally departs from an idealized shape. In this regard, (Mynatt et al., 2007) use the terms dome, antiformal saddle, synformal saddle, and basin for fold types 1–4, respectively (Fig. 28). Such areas are particularly important in the migration of hydrocarbons, as dome and basin structures in impermeable layers can trap hydrocarbons and the connecting saddle points define spill points. Fig. 30 presents the geological curvature distribution of the Sheep Mountain Anticline, a double plunging asymmetric fold located near Greybull, Wyoming, with varying curvature threshold so that by applying this technique, areas on the surface were identified (Mynatt et al., 2007). From a structural point of view, area of non-zero Gaussian curvature can be associated with strained zones, and faults might be recognized on Gaussian curvature plots. Analysis of both continuous and discontinuous curvature provides a very useful way to understand how surficial variations in an area relate to structures. However, in order to fully understand volume changes, especially for hydrocarbons reservoirs, curvature analysis must be accompanied by

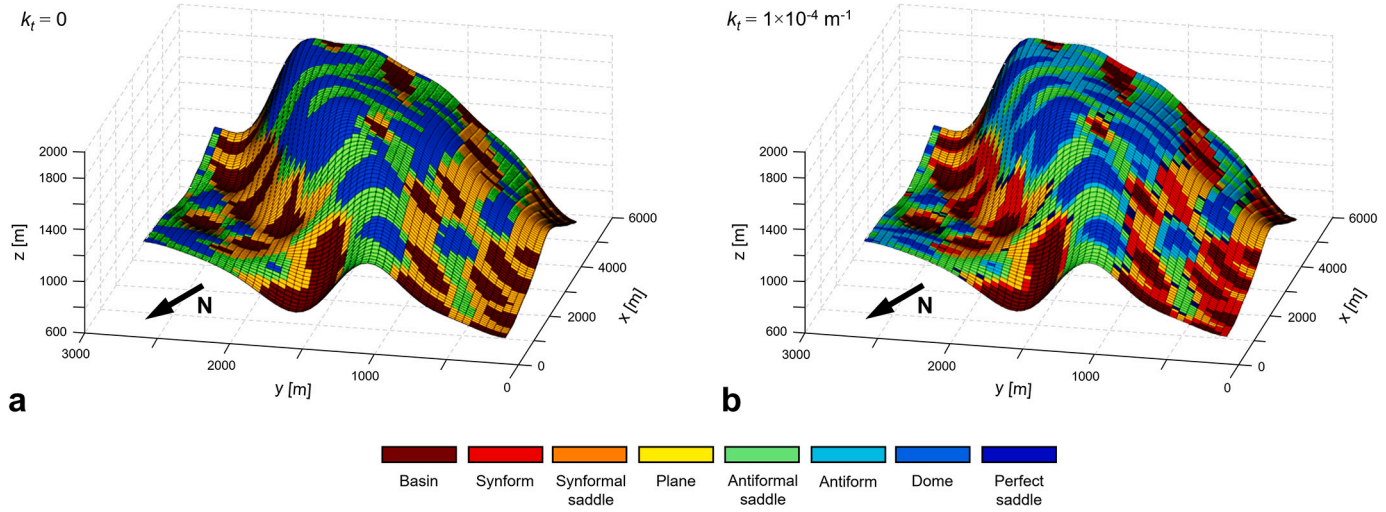

Fig. 30. Geological curvature plotted on the Sheep Mountain Anticline model with varying values of the curvature threshold k_t (after Mynatt et al., 2007).

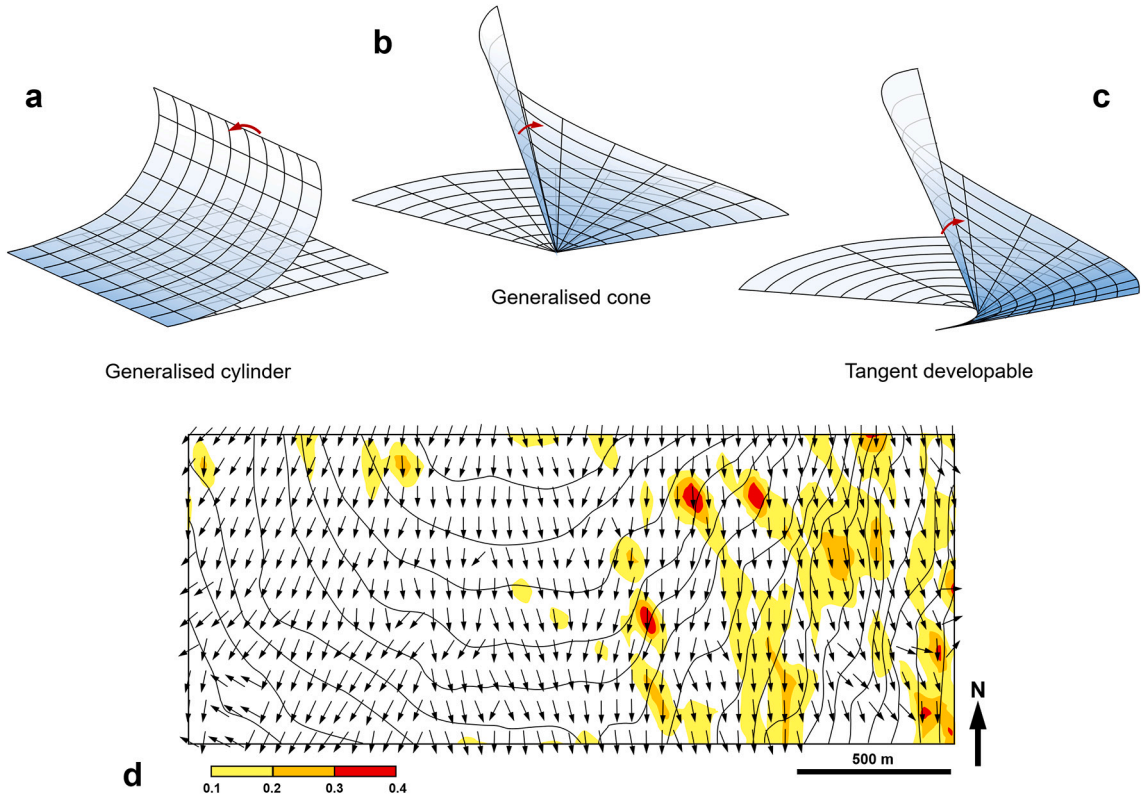

Fig. 31. a-c) Three classes of developable surfaces shown flat and with curvature. d) Structure contour and plunge-line map of the periclinal anticline. The arrows are the calculated plunge lines. The fold crest line is marked by the perpendicular relationship between plunge line and structure contour line trends. The divergence of the plunge lines toward the south indicates that the structure is decreasing in curvature in that direction. The curved pattern of the plunge lines in the west does not accord with the developable fold model. Regions of non-developable surface geometry detected by plunge-line skewness. The coloured areas are those with values of skewness greater than 0.1 and probably represent zones close to faults (modified after Lisle and Fernández-Martínez, 2005).

vertical sections, drilling logs, volumetric curvature and 3D strain analysis (e.g., Al-Dossary and Marfurt, 2006; Pearce et al., 2011; Shaban et al., 2011). However, when analysing the earth's surface, one should not forget to include the effect of erosion.

Zero-curvature surfaces are so well-studied in mathematics that they have special names. Surfaces with zero Gaussian curvature are called *developable surfaces* because they can be developed or flattened out into the plane without any stretching or tearing (Fig. 31a-c). For instance, any part of a cylindrical fold is developable since one of the principal curvatures is zero. On the other hand, a surface is developable if it can be unfolded to a flat surface that preserves lengths and the classical example is class 1B folds. Planes, generalized cylinders (Fig. 31a), generalized cones (Fig. 31b), and tangent developable (Fig. 31c) are the four basic classes of developable surfaces (Fernández-Martínez and Lisle, 2009; Rovenski, 2010). Developable surfaces are composed of ruling or straight lines (generators). In this regard, several researchers

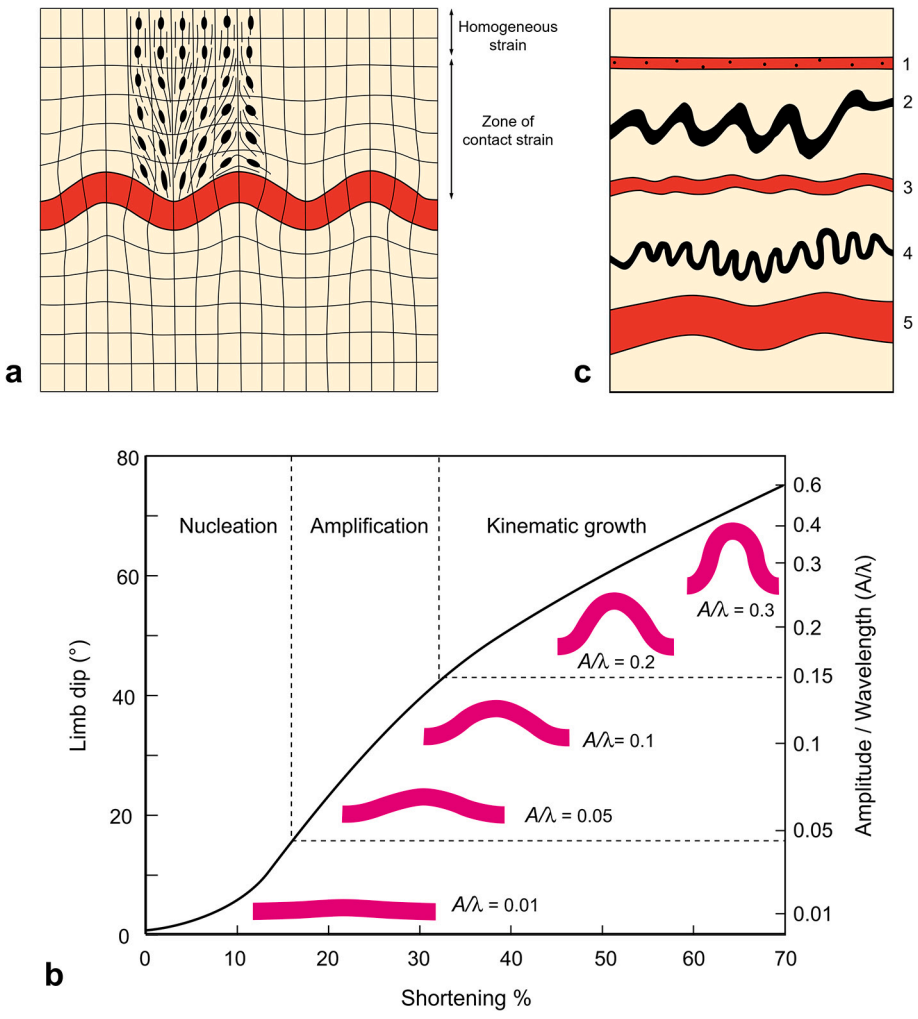

Fig. 32. a) The concept of contact strain around a single buckled layer (Ramberg, 1962; Ramsay, 1967). b) Scaled amplification curve of single layer buckle folds numerically simulated with a viscosity contrast of 50 (after Schmalholz, 2006), plotting limb dip or amplitude/wavelength versus shortening and transition between folding stages have clear mechanical meaning. c) Multilayer buckle folding with layers of increasing competence and the matrix competence equal to that in layer 1 (4 > 2 > 3 > 5 > 1 = matrix) (modified after Ramberg, 1964).

(Lisle, 1992a, 1994; Lisle and Fernández-Martínez, 2005; Thibert et al., 2005; Fernández-Martínez and Lisle, 2009) distinguished cylindrical, developable and non-developable surfaces by looking at how straight lines interrelate. By definition and according to structural and plunge-line maps via the program GenLab (Fig. 31d), which is a MATLAB® code for structural analysis of digitally and seismically mapped horizons (Lisle and Fernández-Martínez, 2005), cylindrical folds are those for which at least one principal curvature vanishes everywhere. Thus, the shape of a perfectly cylindrical fold is given by the translation of one generator in space. In other words, in perfectly cylindrical folds, the generators are constant in orientation across the surface and are therefore mutually parallel so that their orientation is referred to as the fold axis. In contrast, the plunge of a more general fold could be constant at points along a given plunge line but variable from one plunge line to the next (Fig. 31d). On the other hand, generators of non-developable surfaces with non-zero Gaussian curvature will form pairs of skew lines. Measurements of the so-called skewness, the closest distance between neighbouring generators, provides an index of deviation from a developable geometry. Analysing the map pattern can distinguish different domains on a general surface that are closely related to a developable geometry. In such maps, regions of structural complexity can be associated with brittle as well as ductile deformation (Fig. 31d).

6. Kinematic and mechanical aspects of folding

The two most important factors controlling folding and fold type is rheology (viscosity contrasts) and the way forces and strain act on a single layer or a multilayer sequence. Accordingly, folds can be classified as *buckle* (active) folds, *bending* folds, and *passive* folds (Hudleston, 1986; Fossen, 2016). Note that this is an ideal classification, and although they do occur as pure cases in nature, folds may also be a combination of two or all of these end-member fold types.

6.1. Buckle (active) folding

Buckling is a process in which layers and sequences fold when subjected to layer-parallel shortening, and requires a difference in competence (viscosity) between the folding layer(s) and the matrix (Fig. 32) (e.g., Biot, 1961; Ramberg, 1963a; Ramsay, 1967; Ramsay and Huber, 1987; Hudleston and Treagus, 2010). Geological buckling can involve a single (Fig. 32a, b) or multiple layers (Fig. 32c). During perfect buckling, layers maintain their thickness throughout the folding process, producing a parallel, concentric geometry (Currie et al., 1962; Johnson and Ellen, 1974). Buckle folds normally form with axes perpendicular to the maximum shortening direction and either gradually vanish away from the competent layer or are limited by detachment(s) (detachment folding).

The processes of buckling can ideally be divided into the following evolutionary stages: layer-parallel homogeneous shortening, nucleation of a buckling instability, amplification of the buckle, kinematic growth, and locking up (Fig. 32b) (Donath and Parker, 1964; Ramsay, 1974; Ramsay and Huber, 1987; Treagus, 1997; Schmalholz, 2006; Butler et al., 2020). The amplification is at its maximum at the boundary between nucleation and amplification and the transition from

amplification to kinematic growth is where the growth rate vanishes due to mechanical folding instability (Schmalholz, 2006). The position of a fold within a multilayer sequence influences its shape. Indeed, the position of the fold relative to its surroundings may be the most important factor controlling their development (Williams, 1980). The buckling mechanism explains: (1) how fold size and fold shape depend on layer thickness and layer properties, (2) how the thickness of the folded layer varies in its different parts, and (3) relations of the preferred mineral grain orientation to folding (Hudleston, 1986; Ez, 2000).

6.1.1. Single-layer buckle folding

Buckle folding of an isolated competent layer (viscous, elastic, and viscoelastic) in a less competent matrix subjected to layer-parallel shortening was thoroughly investigated in a series of influential studies from around 1960 and onwards (Fig. 32a) (e.g., Biot, 1957, 1961; Biot et al., 1961; Ramberg, 1961, 1963a; Currie et al., 1962; Ramsay, 1967; Fletcher, 1974, 1977; Smith, 1975, 1977; Johnson and Fletcher, 1994; Schmalholz and Podladchikov, 2001; Jeng and Huang, 2008). If the viscosity contrast is large, the amplification rate of buckling is very high and irregular, and isolated trains of rounded folds (ptygmatic folds) form. According to previous studies (e.g., Ramsay, 1974; Cobbold, 1976; Schmalholz, 2006; Hudleston and Treagus, 2010; Frehner, 2014, 2016), five general stages of 3D fold growth of a single-layer buckle fold are distinguished (Fig. 32b): 1) fold nucleation: 2) fold amplification; 3) fold elongation, with growth parallel to the fold axis; 4) kinematic growth, when fold amplification ceases and fold limbs become tighter; and 5) sequential fold growth, representing growth perpendicular to the fold axial surface. In this regard, it is important to study the evolution of folds and how folds grow to finite amplitude to relate fold geometry to strain and rheology. Analogue and numerical models (e.g., Ramberg, 1962; Ramsay, 1967; Reber et al., 2010) show that, in addition to strain magnitude, the long principal strain axis, which is orthogonal to the folded layer in the zone of homogeneous strain away from the buckle layer, converges toward the inner arcs of the layer (Fig. 32a). Several studies (e.g., Cobbold, 1977; Johnson, 1977; Abbassi and Mancktelow, 1990; Mancktelow and Abbassi, 1992; Johnson and Fletcher, 1994) agree that single-layer viscous folds nucleate on small and random mechanical perturbations. However, such analogue experiments focused mainly on large amplitude fold initiation. To avoid such nonlinearities, we consider the infinitesimal displacement and small deflections during buckling of a thin plate. This is the route taken by Biot (1937). Biot's (1937, 1961, 1965) theory predicts that, if the stiff layer is given small sinusoidal perturbations with different wavelengths in an infinitely thin 2D layer and Newtonian viscosity, one such perturbation will grow faster than the others. Even though all wavelengths grow exponentially, there is a fast-growing wavelength that will outpace and progressively dominate the others. The wavelength of this perturbation is known as the dominant wavelength (λ_d):

$$\frac{\lambda_d}{h} = 2\pi\left(\frac{\mu_f}{6\mu_m}\right)^{1/3} \tag{15}$$

where h is the layer thickness, μ_m is the matrix viscosity, and μ_f is the viscosity of the folded layer. If one considers the energy of a buckling system, then the classical Biot solution is the first solution that appears once folding nucleates. In this model, the system immediately switches to a lower energy configuration and continues to do so as deformation proceeds. In this treatment, folds develop sequentially and not simultaneously as predicted by the Biot linear model. Hence, Biot's model is only valid for initial stages of buckling. Also, in the many analogue experiments published in the 1970s did folds develop sequentially (e.g., Cobbold, 1976; Cobbold et al., 1971; Watkinson, 1976). This contrasts with many numerical models (e.g., Hobbs et al., 2008; Schmalholz, 2008; Frehner and Schmid, 2016; Schmalholz and Mancktelow, 2016), and such sequential behaviour is now better described by the nonlinear theory that can handle large deflections (e.g., Burke and Knobloch, 2007).

Numerical models are not currently compatible with natural examples or experiments, and need improvement with regard to material property, interaction and boundary conditions. One of the few three-dimensional time-dependent buckling studies that deforms a non-Newtonian material in a less viscous medium to large displacement was presented by Mühlhaus et al. (1998), the model showed that for non-Newtonian behaviour the dominant wavelength is less than the Biot (Newtonian behaviour) dominant wavelength. However, this study again has a Newtonian matrix. The development of fold trains is better explained by the nonlinear, finite amplitude theory developed by Burke and Knobloch (2007) who show that soon after buckling begins (during which the Biot solution holds) a bifurcation occurs, and the energy of the system is represented by two energy surfaces that intertwine with each other. As the shortening continues the system jumps from one of these surfaces to the other depending on which surface represents the lowest energy configuration for that strain (see Schmalholz and Mancktelow, 2016 and Hobbs, 2019 for details on the physic and mechanics of folding).

Mancktelow (1999) found that, if an initial wavelength is either much smaller or much larger than the dominant wavelength, the introduced waveform for periodic perturbations grows into folds. Mechanical instabilities develop in single layers where (1) there is a rheological contrast between the layer and its matrix, (2) there is an initial irregularity in layer interface, and (3) the layer is shortened or stretched. In general, the temperature and pressure during folding control the rheological behaviours of the folding layer and the matrix. There is a transition between elastic-brittle behaviour at shallow depths of Earth's crust and viscoplastic-ductile behaviour at moderate to deep levels that is related to confining pressure (crustal depth), and temperature. Elastic, viscoelastic, and viscous media are the most common rheologies studied for buckle folding (e.g., Biot, 1961; Ramberg, 1961; Jeng and Huang, 2008). Viscous deformation takes place in situations where stress depends on the strain rate at which the rock is being deformed, while plastic deformation accounts for cases in which the material flows plastically above a critical stress value, and therefore, stress is strain-rate independent.

Following the influence of strain rate on the buckle folding behaviour, Jeng et al. (2002) applied numerical modelling to a single layer marked by elastic-viscous layer-matrix properties. According to Jeng et al. (2002), the response of a competent elastic layer embedded within viscous material under fast strain rate (10^{-11} s^{-1}) will respond elastically. As strain rate was increased to 10^{-10} s^{-1}, buckling continued and the deformation was dominated by a typical elastic response. Moreover, when the strain rate slowed to 10^{-14} s^{-1}, the matrix viscosity reduced the input energy as well as the magnitude of elastic energy stored in the competent layer. As a result, buckling was dampened and the earlier developed folds were amplified. Schmalholz and Podladchikov (1999) introduced the parameter R for visco-elastic folding as: $R = \lambda_{dv}/\lambda_{de}$, where λ_{dv} and λ_{de} are dominant wavelengths for viscous and elastic folding, respectively. In this regard, if $R > 1$ and $R < 1$, folding is dominated by elastic and viscous deformation, respectively. The size and shape of this instability has been studied intensively by structural geologists because folding is very common on all scales in deformed ductile rocks (Johnson and Fletcher, 1994). Fletcher (1977) developed an additional analytical solution for single-layer folding that extended beyond the initial increment of folding to low-amplitude folds. Adamuszek et al. (2013) extended theoretical models and finite amplitude solutions for single sinusoidal layer folds and multiple waveforms represented by a Fourier series from their beginning to propagation.

In addition to analytical studies, analogue experiments and field-based studies, numerical models provide useful insights into fold growth and the evolution of stress and strain during folding, and also the mechanical and rotational behaviour of rocks and layers and the efficiency of the folding process. Early numerical models based on finite element analysis (FEA) have been used to analyse stress and strain

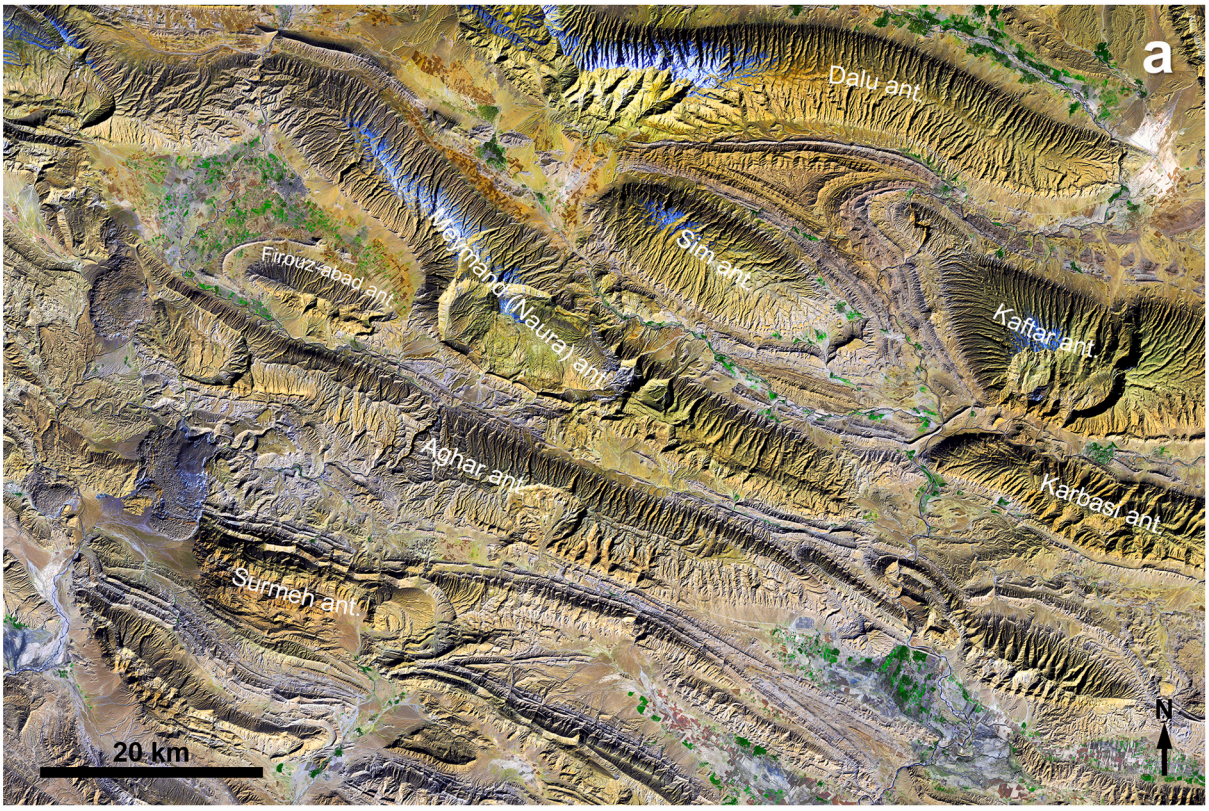

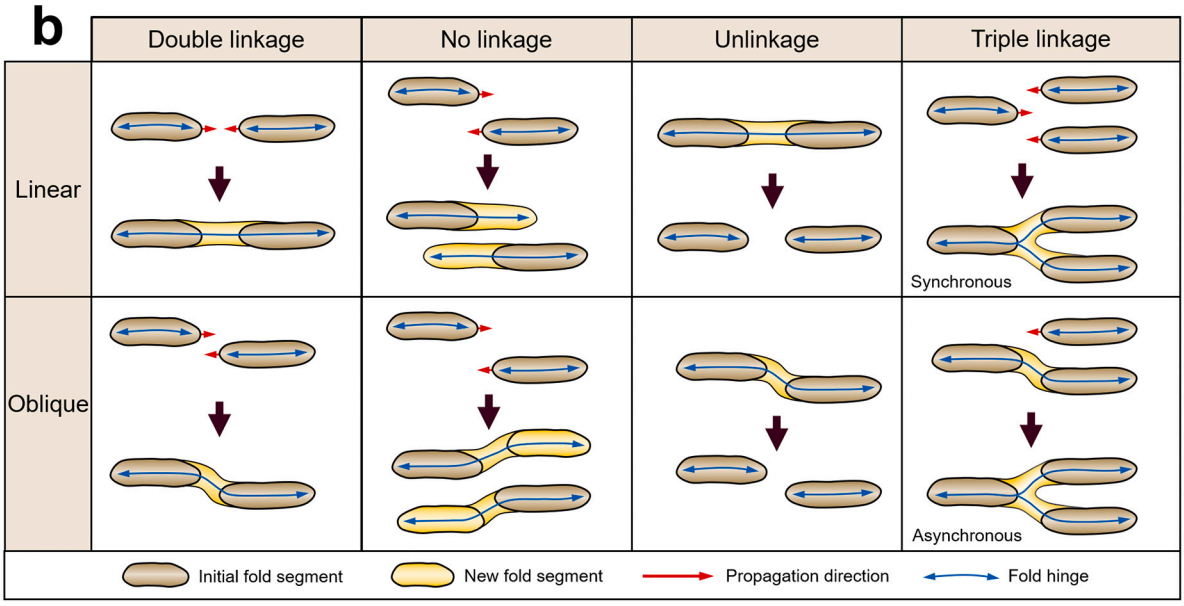

Fig. 33. a) Landsat image of Firouz-abad, Zagros fold-and-thrust belt (Iran) illustrating interacting doubly-plunging anticlines and synclines with curved axes as a result of lateral growth, and also some individual periclines (after Michael Rymer). b) Illustration shows conceptualisation of different fold interactions (after Bretis et al., 2011; Fernandez and Kaus, 2014).

distributions as single layers and multilayers buckled from low to high amplitudes (e.g., Dieterich and Carter, 1969; Hudleston and Stephansson, 1973; Parrish, 1973; Parrish et al., 1976; Shimamoto and Hara, 1976; Cobbold, 1977; De Bremaecker and Becker, 1978; Anthony and Wickham, 1978; Williams, 1980; Lan and Hudleston, 1991). The first fully 2D FE-model of viscous buckle folding was performed by Dieterich and Carter (1969), who calculated the stress evolution (magnitude and orientation) in amplifying single-layer folds. Following these researchers, the growth of single- and multilayer folds in viscous and viscoelastic layers with random initial perturbation at different rates of shortening has been studied intensely using 2D (e.g., Mancktelow, 1999, 2001; Schmalholz and Podladchikov, 2001; Casey and Butler, 2004; Schmalholz, 2006; Reber et al., 2010; Eckert et al., 2014, 2016; Adamuszek et al., 2016; Damasceno et al., 2017) and 3D numerical models (e.g., Kaus and Schmalholz, 2006; Schmid et al., 2008; Reber et al., 2010; Fernandez and Kaus, 2014; Liu et al., 2016, 2020; von Tscharner et al., 2016). Such models have been modified by Houseman et al. (2008) using BASIL, a 2D FE-package that calculates non-linear

plane strain in viscous single layers while also computing the viscous strain rates and associated stress field. However, it was not until 2006 that the first fully 3D FE-model of viscous buckle folding was presented (Kaus and Schmalholz, 2006). Schmid et al. (2008) developed a 3D FE-code with different horizontal shortening scenarios to explore the relationship between single-layer folds and their loading conditions, the linkage and superposition of folds with randomly initially perturbed layers that controls the location and final 3D development of fold patterns (Eckert et al., 2014; Fernandez and Kaus, 2014; Liu et al., 2016). Consequently, as folds grew out laterally in a 3D train, hinge lines of segmented folds can approach and interact depending on the distance or position with respect to other folds, so that they can link and combine to create long, and fully connected hinge lines (Fig. 33a) (e.g., Dubey and Cobbold, 1977; Price and Cosgrove, 1990, p. 265; Bretis et al., 2011; Grasemann and Schmalholz, 2012; Fernandez and Kaus, 2014). However, fold interaction does not always happen, and some folds remain isolated and generate well-developed doubly-plunging folds (periclines) (Fig. 33a). A conceptualisation of different fold interactions situations is shown in Fig. 33b.

Experiments performed on actual rock samples (Ramberg, 1964; Ghosh, 1966; Hudleston, 1973b; Neurath and Smith, 1982) for single-layer folds have also been studied in detail with illuminating results. Despite the widespread assumption that simple shear is very common in nature, most laboratory and numerical simulations of buckling involve pure shear deformation. However, Llorens et al. (2013b, 2019) present numerical models of single-layer folding by simple shear as well as pure shear (Fig. 3v) (e.g., prompted by experiments by Manz and Wickham, 1978). Not unexpectedly, they found that the visual distinction between pure and simple shearing of linear and non-linear viscous single layers is that axial surface orientations and foliation refraction are more variable under simple shear conditions. In addition, the duration of the nucleation stage is larger in folds resulting from simple shear, thus resulting in more layer thickening than in pure shear, whereas the maximum deviatoric shear stress distribution inside the layers indicates that folding a competent layer requires less work in simple shear than pure shear (Llorens, 2019). Hence, analyses of folding of single layers have provided critical information on the development of fold geometries, strain distribution and stress states throughout their evolution.

6.1.2. *Unfolding of buckle folds*

When a folded layer is subjected to layer-parallel extension it may: 1) locally break into boudins, 2) thin in a ductile manner and develop pinch-and-swell structures through necking, or 3) simply unfold. The viscosity ratio between a layer and its surrounding matrix during the extension plays a fundamental role in determining how the layer responds. This ratio may change during progressive deformation, as proposed by Flinn (1962, pp. 387–388), who suggested that rocks undergoing progressive deformation will pass through a continuous series of shape changes until deformation ceases (Fossen et al., 2019) if there are changes in strain rate, metamorphic condition (temperature and pressure) and strain-dependent rheology (e.g., Hobbs et al., 1990). Unfolding is much more complex in multilayer folds (see Ez, 2000; Carreras et al., 2005). Moreover, layer-perpendicular flattening and flexural flow related to the longer fold limbs will promote de-amplification and unfolding (Frehner and Schmid, 2016).

It should be noted that “unfolding” refers to the sequential reconstruction of fold growth backward through time from a geometry observed at present to an initial undeformed state, i.e. restoration or retrodeformation (Fig. 34). For simplicity, it usually assumes preservation of length or area (or volume in 3D models) (e.g., Vergés et al., 1996; Van Noten and Sintubin, 2019).

6.1.3. *Multilayer buckle folding*

Multilayer folds are far more common in nature than single layer folds and their mechanics is much more complicated. Moreover, the structures resulting from multilayer folding can show a wide variety of

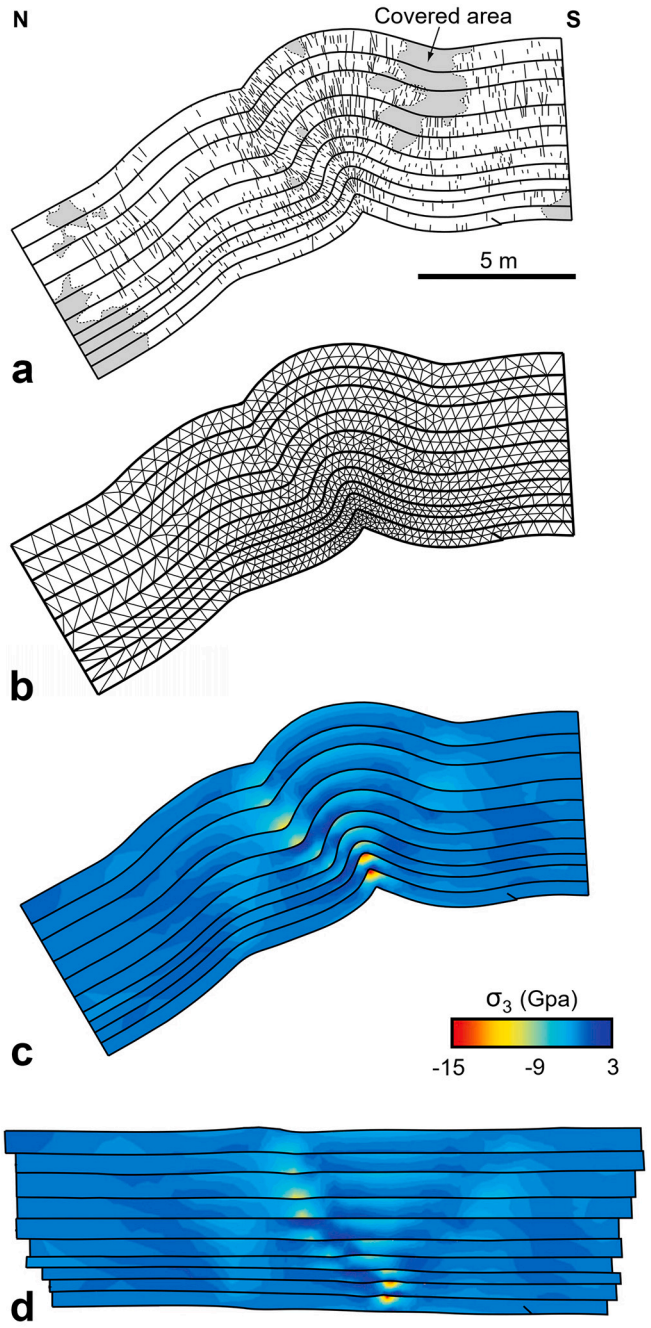

Fig. 34. Example of comparison between observed fold-related fractures and computed stress distribution using finite element modelling (after Maerten and Maerten, 2006). a) Interpreted bedding and fracture patterns in a contractional fold exposed in the Coulazou gully, souther France. b) Finite element mesh designed to replicate the exposed fold geometry. c) Fold-related stress distribution computed from an originally flat-lying sequence of rock into the observed fold shape. d) Unfolded finite element results showing sub-horizontal sequence.

geometries (Fig. 32c). Theoretical treatment of multilayer buckling closely follows that for single-layer buckling, although analytical, experimental and numerical models have shown that stratified rocks will rarely be as regular as these theoretical multilayer models. The behaviour of a multilayers during buckling depends upon many factors: 1) the number of competent layers, 2) thicknesses of competent layers, 3) their spacing and arrangement, 4) the competence contrast between layers, 5) the competence of the matrix (Currie et al., 1962; Handin

et al., 1976; Treagus and Fletcher, 2009; Ghosh and Sengupta, 2010; Hudleston and Treagus, 2010; Schmalholz and Mancktelow, 2016), and 6) the presence of interlayer slip (Damasceno et al., 2017; Wu et al., 2019). In this regard, Currie et al. (1962) introduced the term "*structural lithic unit*" (equivalent to the current term *mechanical stratigraphy*) to distinguish packages of multilayered rock that fold discretely and self-confined within a larger layered system.

The formation of multi-order (i.e., different sizes or scales) and multi-harmonic folds of mechanically competent and less competent layers is a common characteristic of multilayer buckle folds (e.g., Schwerdtner and Van Berkel, 1991; Treagus and Fletcher, 2009). Another common feature is parasitic folds (higher-order fold structures), a concept established by de Sitter (1964), that normally show systematic variation in (a)symmetry (S-, *Z*- and M-shaped) around the main fold, and associated variations in interlimb angle, amplitude and frequency (Fig. 35a-d) (Frehner and Schmalholz, 2006; Schwerdtner et al., 2010; Xypolias and Alsop, 2014; Frehner and Schmid, 2016; Liu et al., 2020). This is otherwise known as "Pumpelly's Rule", after the 19th century American geologist Raphael Pumpelly, who stated that small-scale structures tend to mimic larger-scale structures that formed at the same time (Pumpelly et al., 1894, p. 158), a statement of self-similar or fractal behaviour. A series of folds with the same asymmetry are also said to share the same vergence. The vergence direction is dictated by the sense of displacement of the upper limb relative to the lower limb. In this regard, the vergence of S-folds (sinistral shear, counter clockwise rotation) and Z-folds (dextral shear, clockwise rotation) allow us to predict the location of hinge zone and orientation of lower-order folds, sense of displacement/shear and associated rotated limbs (Fig. 35a, b) (Ramsay, 1967, pp. 351–355; Hazra, 1997; Carreras et al., 2005; Schwerdtner et al., 2010; Xypolias and Alsop, 2014). Vergence is independent of fold plunge and can be deduced from examination of either asymmetric minor folds or cleavage-bedding relationships (Bell, 1981; Weijermars, 1982). However, pre-existing asymmetric structures (Fig. 36a) (Frehner and Schmid, 2016) and obliquely oriented veins or dykes (Fig. 36b) (Carreras et al., 2005; Llorens et al., 2013a; Fossen, 2016; Lloyd, 2020) can result in parasitic folds with "wrong" vergence. Hence, vergence must be interpreted with care, particularly if the initial orientation of the marker is unknown.

In purely mechanical folding, parasitic folds can result from or be influenced by (Ramberg, 1964; Frehner and Schmalholz, 2006; Treagus and Fletcher, 2009; Frehner and Schmid, 2016; Liu et al., 2020): layers of different thicknesses, the number of thin layers, initial asymmetric geometries of thin layers, changes in the effective layer to matrix viscosity ratio, viscosity variations in multilayer systems, matrix anisotropy, strain rate, and the effect of fold trains starting to behave as effectively thicker layers so that larger wavelength folds develop. One of the most important geometrical characteristics of parasitic folds related to major cylindrical folds and folds produced in plane strain field is that their hinge lines are parallel.

There are cases where parasitic folds develop orientations that differ markedly from their related large-scale (lower-order) folds due to non-cylindricity of large-scale folds and the orientation of the layering relative to the axial surface and the principal strain axes. These have been called "incongruous" folds (Ramsay and Sturt, 1973). Moreover, Treagus and Treagus (1981) showed that oblique layers in plane strain can give rise to folds with axes that are oblique to the XY plane of strain ellipsoid and restricted to a narrow space, and generally develop en-échelon doubly-vergent (non-cylindrical) folds as periclines that may become highly non-cylindrical (Zulauf et al., 2020, 2021). In intensely folded units, parasitic folds are particularly well developed near the hinges of major folds, and less developed on the limbs (Fig. 35b-d) (Ramsay and Huber, 1987, p. 454–456). In addition, the thin layers are more deformed on the synclinal hinge zone of the thick layers and more stretched on their anticlinal hinge zone (Fig. 35b-d). Frehner and Schmalholz (2006) generated a 2D algorithm in numerical FE-models that developed parasitic folds during multilayer folding on scales from outcrop to crustal (Yamato et al., 2011) with a softer matrix between stiffer layers.

Asymmetric buckle folds can arise from stiff layers initially oblique to the maximum shortening direction in pure shear (Treagus, 1973), tangential longitudinal strain (or neutral surface folding) (Currie et al., 1962), and flexural flow (Ormand and Hudleston, 2003). Furthermore, in these categories are modifications of pre-existing symmetric and or asymmetric folds between enveloping surfaces oblique to the principal strain directions, the rotation of parasitic folds on the limbs of lower order or larger scale folds and the effects of simple shear or combination of homogeneous simple shear and irrotational deformation (Ramsay and Huber, 1987; Simpson and De Paor, 1993; Carreras et al., 2005; Alsop and Carreras, 2007; Frehner and Schmid, 2016), and or from the amplification of an initial asymmetric perturbation (Abbassi and Mancktelow, 1990).

Buckling of a layer or multilayers embedded in a weaker matrix may be sinusoidal and periodic, if the applied force is a linear function of the layer deflection (see Eq. 10; Fig. 2 in Ord and Hobbs, 2013). Furthermore, buckling can result in localised folds due to geometrically nonlinear systems and non-coaxial deformation. Where different packets of folds interact, chaotic folds can arise (Hobbs et al., 2011; Hobbs and Ord, 2012; Ord and Hobbs, 2013). Overall, folds in strongly competent layers of a multilayer buckle fold are broadly characterized by harmonic trains. Disharmonic and localised folds will develop in less competent layers and in the core of multilayer folds during layer-parallel shortening (Fig. 35). Natural folds do not produce perfectly periodic fold trains, but localised and aperiodic fold trains commonly showing attenuated fold limbs and sharp hinges. Many numerical and physical experiments do not reproduce features seen in real rocks, which suggests that the physics assumption is not correct or complete, so that they do not operate in the classical Biot theory of folding (Biot, 1965), which is rigorously true only in two dimensions for a layer embedded in a linear matrix. However, natural fold examples are not characterized by a single wavelength and are not strictly periodic. A series of cross-sections taken normal to the fold axes show that both the amplitude and wavelength of folds are commonly multi-periodic and irregular (e.g., Price and Cosgrove, 1990). An infinite number of wavelengths start to develop, of which one grows faster and becomes the dominant sinusoidal wavelength. The behaviour of nonlinear systems, however, is more complicated and Fig. 37 shows the buckling behaviour of a single layer embedded in nonlinear material. Here (Fig. 37) we see that the response may be homogeneous, with no buckling behaviour, or a range of buckling behaviours, depending on the sensitively to initial conditions, boundary conditions and the evolution of geometry and mechanical properties of both the layer and the embedding material during buckling. The heterogeneous response may be sinusoidal, periodic but non-localised, localised and periodic, localised and non-periodic, and quasi-periodic or chaotic (Fig. 37) (Burke and Knobloch, 2007; Ord and Hobbs, 2013; Hobbs and Ord, 2015; Hobbs, 2019). Fold trains are predicted by all of the afore-mentioned models (as they must for a linear matrix). However, field observations, experiments, as well as numerical models indicate that folds in 3D can never continue indefinitely along their hinge lines or along a straight line, even if they result from a single phase of folding, so that there must always be another arc- and wavelength parallel to the primary fold axis even for plane strain and also linking interaction zones due to lateral growth (e.g., Schmalholz, 2008; von Tscharner and Schmalholz, 2015; Liu et al., 2016; Welker et al., 2019; Nabavi et al., 2020b).

6.2. *Passive folding*

Folding that does not require layer competence contrast or layer-parallel shortening, is characterized as passive. In these cases, layering is mechanically passive and only serves as a visual marker. Donath and Parker (1964) described the mechanical condition for passive folding as one of high mean ductility and low ductility contrast (Fig. 38a). Note that ductility may be accommodated by frictional as well as crystal-

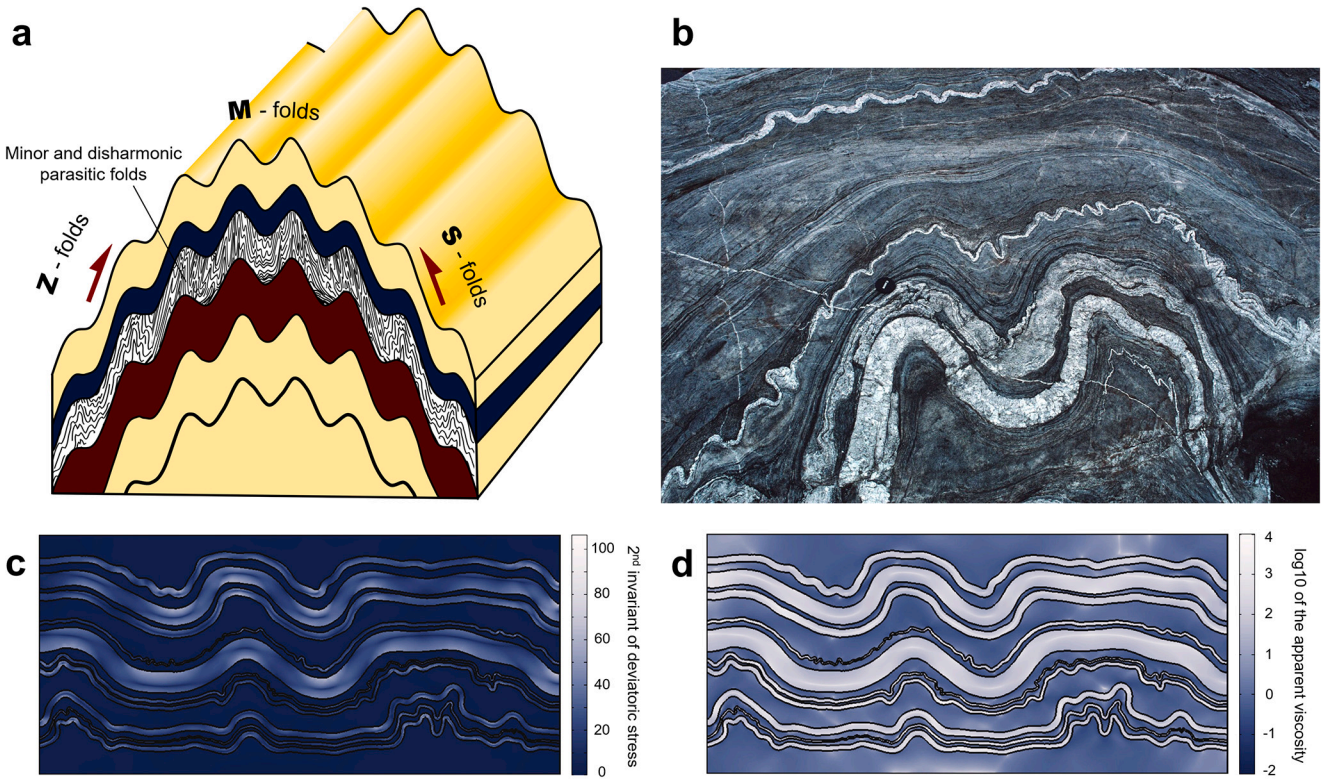

Fig. 35. a) Development of small-scale (higher-order) *Z*-, M-, and S-shaped parasitic folds, in which case they provide information about the geometry of the large-scale (lower-order) folds. b) Multilayer folded pegmatites in different thickness and wavelength within granodiorite unit. Thin folded layers developed as parasitic folds. Loch Cluanie, Northwest Highlands, Scotland. Photograph by David Chew. 2D finite element modelling of non-Newtonian multilayer folding subject to 36% of shortening: c) second invariant of stress, d) apparent viscosity (after Adamuszek et al., 2016).

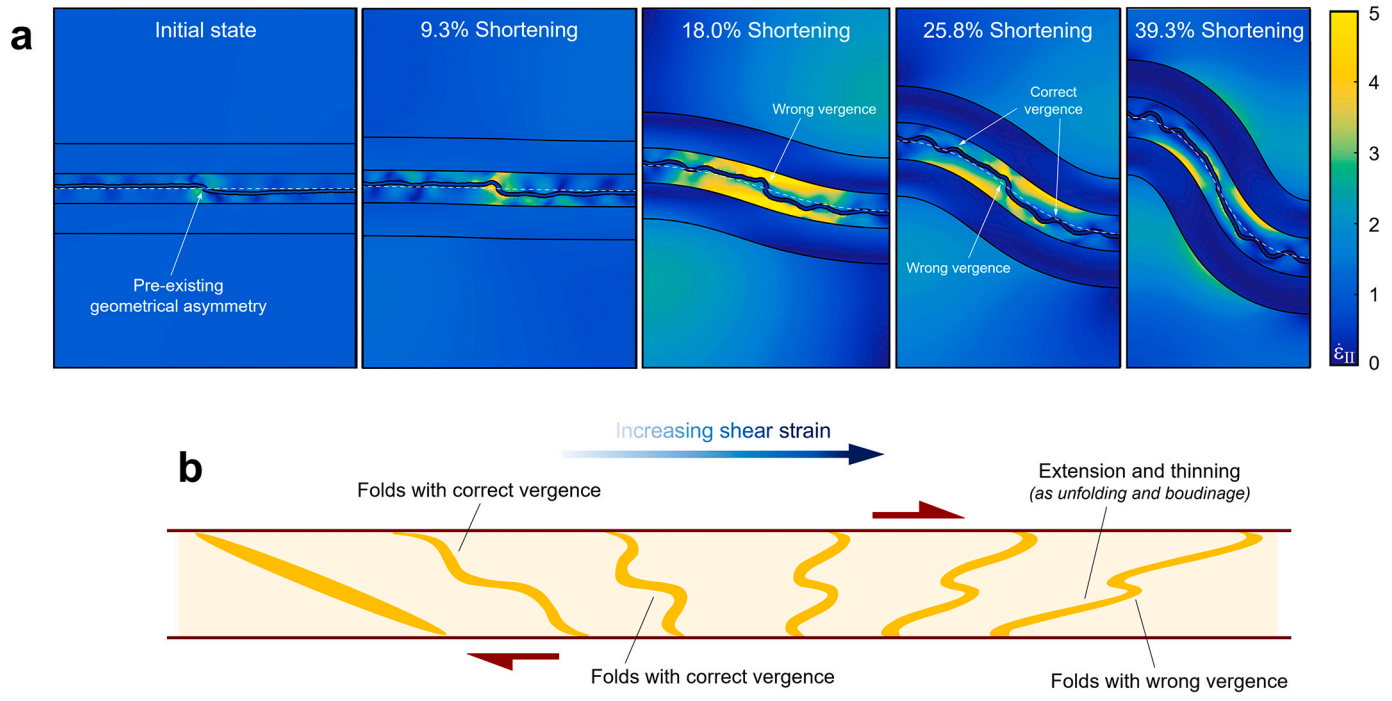

Fig. 36. a) 2D finite-element simulation snapshots of multilayer folding using Newtonian material as a thin layer exhibiting the pre-existing geometrical asymmetry with initial skew angle 60° sandwiched between two thicker layers. Increasing background shortening is indicated in % in each stage of the buckle folding process. Colours correspond to the second invariant of the strain rate tensor $\dot{\varepsilon}_{II}$. The initial asymmetry results in an alleged parasitic fold with wrong vergence, alongside true parasitic folds with correct vergence (after Frehner and Schmid, 2016). b) Progressive development of folds in simple shear model of the syntectonic vein, which is affected by dextral shear zone. This particular initial orientation can result in a "wrong" vergence as a result of increasing shear strain (based on Carreras et al., 2005; Fossen, 2016).

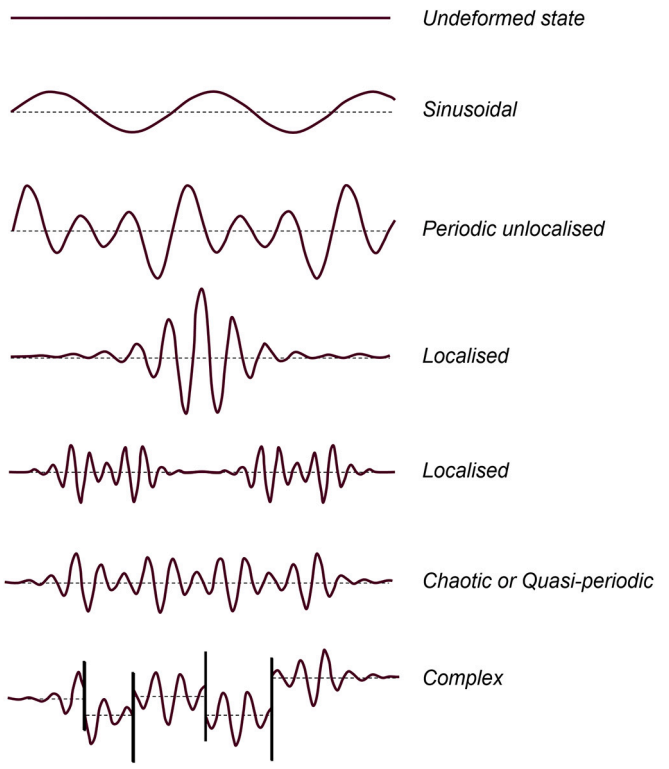

Fig. 37. The various response to the deformation of a layer embedded in a nonlinear material (some of the possible solution of to the stationary nonlinear Swift-Hohenberg equation). The homogeneous and sinusoidal responses are characteristic of linear embedding materials for very small deformation; such structures ultimately evolve to a sinusoidal response (after Ord and Hobbs, 2013; Hobbs and Ord, 2015).

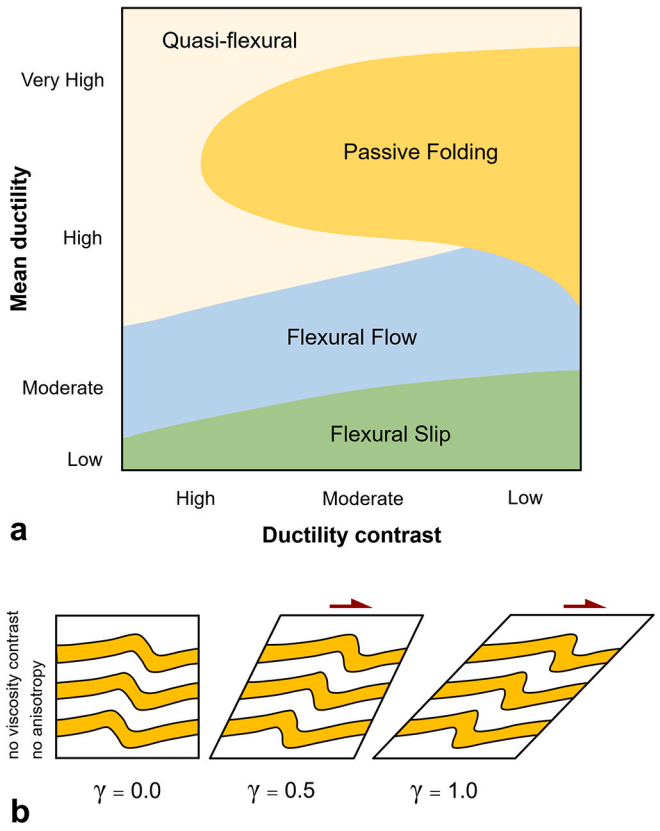

Fig. 38. a) Fields of folding related to mean ductility and ductility contrast (after Donath and Parker, 1964). b) Passive folds form by shearing of disturbances in layering, without an active mechanical influence of the layering. Fold geometry is that of similar folds.

plastic deformation mechanisms at the micro-scale. A common example of the former is soft-sediment passive folding. Passive folding is often associated with shear deformation. The shear (flow) must be heterogeneous for initially planar markers to passively become folds, and the marker must make an angle to the shear plane. Such shear-related folds are often termed shear folds (Fig. 38b), and at high shear strains, such folds tend to develop into sheath folds. Non-planar markers can amplify into passive folds also during homogeneous shearing (e.g., Cobbold and Quinquis, 1980; Vollmer, 1988; Fossen, 2016). Non-planar markers can also amplify into passive folds in almost any strain regime, including pure shear (Fossen, 2016), although amplification is generally faster in simple shear.

No structural softening resulting from the development of internal structures will occur in perfectly passive folds (no instability) (Schmalholz and Schmid, 2012) and the folds are similar (Class 2) and often harmonic and sinusoidal. In addition to heterogeneous strain and amplification of non-planar structures, passive folds may develop due to variations in flow with time (non-steady flow), and ductile accommodation of perturbation of the stress field around the cross-cutting element (like fracture, fault, joint and vein) from the time of opening until closing and subsequently rotation in the form of flanking structures (e.g., Coelho et al., 2005; Druguet, 2019). Passive folds are commonly observed within salt diapirs (in passive marker beds such as salt layer coloured by traces of other minerals), ice layers in glaciers, water-saturated sediments exposed to soft-sediment deformation, and sheared marbles and quartzites, and in magmatic deformation observed in migmatites, intrusive bodies and lavas. Various types of passive folds developing at shallow crustal depths are widely discussed in Section 8. Passive folding is probably common not only throughout the crust but also in the asthenospheric mantle, with its limited variations in composition and high temperature, and shear deformation against the overlying rigid lithosphere.

6.3. *Bending*

Bending is the process of folding that describes flexuring of a plane or layer induced by a force acting perpendicular or at high angle to the layering. Unlike buckling, bending does not depend on any viscosity contrast, and in the absence of such contrasts, bending can occur by passive folding. However, viscosity contrasts may exist, and such contrasts influence the way deformation is taken up by the rocks or sediments. For example, a common result of a viscosity or competence contrast is the occurrence of flexural slip or shear.

There are several kinds of folds that can form by bending, such as fault-bend folds, fault-propagation folds, folds around salt diapirs, folds between boudins (neck folds), folds formed by differential compaction in sedimentary basins, bending of a subducting plate, and very gentle lithospheric bending in response to isostatic readjustments associated with plume heads, sedimentary basin subsidence and post-glacial isostatic rebound (Fig. 39). In general, there are major differences in structural style, fracture and strain patterns associated with buckling and bending folds (e.g., Ramberg, 1963; Withjack et al., 1990; Cosgrove and Ameen, 1999; Cosgrove, 2015; Tavani et al., 2015; Coleman et al., 2019). Unlike buckle folds, bending folds are often long, cylindrical structures with a much higher aspect ratio (length/half-wavelength ratio) than buckle folds, and can form in both contractional, neutral and extensional settings. Also, unlike buckle folds, bending does not produce fold trains, but rather single structures, notably monoclines and domes.

The most common structures resulting from bending processes, are ‘fault-propagation folds’ (Fig. 39a), also known as ‘forced or drape folds’ (Fig. 39a) (Friedman et al., 1976, 1980; Logan et al., 1978; Stearns,

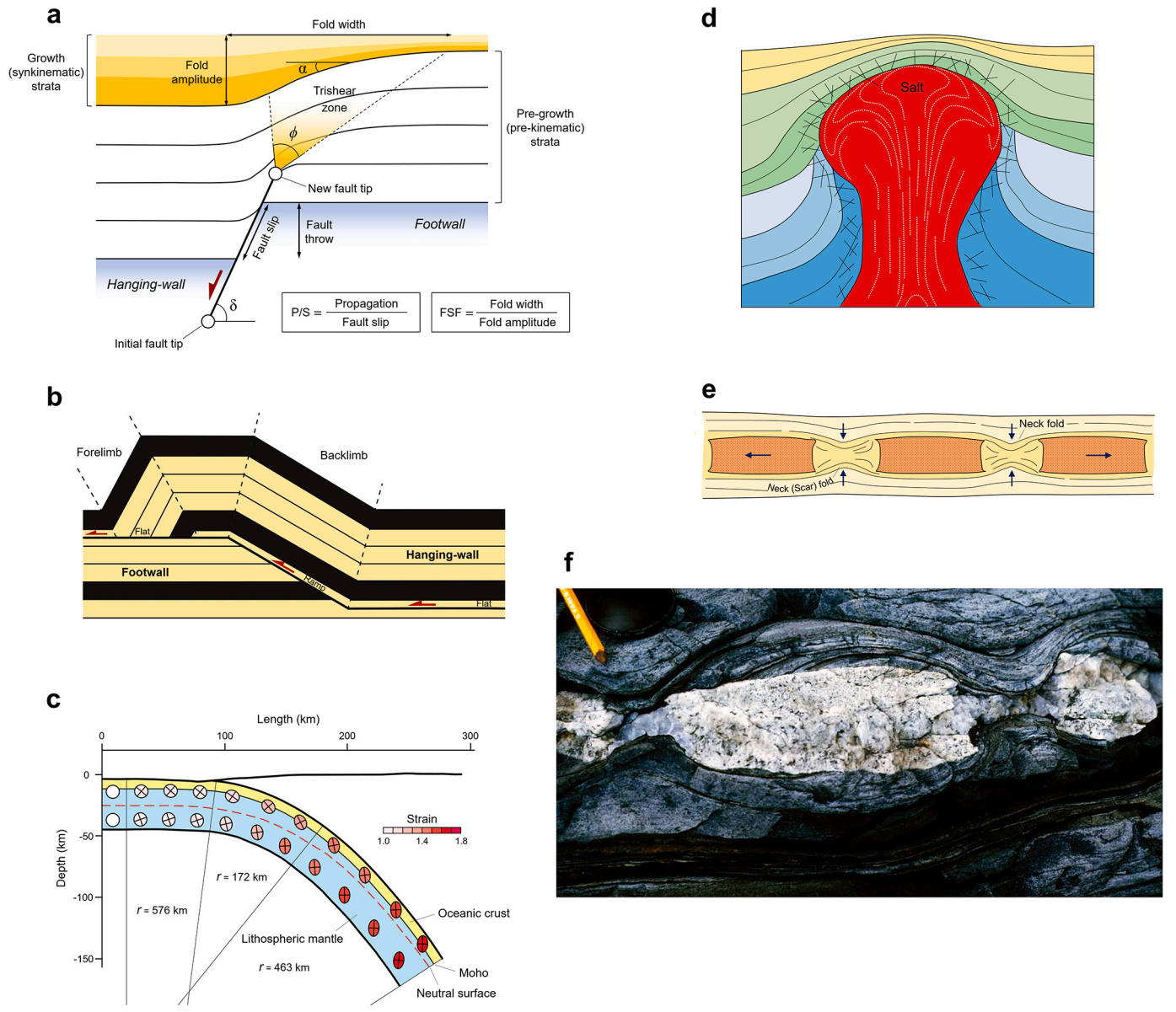

Fig. 39. Examples of bending process in different settings and scales: a) schematic diagram illustrating an extensional fault-propagation fold formed over a planar, dip-slip basement fault. Trishear parameters and terminology for the description of pre- and synkinematic growth strata are also shown (based on Coleman et al., 2019). α, ϕ, and δ are fold limb dip, trishear apical angle, and fault dip, respectively; b) Fault-bend fold kink-style model formed by thrust movement over a ramp (after Suppe, 1983, 1985); c) Flexural model generated by 50% of orthogonal flexure and 50% of flexural flow applied to the real subduction zone on the El Salvador. Ellipses correspond to finite strain ellipses of the bulk deformation accumulated (the ratio between the between long and short axes) from the beginning of subduction (after Romeo and Álvarez-Gómez, 2018); d) Bending folds formed above and adjacent to salt diapir or igneous intrusion; e) Neck folds formed between boudins (after Fossen, 2016); f) Photograph of rectangular boudins formed by stretching of a granitic dike in metasediments with scar folds developed between boudin blocks (after Fossen, 2016).

1978; Withjack et al., 1990; Coleman et al., 2019; Nabavi et al., 2020a). These form as a fault propagates upwards and creates a monoclinal fold ahead of the propagating fault tip. The fault can be normal, vertical or reverse, and is often a reactivated basement fault or, in fold-and-thrust belts, a fault branch extending upwards from a detachment. Deformation occurs in an upward widening zone of ductile deformation that typically involves flexural slip (bedding-plane slip), fracturing, deformation band formation and/or smaller-scale faulting.

Another example is fault-bend folding, which is particularly common in fold-and-thrust belts where a thrust ramps up a competent layer and flattens out at a new weak stratigraphic level (Fig. 39b) (Suppe, 1983, 1985; Suppe et al., 2004; Brandes and Tanner, 2014; Hughes et al., 2014). In this case bending occurs above the kink in the thrust. It can also occur in the hanging-wall to non-planar normal faults, for example as roll-over folds above listric faults (Fossen, 2016; Nabavi et al., 2020a).

The strain patterns and associated small-scale structural networks associated with fault-propagation folds are related to a number of factors, such as the sense of movement on the underlying fault, the absolute and relative mechanical properties of the folded layers, confining pressure (burial depth) and differential stress. Small-scale structures associated with fault-propagation folds may influence fluid flow in a reservoir during injection or production of hydrocarbons (Zuluaga et al., 2016). In some cases, a relation between curvature and density of small-scale structures such as fractures or deformation bands has been demonstrated (Wilson et al., 2016; Fossen et al., 2017). In such cases, curvature analysis of such folded layers may successfully predict density variations in subseismic structures that can affect fluid flow.

A simple kinematic model used to explain fault-propagation folds is

the trishear method. Field observations, seismic reflection data, and analogue, and numerical models all show that an upward-widening triangular 'trishear zone' of heterogeneous strain develops ahead of the propagating fault tip (Erslev, 1991). In the model, this trishear zone is controlled by the fault propagation-to-slip (P/S) ratio (e.g., Erslev, 1991; Hardy and Ford, 1997; Allmendinger, 1998; Allmendinger et al., 2004; Hardy and Allmendinger, 2011). Some parameters can change during deformation, such as fault strength and displacement, stratigraphy and overburden, and the size and shape of the trishear zone. This purely kinematic model of passive folding does not take rheology or strain rate into account. In particular, flexural slip, which often occurs during fault-propagation folding, is not accounted for. When describing the growth fold shapes, the ratio of the fold width to fold amplitude as the 'fold-shape factor' (FSF) is a useful parameter. FSF values depend on fault dip, fault throw, displacement rate, cover rheology, cover thickness, basal detachment thickness, and confining pressure (Coleman et al., 2019; Nabavi et al., 2020a). Overall, fault-propagation folds should be wider if the cover is thicker, if the detachment layer is thicker, if the detachment viscosity decreases, or if slip along the fault is slow. Accordingly, wide folds with small amplitudes have large FSF values (FSF $>$ 1), and narrow folds with large amplitudes have low FSF values (FSF $<$ 1).

A large-scale example of a process involving bending forces is the bending (flexure) of subducting lithosphere along convergent plate margins. This can in part be attributed to the vertical end load and bending moment of the negative buoyancy force acting on the lithospheric slab (slab pull), but is also influenced by other tectonic forces, such as shearing along the plate margins and horizontal forcing across the plate boundary (Fig. 39c). The response of the subducting oceanic lithosphere to these forces can be observed in the seafloor bulge of the plate near the trench, extensional faulting near the outer-arc trench or a folded layer (called bending moment normal faults) along with inferred lithospheric weakening that results in the reduction of effective elastic thickness of the plate closer to the trench (e.g., Kearey et al., 2009; Frisch et al., 2011; Turcotte and Schubert, 2014). Since bending moment normal faults develop from flexure, extensional faults usually display downward-decreasing displacement toward a neutral surface within the plate (Fig. 39c). Lithospheric bending has the first-order dependence on the depth of the slab that is subducting and breaks down when significant in-plane forces are included (Turcotte and Schubert, 2014).

Bending of layers can also occur in response to inflation during shallow magmatic intrusion (e.g., Wilson et al., 2016; Montanari et al., 2017; Reeves et al., 2018). Also, the rise of salt diapirs can cause bending of sedimentary layers into domes or anticlines (Fig. 39d) (e.g., Talbot et al., 2009; Jackson and Hudec, 2017). This effect is accentuated by the formation of synclines or minibasins between the salt structures. Here layers are bend downwards into synclines due to subsidence above the thinning part of the salt layer.

Gentle bending folds can result purely from differential compaction. This typically occurs across large faults where the column of sedimentary fill is much thicker on the hanging-wall side of the fault than on the crest of the fault block. On a smaller scale, bending of layers occurs on each side of rigid boudins in metamorphic rocks, as the host rock fills the gap between boudins as they move apart (Fig. 39e, f) (Price and Cosgrove, 1990; Harris et al., 2002; Goscombe et al., 2004). The hinges of these bending folds are generally thickened with respect to the limbs. Neck folds rapidly die out away from the boudinaged competent layer.

7. Relationship between fold geometry, strain and rheology

The final strain distribution within folded layers results from the accumulation of deformation affecting all the layers, which causes variable strain states along and across the layer. Hence, strain in folded layers is fundamentally heterogeneous. In this regard, the analysis of folds in the field, experimental and numerical studies indicate that the state and distribution of finite strain within mesoscopic samples or orogenic belts are significant parameters in the interpretation of geometry, kinematics and mechanics of folds in rocks sequences, and also in the reconstruction of the history of deformation (e.g., Hobbs, 1971; Roberts and Strömgård, 1972; Hudleston and Holst, 1984; Holst and Fossen, 1987).

Two kinematic models commonly used to explain buckle fold strain patterns are those of the tangential longitudinal strain (TLS) (or orthogonal flexure in Twiss and Moores, 2007) (Fig. 40a) and flexural flow folding (where rock material in incompetent layers flows from fold limbs toward hinges and typically produces similar folds) or flexural-slip folding (involving slip on bedding surfaces and typically develops parallel and concentric folds). These develop in homogeneous isotropic and anisotropic layers, respectively, with potential development of minor structures in folds such as sigmoidal en-échelon tension gashes and saddle reefs (Donath and Parker, 1964; Ramsay, 1974; Harris et al., 2002; Davis, 2014; Fossen, 2016). TLS concentrate strain in the fold hinge zone, with a systematic variation in strain across the folded layer. In contrast, flexural flow is characterized by simple shear that concentrate strain in fold limbs at the inflection points, with no variation in strain across the folded layer and the hinge. The difference between these two strain patterns appears to be the same as the difference between Euler-Bernoulli beam (a beam is a 2D layer that is much longer than thick) theory, where plane sections remain normal to the central line (or neutral axis), and Timoshenko beam theory, where shearing is included so that although plane sections remain plane, they are not necessarily normal to the neutral axis (Timoshenko and Gere, 1963). One fundamental assumption in all versions of the TLS model (including constant area, parallel layer, and FoldModeler) is the neutral line or axis that is continuous along the fold (Fig. 40a) (Ramsay, 1967; Bobillo-Ares et al., 2000, 2004; Lisle et al., 2009; Aller et al., 2010). In analysis of buckle folds, the concept of neutral line (in 2D fold profiles but surface in 3D cases) is one of the fundamental topics and contributors to fold development. The neutral line in a buckle fold divides areas of layer-parallel extension (as layer-perpendicular joints/veins, less frequent normal faults) around the outer arc from areas of tangential, layer-parallel contraction around the inner arc (as layer-parallel joints/veins, reverse faults, stylolites) (Ramsay and Huber, 1987; Lisle et al., 2009; Frehner, 2011) (Fig. 40a-c), which control the pattern, distribution, and density of fractures.

If there is no transport of material from the inner to the outer arc, the finite neutral surface migrates toward the outer arc so that the outer arc thins while the inner arc thickens (Ramsay, 1967). This migration of the finite neutral line results in switch from a convergent fan in the inner arc to a divergent fan in the outer arc, in the other words, the XY planes of the strain ellipsoid fan across the fold (Frehner and Exner, 2014; Bobillo-Ares et al., 2017). However, if shortening is accomplished by dissolution of material in the inner arc and precipitation in the outer arc, the neutral surface may remain in a central location (Hudleston and Tabor, 1988). Apart from the fact that fractures in a folded area can be either pre-, *syn*- or post folding deduced from abutting and cross-cutting relationships, fracture patterns in buckle folds cannot be explained simply by the neutral line in an elastic buckle fold model. In this regard and according to a rheological FE-models (Jäger et al., 2008; Frehner, 2011, 2014; Eckert et al., 2014; Liu et al., 2016), two neutral lines can be identified: the incremental neutral line (zero layer-parallel strain rate) and the finite neutral line (zero finite layer-parallel strain) (Fig. 40c, d). A transition zone also develops between these two neutral lines (surfaces in 3D cases) that exhibits finite shortening but undergoing extension (a low strain zone next to the finite neutral line) (Fig. 40c, d). Frehner (2014) shows that, in addition to overburden pressure, viscosity, permeability and fluid pressure (Eckert et al., 2014), the extensional area in the hinge of a buckle fold is broader than that in the limbs, which can explain the distribution of fractures. Since the curvature of a fold is maximal at the hinge and decreases to a minimum or zero at inflection points, the absolute values of TLS decrease from the hinge to inflection points and also to neutral surfaces. The study of different strain patterns

provides insight into the kinematic evolution of folds from the initial undeformed stage to the final stage. Such studies represent an essential basis for the restoration or balancing of structures and calculation of shortening.

In the case of the initially flat layer undergoing buckling in a xyz-coordinate system, stress is homogeneously distributed within both the layer and the matrix during the initial stages of folding. Indeed, the introduction of an interface perturbation during the amplification stage of folding results in a mechanical instability through the difference in shear stress (Fig. 41a-c), which it varies at every stage of folding, so that stress distribution becomes significantly heterogeneous. This results in the creation of a rotational flow (w) with non-zero vorticity in the folded surface (S_0) (as clock- and counter-clockwise rotation) superimposed upon the background irrotational flow, which has zero vorticity. This rotational flow is responsible for the folding process, so that it amplifies the perturbation and develops the fold train emerging from the initial perturbation. The rotational flow dominates the folding process and it constitutes a key element to understand the folding pattern observed in 3D models. When the fold limb is well developed, the vorticity flow is oriented along the y-axis (Fig. 41d). The sense and magnitude of vorticity depends on the dip direction of the layer(s) relative to the horizontal shortening direction. At the lateral termination of the fold, the rotational flow makes the layer spin about the x-axis, which causes the fold to grow laterally. This x-spin is accommodated by a y-spin, which increases the layer dip. Moreover, the fold amplification and tightness increase continuously as a result of the rotation about the z-axis (vertical component of the vorticity). This fold and or fold train continues its grow cylindrically with a hinge normal to the shortening direction which can be deflected as a result of strain localisation and/or through interaction and linkage with other folds (Fig. 41d). Hence, the vorticity flow is an important controlling factor in folding and the fold interplay processes. Overall, antiformal and synformal fold geometries,

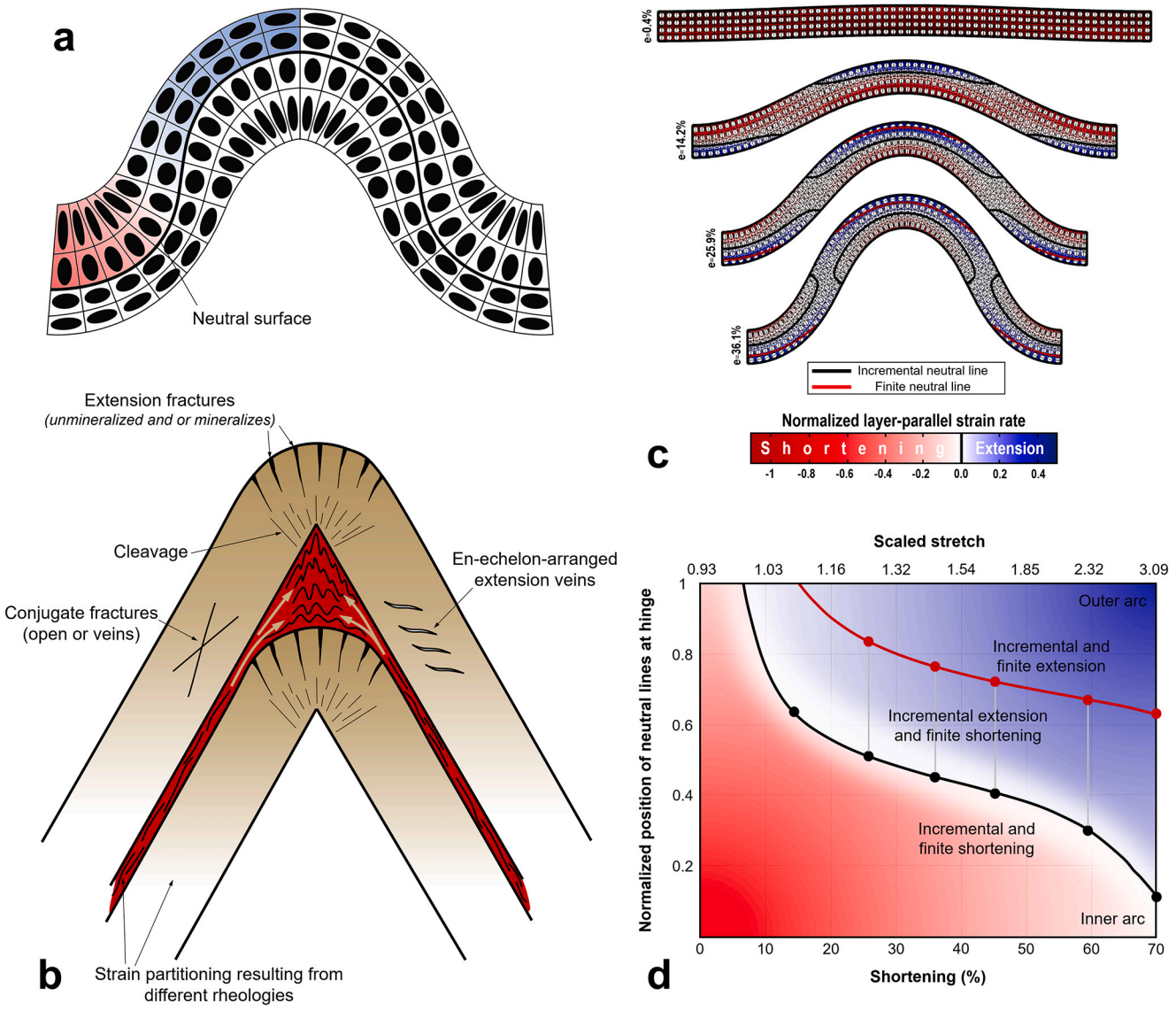

Fig. 40. a) The strain distribution within a buckle formed in a homogeneous, isotropic layer as a result of tangential longitudinal strain (TLS) such as a massive, unbedded limestone or sandstone bed (modified after Ramsay, 1967). b) A sketch of open and mineralized extensional fractures in the outer arc of the chevron fold from Varanger, northern Norway. c) Simulation snapshots of a progressively shortened Newtonian single-layer fold with the indicated modelling parameters. Colours represent the layer-parallel strain rate normalised by the absolute value of the externally applied strain rate. Finite strain ellipses with their major axis and a passive, initially orthogonal marker-grid are plotted (after Frehner, 2011). d) The diagram shows the layer-parallel strain rate and the positions of the two neutral lines on the axial surface trace, normalised by the current thickness of the layer at the hinge, with increasing shortening and scaled stretch. The dots indicate the shortening for which the different simulation snapshots are plotted (modified after Frehner, 2011).

respectively, are characterized by a counter-clockwise and clockwise oriented vorticity lines.

The competent and incompetent layers undergo different types of strain during folding. Although these different types of strain occur together and because there is no unique relationship between fold shape and the state of strain within folded sequences, relationships have to be established separately to describe their effects under the number of specific models and mechanisms of folding as mentioned in Section 6. One of the goals of geometrical analyses of buckle folds is to understand the relation between the rheological parameters of the rocks and shortening (strain), and also to quantify strain and rheology.

There are several methods to estimate viscosity contrasts and shortening during folding of single and multi-layers such as (1) arc length method which measuring the arc length relative to the thickness of a folded layer (e.g., Bastida et al., 2005, 2) using thickness versus wavelength measurements of folded markers as an indicator of viscosity contrast, (3) using wavelength/thickness ratios of single layer folds (Fig. 3 in Schmalholz, 2006, 4) using interlimb angle versus length of limbs/layer thickness ratio graph for single layer folds; and dip angle of the limb versus the thickness of the layer on the limb/thickness of the layer on the hinge ratio graph for multilayer folds (Yakovlev, 2012a, 2012b), (5) curvature-based methods to predict deformation patterns, intensity and orientation of structures, (6) cross-section balancing principles as kinematic methods. (7) As a common and applicable method, amplitude (A), wavelength (λ) (Fig. 42a-d), and layer thickness (h) (measured orthogonal to the folded layer) (Fig. 42e-h) of single-layer folds may be measured to estimate the bulk strain accommodated from a point at which the nucleation amplitude is reached during initial buckling development and viscosity contrast between layers during folding (e.g., Schmalholz and Podladchikov, 2001; Druguet et al., 2009; Hudleston and Treagus, 2010; Llorens et al., 2013b). Within individual fold trains, the fold wavelength reduces as amplitude increases, so that the A/λ ratio defines a general trend when plotted against λ. In detail, when compared to wavelength, the A/λ ratio is not a straight line, with amplitude increasing more slowly than wavelength. In general, steeper folds typically have lower A/λ ratio, as recumbent folds can develop proportionally greater amplitudes that may be a product of increased simple shear, which rotates the axial surface toward the shear plane. Overall analysis of individual fold datasets on the strain contour graph (Schmalholz and Podladchikov, 2001) reveals that most folded layers display viscosity contrasts in range between 20 and > 250, while layer shortening is generally estimated between 39 and > 70% (Fig. 42b). Within individual fold trains, the percentage of concentration typically increases as folds become more inclined, or recumbent.

When plotted on a strain contour graph, the overall trends of data from individual fold trains are slightly deviated from the established lines marking fixed viscosity contrasts, with some plots suggesting that folds with a lower percentage of shortening are marked by lower viscosity contrasts compared to folds with a higher percentage of shortening. In more typical cases, folds with a lower shortening percentage have greater viscosity contrasts compared to adjacent folds with a higher shortening percentage, resulting in more gentle trends on strain contour graphs. Schmalholz and Podladchikov (2001) also noted that not all folds in a layer grow to the nucleation amplitude simultaneously, depending on both initial amplitude and the initial wavelength. Hence, folds in the same fold train can be at different points on the scaled amplification curve at the same time. Such variations can also result in the values of heterogeneous flattening deformation on quite a small scale in a fold train (e.g., Hudleston and Stephansson, 1973).

Guiting (1998, 2005, 2009) has used rheological factors and self-similarity in fractal geometry to classify folds assuming that any portion of any structure is a scaled-down version of the whole and remain so over specified scale ranges. Major factors affecting fold patterns in this classification scheme are elucidated in fractal simulations of

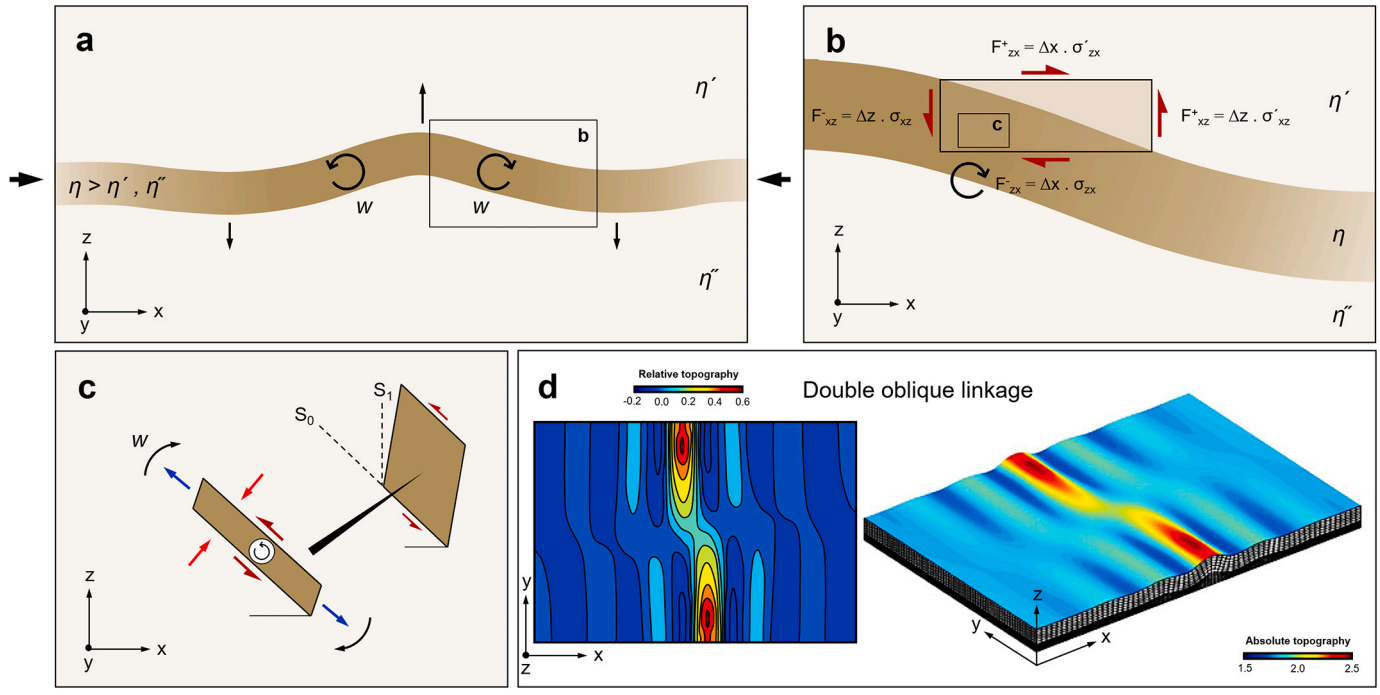

Fig. 41. a) Illustration of the non-zero vorticity flow in the case of perturbed interface. The opposite horizontal arrows show the shortening direction. The curved arrows show the movement of the layer delimited by the interface. The opposite vertical arrows show velocity distribution characteristic of nucleation and amplification of fold during compression. b) Representation of an arbitrary volume undergoing a differential shear stress across the interface. c) Flow in a homogeneous domain in the right limb of an upright symmetric fold. The bulk shear strain imposed by the bulk folding is partitioned differently in the layers. S_0 and S_1 are folded layer and axial surface reference frame, respectively (c). d) Numerical result of three-dimensional Buckling (detachment folding) (right column) for 17.4% bulk shortening showing absolute topography distribution with respect to model bottom. Left column shows contours of relative topography with respect to mean height of surface in x-y space (after Grasemann and Schmalholz, 2012).

a fold (i.e., position of interpolation points (x, y)) and the disturbance coefficient d of the fold ($-1 < d < +1$) so that if $d > 0$ and $d < 0$, folds are upward convex and downward convex, respectively. Furthermore, an increase in d-value correspond to more complex fold patterns. However, there is a critical problem: if folds are fractals, how can they be periodic? In this regard, if folds are fractal, by definition, they cannot be represented by Fourier series, and also not by power functions and Bézier curves. By nature, the fractal dimension increases as the complexity increases. That is almost the definition of fractal dimension. However, 3D models of natural fold systems established by photogrammetry show that folds include multifractal geometries, recurrence phenomena, and their profiles are treated nonlinear dynamical systems (Ord et al., 2018; Ord and Hobbs, 2019).

8. Folding at shallow crustal depths

In contrast to faulting and fracturing, folding is a ductile deformation process that preserves continuity of layers at the scale of observation. In the predominantly plastic middle and lower crust, folding is accommodated by crystal-plastic and diffusion processes at the microscale. In the upper and mostly brittle crust, folding is mainly accommodated by brittle deformation mechanisms, i.e., microfracture, grain rotation and frictional grain sliding, except for carbonaceous layers where also wet solution (pressure solution) and twinning are important, and salt layers where crystal-plastic processes occur. However, fold geometry is not directly dependent on deformation mechanism, but on viscosity contrasts (or the lack of such) between layers involved (Hudleston and Treagus, 2010). For example, active folding experiments are typically performed in room temperature on clay and sand layers that deform frictionally. These experiments produce folds with geometric characteristics that are directly comparable to natural folds formed at high P-T conditions deep in the crust, with completely different microscale deformation mechanisms. For buckling, elasticity also plays a role, but there is no direct relationship between viscosity and elasticity on one hand, and temperature-controlled deformation mechanisms on the other. The same is true for passive folding, which requires that there is no or very little viscosity contrast between the layers. Hence, the same principles and laws apply to folds formed in any material at any crustal level. Still, folding of rocks and sediments in the upper crust have characteristics that carry important implications, for example for strain estimates, hydrocarbon exploration/exploitation, CO_2 sequestration, and quantifying the fold evolution by using *syn*-kinematic sedimentary sequences. In this section we will focus on these characteristics.

Although the full geometric range of fold types can form under the low temperature and pressure conditions of the upper crust, observations of upper crustal folds reveal two overarching characteristic features. First, bending and passive folding are particularly common. This is particularly true in soft sediments and sedimentary rocks that are easily bent and sheared. Second, upper crustal folding is commonly closely related to faulting. Indeed, faults are a trademark of upper crustal deformation, and provide very localised deformation that easily affect their walls, particularly in soft sediments and lithologies. The combination of faults and folds is an expression of brittle-ductile behaviour, where ductile is to be understood as deformation that preserves layer continuity at the scale of observation while brittle deformation disrupts layers and other markers. Because of the importance of fault-related folds to petroleum geology and foreland orogenic deformation, we will discuss such fault-related folds in some more detail below.

8.1. Detachment folding

Folding of more competent layers above a weak detachment or décollement, without a ramp fault coring the uplift, occurs at various scales in the uppermost crust (Fig. 43a). They are commonly found in both subaerial and deep-water fold-and-thrust belts, such as the Jura Mountains (Fig. 43b) (e.g., Buxtorf, 1916; Humair et al., 2020), the Appalachian fold belt (e.g., Chamberlin, 1910; Wiltschko and Chapple, 1977), the Canadian Rocky Mountains (e.g., Dahlstrom, 1970), the western Gulf of Mexico (e.g., Yarbuh and Contreras, 2015), and the Zagros fold-and-thrust belt (e.g., Sherkati et al., 2005; Vergés et al., 2011) (Fig. 2a) and have played a dominant role in the kinematics of thin-skinned tectonics (e.g., Dahlstrom, 1969; Jamison, 1987; Poblet and McClay, 1996; Mitra, 2003; Brandes and Tanner, 2014; Li and Mitra, 2020 and reference therein). They also form as gravity-driven structures above weak layers, for instance downslope continental margins (e.g., Morley et al., 2017; Alsop et al., 2021). The detachment is typically overpressured shale or salt, overlain by more competent layers of sandstone or limestone. These competent layers develop buckle folds whose wavelength, amplitude and other geometric properties follow the general rules of buckling described earlier in this paper. They may be concentric, chevron or box shaped, showing symmetric, asymmetric, disharmonic, lift-off, and multi-detachment styles. However, the folds vanish abruptly toward the underlying detachment. This detachment separates less- or undeformed footwall from the shortened hanging wall, and their formation can be compared to folds formed by pushing a carpet on a floor. Tight and disharmonic folds may be evolved in the core of detachment folds if there is enough ductile material present in the detachment to penetrate the core of the growing anticline. If there is not enough material to fill the core of the fold, shortening commonly accommodates by secondary faults in the antiform as a result of local space problems, as indicated in Fig. 43b.

Fold geometries at shallow crustal depths can also be used to evaluate the dominant folding mechanism. Schmalholz et al. (2002) distinguished three types of folding mechanism depending on the controlling material parameters: (i) matrix-controlled folding (controlled by viscosity ratio between layer and matrix), (ii) detachment folding (controlled by the thickness of the weak layer below a strong layer) and (iii) gravity folding (controlled by the ratio of gravity to viscous stress). They also presented a phase diagram that was based on the ratio of matrix thickness to layer thickness and the ratio of wavelength to total thickness. This diagram allows estimation of the dominant folding mechanism from the fold geometry alone.

8.2. Fault-bend folding

Fault-bend folding is the imposed folding of hanging-wall layers as they move above a fault kink or bend with flat-ramp-flat geometry (i.e. a staircase trajectory) (Fig. 43c). Such folds were first recognized by Rich (1934) in the Pine Mountain of the southern Appalachian fold-and-thrust belt. For thrusting, the bend is typically associated with a ramp as the detachment fault transfers displacement to a higher stratigraphic level, connecting two weak detachment levels. Fault-bend folds tend to have relatively symmetric limbs (Fig. 43c). Movement of the hanging-wall layer over the fault bend result in an anticline-syncline pair. Folding occurs in two situations. First, the hanging-wall layers are bent upwards along the ramp with constant limb dips (the backlimb of the fault-bend fold), and second, they bend back to horizontal at the upper detachment level (Fig. 43c). In contrast, the forelimb of fault-bend folds is passively transported along the upper flat. Because of the layering being parallel to the fault, slip easily occurs along bedding interfaces so that the folds become flexural-slip folds. Flexural slip and flow imply conservation of area and bed-length, and this formed the basis for the first geometric models of fault-bend folds. These were somewhat idealized kink-like models that allowed for easy geometric construction based on well and outcrop data (Suppe, 1983, 1985).

A related model is the fault parallel flow model, where hanging-wall particles move with the same velocity along trajectories parallel to the fault (Ziesch et al., 2014). In this model, bed thickness is not constant. The vertical or inclined shear models, where particles only move along vertical or constantly inclined paths, also imply layer thickness variations and produces kink-like geometries. Most fault-bend folds are not kink-like but curved, and the more recent trishear model has been

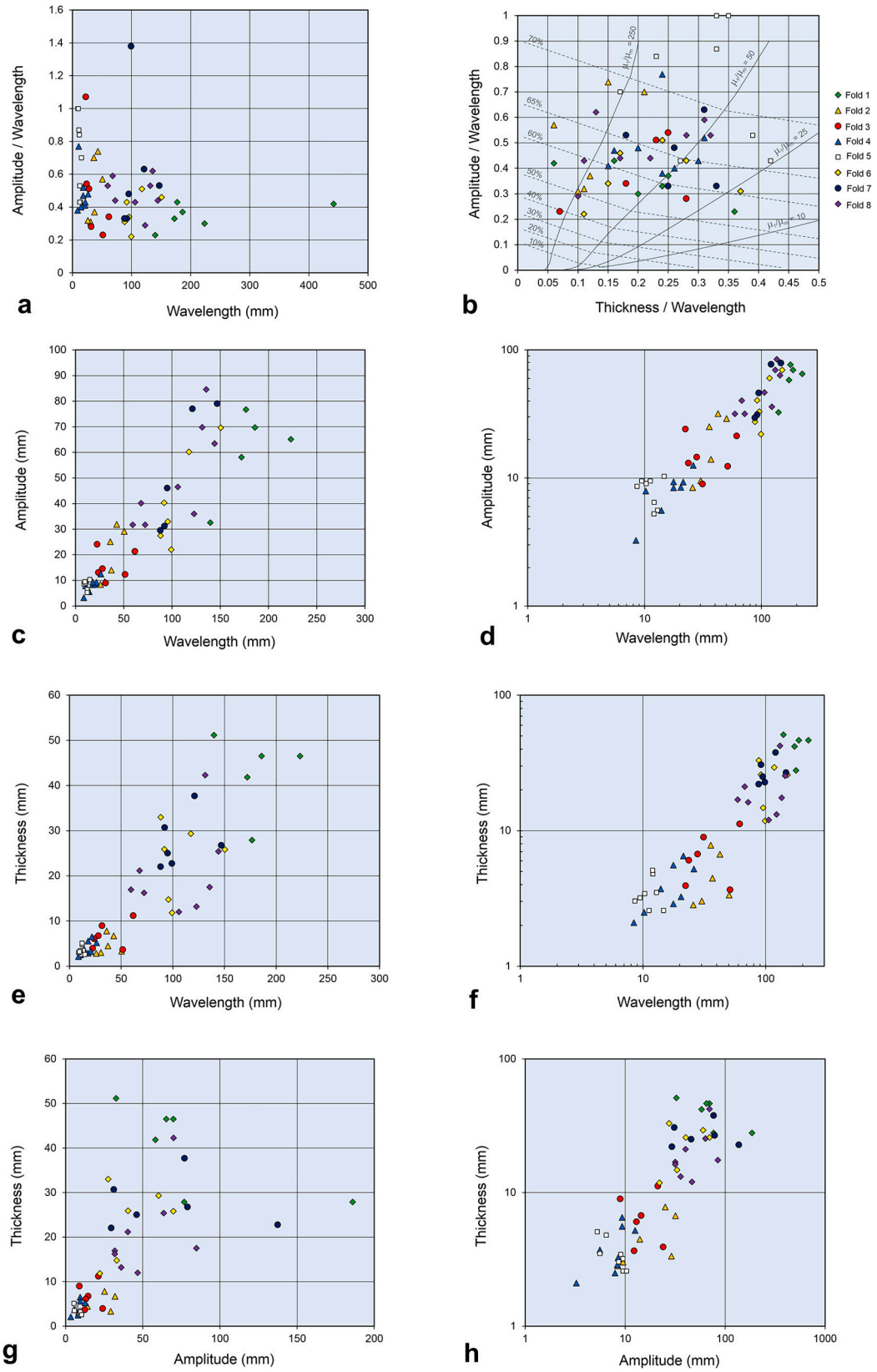

Fig. 42. a-b) Graphs showing wavelength plotted against amplitude/wavelength, and strain contour maps of Schmalholz and Podladchikov (2001) for a series of individual fold trains. Wavelength is defined as the distance between two points that occupy a similar position on the fold train (i.e. between adjacent synform hinges). The thickness of a layer is measured orthogonal to the folded bed, while amplitude is defined as half the distance from trough to the crest of upright folds. Strain contour plots of Schmalholz and Podladchikov (2001) show the estimated percentage of shortening and viscosity contrasts for folded layers. In each of the graphs, different coloured symbols represent different individual fold trains. c) Graph showing fold amplitude plotted against fold wavelength, and d) overall data on a log-log plot. e) Graph showing folded layer thickness against fold wavelength, and f) overall data on a log-log plot. g) Graph showing folded layer thickness against fold amplitude, and h) overall data on a log-log plot.

applied to produce models with rounded hinges that better capture natural and experimental examples (Connors et al., 2021; Plotek et al., 2021).

Fault-bend folds can form in any tectonic regime, also in the extensional regime where a normal fault makes gradual or abrupt changes in dip. Normal faults are typically steeper and make a higher angle to any sub-horizontal layering, although bedding-parallel faults also occur (Fig. 34d) (e.g., Xiao and Suppe, 1992; Shaw et al., 1997; Withjack and Schlische, 2006). Overall, extensional fault-bend folds can be modelled in the same ways as thrust-related fault-bend folds. While the ramp model shown in Fig. 43c is particularly common for fold-and-thrust belts, extensional examples show a much larger variety. Fault bends may be either concave or convex toward the hanging-wall depending on the mechanical stratigraphy that result in different evolution of the hanging-wall deformation, strain partitioning and associated structures (e.g., Withjack et al., 1995; Delogkos et al., 2020; Nabavi et al., 2020a). Listric fault geometry is a classic example of an extensional fault-bend fold, where a relationship exists between the geometry of the fault and the rollover fold and subsequent basin with either post- or syn-kinematic sediment in the hanging wall (Fig. 43e). Anti-listric faults give the opposite geometry.

8.3. *Fault-propagation folding*

Fault-propagation folding is the folding of layers ahead of a propagating fault tip, and this is most commonly observed where deeper faults propagate upwards into and through an overlying sedimentary sequence (Fig. 43f). Fault-propagation folding was first documented for thrust faults by Heim (1878) under the name "*stretch thrust*" (Heim, 1878), and later by Willis (1894), Gallup (1951) and Goguel (1952), but are equally important in the extensional regime. Fault-propagation folds related to thrusting are characterized by an overall asymmetry in the direction of transport, upward widening zone of ductile deformation, long, gently-dipping backlimb, and short, narrow, steep to overturned forelimb (Fig. 43f) (e.g., Suppe and Medwedeff, 1990; Mitra, 1990; Hughes et al., 2014; Hughes and Shaw, 2015). The geometry and kinematics of fault-propagation folds depend on the amount of displacement along the basal detachment, the footwall cut-off angle (or ramp angle), and the propagation-to-slip ratio. Steeper basement-rooted reverse faults produce fault-propagation folds in the sedimentary cover as they propagate up-section into the overlying stratigraphic sequence (e.g., Withjack et al., 1990; Jin and Groshong Jr, 2006; Ferrill et al., 2012; Paul and Mitra, 2015). Large-scale examples are represented by the forced monoclines of the Colorado Plateau (Davis and Bump, 2009). Normal faults also form fault-propagation folds as they propagate up-section, then with an asymmetry consistent with their extensional nature. Although less common, fault-propagation folds can also form where normal faults propagate downwards through a sedimentary sequence.

As for fault-bend folding, different kinematic models can be applied to explain the formation of fault-propagation folds, including flexural slip, inclined shear and the trishear models (Fig. 34g) (e.g., Suppe and Medwedeff, 1990; Erslev, 1991; Allmendinger, 1998; Allmendinger et al., 2004; Hardy and Allmendinger, 2011). Field evidence of bed-parallel slip (flexural slip) and small-scale structures cross-cutting bedding are commonly observed, suggesting that more than one mechanism may be involved and even vary throughout the folding history. For example, Zuluaga et al. (2014) noted that flexural slip was common at early stages of folding, whereas inclined shear became important after 30–50 degrees of forelimb rotation.

8.4. *Slump folding*

Slumping of unconsolidated sediments typically produce folds that appear as intraformational in the stratigraphic record. They encompass detachment folds and fault-propagation folds, but also sheath folds and more complex structures related to shearing of soft and fluidized sediment (Fig. 2i). Not only can the hinges become highly curved, but also their axial surfaces may become folded during progressive soft-sediment flow (Alsop and Marco, 2013). Chaotic folding is promoted by the high pore fluid pressures that characterize deformation of unconsolidated porous sediments.

Comparison of curvilinear fold patterns in metamorphic rocks and soft sediments also reveals no significant geometric difference between aspects of curvilinear fold geometries. While folding within metamorphic rocks is generally created by deformation associated with recrystallization, folding within soft sediments is typically achieved via micro-fracturing, pore-collapse accommodating compaction, and independent particulate flow, where individual grains move relative to one another to create a range of structures (e.g., Alsop et al., 2017, 2020).

Folds resulting from soft sediment deformation are often found to vary from gentle to isoclinal and upright to recumbent, with non-cylindrical geometry. Correct identification of folds and fabrics created during gravity-driven deformation of unlithified sediments from those tectonic structures formed during regional deformation is essential when interpreting geological histories preserved within the rock record. In this regard, veins developed along fractures, cleavage forming axial-planar to folds, truncated folds in their hinges and limbs by overlying sequences, incorporation of deformed fragile fragments into overlying sediment, cross-cutting clastic dykes, vergence of folds toward the sedimentary depocenter, and the sedimentary infill of irregular erosive surfaces that truncate underlying structures are all indicative of soft-sediment deformation (Fig. 2i) (Alsop et al., 2017, 2019, 2020).

8.5. *Drag folding*

Folds in the hanging wall and/or footwall of faults that can be related to the faulting process are generally referred to as drag folds or fault drag (Fig. 44). While they were originally thought to be results of friction along the associated fault (e.g., Kamen-Kaye, 1953; Laubscher, 1956; Hamblin, 1965; Ramsay and Huber, 1987), this view has been challenged in a number of works (e.g., Reches and Eidelman, 1995; Grasemann et al., 2005; Gomez-Rivas et al., 2007; Resor and Pollard, 2012; Ferrill et al., 2016). It is now clear that they can originate in a variety of ways. Many are former fault propagation folds that were preserved in the wall rock as the fold was transected by the fault. Others are fault-bend folds or folds that originated from geometric complications along the fault, including fault overlaps or fault relay structures (Childs et al., 2017). Depending on the geometric situation, drag can be normal or reverse, and for fault-bend folds, this relates directly to fault geometry. Normal drag and reverse drag are indicators of ductile deformation of geological markers cut by a fault segment in which deformed markers are convex and concave in the direction of transport along the fault segments, respectively, for normal drag and reverse drag (Fig. 44) (Grasemann et al., 2005; Mukherjee, 2014; Fossen, 2016). Hence, the sense of displacement along the fault segment can be determined by the sense of drag. Drag folds are particularly important where reservoir contact relations are a concern, such as in an oil field. In these cases, it should be taken into consideration that drag folds are not always imaged on seismic data.

8.6. *Salt-related folding*

The presence of a salt layer affects a wide range of deformation and structural styles in contractional, extensional and strike-slip regimes both in thin- and skinned tectonic. Examples of well-studied structural settings are the Gulf of Mexico (e.g., Hudec et al., 2013), the Santos Basins in offshore Brazil (Fig. 45a) (e.g., Jackson et al., 2015), the Zagros fold-and-thrust belt of Iran (e.g., Jahani et al., 2009, 2017), the Jura Mountains and the Alps (e.g., Sommaruga et al., 2017), the Pyrenees (e.g., Cámara and Flinch, 2017), and the German Zechstein basin (e.g., Strozyk et al., 2017). Faults, folds, and fault-related folds in the tectonic system are often associated with differential flow of ductile salt with the

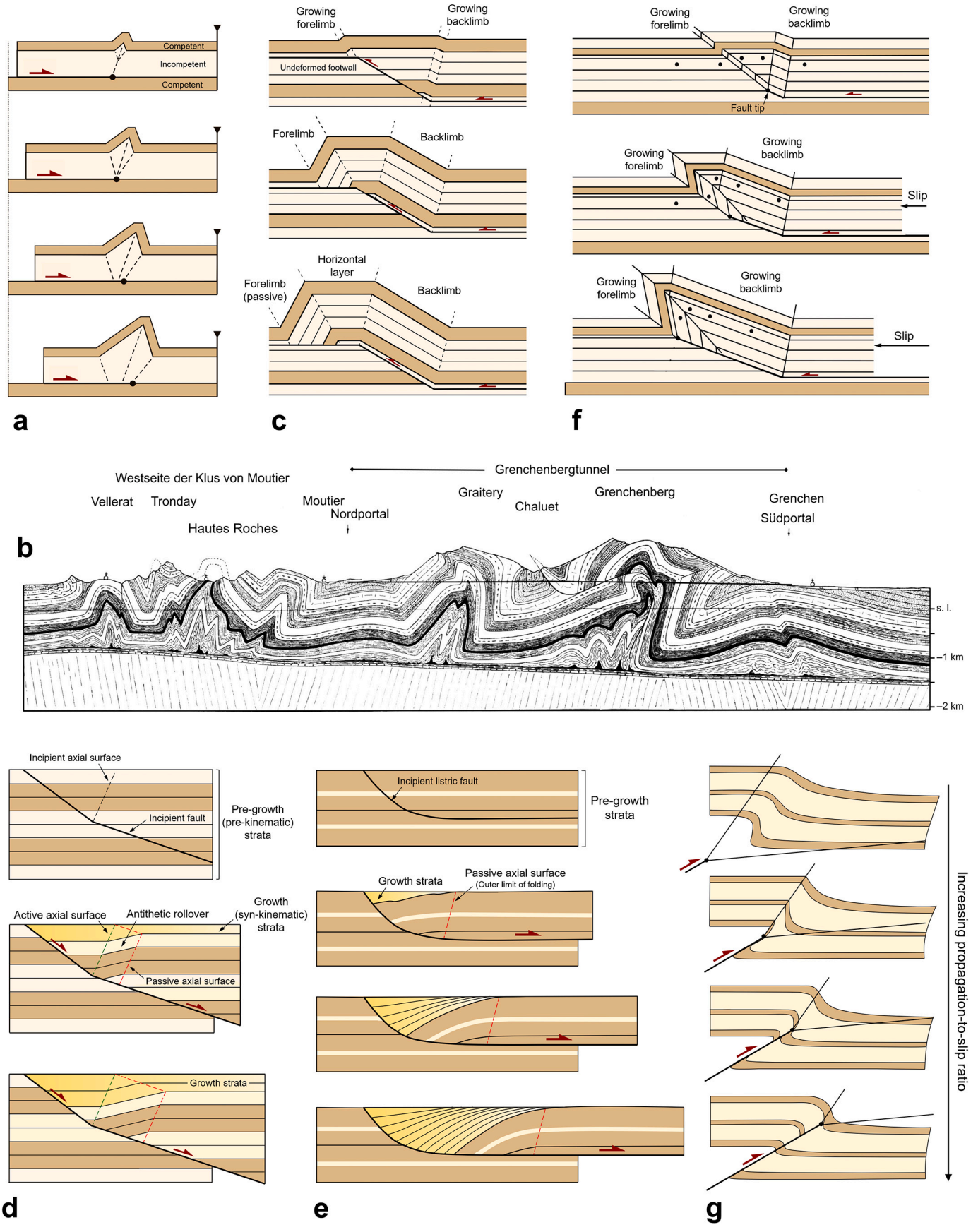

(caption on next page)

Fig. 43. a) Sketch of the progressive evolution of a detachment fold by kink-band migration and variable limb length. In this model, fold limbs lengthen but have constant dip (after Poblet and McClay, 1996). b) Buxtorf's (1916) interpretation of the geological structures of the Jura Mountains of Switzerland showing detachment folding of Mesozoic and Cenozoic strata above undeformed basement. c) Three stages of the evolution of a fault-bend fold by thrust movement over a ramp that cuts through the stratigraphy to link two bedding-parallel flats (after Suppe, 1983). d) Three stages of the evolution of an extensional fault-bend fold developed above a normal fault that flattens with depth (modified after Xiao and Suppe, 1992). e) Geometric model showing the effect of fault displacement on the listric fault that flatten at depth (after Withjack and Schlische, 2006). f) Three stages of the evolution of a fault-propagation fold (after Suppe and Medwedeff, 1990). g) Trishear model of a reverse fault affecting an overlying sedimentary sequence (modified after Allmendinger, 1998).

depth with respect to surrounding rocks (Figs. 2b, 45a,b) so that the presence of salt in the tectonic setting will permit folding and faulting to develop over a wide belt. Shortening of the overlying cover result in one of three classic geometries of fault-related folds mentioned above (Fig. 44a). Salt layers also form efficient detachment levels in extensional settings, particularly on continental margins (Fig. 45b) (Brun and Fort, 2011). Internally, a deforming salt layer would deform internally by flow folding (a passive folding mechanism) to form similar folds, although more competent non-salt layers would easily respond to deformation by buckling.

The geometry and style of salt-influenced structures depend on the thickness ratio of the underlaying salt layer and overlying cover, shear resistance of a detachment, tectonic setting, the geometry of pre-existing weak and fault zone especially in strike-slip settings, as well as the effects of mechanical stratigraphy (i.e. competency contrast) and strain rate (Davis and Engelder, 1985; Stewart, 1996, 1999; Fossen, 2016; Jackson and Hudec, 2017; Duffy et al., 2018; Rowan et al., 2020 and references therein). However, multiple layers of salt (or detachment level) may produce ramp-flat geometries with ramps connecting slip detached on salt layers, disharmonic folds, and more complex structural style in the setting as described in the Dezful Embayement of the Zagros fold-and-thrust belt, SW Iran (e.g., Sherkati et al., 2006; Ghanadian et al., 2017; Najafi et al., 2018). If the rheology of the overburden significantly differs from that of the salt, the overburden layers are active strain markers that can be thickened, thinned, buckled, and bent. Salt-related folds have commonly a gradually, asymmetric and long-term growth process with respect to tectonic folding, and the neutral surface is less developed within them in which shortening domain is accommodated by salt flow. Shortening of a thick overburden on a thin salt detachment layer produce thrusting rather than buckling, whereas thick salt detachment layers tend, in addition to the characteristic rounded, sinusoidal symmetric to overturned folds, to develop box and concentric folds with tight to isoclinal cores and gentle crests on multiple wavelengths in which salt can flow under relatively small stresses either into an anticlinal fold core (e.g., salt-cored anticlines in the Zagros fold-and-thrust belt and the Jura Mountains), where evaporite folds are parasitic or rounded chevron shaped, or from a synclinal fold crest due to the welding (Fig. 45a). Given the weak nature of salt, minor changes in the flow geometry of the deforming salt body may produce well-developed sheath folds and interference folds that have steeply plunging to vertical hinges. Furthermore, shortening of the thick salt body leads to squeezing and upward flow of salt to shallower levels in the form of diapirs and even extrude onto the surface to form salt sheets and glaciers. In this regard, in addition to the role of the regional tectonic system (e.g., contractional, extensional and strike-slip), rising salt flow may affect the wall rock and overburden by a bending process and localised strain in the form of drag folds resulting from rotation into the direction of salt movement, domal structure, minibasins, and monoclinal forced (drape or flap) folds with associated fracture and fault networks (Fig. 39d) (e.g., Alsop et al., 2000; Schultz-Ela, 2003; Talbot and Pohjola, 2009; Giles and Rowan, 2012).

9. Discussion

9.1. Applied aspects of folds and folding in the uppermost crust

Understanding folds and folding has a long range of applied aspects, from predicting the geometry of ore bodies, coal layers and hydrocarbon traps to the prediction of deeper faults and evaluation of seismic hazards. Prediction of ore body geometry is directly based on the body of geometric and kinematic analyses presented in the main text, and will not be specifically discussed. Instead, we find it useful to focus on application at shallow and near-surface situations, where they can be linked to the growth of faults and fractures, and to depositional patterns.

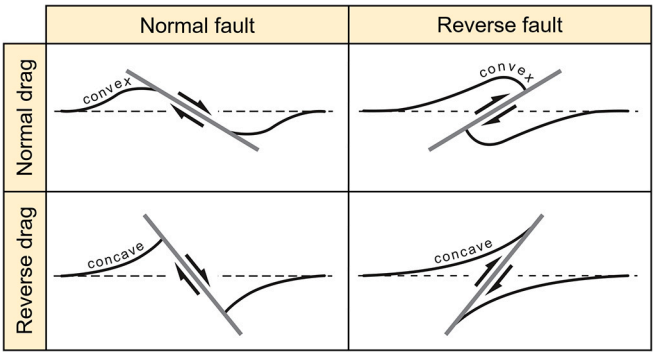

Fig. 44. Different types of drag folds develop along normal faults and reverse faults. Dashed lines indicate the position of the regional before deformation for each case (after Grasemann et al., 2005).

9.1.1. Syn-kinematic fold growth

Syn-kinematic deposition of sediments provides a record of fault evolution that can be used to understand fold growth. Vice versa, fold growth can be used to predict variations in depositional patterns that lead to variations in the distribution and properties of stratigraphic units. Sediments deposited during folding and faulting are often termed growth strata, as they exhibit thickness variations that correspond to the location and formation of such tectonic structures. In converging setting, deformation causes folding of the pre-kinematic sedimentary sequence and when sedimentation progressively continues during contractional deformation, *syn*-kinematic sediments or growth strata are deposited synchronously with folding. The relief caused by shallow folding generate a topography that causes thickness variations, with expansion away from elevated fault crests (Fig. 46). Fold amplification progressively rotates already deposited layers, causing a characteristic decrease in dip and formation of unconformities that may reflect irregular or episodic fold growth (Fig. 46) (e.g., Storti and Poblet, 1997; Vergés et al., 2002; Poblet, 2012).

9.1.2. Folds and fractures

Fractures are, together with the closely related veins and deformation band structures, important geological features that can have a dramatic impact on mechanical strength and flow performance of hydrocarbon reservoirs. Since these structures are not directly detectable from seismic data, any relationship to larger-scale folds can be of great interest. Fracture formation within a folded sequence may relate to both regional and local fold-related stresses. The strain distribution and fracture patterns vary with different types of folding mechanism (e.g., Cosgrove and Ameen, 1999; Cosgrove, 2015). Moreover, fractures can be generated either pre-folding, syn-folding or post-folding. Pre-folding fractures show no systematic relationship to fold geometry, while syn-folding fractures form in response to the stress field that exist any time during folding. The local state of stress usually changes both

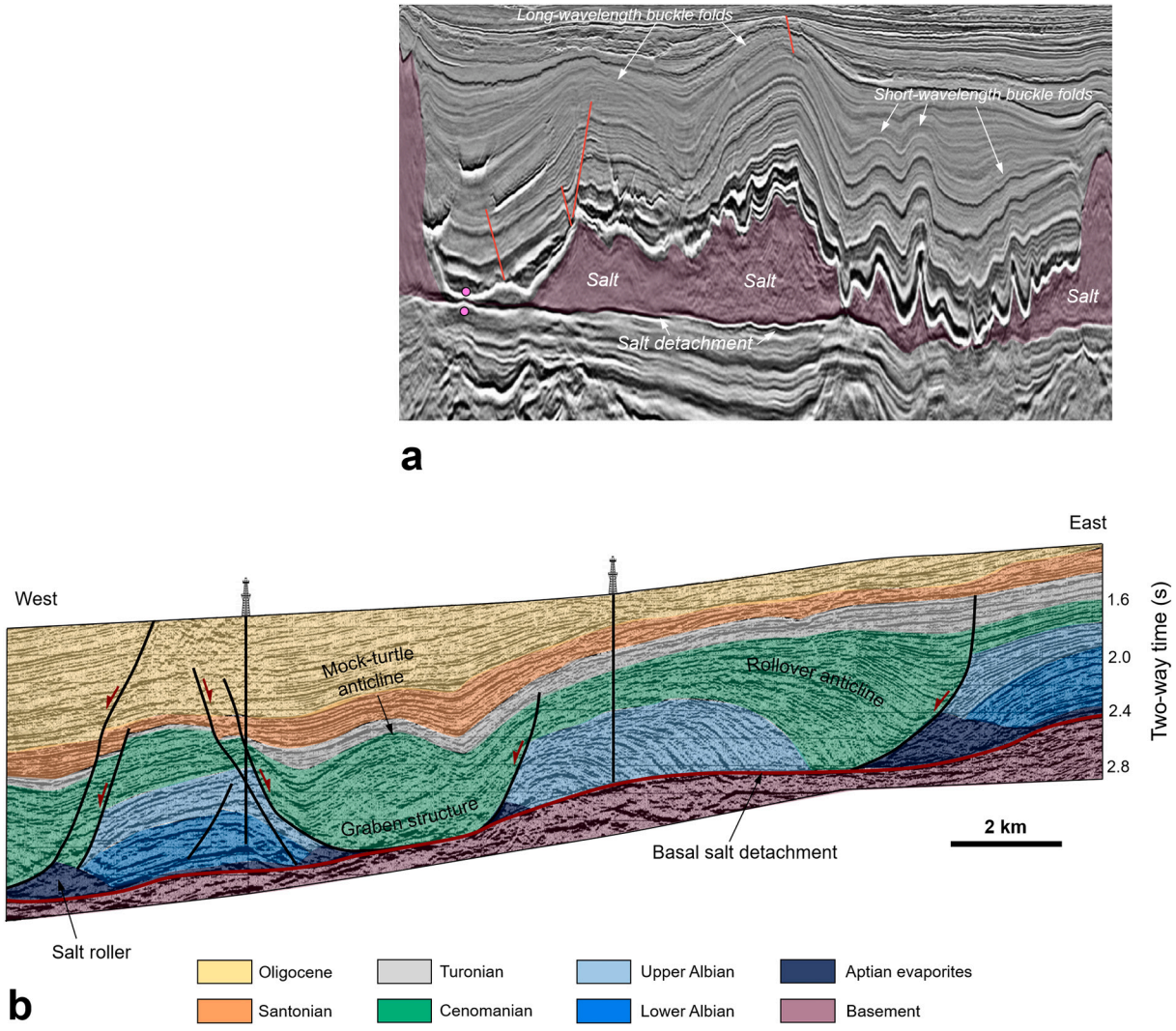

Fig. 45. a) Polyharmonic buckle folds detached on salt in the Campos Basin of offshore Brazil, with two long-wavelength anticlines with young growth strata superposed on numerous short-wavelength anticlines in older strata (modified after Twigger, 2015). No scale and orientation provided in original figure. Folding is controlled by the competent layers (carbonates) immediately above the salt. b) Seismic section from Lower Congo Basin of offshore Angola showing sedimentary sequences detached on salt in the extensional salt-tectonic system (modified after Rouby et al., 2002).

spatially and over time, which can complicate fracture patterns in detail (Silliphant et al., 2002; Amrouch et al., 2010; Cosgrove, 2015). Complications also arise because of rotation of early-formed fractures during folding and overprinting by subsequent structures (e.g., Zuluaga et al., 2014). Post-folding fractures may be influenced by the fold geometry and the release of stress that was locked inn during folding (Engelder, 1985). Fold curvature is used as a predictor of the distribution, orientation and intensity of fractures. For example, Watkins et al. (2015, 2018) demonstrated that high-curvature portions of the fold structure are characterized by high fracture intensity, and by discontinuous and short fractures oriented parallel to the fold hinge line. In contrast, low-curvature portions are characterized by low intensity, continuous and long fractures with a variation in orientations controlled by mechanical stratigraphy.

Understanding the relative age relationships or chronology between fracture networks and folds can be distinguished using criteria such as relationships between the orientation of fractures and the fold axis, abutting and cross-cutting relationships (i.e. topology) (see Peacock et al., 2018, Peacock and Sanderson, 2018 for details), and fracture dip angle with respect to bedding. Regional fractures typically develop during early stages of layer-parallel shortening. They are oriented orthogonal to bedding and usually trend perpendicular and less-commonly parallel to the fold axis. Local fold-related fractures usually exhibit more complex patterns and their orientations and topology tend to vary according to the structural positions and stratal curvature in the fold structure (e.g., Fischer and Wilkerson, 2000; Watkins et al., 2015). As an example, a schematic block diagram of fracture networks within a periclinal fold structure for the Maleh-Kuh anticline in the Lurestan structural zone of the Zagros fold-and-thrust belt, Iran is shown in Fig. 47. This relatively simple example, which is based on Stearns (1969), shows to show the topology (i.e. the abutting relationships of fractures that illustrating different node and branch types) and relationships between fractures and folds in different structural position of the fold structure, including nose (sample 1), limb (samples 2 and 3), plunging part (sample 4) and hinge (sample 5) (Fig. 47a). Other cases may be more complex, although some relationship between fold geometry and fracture distribution, orientation and/or property is usually present. Fluid flow in fracture systems is influenced by fracture orientations, heterogeneities, density, and connectivity. In general, portions with higher fracture density have more connected fractures and potentially have a higher permeability. However, fracture density is not always a reliable criterion for predicting reservoir flow properties, for which fracture connectivity analysis is needed. In this regard, connection per branch (C_B) (Sanderson and Nixon, 2015, 2018) values can be

represented on ternary diagrams, where higher C_B values means higher connectivity with a high proportion of Y- or X-nodes, as well as connected branches in ternary diagrams (Fig. 47b, c).

While the role and effect of folding and fracturing has become increasingly evident in many case studies, there is room for improvement and further implementation of these results in the petroleum industry. During the life cycle of many exploration and production projects, the interpretation of the trap in terms of fold geometry is primarily done during the exploration phase, in the context of prospectivity. In contrast, during the appraisal and production phase, the interpretation of the field and its reservoir in terms of fold structures, is often underappreciated. Consequently, recognition and analysis of the fold geometry, folding mechanism, the type and mechanism of fold growth and linkage, and also fractures and faults related to different types of folding are important for understanding how fluids flow in fold structures or which parts of folds represent a better productive sector of reservoirs caused by, for example, changes in the intensity, distribution and connectivity of fractures (see Evans and Fischer, 2012) for details on the distribution of fluids in folds).

9.1.3. Folds and seismicity

It is well known that the growth of some folds is linked to faulting, notably fault-propagation folds (Barnes, 1996; Mueller and Suppe, 1997). As such folds become apparent on the Earth's surface, they mark the surface projection of the fault and thus indicate its location at depth. For large buried faults in tectonically active regions, this may be used to predict the location of potential future seismic hazards.

Large fault-bend folds above thrusts may also be linked to seismic activity, as suggested for the Main Himalayan Thrust (Sathiakumar and Barbot, 2021). Fault-bend folding rotates stratigraphy to become oblique to the underlying thrust, and this can change the loading rate across the fold and cause shallower earthquakes (Sathiakumar et al., 2020). Hence, knowledge about the type of fold and their geometry in relation to associated faults can be important to predict seismic hazards.

Also larger situations of bending can be connected with seismicity. One is the bending of subducting oceanic lithosphere at oceanic trenches. Seismicity is clearly related to this bending, but the mechanism of folding is debated. Orthogonal flexure, with outer-arc extension and inner-arc shortening is often assumed, but flexural slip folding has also been suggested (Romeo and Álvarez-Gómez, 2018). These two models predict different seismic patterns. For example, flexural slip-related earthquakes would be expected to form along interfaces parallel to the slab top, which would result in lower seismic moments than the orthogonal flexure model, with reduced tsunami risk in the surrounding region. Hence, this serves as an example where a correct determination of folding mechanism is important for seismic risk assessment.

9.2. Future research on folds and folding

As argued above, characterizing folds and folding are important aspects of structural analysis with a large range of applications. Even though our knowledge of folds and folding has advanced a lot over the last 50 years, there is still great potential for further progress. We still need to simplify the complexity of natural folds, particularly when generalizing the results of detailed geometric observations, experiments and numerical models. Quantitatively we should keep in mind that the fold classification schemes and geometrical methods mentioned above involve several assumptions, simplifications and uncertainties, and it has been demonstrated that some methods consistently give different results and accuracy. This could relate to the geometrical parameters

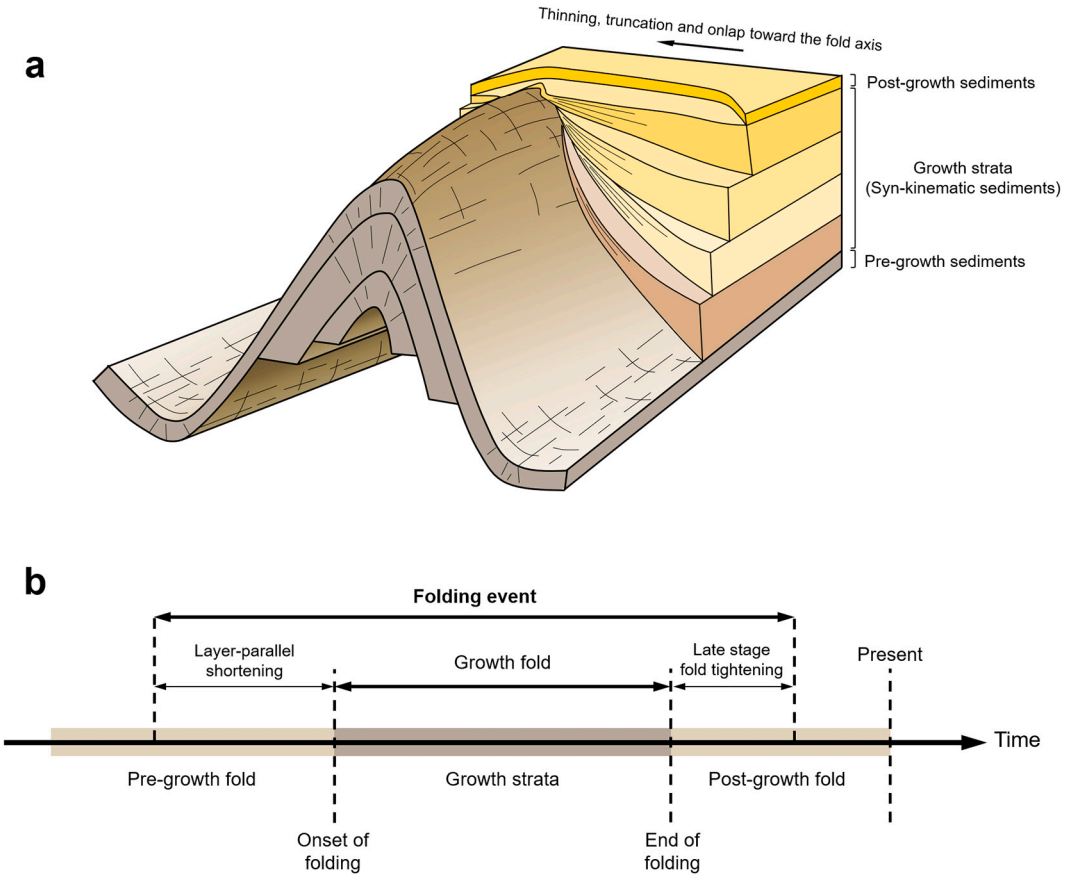

Fig. 46. Schematic illustration of (a) a fold with associated growth strata and (b) a time line showing the evolution of the fold and relevant terminology for the description of affected *syn*-kinematic growth strata geometry. Growth strata thin and steepen toward the anticline and show a characteristic fanning geometry.

used, accuracy of approaches used to measure them, and accuracy of fold geometry classification. It could also mean that some of the schemes record the fold geometry well only in certain parts of fold structures, or that some of the underlying assumptions are inaccurate or incorrect. However, such variations in results and accuracy of classification schemes may also result from various fold geometries in different deformation zones and tectonic settings, geometrical and/or kinematic interactions of fold structures, different rheology, pressure and temperature conditions.

The idealized fold forms are by necessity, simple and idealized. Researchers that use only 2D idealized schemes entrench rather than challenge these idealized models and remove themselves from the complexity of natural fold structures. Along the same lines, 2D fold profiles are useful for some purposes, but when considering the fact that folds are inherently 3D structures and may differ in length scale, amplitude, wavelength, arc-length, closure direction, fracture patterns etc. so that most of them show non-cylindrical geometries and non-planar axial surfaces and associated cleavage, and are better treated in three dimensions. On the other hand, it is usually difficult to obtain enough data from natural macroscopic and regional folds to properly evaluate their geometry, kinematics and mechanics. In other words, geometric descriptions of folds such as amplitude-wavelength ratio, thickness variations and interlimb angles, based only on field observations, provide limited information of both type and mechanism of deformation. In this regard, future work should focus on integrating field-based observations, sub-surface data sets, and 3D numerical modelling of folds in different model configurations (number of layers, layer thickness, type of perturbation and its amplitude in the layer

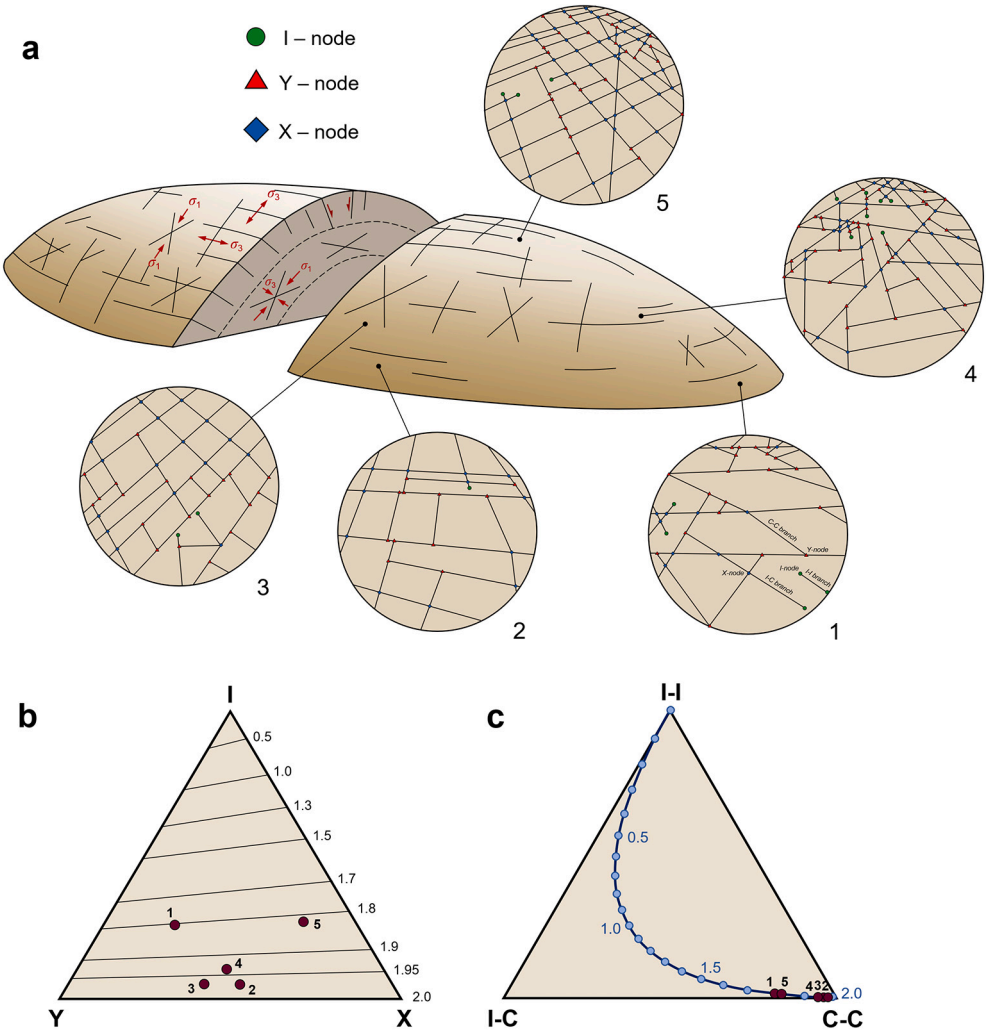

Fig. 47. a) Schematic illustration of fold-related fracture networks on the Maleh-Kuh periclinal fold structure, showing how the orientations and topology of fracture networks vary depending on the structural position. Circular trace maps of five fracture networks exhibit different node and branch types. The diameter of each circle is 2 m. b and c) Ternary diagrams of the different node and branch types with dark purple dots representing the topology of fracture network traces in (a). The contours represent the average number of connections per branch (C_B) (i.e. node triangle) (b) and distribution of I-I (isolated), I-C (partly connected) and C-C (doubly connected) branches (i.e. branch triangle) (c), along with the table of computed data, and how they change relative to the topology. N_I, N_Y, N_X and N_B, respectively, are the number of I-node, the number of Y-node, the number of X-node, and the number of total branches (see Sanderson and Nixon, 2015, 2018 for details on fracture network topology and connectivity).t. (For interpretation of the references to colour in this figure legend, the reader is referred to the web version of this article.)

Sample Number	N_I	N_Y	N_X	N_B	C_B	I – I	I – C	C – C
1	6	18	11	52	1.8	1	3	37
2	1	11	12	41	1.97	0	1	30
3	2	20	14	59	1.96	0	2	51
4	7	36	34	126	1.94	0	7	69
5	3	26	44	128	1.82	0	3	123

interface, type of contact between interacting layers such as free-slip and or no-slip interfaces), different geological and tectonic settings (i.e., the type of applied boundary conditions and also in the form of displacement-based and strain-rate-based boundaries), different mechanical properties, and at different scales. In this way we may better predict and understand the spatial and temporal evolution of geological structures, stress distribution and strain localization, the process of fold interaction, identify the parameters that effectively control folding, and the distribution and pattern of small-scale structural features such as fractures and deformation bands. Continuum mechanics-based FE-models can provide a system of equations that describe such deformation processes and interactions. Due to the continuum nature of the FE-analysis, discrete fracturing and faulting cannot be modelled as the solution does not support the development of discontinuities in the mesh. However, the FE-solution, together with the strain-softening rheology, results in the development of localised deformation zones that effectively behave as discrete fractures and faults at a macroscopic scale (Nabavi et al., 2017b, 2018b, 2020b). Furthermore, numerical models using the extended finite element (XFEM) can provide a wide range of discontinuity applications in the geological structures including fracture and fault propagation problems in different modes (Mohammadi, 2012).

For future studies using 3D numerical models, it is also necessary to introduce more complicated physical and geological parameters such as temperature, mechanical stratigraphy, structural inheritance, mechanical anisotropy, and overburden pressure for realistic modelling. Moreover, all relevant geometric parameters of the folded layer(s) should be recorded and documented to better inform numerical and experimental modelling studies. The traditional limitation associated with numerical simulation of geological structures have been removed by recent computational advances in the form of multiscale models. Most problems in structural geology involve many scales in time and space. An example is the overall stress state and strain pattern in a folded sequence which can well be described by macro-scale continuum equations, but requires details on a meso- and microscale at the folded layer. In a multiscale method, a part of the model which requires a more accurate theoretical basis or numerical approximation, due to lack of theoretical bases or existing inconsistencies of many conventional models, is simulated by a finer modelling scale, which can better represent details of the mechanical evolution, material behaviour and the interacting effects of material constituents. Hence, another path for future works on numerical fold modelling is to use multi-approach (for example, combined finite-discrete element method) and multiscale model results from progressive and or multiphase deformation that can avoid the scale-limitation of the results. However, it should be noted that forcing interpretations of numerical modelling results to conform to idealized models may lead to misleading results. A number of field-based observations (e.g., Fossen et al., 2019; Carreras and Druguet, 2019), 3D numerical (e.g., Schmalholz, 2008; Welker et al., 2019) and analogue (e.g., Ghosh, 1993; Ghosh et al., 2014) models indicate how complex and interfering fold structures can form by single-phase progressive deformation as strain heterogeneously accumulates as a function of geometry, boundary conditions, pre-existing structures, and material properties. The importance of strain partitioning has also been emphasized, where different domains are characterized by different fold geometries and styles (Holdsworth et al., 2002). Hence, paying attention to fold geometry may help to define structural domains and the nature of deformation partitioning in a region (Fossen et al., 2019).

It seems like the potential to make progress in understanding folding largely lies in the development of numerical modelling and available computing power. As more sophisticated programs can be run, taking into consideration more physical variables and complex geometries, we are likely to see further advance in our understanding of fold processes. This includes studies of the effect of elastic deformation during folding (i.e., visco-elastic rather than just viscous behaviour; Hudleston and Treagus, 2010), time-dependent rheology, and thermo-mechanical feedback processes.

10. Concluding remarks

Folds and folding are some of the most important structures and deformation processes at all scales and a wide range of different tectonic settings. Folds contain valuable information that can be extracted by analysis of meso-scale structures, with both local structural and regional tectonic implications. In this study, we have reviewed different aspects of fold geometry and much of the relevant literature on folds and folding. We have discussed classification schemes as well as development, advantages, limitations and improvements in their interpretation and application. Which ones are more useful depend on the goal of the work and nature of the folds in question.

Even though much valuable and applicable research has been carried out on folds and folding during the past decades and centuries, this is still a key field of research with a large potential for improvement because in many cases, classification schemes have been applied to natural examples that do not fulfil fundamental requirements or were developed on the basis of unrealistic conceptual models. It is necessary to look back to the conceptual and methodological basis of the geometric interpretation of folds, paying attention to the basic assumptions, and hence to the limits of existing classification schemes, as well as following rigorous and accurate approaches of data collection, critically evaluating the structural style and tectonic setting of the analysed area, and pondering the important role of field-based observations. Furthermore, several first-order parameters controlling fold geometry and folding mechanisms have been intensively investigated using analogue and numerical models. Hence, there is still potential for further research on integrating mechanical models and natural examples to consider and predict the parameters affecting fold geometries and kinematic evolution including choices of modelling method, material properties (i.e. mechanical stratigraphy), thickness, mechanical anisotropies, boundary conditions, orientation of initial configuration with respect to the applied load, interaction relations, inherited structures and deformation mechanisms, the orientation of fold-related fractures and associated mineralisation, temperature, confining pressure and ages. Hence, folds and folding are sensitive to multiple factors that frequently work together to dictate the final fold geometry and attitude.

It is a challenge that most classification schemes are so personalized and complex that they are unlikely to be covered in undergraduate and even graduate level courses. However, each scheme has its advantages, and the different classification schemes and approaches to geometrical fold analysis must be known to select the ones that are most appropriate for a particular project or purpose. For example, (a)symmetry and vergence should receive particular attention for kinematic analysis. If strain is to be quantified, fold tightness (Figs. 5-7, 12c-d), wavelength, amplitude (Figs. 25, 32, 42) and variations in layer thickness (Figs. 13, 16-18, 42) may be essential. The shear strain related orientation and non-cylindricity of folds in shear zone may be quantified by plots such as Figs. 19, 21, 22 and 25c. An investigation of the role of mechanical layering may be supported by dip isogon classifications (Fig. 14). Fault-propagation folds could be analysed to determine the depth to the underlying fault through either kinematic (trishear; Fig. 38a) or mechanical modelling (Fig. 34). Curvature analysis is appropriate in cases where curvature can be related to structural complexity through strain variations, in which case active (Fig. 40) and passive folds (Fig. 27-30) must be treated differently. Specific cases need to be taken beyond the generalized plots and examples shown here, and should be further analysed in the light of existing or specifically designed mechanical and/or kinematic modelling. However, geometrical analysis and classification forms the foundation for the use of folds in structural/tectonic analysis. In general, understanding fold geometries, folding mechanism, strain history, as well as relationships in fracture networks are critical for prediction of the structural style and variations, and important in a wide range of applications, including fractured reservoir exploration, carbon capture and storage, aquifer characterization, civil engineering, mining industry and seismic hazard prediction.

Geometrical methods for fold classification must focus on practical methods in the sense that geologists must be able to apply them in the field to quickly recognize and describe different types of folds. The large number of schemes and methods used for fold characterizations and classification may be a challenge. At the same time, each scheme has its advantages, and is necessary to be aware of the different schemes to choose the most appropriate ones for a specific data set or region. Hence one of the purposes of the present paper was to provide an overview of the most important methods and classification schemes. However, we encourage more researchers to take into account both kinematics and mechanics in their interpretation of folds, and emphasize that variations in fold style, attitude and geometry often relate to the way strain is partitioned into different elements or domains of a deformed rock region.

Declaration of Competing Interest

The authors declare that they have no known competing financial interests or personal relationships that could have appeared to influence the work reported in this paper.

Acknowledgements

Seyed Tohid Nabavi thanks Prof. Jordi Carreras and Dr. Elena Druguet for their constructive discussions on progressive deformation and folding during scientific field trips in the Cap de Creus, the Roses and the Axial Zone of Pyrenees. We thank reviewer Clare Bond for constructive comments that allowed us to improve the original manuscript. Editorial and handling and advice by Prof. Carlo Doglioni are also gratefully acknowledged.

References

Abbassi, M.R., Mancktelow, N.S., 1990. The effect of initial perturbation shape and symmetry on fold development. J. Struct. Geol. 12, 273–282.
Adamuszek, M., Schmid, D.W., Dabrowski, M., 2011. Fold geometry toolbox-automated determination of fold shape, shortening, and material properties. J. Struct. Geol. 33, 1406–1416.
Adamuszek, M., Schmid, D.W., Dabrowski, M., 2013. Theoretical analysis of large amplitude folding of a single viscous layer. J. Struct. Geol. 48, 137–152.
Adamuszek, M., Dabrowski, M., Schmid, D.W., 2016. Folder: a numerical tool to simulate the development of structures in layered media. J. Struct. Geol. 84, 85–101.
Al-Dossary, S., Marfurt, K.J., 2006. 3D volumetric multispectral estimate of reflector curvature and rotation. Geophysics 71, P41–P51.
Aller, J., Bastida, F., Toimil, N.C., Bobillo-Ares, N.C., 2004. The use of conic sections for the geometrical analysis of folded surface profiles. Tectonopgysics 379, 239–254.
Aller, J., Bobillo-Ares, N.C., Bastida, F., Lisle, R.J., Menéndez, C.O., 2010. Kinematic analysis of asymmetric folds in competent layers using mathematical modelling. J. Struct. Geol. 32, 1170–1184.
Allmendinger, R.W., 1998. Inverse and forward numerical modelling of trishear fault-propagation folds. Tectonics 17, 640–656.
Allmendinger, R.W., Zapata, T.R., Manceda, R., Dzelalija, F., 2004. Trishear kinematic modelling of structures, with examples from the Neuquén Basin, Argentina. In: McClay, K.R. (Ed.), Thrust Tectonics and Hydrocarbon Systems, American Association of Petroleum Geologists Memoir, 82, pp. 356–371.
Allwardt, P.F., Bellahson, N., Pollard, D.D., 2007. Curvature and fracturing based on global positioning system data collected at Sheep Mountain anticline, Wyoming. Geosphere 3, 408–421.
Alsop, G.I., Carreras, J., 2007. The structural evolution of sheath folds: a study case from Cap de Creus. J. Struct. Geol. 29, 1915–1930.
Alsop, G.I., Holdsworth, R.E., 2012. The three dimensional shape and localisation of deformation within multilayer sheath folds. J. Struct. Geol. 44, 110–128.
Alsop, G.I., Marco, S., 2013. Seismogenic slump folds formed by gravity-driven tectonics down a negligible subaqueous slope. Tectonophysics 605, 48–69.
Alsop, G.I., Brown, J.P., Davison, I., Gibling, M.R., 2000. The geometry of drag zones adjacent to salt diapirs. J. Geol. Soc. 157, 1019–1029.
Alsop, G.I., Marco, S., Levi, T., Weinberger, R., 2017. Fold and thrust systems in mass transport deposits. J. Struct. Geol. 94, 98–115.
Alsop, G.I., Weinberger, R., Marco, S., Levi, T., 2019. Identifying soft-sediment deformation in rocks. J. Struct. Geol. 125, 248–255.
Alsop, G.I., Wienberger, R., Marco, S., Levi, T., 2020. Folding during soft-sediment deformation. In: Bond, C.E., Lebit, H.D. (Eds.), Folding and Fracturing of Rocks: 50 Years of Research since the Seminal Text Book of J. G. Ramsay, Geological Society of London, Special Publications, 487, pp. 81–104.
Alsop, G.I., Weinberger, R., Marco, S., Levi, T., 2021. Detachment fold duplexes within gravity-driven fold and thrust systems. J. Struct. Geol. 142 https://doi.org/10.1016/j.jsg.2020.104207.
Amrouch, K., Lacombe, O., Bellahsen, N., Daniel, J.-M., Callot, J.-P., 2010. Stress and strain patterns, kinematics and deformation mechanisms in a basement-cored anticline: Sheep Mountain Anticline. Wyoming. Tectonics 29. https://doi.org/10.1029/2009TC002525.
Anthony, M., Wickham, J., 1978. Finite-element simulation of asymmetric folding. Tectonophysics 47, 1–14.
Avebury, P.C., 1903. An experiment in mountain-building. Q. J. Geol. Soc. 59, 348–355.
Avebury, P.C., 1905. An experiment in mountain-building: part II. Q. J. Geol. Soc. 61, 345–357.
Barnes, P.M., 1996. Active folding of Pleistosene unconformities on the edge of the Australian-Pacific plate boundary zone, offshore North Canterburry, New Zealand. Tectonics 15, 623–640.
Bastida, F., 1993. A new method for the geometrical classification of large data sets of folds. J. Struct. Geol. 15, 69–78.
Bastida, F., Aller, J., Bobillo-Ares, N.C., 1999. Geometrical analysis of folded surfaces using simple function. J. Struct. Geol. 21, 729–742.
Bastida, F., Aller, J., Bobillo-Ares, N.C., Toimil, N.C., 2005. Fold geometry: a basis for their kinematical analysis. Earth-Sci. Rev. 70, 129–164.
Bastida, F., Aller, J., Toimil, N.C., Lisle, R.J., Bobillo-Ares, N.C., 2007. Some considerations on the kinematics of chevron folds. J. Struct. Geol. 29, 1185–1200.
Bastida, F., Aller, J., Fernández, F.J., Lisle, R.J., Bobillo-Ares, N.C., Menéndez, O., 2014. Recumbent folds: key structural elements in orogenic belts. Earth Sci. Rev. 135, 162–183.
Becker, G.F., 1893. Finite homogeneous strain, flow and rupture of rocks. Bull. Geol. Soc. Am. 4, 13–90.
Becker, G.F., 1896. Schistosity and slaty cleavage. J. Geol. 4, 429–448.
Behzadi, H., Dubey, A.K., 1980. Variation of interlayer slip in space and time during flexural folding. J. Struct. Geol. 2, 453–457.
Bell, A.M., 1981. Vergence: an evaluation. J. Struct. Geol. 3, 197–202.
Benediktsson, Í.Ö., Schomacker, A., Lokrantz, H., Ingólfsson, Ó., 2010. The 1890 surge end moraine at Eyjabakkajökull, Iceland: a re-assessment of a classic glaciotectonic locality. Quat. Sci. Rev. 29 (3–4), 484–506.
Bengston, C.A., 1980. Structural uses of tangent diagrams. Geology 8, 599–602.
Bengston, C.A., 1981. Statistical curvature analysis techniques for structural interpretation of dipmeter data. Am. Assoc. Petrol. Geolog. Bull. 65, 312–332.
Bergbauer, S., 2007. Testing the predictive capability of curvature analyses. In: Jolley, S. J., Walsh, J.J., Knipe, R.J. (Eds.), Structurally Complex Reservoirs, Geological Society of London, Special Publication, 292, pp. 185–202.
Bergbauer, S., Pollard, D.D., 2003. How to calculate normal curvatures of sampled geological surfaces. J. Struct. Geol. 25, 277–289.
Bergbauer, S., Mukerji, T., Hennings, P., 2003. Improving curvature analysis of deformed horizons using scale dependent filtering techniques. Am. Assoc. Petrol. Geolog. Bull. 87, 1255–1277.
Bézier, P., 1966. Definition numérique des corbes et surfaces-I. Automatisme 12, 625–632.
Bézier, P., 1967. Definition numérique des corbes et surfaces-II. Automatisme 12, 17–21.
Billings, M.P., 1946. Structural Geology. Prentice-Hall.
Biot, M.A., 1937. A hydrodynamic analogy for shearing stress distribution in bending. J. Appl. Phys. 9, 39–43.
Biot, M.A., 1957. Folding instability of a layered viscoelastic medium under compression. Proc. Roy. Soc. London, Ser. A 242, 444.
Biot, M.A., 1959. On the instability and folding deformation of layered viscoelastic medium in compression. J. Appl. Mech. 26, 393–400.
Biot, M.A., 1961. Theory of folding of stratified viscoelastic media and its implications in tectonics and orogenies. Geol. Soc. Am. Bull. 72, 1595–1620.
Biot, M.A., 1964. Theory of internal buckling of a confined multilayered structure. Geol. Soc. Am. Bull. 75, 563–568.
Biot, M.A., 1965. Further development in the theory of internal buckling of multilayers. Geol. Soc. Am. Bull. 76, 833–840.
Biot, M.A., Ode, H., Roever, W.L., 1961. Experimental vertification of the theory of folding of stratified viscoelastic media. Geol. Soc. Am. Bull. 72, 1621–1632.
Bobillo-Ares, N.C., Bastida, F., Aller, J., 2000. On tangential longitudinal strain folding. Tectonophysics 319, 53–68.
Bobillo-Ares, Toimil, N.C., Aller, J., Bastida, F., 2004. FoldModeler: a tool for the geometrical and kinematical analysis of folds. Comput. Geosci. 30, 147–159.
Bobillo-Ares, N.C., Bastida, F., Aller, J., Lisle, J., 2009. An approach to folding kinematics from the analysis of folded oblique surfaces. J. Struct. Geol. 31, 842–852.
Bobillo-Ares, N.C., Bastida, F., Aller, J., Lisle, J., 2017. A new mechanism for producing cleavage in preexisting folds: the transation mechanism. An example in the Burela section (Variscan belt, NW Spain). J. Struct. Geol. 94, 213–226.
Bobillo-Ares, N.C., Bastida, F., Aller, J., Lisle, J., 2018. Some kinematical patterns leading to the formation of similar folds. J. Struct. Geol. 112, 69–80.
Borradaile, G.J., 1978. Transected folds: a study illustrated with examples from Canada and Scotland. Geol. Soc. Am. Bull. 89, 481–493.
Boyer, S.E., 1986. Styles of folding within thrust sheets: axamples from the Appalachian and Rocky Mountains of the U.S.a. and Canada. J. Struct. Geol. 8, 325–339.
Brandes, C., Tanner, D.C., 2014. Fault-related folding: a review of kinematic models and their application. Earth Sci. Rev. https://doi.org/10.1016/j.earscirev.2014.06.008.
Bretis, B., Bartl, N., Grasemann, B., 2011. Lateral fold growth and linkage in the Zagros fold and thrust belt (Kurdistan, NE Iraq). Basin Res. 23, 615–630.
Brun, J.-P., Fort, X., 2011. Salt tectonics at passive margins: geology versus models. Mar. Pet. Geol. 28 (6), 1123–1145.

Burke, J., Knobloch, E., 2007. Homoclinic snaking: structure and stability. Chaos 17. https://doi.org/10.1063/1.2746816.
Burtscher, A., Frehner, M., Grasemann, B., 2012. Tectonic geomorphological investigations of antiforms using differential geometry: Permam anticline, northern Iraq. Am. Assoc. Petrol. Geolog. Bull. 96, 301–314.
Butler, R.W.H., Bond, C.E., Cooper, M.A., Watkins, H.M., 2020. Fold-thrust structures – where have all the buckles gone? In: Bond, C.E., Lebit, H.D. (Eds.), Folding and Fracturing of Rocks: 50 years of Research since the Seminal Text Book of J. G. Ramsay, Geological Society of London, Special Publications, 487, pp. 21–44.
Buxtorf, A., 1916. Prognosen und befunde beim Hauensteinbasis-und Grenchenberg-tunnel und die Bedeutung der letzeren fur die geologie des Juragebirges. Verh. Naturforsch. Ges. Basel 27, 184–205.
Cadell, H.M., 1889. Experimental researches in mountain building. Trans. Roy. Soc. Edin. 35, 337–357.
Cadell, H.M., 1896. The Geology and Scenery of Sutherland, Second edition. D Douglas, Edinburgh.
Cámara, P., Flinch, J.F., 2017. The southern Pyrenees: a salt-based fold-and-thrust belt. In: Soto, J.I., Flinch, J.F., Tari, G. (Eds.), Permo-Triassic Salt Provinces of Europe, North Africa and the Atlantic Margins: Tectonics and Hydrocarbon Potential. Elsevier, pp. 395–415.
Cardozo, N., Allmendinger, R.W., 2013. Spherical projections with OSXStereonet. Comput. Geosci. 51, 193–205.
Carey, S.W., 1953. The rheid concept in geotectonics. J. Geol. Soc. Aust. 1, 67–117.
Carey, S.W., 1962. Folding. J. Alberta Soc. Petrol. Geol. 10, 95–144.
Carosi, R., Montomoli, C., 1999. Relations between folds and stretching lineations in the Verrucano of Pisani Mounts (northern Apennines). C. R. Acad. Sci. Ser. IIA Earth Planet. Sci. 328, 485–492.
Carreras, J., Druguet, E., 2019. Complex fold patterns developed by progressive deformation. J. Struct. Geol. 125, 195–201.
Carreras, J., Estrada, A., White, S., 1977. The effects of folding on the C-axis fabrics of a quartz mylonite. Tectonophysics 39, 3–24.
Carreras, J., Druguet, E., Griera, A., 2005. Shear zone-related folds. J. Struct. Geol. 27, 1229–1251.
Casey, M., 1976. Application of Finite Element Analysis to Some Problem in Structural Geology. PhD Thesis. University of London.
Casey, M., Butler, R.W.H., 2004. Modelling approaches to understanding fold development: implication for hydrocarbon reservoirs. Mar. Pet. Geol. 21, 933–946.
Chadwick, P., 1976. Tectonic structures – a classification. Tectonophysics 30, T3–T9.
Chamberlin, R.T., 1910. The Appalachian folds of Central Pennsylvania. J. Geol. 18, 228–251.
Chamberlin, R.T., 1925. The wedge theory of diastrophism. J. Geol. 33, 755–792.
Chamberlin, R.T., Shepard, F.P., 1923. Some experiments in folding. J. Geol. 31, 490–512.
Chapple, W.M., 1964. A Mthematical Study of Finite-Amplitude Rock-Folding. PhD Thesis. California Institute of Technology, Pasadena, California.
Chapple, W.M., 1968. A mathematical theory of finite amplitude rock-folding. Geol. Soc. Am. Bull. 79, 47–68.
Childs, C., Manzocchi, T., Nicol, A., Walsh, J.J., Soden, A.M., Conneally, J.C., Delogkos, E., 2017. The relationship between normal drag, relay ramp aspect ratio and fault zone structure. Geol. Soc. Lond., Spec. Publ. 439, 355–372.
Cobbold, P.R., 1976. Fold shapes as functions of progressive strain. Philos. Trans. R. Soc. Lond. Ser. A 283, 129–138.
Cobbold, P.R., 1977. Finite-element analysis of fold propagation-a problematic application. Tectonophysics 38, 339–353.
Cobbold, P.R., Quinquis, H., 1980. Development of sheath folds in shear regimes. J. Struct. Geol. 2, 119–126.
Cobbold, P.R., Cosgrove, J.W., Summers, J.M., 1971. Development of internal structures in deformed anisotropic rocks. Tectonophysics 12, 23–53.
Coelho, S., Passchier, C.W., Grasemann, B., 2005. Geometric description of flanking structures. J. Struct. Geol. 27, 597–606.
Coleman, A.J., Duffy, O.B., Jackson, C.A.-L., 2019. Growth folds above propagating normal faults. Earth Sci. Rev. 196 https://doi.org/10.1016/j.earscirev.2019.102885.
Connors, C.D., Hughes, A.N., Ball, S.M., 2021. Forward kinematic modeling of fault-bend folding. J. Struct. Geol. 143 https://doi.org/10.1016/j.jsg.2020.104252.
Cosgrove, J.W., 2015. The association of folds and fractures and the link between folding, fracturing and fluid flow during the evolution of a fold-thrust belt: a brief review. In: Richards, F.L., Richardson, N.J., Rippington, S.J., Wilson, R.W., Bond, C. E. (Eds.), Industrial Structural Geology: Principles, Techniques and Integration, Geological Society of London, Special Publications, 421, pp. 41–68.
Cosgrove, J.W., Ameen, M.S., 1999. A comparison of the geometry, spatial organisation and fracture patterns associated with forced folds and buckle folds. In: Cosgrove, J. W., Ameen, M.S. (Eds.), Forced Folds and Fractures, Geological Society of London, Special Publication, 169, pp. 7–21.
Cruden, D.M., Charlesworth, H.A.K., 1972. Observation on numerical determination of Axes of cylindrical and conical folds. Geol. Soc. Am. Bull. 83, 2019–2024.
Cruikshank, K.M., Johnson, A.M., 1993. High amplitude folding of linear-viscous multilayers. J. Struct. Geol. 15, 79–94.
Currie, J.B., Patnode, H.W., Trump, R.P., 1962. Development of folds in sedimentary strata. Geol. Soc. Am. Bull. 73, 655–674.
Curtis, M.L., Flowerdew, M.J., Riley, T.R., Whitehouse, M.J., Daly, J.S., 2010. Andean sinistral transpression and kinematic partitioning in South Georgia. J. Struct. Geol. 32, 464–477.
Dabrowski, M., Krotkiewski, M., Schmid, D.W., 2008. MILAMIN: MATLAB-based finite element method solver for large problems. Geochem. Geophys. Geosyst. 9 https://doi.org/10.1029/2007GC001719.
Dahlstrom, C.D.A., 1954. Statistical analysis of cylindrical folds. Trans. Can. Inst. Min. Metall. 57, 140–145.
Dahlstrom, C.D.A., 1969. The upper detachment in concentric folding. Bull. Can. Petrol. Geol. 17, 326–346.
Dahlstrom, C.D.A., 1970. Structural geology in the eastern margin of the Canadian Rocky Mountains. Bull. Can. Petrol. Geol. 18, 332–406.
Damasceno, D.R., Eckert, A., Liu, X., 2017. Flexural-slip during visco-elastic buckle folding. J. Struct. Geol. 100, 62–76.
Darnault, R., Callot, J.-P., Ballard, J.-F., Fraisse, G., Mengus, J.-M., Ringenbach, J.-C., 2016. Control of syntectonic erosion and sedimentation on kinematic evolution of a multidecollement fold and thrust zone: Analogue modeling of folding in the southern subandean of Bolivia. J. Struct. Geol. 89, 30–43.
Daubrée, G.A., 1879. Etudes synthétiques de Géologie Expérimentale. Dunod, Paris.
Davis, G.H., 2014. Quasi-flexural folding of pseudo-bedding. Geol. Soc. Am. Bull. 126, 680–701.
Davis, G.H., Bump, A.P., 2009. Structural geologic evolution of the Colorado Plateau. In: Kay, S.M., Ramos, V.A., Dickinson, W.R. (Eds.), Backbone of the Americas: Shallow Subduction, Plateau Uplift, and Ridge and Terrane Collision, Geological Society of America Memoir, 204, pp. 99–124.
Davis, D.M., Engelder, T., 1985. The role of salt in fold-and-thrust belts. Tectonophysics 119, 67–88.
Davis, G.H., Reynolds, S.J., Kluth, C.F., 2011. Structural Geology of Rocks and Regions, third edition. John Wiley & Sons, Inc.
De Bremaecker, J.-C., Becker, E.B., 1978. Finite element models of folding. Tectonophysics 50, 349–367.
De Margerie, E., Heim, A., 1888. Les dislocations de l'écorce terrestre: Die dislocationen der erdrinde. Essai de definition et de nomenclature. Versuch einer definition und bezeichnung, Wurster.
De Paor, D.G., 1996. Bézier curves and geological design. In: Paor, De (Ed.), Structural Geology and Personal Computers. Pergamon Press, pp. 389–417.
De Saussure, H.-B., 1796. Voyages dans les Alpes. Précédés d'un essai sur l'histoire naturelle des environs de Genève. Louis Fauche-Borel (tomes III and IV), Geneva.
de Sitter, L.U., 1964. Structural Geology, Second edition. McGraw-Hill Book Company, New York.
de Sitter, L.U., Zwart, H.J., 1960. Tectonic development in sepra- and infra-structures of a mountain chain. In: Proc. 21st Int. Geol. Congr. Copenhagen 18, pp. 248–256.
Debacker, T.N., 2012. Folds and cleavage/fold relationships in the Brabant Massif, southeastern Anglo-Brabant Deformation Belt. Geol. Belg. 15, 81–95.
Delogkos, E., Saqab, M.M., Walsh, J.J., Roche, V., Childs, C., 2020. Throw variations and strain partitioning associated with fault-bend folding along normal faults. Solid Earth 11, 935–945.
Deng, H., Zhang, C., Koyi, H.A., 2013. Identifying the characteristic signatures of fold-accommodation faults. J. Struct. Geol. 56, 1–19.
Dieterich, J.H., 1970. Computer experiments on mechanics of finite amplitude folds. Can. J. Earth Sci. 7, 467–476.
Dieterich, J.H., Carter, N.L., 1969. Stress history of folding. Am. J. Sci. 267, 129–154.
Donath, F.A., Parker, R.B., 1964. Folds and folding. Geol. Soc. Am. Bull. 75, 45–62.
Druguet, E., 2019. Deciphering the presence of axial-planar veins in tectonites. Geosci. Front. 10, 2101–2115.
Druguet, E., Alsop, G.I., Carreras, I., 2009. Coeval brittle and ductile structures associated with extreme deformation partitioning in a multilayer sequence. J. Struct. Geol. 31, 498–511.
Dubey, A.K., 1980. Late stages in the development of folds as deduced from model experiments. Tectonophysics 65, 311–322.
Dubey, A.K., Behzadi, H., 1981. Development of flexural slip folds, overlapping boudins and extension faults in multi-layered materials: field evidence and experimental model. J. Geol. Soc. India 22, 274–284.
Dubey, A.K., Cobbold, P.R., 1977. Noncylindrical flexural slip folds in nature and experiment. Tectonophysics 38, 223–239.
Duffy, O.B., Dooley, T.P., Hudec, M.R., Jackson, M.P.A., Fernandez, N., Jackson, C.A.-L., Soto, J.I., 2018. Structural evolution of salt-influenced fold-and-thrust belts: a synthesis and new insights from basins containing isolated diapirs. J. Struct. Geol. 114, 206–221.
Dunham, R.E., Crider, J.G., 2012. Geometric curvature analysis of intersecting kink bands: a new perspective on the 3D geometry of kink folds. J. Struct. Geol. 37, 236–247.
Dutta, D., Mukherjee, S., 2019. Opposite shear senses: geneses, global occurrences, numerical simulations and a case study from the Indian western Himalaya. J. Struct. Geol. 126, 357–392.
Eckert, A., Connolly, P., Liu, X., 2014. Large-scale mechanical buckle fold development and the initiation of tensile fractures. Geochem. Geophys. Geosyst. 15, 4570–4587.
Eckert, A., Liu, X., Connolly, P., 2016. Pore pressure evolution and fluid flow during visco-elastic single-layer buckle folding. Geofluids 16, 231–248.
Ellenberger, F., 1995. Johann Scheuchzer, pionnier de la tectonique alpine. Mémoires de la Société géologique de France 168, 39–53.
Elliott, D., 1965. The quantitative mapping of directional minor structures. J. Geol. 73, 865–880.
Engelder, T., 1985. Loading paths to joint propagation during a tectonic cycle: an example from the Appalachian Plateau, U.S.A. J. Struct. Geol. 7, 459–476.
Erslev, E.A., 1991. Trishear fault-propagation folding. Geology 19, 617–620.
Evans, M.A., Fischer, M.P., 2012. On the distribution of fluids in folds: a review of controlling factors and processes. J. Struct. Geol. 44, 2–24.
Ez, V., 2000. When shearing is a cause of folding. Earth-Sci. Rev. 51, 155–172.
Favre, A., 1878. Expériences sur les effets des refoulments ou écrasements latéraux en géologie. Bibliothèque Universelle, Sciences Physiques Et Naturelles, N° 246, pp. 193–211.

Fernandez, N., Kaus, B.J.P., 2014. Fold interaction and wavelength selection in 3D models of multilayer detachment folding. Tectonophysics. https://doi.org/10.1016/j.tecto.2014.06.013.
Fernández-Martínez, J.L., Lisle, R.J., 2009. GenLab: a MATLAB®-based program for structural analysis of folds mapped by GPS or seismic methods. Comput. Geosci. 35, 317–326.
Ferrill, D.A., Morris, A.P., McGinnis, R.N., 2012. Extensional fault-propagation folding in mechanically layered rocks: the case against the frictional drag mechanisms. Tectonophysics 576-577, 78–85.
Ferrill, D.A., Morris, A.P., Wigginton, S.S., Smart, K.J., McGinnis, R.N., Lehrmann, D., 2016. Deciphering thrust fault nucleation and propagation and the importance of footwall synclines. J. Struct. Geol. 85, 1–11.
Fischer, M.P., Wilkerson, M.S., 2000. Predicting the orientation of joints from fold shape: results of pseudo-three-dimensional modelling and curvature analysis. Geology 28, 15–18.
Fisher, O., 1884. III. – on cleavage and distortion. Geol. Mag. 1, 396–406.
Fitz-Díaz, E., Tolson, G., Hudleston, P.J., Bolaños-Rodríguez, D., Ortega-Flores, B., Vázquez-Serrano, A., 2012. The role of folding in the development of the Mexican fold-and-thrust belt. Geosphere 8, 931–949.
Fletcher, R.C., 1974. Wavelength selection in the folding of single layer with power-law rheology. Am. J. Sci. 274, 1029–1043.
Fletcher, R.C., 1977. Folding of a single viscous layer: exact infinitesimal-amplitude solution. Tectonophysics 39, 593–606.
Fletcher, R.C., 1979. The shape of single-layer folds at small but finite amplitude. Tectonophysics 60, 77–87.
Fleuty, M.J., 1964. The description of folds. Proc. Geolog. Assoc. London 75, 461–492.
Fleuty, M.J., 1987. Folds and folding. In: Seyfert, C. (Ed.), Encyclopedia of Structural Geology and Plate Tectonics. Springer, Berlin. https://doi.org/10.1007/3-540-31080-0_41.
Flinn, D., 1962. On folding during three-dimensional progressive deformation. Q. J. Geol. Soc. Lond. 118, 385–433.
Florinsky, I.V., 2016. Digital Terrain Analysis in Soil Science and Geology, second edition. Academic Press-Elsevier.
Forchheimer, P., 1883. Uber sanddruck und Bewegungserscheinungen im inneren trockenen sandes. Tübingen, Aachen.
Fossen, H., 2016. Structural Geology, second edition. Cambridge University Press.
Fossen, H., Cavalcante, G.C.G., 2017. Shear zones – a review. Earth Sci. Rev. 171, 434–455.
Fossen, H., Holst, T.B., 1995. Northwest-verging folds and the northwestward movement of Caledonian Jotun Nappe, Norway. J. Struct. Geol. 17, 1–16.
Fossen, H., Teyssier, C., Whitney, D.L., 2013. Transtensional folding. J. Struct. Geol. 56, 89–102.
Fossen, H., Soliva, R., Ballas, G., Trzaskos, B., Cavalcante, C., Schultz, R.A., 2017. A review of deformation bands in reservoir sandstones: geometries, mechanisms and distribution. Geol. Soc. Lond., Spec. Publ. 459, 9–33.
Fossen, H., Cavalcante, G.C.G., Pinheiro, R.V.L., Archanio, C.J., 2019. Deformation – progressive or multiphase? J. Struct. Geol. 125, 82–99.
Fowler, T.J., Winsor, C.N., 1996. Evolution of chevron folds by profile shape changes: comparison between multilayer deformation experiments and folds of the Bendigo-Castlemaine goldfields, Australia. Tectonophysics 258, 125–150.
France, D., 1987. Recumbent folds. In: Seyfert, C. (Ed.), Encyclopedia of Structural Geology and Plate Tectonics. Springer, Berlin. https://doi.org/10.1007/3-540-31080-0_86.
Frehner, M., 2011. The neutral lines in buckle folds. J. Struct. Geol. 33, 1501–1508.
Frehner, M., 2014. 3D fold growth rates. Terra Nova 26, 417–424.
Frehner, M., 2016. 3D fold growth in transpression. Tectonophysics 693, 183–196.
Frehner, M., Exner, U., 2014. Strain and foliation patterns around buckle folds. In: Llana-Fúnez, S., Marcos, A., Bastida, F. (Eds.), Deformation Structures and Processes within the Continental Crust, Geological Society of London, Special Publication, 394, pp. 21–37.
Frehner, M., Schmalholz, S.M., 2006. Numerical simulations of parasitic folding in multilayers. J. Struct. Geol. 28, 1647–1657.
Frehner, M., Schmid, T., 2016. Parasitic folds with wrong vergence: how pre-existing geometrical asymmetries can be inherited during multilayer buckle folding. J. Struct. Geol. 87, 19–29.
Friedman, M., Handin, J., Logan, J.M., Min, K.D., Stearns, D.W., 1976. Experimental folding of rocks under confining pressure: Part III. Faulted drape folds in multilithologic layered specimens. Geol. Soc. Am. Bull. 87, 1049–1066.
Friedman, M., Hugman III, R.H.H., Handin, J., 1980. Experimental folding of rocks under confining pressure, Part VIII – forced folding of unconsolidated sand and of lubricated layers of limestone and sandstone. Geol. Soc. Am. Bull. 91, 307–312.
Frisch, W., Meschede, M., Blakey, R., 2011. Plate Tectonics: Continental Drift and Mountain Building. Springer.
Gallup, W.B., 1951. Geology of Turner Valley oil and gas field, Albertam Canada. Am. Assoc. Petrol. Geolog. Bull. 34, 797–821.
Geikie, J., 1908. Structural and Field Geology for Students of Pure and Applied Science. Oliver and Boyd.
Ghanadian, M., Faghih, A., Abdollahie-Fard, I., Kusky, T., Maleki, M., 2017. On the role of incompetent strata in the structural evolution of the Zagros Fold-Thrust Belt, Dezful Embayment, Iran. Mar. Pet. Geol. 81, 320–333.
Ghassemi, M.R., Schmalholz, S.M., Ghassemi, A.R., 2010. Kinematics of constant arc length folding for different fold shapes. J. Struct. Geol. 32, 755–765.
Ghosh, S.K., 1966. Experimental tests of buckling folds in relation to strain ellipsoid in simple shear deformations. Tectonophysics 3, 169–185.
Ghosh, S.K., 1993. Structural Geology – Fundementals and Modern Developments. Pergamon Press.
Ghosh, S.K., Sengupta, S., 2010. A paradoxical situation in determining relative competence from wavelength/arclength ratios within buckle folded multilayers. In: Mamtani, M.A. (Ed.), Structural Geology – From Classical to Modern Concepts, Journal Geological Society of India, 75, pp. 13–17.
Ghosh, N., Chakra, M., Chattopadhyay, A., 2014. An experimental approach to strain pattern and folding in unconfined and/or partitioned transpressional deformation. Int. J. Earth Sci. 103, 349–365.
Giles, K.A., Rowan, M.G., 2012. Concepts in halokinetic-sequence deformation and stratigraphy. In: Alsop, G.I., Archer, S.G., Hartley, A.J., Grant, N.T., Hodgkinson, R. (Eds.), Salt Tectonics, Sediments and Prospectivity, Geological Society of London, Special Publications, 363, pp. 7–31.
Gogoi, M.P., Mukherjee, S., 2019. Synthesis of folds in 3D with Bézier surface. In: Mukherjee, S. (Ed.), Developments in Structural Geology and Tectonics, Vol. 5. Elsevier, pp. 279–290.
Goguel, J., 1952. Traité de tectonique. Masson et Cie, Paris.
Gomez-Rivas, E., Bons, P.D., Griera, A., Carreras, J., Druguet, E., Evans, L., 2007. Strain and vorticity analysis using small-scale faults and associated drag folds. J. Struct. Geol. 29, 1882–1899.
Goscombe, B.D., Passchier, C.W., Hand, M., 2004. Boudinage classification: end-member boudin types and modified boudin structures. J. Struct. Geol. 26, 739–763.
Grasemann, B., Schmalholz, S.M., 2012. Lateral fold growth and fold linkage. Geology 40, 1039–1042.
Grasemann, B., Martel, S., Passchier, C.W., 2005. Reverse and normal drag along a fault. J. Struct. Geol. 27, 999–1010.
Gray, N.H., Geiser, P.A., Geiser, J.R., 1980. On the least-squares fit of small and great circles to Spherically projected orientation data. Math. Geol. 12, 173–184.
Grohmann, C.H., Campanha, G.A., 2010. OpenStereo: Open Source, Cross-Platform Software for Structural Geology Analysis. AGU Fall Meeting abstract.
Grose, L., Laurent, G., Aillères, L., Armit, R., Jessel, M., Caumon, G., 2017. Structural data constraints for implicit modelling of folds. J. Struct. Geol. 104, 80–92.
Grose, L., Aillères, L., Laurent, G., Armit, R., Jessel, M., 2019. Inversion of geological knowledge for fold geometry. J. Struct. Geol. 119, 1–14.
Grujic, D., Mancktelow, N.S., 1995. Fold with axes parallel to the extension direction: an experimental study. J. Struct. Geol. 17, 279–291.
Guiting, H., 1998. Fractal simulation and classification of folds. Acta Geol. Sin. 72, 217–223.
Guiting, H., 2005. Rock rheology and complexity of fractal folds. Earth Sci. Front. 12, 347–351.
Guiting, H., 2009. Rheological properties of fractal deformation in multilayer folds. Acta Geol. Sin. 83, 544–549.
Hall, J., 1815. On the vertical position and convolutions of certain strata and their relation with granite. Trans. Roy. Soc. Edin. 7, 79–108.
Hamblin, W.K., 1965. Origin of "reverse drag" on the downthrown side of normal faults. Geol. Soc. Am. Bull. 76, 1145–1164.
Handin, J., Friedman, M., Min, K.D., Pattison, L.J., 1976. Experimental folding of rocks under confining pressure: Part II. Buckling of multi-layered rock beams. Geol. Soc. Am. Bull. 87, 1035–1048.
Hardy, S., Allmendinger, R.W., 2011. Trishear: A review of kinematics, mechanics, and applications. In: McClay, K.R., Shaw, J., Suppe, J. (Eds.), Thrust Fault-Related Folding, American Association of Petroleum Geologists Memoir, 94, pp. 95–119.
Hardy, S., Ford, M., 1997. Numerical modelling of trishear fault-propagation folding. Tectonics 16, 841–854.
Harker, A., 1885. V. – on the successive stages of slaty cleavage. Geol. Mag. 2, 266–268.
Harris, L.B., Koyi, H.A., Fossen, H., 2002. Mechanism for folding of high-grade rocks in extensional tectonic settings. Earth Sci. Rev. 59, 163–210.
Hazra, S., 1997. Sense of fold asymmetry in single-phase and superposed folding. In: Sengupta, S. (Ed.), Evolution of Geological Structures in Micro- to Macro-Scales. Chapman & Hall, London, pp. 397–408.
Heim, A., 1878. Untersuchungen uber den Mechanismus der Gebirgsbildung im Anschluss an die Geologische Monographie der Tödi-Windgällen-Gruppe: mit einem Atlas (Vol. 1), Schwabe, Basel.
Higgins, C.G., 1962. Reconstruction of flexure fold by concentric arc method. Am. Assoc. Petrol. Geolog. Bull. 46, 1737–1739.
Hills, E.S., 1963. Elements of Structural Geology. Methuen & Co. Ltd., London.
Hobbs, B.E., 1971. The analysis of strain in folded layers. Tectonophysics 11, 329–375.
Hobbs, B.E., 2019. The development of structural geology and the historical context of the journal of structural geology: a reflection by Bruce Hobbs. J. Struct. Geol. 125, 3–19.
Hobbs, B.E., Ord, A., 2012. Localised and chaotic folding: the role of axial plane structures. Philos. Trans. R. Soc. Lond. Ser. A 370, 1966–2009.
Hobbs, B.E., Ord, A., 2015. Structural Geology: The Mechanics of Deforming Metamorphic Rocks, vol. 1: Principles. Elsevier, Netherlands.
Hobbs, B.E., Mühlhaus, H.B., Ord, A., 1990. Instability, softening and localisation of deformation. In: Knipe, R.J., Rutter, E.H. (Eds.), Deformation Mechanisms, Rheology and Tectonics, Geological Society of London, Special Publications, 54, pp. 143–165.
Hobbs, B.E., Ord, A., Regenauer-Lieb, K., 2011. The thermodynamics of deformed metamorphic rocks: a review. J. Struct. Geol. 33, 758–818.
Hobbs, B.E., Regenauer-Lieb, K., Ord, A., 2008. Folding with thermal–mechanical feedback. J. Struct. Geol. 30 (12), 1572–1592.
Holcombe, R., 2013. GEOrient version 9. http://www.holcombe.net.au/software/rodh_software_georient.htm.
Holdsworth, R.E., Tavarnelli, E., Clegg, P., Pinheiro, R.V.L., Jones, J.J., McCaffrey, K.J.W., 2002. Dominal deformation patterns and strain partitioning during transpression: an example from the Southern Uplands terrane, Scotland. J. Geol. Soc. 159, 401–415.

Holst, T.B., Fossen, H., 1987. Strain distribution in a fold in the West Norwegian Caledonides. J. Struct. Geol. 9, 915–924.
Honea, E., Johnson, A.M., 1976. A theory of concentric, kink, and sinusoidal folding and of monoclonal flexuring of compressible, elastic multilayers. Part VI: Development of sinusoidal and kink folds in multilayers confined by rigid boundaries. Tectonophysics 30, 197–239.
Houseman, G., Barr, T., Evans, L., 2008. Basil: Stress and Deformation in a Viscous Material. Microdynamics Simulation. Springer-Verlag, Berlin, pp. 139–154.
Hubbert, M.K., 1937. Theory of scale models as applied to the study of geologic structures. Bull. Geol. Soc. Am. 48, 1459–1519.
Hudec, M.R., Norton, I.O., Jackson, M.P.A., Peel, F.J., 2013. Jurassic evolution of the Gulf of Mexico salt basin. Am. Assoc. Petrol. Geolog. Bull. 97, 1683–1710.
Hudleston, P.J., 1969. The morphology and development of folds. PhD Thesis. University of London, UK.
Hudleston, P.J., 1973a. Fold morphology and some geometrical implication of theories of fold development. Tectonophysics 16, 1–46.
Hudleston, P.J., 1973b. An analysis and interpretation of minor folds in the Moine rocks of Monar, Scotland. Tectonophysics 16, 89–132.
Hudleston, P.J., 1973c. An analysis of "single layer" folds developed experimentally in viscous media. Tectonophysics 16, 89–132.
Hudleston, P.J., 1977. Similar folds, recumbent folds, and gravity tectonics in ice and rocks. J. Geol. 85, 113–122.
Hudleston, P.J., 1986. Extracting information from folds in rocks. J. Geol. Educ. 34, 237–245.
Hudleston, P.J., Holst, T.B., 1984. Strain analysis and fold shape in a limestone layer and implications for layer rheology. Tectonophysics 106, 321–347.
Hudleston, P.J., Lan, L., 1993. Information from fold shapes. J. Struct. Geol. 15, 253–264.
Hudleston, P.J., Lan, L., 1994. Rheological controls on the shapes of single-layer folds. J. Struct. Geol. 16, 1007–1021.
Hudleston, P.J., Stephansson, O., 1973. Layer shortening and fold shape development in the buckling of single layers. Tectonophysics 17, 299–321.
Hudleston, P.J., Tabor, J.R., 1988. Strain and fabric development in a buckled calcite vein and rheological implications. Bull. Geol. Institute, University of Uppsala, N.S 14, 79–94.
Hudleston, P.J., Treagus, S.H., 2010. Information from folds: a review. J. Struct. Geol. 32, 2042–2071.
Hudleston, P.J., Treagus, S.H., Lan, L., 1996. Flexural flow folding: does it occur in nature? Geology 24, 203–206.
Hughes, A.N., Benesh, N.P., Shaw, J.H., 2014. Factors that control the development of fault-bend versus fault-propagation folds: insights from mechanical models based on the discrete element method (DEM). J. Struct. Geol. 68, 121–141.
Hughes, A.N., Shaw, J.H., 2015. Insights into the mechanics of fault-propagation folding styles. GSA Bull. 127 (11–12), 1752–1765.
Humair, F., Bauville, A., Epard, J.L., Schmalholz, S.M., 2020. Interaction of folding and thrusting during fold-and-thrust-belt evolution: insights from numerical simulations and application to the Swiss Jura and the Canadian Foothills. Tectonophysics 789. https://doi.org/10.1016/j.tecto.2020.228474.
Hyde, S., Blum, Z., Landh, T., Lidin, S., Ninham, B.W., 1996. The Language of Shape: The Role of Curvature in Condensed Matter: Physics. Elsevier, Chemistry and Biology.
Ickes, E.L., 1923. Similar, parallel and neutral surface types of folding. Econ. Geol. 18, 575–591.
Jackson, M.P.A., Hudec, M.R., 2017. Salt Tectonics – Principles and Practice. Cambridge University Press, Cambridge.
Jackson, C.A.-L., Jackson, M.P.A., Hudec, M.R., 2015. Understanding the kinematics of salt-bearing passive margins: a critical test of competing hypotheses for the origin of the Albian Gap, Santos Basin, offshore Brazil. Geol. Soc. Am. Bull. 127, 1730–1751.
Jacques, D., Derez, T., Muchez, P., Sintubin, M., 2014. Regional significance of non-cylindrical folding in the northwestern part of the High-Ardenne slate belt (Redu-Daverdisse, Belgium). Geol. Belg. 17, 252–267.
Jäger, P., Schmalholz, S.M., Schmid, D.W., Kuhl, E., 2008. Brittle fracture during folding of rocks: a finite element study. Philos. Mag. 88, 3245–3263.
Jahani, S., Callot, J.-P., Letouzey, J., Frizon de Lamotte, D., 2009. The eastern termination of the Zagros Fold-and-Thrust Belt, Iran: Structures, evolution, and relationships between salt plugs, folding, and faulting. Tectonics 28. https://doi.org/10.1029/2008TC002418.
Jahani, S., Hassanpour, J., Mohammadi-Firouz, S., Letouzey, J., Frizon de Lamotte, D., Alavi, S.A., Soleimany, B., 2017. Salt tectonics and tear faulting in the central part of the Zagros Fold-Thrust Belt, Iran. Mar. Pet. Geol. 86, 426–446.
Jamison, W.R., 1987. Geometric analysis of fold development in overthrust terranes. J. Struct. Geol. 9, 207–219.
Jeng, F.S., Huang, K.P., 2008. Buckling folds of a single layer embedded in matrix-Theoretical solutions and characteristics. J. Struct. Geol. 30, 633–648.
Jeng, F.S., Lin, M.L., Lai, Y.C., Teng, M.H., 2002. Influence of strain rate on buckle folding of an elasto-viscous single layer. J. Struct. Geol. 24, 501–516.
Jin, G., Groshong Jr., R.H., 2006. Trishear kinematic modeling of extensional fault propagation folding. J. Struct. Geol. 28, 170–183.
Johnson, A.M., 1977. Styles of folding: mechanics and mechanisms of folding of natural elastic materials. Dev. Geotectonics 11. Elsevier, Amsterdamcon.
Johnson, T.E., 1991. Nomenclature and geometric classification of cleavage-transected folds. J. Struct. Geol. 13, 261–274.
Johnson, A.M., Ellen, S.D., 1974. A theory of concentric, kink, and sinusoidal folding and of monoclonal flexuring of compressible, elastic multilayers. Part I: Introduction. Tectonophysics 21, 301–339.
Johnson, A.M., Fletcher, R.C., 1994. Folding of Viscous Layers. Columbia University Press, New York.
Johnson, A.M., Honea, E., 1975. A theory of concentric, kink, and sinusoidal folding and of monoclonal flexuring of compressible, elastic multilayers. Part III: Transition from sinusoidal to concentric-like to chevron folds. Tectonophysics 27, 1–38.
Johnson, A.M., Pfaff, V.J., 1989. Parallel, similar and constrained folds. Eng. Geol. 27, 115–180.
Jones, R.R., Holdsworth, R.E., Clegg, P., McCaffrey, K., Tavarnelli, E., 2004. Inclined transpression. J. Struct. Geol. 26, 1531–1548.
Kamen-Kaye, M., 1953. Curvature of low angle faults at Las Mercedes, Venezuela. Am. Assoc. Petrol. Geolog. Bull. 37, 2178–2182.
Kaus, B.J.P., Schmalholz, S.M., 2006. 3D finite amplitude folding: implications for stress evolution during crustal and lithospheric deformation. Geophys. Res. Lett. 33, L14309.
Kearey, P., Klepeis, K.A., Vine, F.J., 2009. Global Tectonics. Third edition, Wiley-Blackwell.
Kelker, D., Langenberg, C.W., 1976. Mathematical-model for orientation data from macroscopic cylindrical folds. Math. Geol. 8, 549–559.
Kelker, D., Langenberg, C.W., 1982. A mathematical-model for orientation data from macroscopic conical folds. Math. Geol. 14, 289–307.
Kelker, D., Langenberg, C.W., 1987. A mathematical-model for orientation data from macroscopic elliptic conical folds. Math. Geol. 19, 729–743.
Kelker, D., Langenberg, C.W., 1988. Statistical classification of macroscopic folds as cylindrical, circular conical, or elliptical conical. Math. Geol. 20, 717–730.
Koenigsberger, J., Morath, O., 1913. Theoretische Grundlagen der experimentellen Tektonik. Z. Dtsch. Geol. Ges. 65, 65–86.
Kruckenberg, S.C., Vandergaeghe, O., Ferré, E.C., Teyssier, C., Whitney, D.L., 2011. Flow of partially molten crust and the internal dynamics of a migmatite dome, Naxos, Greece. Tectonics 30. https://doi.org/10.1029/2010TC002751.
Kuenen, P.H., de Sitter, L.U., 1938. Experimental investigation into the mechanism of folding. Leidse. Geol. Meded. 10, 217–239.
Lan, L., Hudleston, P.J., 1991. Finite-element models of buckle folds in non-linear materials. Tectonophysics 199, 1–12.
Lan, L., Hudleston, P.J., 1995. The effects of rheology on the strain distribution in single layer buckle folds. J. Struct. Geol. 17, 727–738.
Laubscher, H.P., 1956. Structural and seismic deformations along normal faults in the eastern Venezuelan Basin. Geophysics 21, 368–387.
Laubscher, H.P., 1978. Foreland folding. Tectonophysics 47, 325–337.
Leith, C.K., 1913. Structural Geology. Henry Holt and Company.
Li, J., Mitra, S., 2020. Seismic models of detachment and faulted detachment folds. Mar. Pet. Geol. 117 https://doi.org/10.1016/j.marpetgeo.2020.104385.
Link, T.A., 1928. En echelon folds and arcuate mountains. J. Geol. 36, 526–538.
Lisle, R.J., 1992a. Constant bed-length folding: three-dimensional geometrical implications. J. Struct. Geol. 14, 245–252.
Lisle, R.J., 1992b. Strain estimation from flattened buckle folds. J. Struct. Geol. 14, 369–271.
Lisle, R.J., 1994. Detection of zones of abnormal strains in structures using Gaussian curvature analysis. Am. Assoc. Petrol. Geolog. Bull. 78, 1811–1819.
Lisle, R.J., 1997. A fold classification scheme based on a polar plot of inverse layer thickness. In: Sengupta, S. (Ed.), Evolution of Geological Structures in Micro to Macro-Scales. Chapman & Hall, pp. 323–339.
Lisle, R.J., 2003. Dupin's indicatrix: a tool for quantifying periclinal folds on maps. Geol. Mag. 140, 721–726.
Lisle, R.J., Fernández-Martínez, J.L., 2005. Structural analysis of seismically mapped horizons using the developable surface model. Am. Assoc. Petrol. Geolog. Bull. 89, 839–848.
Lisle, R.J., Robinson, J.M., 1995. The Mohr circle for curvature and its application to fold description. J. Struct. Geol. 17, 739–750.
Lisle, R.J., Toimil, N.C., 2007. Defining folds on three-dimensional surfaces. Geology 35, 519–522.
Lisle, R.J., Fernández Martínez, J.L., Bobillo-Ares, N., Menéndez, O., Aller, J., Bastida, F., 2006. FOLD PROFILER: a MATLAB® - based program for fold shape classification. Comput. Geosci. 32, 102–108.
Lisle, R.J., Aller, J., Bastida, F., Bobillo-Ares, N.C., Toimil, N.C., 2009. Volumetric strains in neutral surface folding. Terra Nova 21, 14–20.
Lisle, R.J., Toimil, N.C., Aller, J., Bobillo-Ares, N.C., Bastida, F., 2010. The hinge lines of non-cylindrical folds. J. Struct. Geol. 32, 166–171.
Little, T.A., 1992. Development of wrench folds along the Border Ranges fault systems, southern Alaska, U.S.A. J. Struct. Geol. 14, 343–359.
Liu, C., Zhang, Y., Wang, Y., 2009. Analysis of complete fold shape based in quadratic Bézier curves. J. Struct. Geol. 31, 575–581.
Liu, X., Eckert, A., Connolly, P., 2016. Stress evolution during 3D single-layer visco-elastic buckle folding: Implications for the initiation of fractures. Tectonophysics 679, 140–155.
Liu, X., Eckert, A., Connolly, P., Thornton, D., 2020. Visco-elastic parasitic folding: Influences on the resulting porosity distribution. J. Struct. Geol. 130, 10.1016.j.jsg.2019.103892.
Llorens, M.G., 2019. Stress and stress evolution during single-layer folding under pure and simple shear. J. Struct. Geol. 126, 245–257.
Llorens, M.G., Bons, P.D., Griera, A., Gomez-Rivas, E., 2013a. When do folds unfold during progressive shear? Geology 41, 563–566.
Llorens, M.G., Bons, P.D., Griera, A., Gomez-Rivas, E., Evans, L.A., 2013b. Single layer folding in simple shear. J. Struct. Geol. 50, 209–220.
Lloyd, G.E., 2020. Syntectonic quartz vein evolution during progressive deformation. In: Bond, C.E., Lebit, H.D. (Eds.), Folding and Fracturing of Rocks: 50 Years of Research since the Seminal Text Book of J. G. Ramsay, Geological Society of London, Special Publications, 487, pp. 127–151.

Logan, J.M., Friedman, M., Stearns, M.T., 1978. Experimental folding of rocks under confining pressure: Part VI. Further studies of faulted drape folds. In: Matthews III, V. (Ed.), Laramide Folding Associated with Basement Block Faulting in the Western United States, The Geological Society of America Memoir, 151, pp. 79–100.
Lohest, M., 1913. Expériences de Tectonique. Annales de la Societe Geologique de Belgique, Mémoires 39, pp. 547–585.
Loudon, T.V., 1964. Computer analysis of orientation data in structural geology. Tech. Report Geog. Branch Off. Naval Res., O.N.R. Task No. 389-135, Contr. No. 1228, No. 13, pp. 1–130.
Maerten, L., Maerten, F., 2006. Chronologic modeling of faulted and fractured reservoirs using geomechanically based restoration: technique and industry applications. AAPG bull. 90 (8), 1201–1226.
Mancktelow, N.S., 1999. Finite-element modelling of single-layer folding in elastoviscous materials; the effect of initial perturbation geometry. J. Struct. Geol. 21, 161–177.
Mancktelow, N.S., 2001. Single-layer folds developed from initial random perturbations; the effects of probability distribution, fractal dimension, phase, and amplitude. In: Koyi, H.A., Mancktelow, N.S. (Eds.), Tectonic Modelling: A Volume in Honor of Hans Ramberg. Geological Society of America Memoir, vol. 193, pp. 69–87.
Mancktelow, N.S., Abbassi, M.R., 1992. Single layer buckle folding in non-linear material; II, Comparison between theory and experiment. J. Struct. Geol. 14, 105–120.
Mandujano, J.J., Keppie, J.D., 2006. Cylindrical and conical fold geometries in the Cantarell structure, southern Gulf of Mexico: implication for hydrocarbon exploration. J. Pet. Geol. 29, 215–225.
Mandujano, J.J., Khachaturov, R.V., Tolson, G., Duncan Keppie, J., 2005. Curvature analysis applied to the Cantarell structure, southern Gulf of Mexico: implication for hydrocarbon exploration. Comput. Geosci. 31, 641–647.
Manz, R., Wickham, J., 1978. Experimental analysis of folding in simple shear. Tectonophysics 44, 79–90.
Mead, W.J., 1920. Notes on the mechanics of geologic structures. J. Geol. 28, 505–523.
Meunier, S., 1904. La géologie expérimentale. Alcan, Paris.
Mitra, S., 1990. Fault-propagation folds: geometry, kinematic evolution, and hydrocarbon traps. AAPG bull. 74 (6), 921–945.
Mitra, S., 2002. Fold-accommodation fault. Am. Assoc. Petrol. Geolog. Bull. 86, 671–693.
Mitra, S., 2003. A unified kinematic model for the evolution of detachment folds. J. Struct. Geol. 25, 1659–1673.
Mohammadi, S., 2012. XFEM Fracture Analysis of Composites. John Wiley & Sons, Ltd.
Montanari, D., Bonini, M., Corti, G., Agostini, A., Del Ventisette, C., 2017. Forced folding above shallow magma intrusions: insights on supercritical fluid flow from analogue modelling. J. Volcanol. Geotherm. Res. 345, 67–80.
Morales, L.F.G., Casey, M., Lloyd, G.E., Williams, D.M., 2011. Kinematic and temporal relationships between parallel fold hinge lines and stretching lineations: a microstructural and crystallographic preferred orientation approach. Tectonophysics 503, 207–221.
Morley, C.K., Waples, D.W., Boonyasaknanon, P., Julapour, A., Loviruchsutee, P., 2013. The origin of separate oil and gas accumulations in adjacent anticlines in Central Iran. Mar. Pet. Geol. 44, 96–111.
Morley, C.K., von Hagke, C., Hansberry, R.L., Collins, A.S., Kanitpanyacharoen, W., King, R., 2017. Review of major shale-dominated detachment and thrust characteristics in the diagenetic zone: part 1, meso- and macroscopic scale. Earth Sci. Rev. 173, 168–228.
Mueller, K., Suppe, J., 1997. Growth of Wheeler Ridge anticline, California: geometric evidence for fault-bend folding behavior during earthquakes. J. Struct. Geol. 19, 383–396.
Mühlhaus, H.-B., Sakaguchi, H., Hobbs, B.E., 1998. Evolution of three-dimensional folds for a non-Newtonian plate in a viscous medium. Proc. Roy. Soc. A 454, 3121–3143.
Mukherjee, S., 2014. Review of flanking structures in meso- and micro-scales. Geol. Mag. 151, 957–974.
Mulchrone, K.F., Pastor-Galán, D., Gutiérrez-Alonso, G., 2013. Mathematica code for least-squares cone fitting and equal-area stereonet representation. Comput. Geosci. 54, 203–210.
Nabavi, S.T., Díaz-Azpiroz, M., Talbot, C.J., 2017a. Inclined transpression in the Neka Valley, eastern Alborz, Iran. Int. J. Earth Sci. 106, 1815–1840.
Nabavi, S.T., Alavi, S.A., Mohammadi, S., Ghassemi, M.R., Frehner, M., 2017b. Analysis of transpression within contractional fault steps using finite-element method. J. Struct. Geol. 96, 1–20.
Nabavi, S.T., Alavi, S.A., Maerten, F., 2018a. 2D finite-element elastic models of transtensional pull-apart basins. Compt. Rendus Geosci. 350, 222–230.
Nabavi, S.T., Alavi, S.A., Mohammadi, S., Ghassemi, M.R., 2018b. Mechanical evolution of transpression zones affected by fault interactions: Insights from 3D elasto-plastic finite element models. J. Struct. Geol. 106, 19–40.
Nabavi, S.T., Alavi, S.A., Javanbakht, H., 2019. The Dinevar transtensional pull-apart basin, NW Zagros Mountains, Iran: a geological study and comparison to 2D finite element elastic models. Int. J. Earth Sci. 108, 329–346.
Nabavi, S.T., Alavi, S.A., Wibberley, C.A.J., Jahangiri, M., 2020a. Normal fault networks and their spatial relationships in Plio-Quaternary sedimentary series: a case study in the Zanjan Depression, NW Iran. J. Struct. Geol. 136 https://doi.org/10.1016/j.jsg.2020.104072.
Mynatt, I., Bergbauer, S., Pollard, D.D., 2007. Using differential geometry to describe 3-D folds. J. Struct. Geol. 29 (7), 1256–1266.
Nabavi, S.T., Alavi, S.A., Díaz-Azpiroz, M., Mohammadi, S., Ghassemi, M.R., Fernández, C., Barcos, L., Frehner, M., 2020b. Deformtion mechanics in inclined, brittle-ductile transpression zones: insights from 3D finite element modelling. J. Struct. Geol. 137 https://doi.org/10.1016/j.jsg.2020.104082.
Najafi, M., Vergés, J., Etemad-Saeed, N., Karimnejad, H.R., 2018. Folding, thrusting and diapirism: competing mechanisms for shaping the structure of the north Dezful Embayment, Zagros, Iran. Basin Res. 30, 1200–1229.
Neurath, C., Smith, R.B., 1982. The effect of material properties on growth rates of folding and boudinage: experiments with wax models. J. Struct. Geol. 4, 215–229.
Nevin, C.M., 1931. Principles of Structural Geology. John Wiley & Sons, New York.
Nicol, A., 1993. Conical folds produced by dome and basin fold interference and their application to determining strain: examples from North Canterbury, New Zealand. J. Struct. Geol. 15, 785–792.
Ord, A., Hobbs, B.E., 2013. Localised folding in general deformations. Tectonophysics 587, 30–45.
Ord, A., Hobbs, B.E., 2019. Quantitative measures of deformed rocks: the links to dynamics. J. Struct. Geol. 125, 74–81.
Ord, A., Hobbs, B.E., Dering, G., Gessner, K., 2018. Nonlinear analysis of natural folds using wavelet transforms and recurrence plots. Philosop. Trans. A 376. https://doi.org/10.1098/rsta.2017.0257.
Ormand, C.J., Hudleston, P.J., 2003. Strain paths of three small folds from the Appalachian Valley and Ridge, Maryland. J. Struct. Geol. 25, 1841–1854.
Ozkaya, S.I., 2002a. CURVAZ-a program to calculate magnitude and direction of maximum curvature and fracture-flow index. Comput. Geosci. 28, 399–407.
Ozkaya, S.I., 2002b. QUADRO-A program to estimate principal curvatures of folds. Comput. Geosci. 28, 467–472.
Parrish, D.K., 1973. A nonlinear finite-element fold model. Am. J. Sci. 273, 318–334.
Parrish, D.K., Krivz, A.L., Carter, N.L., 1976. Finite-element folds of similar geometry. Tectonophysics 32, 183–207.
Pastor-Galán, D., Gutiérrez-Alonso, G., Mulchrone, K.F., Huerta, P., 2012. Conical folding in the core of an orocline. A geometric analysis from the Cantabrian Arc (Variscan Belt of NW Iberia). J. Struct. Geol. 39, 210–223.
Paul, D., Mitra, S., 2015. Fault patterns associated with extensional fault-propagation folding. Mar. Pet. Geol. 67, 120–143.
Paulcke, W., 1912. Das Experiment in de Geologie. Festschrift zur Feier des fünfünd-fündfzigsten Geburtstages Seiner Königlichen Hohiet des GroBherzogs Friedrich II, Karlsruhe.
Peacock, D.C.P., Sanderson, D.J., 2018. Structural analyses and fracture network characterisation: seven pillars of wisdom. Earth Sci. Rev. 184, 13–28.
Peacock, D.C.P., Sanderson, D.J., Rotevatn, A., 2018. Relationships between fractures. J. Struct. Geol. 106, 41–53.
Pearce, M.A., Jones, R.R., Smith, S.A.F., McCaffrey, K.J.W., Clegg, P., 2006. Numerical analysis of fold curvature using data acquired by high-precision GPS. J. Struct. Geol. 28, 1640–1646.
Pearce, M.A., Jones, R.R., Smith, S.A.F., McCaffrey, K.J.W., 2011. Quantification of fold curvature and fracturing terrestrial laser scanning. Am. Assoc. Pet. Geol. Bull. 95, 771–794.
Peña, J.M.V., 2001. Isogons: a program in Pascal to draw the dip isogons of folds. Comput. Geosci. 27, 601–606.
Phillips, E.R., 2018. Glacitectonics. In: Menzies, J., van der Meer, J.J.M. (Eds.), Past Glacial Environments. Elsevier, pp. 467–502.
Playfair, J., 1802. Illustrations of the Huttonian Theory of the Earth. Edinburgh, W. Creech. University of Illinois Press, Urbana, Illinois, 1956, 527 p.
Plotek, B., Guzmán, C., Cristallini, E., Yagupsky, D., 2021. Analysis of fault bend folding kinematic models and comparison with an analog experiment. J. Struct. Geol. 146 https://doi.org/10.1016/j.jsg.2021.104316.
Poblet, J., 2012. 2D kinematic models of growth fault-related folds in contractional settings. In: Busby, C., Azor, A. (Eds.), Tectonics of Sedimentary Basins: Recent Advances. Blackwell, pp. 538–564.
Poblet, J., McClay, K.R., 1996. Geometry and kinematics of single-layer detachment folds. Am. Assoc. Petrol. Geolog. Bull. 80, 1085–1109.
Pollard, D.D., Fletcher, R.C., 2005. Fundamental of Structural Geology. Cambridge University Press, UK.
Prasicek, G., Otto, J.-C., Montgomery, D.R., Schrott, L., 2014. Multi-scale curvature for automated identification of glaciated mountain landscapes. Geomorphology 209, 53–65.
Price, N.J., Cosgrove, J.W., 1990. Analysis of Geological Structures. Cambridge University Press, Great Britain.
Pueyo, E.L., Parés, J.M., Millan, H., Pocovi, A., 2003. Conical folds and apparent rotations in paleomagnetism (a case study in the Southern Pyrnees). Tectonophysics 362, 345–366.
Pumpelly, R., Wolff, J.E., Dale, T.N., 1894. Geology of the Green Mountains in Massachusetts. Report No. 23, Washington. Government Printing Office. https://doi.org/10.3133/m23.
Ramberg, H., 1959. Evolution of ptygmatic folding. Norsk Geologisk Tiddskrift 39, 99–155.
Ramberg, H., 1961. Relationship between concentric longitudinal strain and concentric shearing strain during folding of homogeneous sheets of rocks. Am. J. Sci. 259, 382–390.
Ramberg, H., 1962. Contact strain and folding instability of a multi-layered body under compression. Geol. Rundsch. 51, 405–439.
Ramberg, H., 1963. Strain distribution and geometry of folds. Bull. Geol. Institut. Univ. Uppsala 42, 1–20.
Ramberg, H., 1963a. Fluid dynamics of viscous buckling applicable to folding of layered rocks. Bull. Am. Assoc. Pet. Geol. 47, 484–505.
Ramberg, H., 1964. Selective buckling of composite layers with contrasted rheological properties, a theory for the simultaneous formation of several orders of folds. Tectonophysics 1, 307–341.
Ramberg, I.B., Johnson, A.M., 1976. A theory of concentric, kink, and sinusoidal folding and of monoclonal flexuring of compressible, elastic multilayers. Part V: Asymmetric

folding in interbedded chert and shale of the Franciscan complex, San Francisco Bay area, California. Tectonophysics 32, 295–320.
Ramón-Lluch, R., Martínez-Torres, L.M., Eguiluz, L., 1989. RAFOLD: a basic program for the geometric classification of folds. Comput. Geosci. 15, 989–996.
Ramsay, J.G., 1962. The geometry and mechanics of formation of "similar" type folds. J. Geol. 70, 309–327.
Ramsay, J.G., 1964. The uses and limitation of beta-diagrams and pi-diagrams in the geometrical analysis of folds. Q. J. Geol. Soc. Lond. 120, 435–454.
Ramsay, J.G., 1967. Folding and Fracturing of Rocks. McGraw-ill Book, New York.
Ramsay, J.G., 1974. Development of chevron folds. Geol. Soc. Am. Bull. 85, 1741–1754.
Ramsay, J.G., 1980. Shear zone geometry: a review. J. Struct. Geol. 2, 83–99.
Ramsay, J.G., 1981. Tectonics of the Helvetic nappes. In: McClay, K.R., Price, N.J. (Eds.), Thrust and Nappe Tectonics, Geological Society, London, Special Publications, 9, pp. 293–309.
Ramsay, J.G., Huber, M.I., 1987. The Techniques of Modern Structural Geology: Folds and Fractures, vol. 2. Academic Press, London.
Ramsay, D.M., Sturt, B.A., 1973. An analysis of noncylindrical and incongruous fold pattern from the eo-cambrian rocks of söröy, northern Norway: I. Noncylindrical, incongruous and aberrant folding. Tectonophysics 18 (1–2), 81–107.
Ramsay, J.G., Wood, D.S., 1973. The geometries effects of volume change during deformation processes. Tectonophysics 16, 263–277.
Ramsay, J.G., Casey, M., Kligfield, R., 1983. Role of shear in development of the Helvetic fold-thrust belt of Switzerland. Geology 11, 439–442.
Rattey, P.R., Sanderson, D.J., 1982. Patterns of folding within nappes and thrust sheets: examples from the Variscan of Southwest England. Tectonophysics 88, 247–267.
Reade, T.M., 1886. The Origin of Mountain Ranges Considered Experimentally, Structurally, Dynamically, and in Relation to their Geological History. Taylor and Francis, London.
Reber, J.E., Schmalholz, S.M., Burg, J.P., 2010. Stress orientation and fracturing during three-dimensional buckling: Numerical simulation and application to chocolate-tablet structures in folded turbidites, SW Portugal. Tectonophysics 493, 187–195.
Reches, Z., Eidelman, A., 1995. Drag along faults. Tectonophysics 247, 145–156.
Reeves, J., Magee, C., Jackson, C.A.-L., 2018. Unravelling intrusion-induced forced fold kinematics and ground deformation using 3D seismic reflection data. Volcanica 1 (1), 1–17. https://doi.org/10.30909/VOL.01.01.0117.
Resor, P.G., Pollard, D.D., 2012. Reverse drag revisited: why footwall deformation may be the key to inferring listric fault geometry. J. Struct. Geol. 41, 98–109.
Rich, J.L., 1934. Mechanics of low-angle overthrust faulting as illustrated by Cumberland thrust block, Virginia, Kentucky and Tennessee. Am. Assoc. Petrol. Geolog. Bull. 18, 1584–1596.
Rickard, M.J., 1971. A classification diagram for fold orientation. Geol. Mag. 108, 23–26.
Roberts, A., 2001. Curvature attributes and their application to 3D interpreted horizons. First Break 19, 85–100.
Roberts, D., Strömgård, K.-E., 1972. A comparison of natural and experimental strain patterns around fold hinge zones. Tectonophysics 14, 105–120.
Roder, G.H., 1978. Fold shape: the problem, expansion of use of dip isogons, and implications of preliminary investigation. Tectonophysics 51, T1–T7.
Röller, K., Trepmann, C., 2008. Stereo32 Version 1.01. http://www.ruhr-uni-bochum.de/hardrock/downloads.html.
Romeo, I., Álvarez-Gómez, J.A., 2018. Lithospheric folding by flexural slip in subduction zones as source for reverse fault intraslab earthquakes. Sci. Rep. 8, 1367. https://doi.org/10.1038/s41598-018-19682-7.
Romstad, B., Etzelmüller, B., 2012. Mean-curvature watersheds: a simple method for segmentation of a digital elevation model into terrain units. Geomorphology 139-140, 293–302.
Rouby, D., Riallard, S., Guillocheau, F., Bouroullec, R., Naplas, T., 2002. Kinematics of a growth fault/raft system on the West African margin using 3-D restoration. J. Struct. Geol. 24, 783–796.
Rovenski, V., 2010. Modeling of Curves and Surfaces with MATLAB®. Springer Science & Business Media.
Rowan, M.G., Muñoz, J.A., Giles, K.A., Roca, E., Hearon IV, T.E., Fiduk, J.C., Ferrer, O., Fischer, M.P., 2020. Folding and fracturing of rocks adjacent to salt diapirs. J. Struct. Geol. 141 https://doi.org/10.1016/j.jsg.2020.104187.
Sanderson, D.J., 1979. The transition from upright to recumbent folding in the Variscan fold belt of southwest England: a model based on kinematics of simple shear. J. Struct. Geol. 1, 171–180.
Sanderson, D.J., Marchini, W.R.D., 1984. Transpression. J. Struct. Geol. 6, 449–458.
Sanderson, D.J., Nixon, C.W., 2015. The use of topology in fracture network characterization. J. Struct. Geol. 72, 55–66.
Sanderson, D.J., Nixon, C.W., 2018. Topology, connectivity and percolation in fracture networks. J. Struct. Geol. 115, 167–177.
Sathiakumar, S., Barbot, S., 2021. The stop-start control of seismicity by fault bends along the Main Himalayan Thrust. Commun. Earth Environ. 2, 87. https://doi.org/10.1038/s43247-021-00153-3.
Sathiakumar, S., Barbot, S., Hubbard, J., 2020. Earthquake cycles in fault-bend folds. J. Geophys. Res. Solid Earth 125. https://doi.org/10.1029/2019JB018557.
Schardt, H., 1884. Geological studies in the Pays-D'Enhaut Vaudois. Bulletin de la Société Vaudoise des Sciences Naturelles 20, 139–167.
Schmalholz, S.M., 2006. Scaled amplification equation: a key to the folding history of buckled viscous single-layers. Tectonophysics 419, 41–53.
Schmalholz, S.M., 2008. 3D numerical modelling of forward folding and reverse unfolding of a viscous single-layer: implications for the formation of folds and fold patterns. Tectonophysics 446, 31–41.
Schmalholz, S.M., Mancktelow, N.S., 2016. Folding and necking across the scales: a review of theoretical and experimental results and their applications. Solid Earth 7, 1417–1465.
Schmalholz, S.M., Podladchikov, Y.Y., 1999. Buckling versus folding: importance of viscoelasticity. Geophys. Res. Lett. 26 (17), 2641–2644.
Schmalholz, S.M., Podladchikov, Y.Y., 2001. Strain and competence contrast estimation from fold shape. Tectonophysics 340, 195–213.
Schmalholz, S.M., Podladchikov, Y.Y., Burg, J.P., 2002. Control of folding by gravity and matrix thickness: implications for large-scale folding. J. Geophys. Res. Solid Earth 107 (B1). https://doi.org/10.1029/2001JB000355.
Schmalholz, S.M., Schmid, D.W., 2012. Folding in power-law viscous multi-layers. Philosophical Transactions of the Royal Society A: Mathematical, Physical and Engineering Sciences 370 (1965), 1798–1826.
Schmid, D.W., Dabrowski, M., Kritkiewski, M., 2008. Evolution of large amplitude 3D fold pattern: a FEM study. Physics Earth Planatary Inter. 171, 400–408.
Schultz-Ela, D.D., 2003. Origin of drag folds bordering salt diapirs. Am. Assoc. Petrol. Geolog. Bull. 87, 757–780.
Schwerdtner, W.M., Van Berkel, J.T., 1991. The origin of fold abutments in the map pattern of the westernmost Grenville Province, Central Ontario. Precambrian Res. 49, 39–59.
Schwerdtner, W.M., Lu, S.J., Landa, D., 2010. S and Z buckle folds as shear-sense indicators in the ductile realm: Field examples from the Grenville Province of Ontario and the Appalachians of South Carolina. In: Tollo, R.P., Bartholomew, M.J., Hibbard, J.P., Karabinos, P.M. (Eds.), From Rodinia to Pangea: The Lithotectonic Record of the Appalachian Region, Karabinos, Geological Society of America Memoir, 206, pp. 773–794.
Shaban, A., Sherkati, S., Miri, S.A., 2011. Comparison between curvature and 3D strain analysis methods for fracture predicting in the Gachsaran oil field (Iran). Geol. Mag. 148, 868–878.
Sharpe, D., 1847. On slaty cleavage. Q. J. Geol. Soc. 3, 74–105.
Shaw, J.H., Hook, S.C., Sitohang, E.P., 1997. Extensional fault-bend folding and synrift deposition: an example from the Central Sumatra Basin, Indonesia. Am. Assoc. Petrol. Geolog. Bull. 81, 367–379.
Sherkati, S., Letouzey, J., Frizon de Lamotte, D., 2006. Central Zagros fold-thrust belt (Iran): new insights from seismic data, field observation, and sandbox modeling. Tectonics 25 (4). https://doi.org/10.1029/2004TC001766.
Sherkati, S., Molinaro, M., de Lamotte, D.F., Letouzey, J., 2005. Detachment folding in the Central and Eastern Zagros fold-belt (Iran): salt mobility, multiple detachments and late basement control. J. Struct. Geol. 27 (9), 1680–1696.
Sherwin, J.-A., Chapple, W.M., 1968. Wavelengths of single layer folds: a comparison between theory and observation. Am. J. Sci. 266, 167–179.
Shimamoto, T., Hara, I., 1976. Geometry and strain distribution of single-layer folds. Tectonophysics 30, 1–34.
Silliphant, L.J., Engelder, T., Gross, M.R., 2002. The state of stress in the limb of the Split Mountains anticline, Utah: constraints placed by transected joints. J. Struct. Geol. 24, 155–172.
Simpson, C., De Paor, D.G., 1993. Strain and kinematic analysis in general shear zones. J. Struct. Geol. 15, 1–20.
Singh, R.A., Gairola, V.K., 1992. Fold shape analysis on the vicinity of North Almora Thrust in District Chamoli, Garhwal Himalaya. J. Himal. Geol. 3, 121–129.
Smith, R.B., 1975. Unified theory of the onset of folding, boudinage, and mullion structure. Geol. Soc. Am. Bull. 86, 1601–1609.
Smith, R.B., 1977. Formation of folds, boudinage, and mullions in non-Newtonian materials. Geol. Soc. Am. Bull. 88, 312–320.
Smoluchowski, M., 1909. Über ein gewisses stabilitätsproblem der elastizitätslehre und dessen beziehung zur entstehung von faltengbirgen. B. Acad. Sci. Cracov. 2, 3–20.
Sommaruga, A., Mosar, J., Schori, M., Gruber, M., 2017. The role of the triassic evaporites underneath the north Alpine foreland. In: Soto, J.I., Flinch, J.F., Tari, G. (Eds.), Permo-Triassic Salt Provinces of Europe, North Africa and the Atlantic Margins: Tectonics and Hydrocarbon Potential. Elsevier, pp. 447–466.
Sorby, H.C., 1849. On slaty cleavage. Proc. Geol. Polytechnic Soc. West RidingYorkshire 3, 300–312.
Sou, C., Peng, S., Chang, S., Duan, R., Wang, G., 2012. A new calculating method of the curvature to predicting the reservoir fractures. Procedia Environ. Sci. 12, 576–582.
Srivastava, H.B., 2003. Strain determination from concentric folds. Tectonophysics 364, 237–241.
Srivastava, V., Gairola, V.K., 1997. Classification of multilayerd folds based on harmonic analysis: example from central India. J. Struct. Geol. 19, 107–112.
Srivastava, V., Gairola, V.K., 1999. Geometrical classification of multi-layered folds. Tectonophysics 301, 159–171.
Srivastava, V., Gairola, V.K., 2003. Recent Classification Schemes for Multi-Layered Folds: An Overview. Memoir Geological Society of India: 52, pp. 395–408.
Srivastava, D.C., Lisle, R.J., 2004. Rapid analysis of fold shape using Bézier curves. J. Struct. Geol. 26, 1553–1559.
Srivastava, D.C., Rastogi, V., 2010. HingeInflex: a MATLAB-based method for precise selection of the hinge and the inflection points in folds. Geol. Mag. 147, 233–241.
Srivastava, D.C., Shah, J., 2008. The "isogon rosette" method for rapid estimation of strain in flattened folds. J. Struct. Geol. 30, 444–450.
Srivastava, D.C., Rastogi, V., Ghosh, R., 2010. A rapid Bézier curve method for shape analysis and point representation of asymmetric folds. J. Struct. Geol. 32, 685–692.
Stabler, C.L., 1968. Simplified Fourier analysis of fold shapes. Tectonophysics 6, 343–350.
Stauffer, M.R., 1964. The geometry of conical folds. N. Z. J. Geol. Geophys. 7, 340–347.
Stauffer, M.R., 1967. The problem of conical folding around the Barrack Creek Adamellite, Queanbeyan, New South Wales. J. Geol. Soc. Aust. 14, 49–56.
Stauffer, M.R., 1973. New method for mapping fold axial surfaces. Geol. Soc. Am. Bull. 84, 2307–2318.
Stead, D., Wolter, A., 2015. A critical review of rock slope failure mechanisms: the importance of structural geology. J. Struct. Geol. 74, 1–23.

Stearns, D.W., 1969. Fracture as a mechanism of flow in naturally deformed layered rocks. In: Proceedings, Conference on Research in Tectonics, Kink Bands and Brittle Deformation. Geological Survey of Canada Paper 68, No. 52, pp. 79–96.
Stearns, D.W., 1978. Faulting and forced folding in the Rocky Mountain Foreland. In: Matthews III, V. (Ed.), Laramide Folding Associated with Basement Block Faulting in the Western United States, The Geological Society of America Memoir, 151, pp. 1–37.
Stecchi, F., Antonellini, M., Gabbianelli, G., 2009. Curvature analysis as a tool for subsidence-related risk zones identification in the city of Tuzla (BiH). Geomorphology 107, 316–325.
Stephenson, B., Koopman, A., Hillgartner, H., McQuillan, H., Bourne, S., Noad, J., Rawnsley, K., 2007. Structural and stratigraphic controls on fold-related fracturing in the Zagros Mountains, Iran: Implications for reservoir development. In: Lonergan, L., Jolly, R., Rawnsley, K., Sanderson, D.J. (Eds.), Fractured Reservoirs, Geological Society of London, Special Publication, 270, pp. 1–21.
Stewart, S.A., 1996. Influence of detachment layer thickness on style of thin-skinned shortening. J. Struct. Geol. 18, 1271–1274.
Stewart, S.A., 1999. Geometry of thin-skinned tectonic systems in relation to detachment layer thickness in sedimentary basins. Tectonics 18, 719–732.
Stewart, S.A., Podoloski, R., 1998. Curvature analysis of gridded geological surfaces. In: Coward, M.P., Daltaban, T.S., Johnson, H. (Eds.), Structural Geology in Reservoir Characterization, Geological Society of London, Special Publications, 127, pp. 133–147.
Stockmal, G.S., Spang, J.H., 1982. A method for the Distinction of circular conical from cylindrical folds. Can. J. Earth Sci. 19, 1101–1105.
Storti, F., Poblet, J., 1997. Growth stratal architectures associated to decollement folds and fault-propagation folds. Inferences on fold kinematics. Tectonophysics 282, 353–373.
Stowe, C.W., 1988. Application of Fourier analysis for computer representation of fold profiles. Tectonophysics 156, 303–311.
Strozyk, F., Reuning, L., Scheck-Wenderoth, M., Tanner, D.C., 2017. The tectonic history of the Zechstein basin in the Netherlands and Germany. In: Soto, J.I., Flinch, J.F., Tari, G. (Eds.), Permo-Triassic Salt Provinces of Europe, North Africa and the Atlantic Margins: Tectonics and Hydrocarbon Potential. Elsevier, pp. 221–241.
Suppe, J., 1983. Geometry and kinematics of fault-bend folding. Am. J. Sci. 283, 684–721.
Suppe, J., 1985. Principles of Structural Geology. Prentice-Hall, Englewood Cliffs, NJ.
Suppe, J., Connors, C.D., Zhang, Y., 2004. Shear fault-bend folding. In: McClay, K.R. (Ed.), Thrust Tectonics and Hydrocarbon Systems, American Association of Petroleum Geologists Memoir, vol. 82, pp. 303–323.
Suppe, J., Medwedeff, D.A., 1990. Geometry and kinematics of fault-propagation folding. Eclogae Geologicae Helvetiae 83 (3), 409–454.
Swift, J., Hohenberg, P.C., 1977. Hydrodynamic fluctuations at convective instability. Phys. Rev. A15, 319–328.
Sylvester, A.G., 1988. Strike-slip faults. Geol. Soc. Am. Bull. 100, 1666–1703.
Talbot, C.J., Pohjola, V., 2009. Subaerial salt extrusion in Iran as analogues of ice sheets, streams and glaciers. Earth Sci. Rev. 97, 167–195.
Talbot, C.J., Sokoutis, D., 1992. The importance of incompetence. Geology 20, 951–953.
Talbot, C.J., Aftabi, P., Chemia, Z., 2009. Potash in a salt mushroom at Hormoz Island, Hormoz Strait, Iran. Ore Geol. Rev. 35, 317–332.
Tanner, G.P.W., 1989. The flexural-slip mechanism. J. Struct. Geol. 11, 635–655.
Tavani, S., Storti, F., Lacombe, O., Corradetti, A., Muñoz, J.A., Mazzoli, S., 2015. A review of deformation pattern templates in foreland basin systems and fold-and-thrust belts: Implications for the state of stress in the frontal regions of thrust wedges. Earth Sci. Rev. 141, 82–104.
Terada, T., Miyabe, N., 1929. Experimental investigations of the deformation of sand mass by lateral pressure. Bull. Earthquake Res. Instit. 6, 109–126. University of Tokyo.
Thibert, B., Gratier, J.-P., Morvan, J.-M., 2005. A direct method for modelling and unfolding developable surfaces and its application to the Ventura Basin (California). J. Struct. Geol. 27, 303–316.
Timoshenko, S.P., Gere, J.M., 1963. Theory of Elastic Stability. Dover Publications, Inc., Mineola, New York.
Toimil, N.C., Griera, A., 2007. Influence of viscosity contrast and anisotropy on strain accommodation in competent layers. J. Struct. Geol. 29, 787–801.
Torremans, K., Muchez, P., Sintubin, M., 2014. Mechanisms of flexural folding of competent single-layers as evidenced by folded fibrous dolomite veins. J. Struct. Geol. 69, 75–90.
Treagus, S.H., 1973. Buckling instability of a viscous single-layer system, oblique to the principal compression. Tectonophysics 19, 271–289.
Treagus, S.H., 1982. A new isogon-cleavage classification and its application to natural and model fold studies. Geol. J. 17, 49–64.
Treagus, S.H., 1997. Modelling deformation partitioning in folds. In: Sengupta, S. (Ed.), Evolution of Geological Structures in Micro- to Macro-Scales. Chapman & Hall, London, pp. 341–372.
Treagus, S.H., Fletcher, R.C., 2009. Controls of folding on different scales in multilayered rocks. J. Struct. Geol. 31, 1340–1349.
Treagus, J.E., Treagus, S.H., 1981. Folds and the strain ellipsoid: a general model. J. Struct. Geol. 3, 1–17.
Tremlett, W.E., 1976. The definition of isoclinal folds. Tectonophysics 32, T1–T2.
Tripathi, A., Gairola, V.K., 1999. Fold symmetry – a quantitative description. J. Struct. Geol. 21, 719–727.
Trumpy, R., 1960. Paleotectonic evolution of the Central and Western Alps. Bull. Geol. Soc. Am. 71, 843–908.
Turcotte, D., Schubert, G., 2014. Geodynamics, Third edition. Cambridge University Press.
Turner, F.J., Weiss, L.E., 1963. Structural Analysis of Metamorphic Tectonites. McGraw-Hill, New York.
Twigger, L., 2015. Seeing safety thorugh to the subsalt. Oilfield Technol 8, 16–20.
Twiss, R.J., 1988. Description of folds in single surfaces. J. Struct. Geol. 10, 607–626.
Twiss, R.J., Moores, E.M., 2007. Structural Geology, Second ed. Freeman, New York.
Vai, G.B., 2003. l viaggi di Leonardo lungo le valli romagnole: riflessi di geologia nei quadri, disegni e codici. Leonardo, Machiavelli, Cesare Borgia. Arte, storia e scienza in Romagna (1500–1503). De Luca Editori d'Arte.
Vai, G.B., Marabini, C., Della Monica, W., 1986. Leonardo, la Romagna e la geologia. Romagna. Vicende e protagonisti. Bologna, Edison ed. 1, pp. 30–52.
van der Pluijm, B.A., Marshak, S., 2004. Earth Structure: An Introduction to Structural Geology and Tectonics, Second ed. W.W.North & Company.
Van Hise, C.R., 1896a. Principles of North American Pre-Cambrian Geology. US Government Printing Office.
Van Hise, C.R., 1896b. Studies for students: deformation of rocks: II. An analysis of folds. J. Geol. 4, 312–353.
Van Noten, K., Sintubin, M., 2019. Unfolding veined fold limbs to deduce a basin's prefolding stress state. In: Mukherjee, S. (Ed.), Developments in Structural Geology and Tectonics, Vol. 5. Elsevier, pp. 105–116.
Venkat-Raman, M., Tikoff, B., 2002. Physical models of trantensional folding. Geology 30, 523–526.
Venkitasubramanyan, C.S., 1971. Least-squares analysis of fabric data – note on conical, cylindroidal and near-cylindroidal folds. Can. J. Earth Sci. 8, 649–697.
Vergés, J., Burbank, D.W., Meigs, A., 1996. Unfolding: a inverse approach to fold kinematics. Geology 24, 175–178.
Vergés, J., Marzo, M., Muñoz, J.A., 2002. Growth strata in foreland settings. Sediment. Geol. 146, 1–9.
Vergés, J., Saura, E., Casciello, E., Fernàndez, M., Villaseñor, A., Jiménez-Munt, I., García-Castellanos, D., 2011. Crustal-scale cross-section across the NW Zagros belt: implications for the Arabian margin reconstruction. Geol. Mag. 148, 739–761.
Vollmer, F.W., 1988. A computer model of sheath-nappe formed during crustal shear in the Western Gneiss Region, central Norwegian Caledonides. J. Struct. Geol. 10, 735–745.
von Tscharner, M., Schmalholz, S.M., 2015. A 3-D Lagrangian finite element algorithm with remeshing for simulating large-strain hydrodynamic instabilities in power law viscoelastic fluids. Geochem. Geophys. Geosyst. 16, 215–246.
von Tscharner, M., Schmalholz, S.M., Epard, J.-L., 2016. 3-D numerical models of viscous flow applied to fold nappes and the Rawil depression in the Helvetic nappe system (western Switzerland). J. Struct. Geol. 86, 32–46.
Watkins, H., Butler, R.W.H., Bond, C.E., Healy, D., 2015. Influence of structural position on fracture networks in the Torridon Group, Achnashellach fold and thrust belt, NW Scotland. J. Struct. Geol. 74, 64–80.
Watkins, H., Healy, D., Bond, C.E., Butler, R.W.H., 2018. Implications of heterogeneous fracture distribution on reservoir quality; an analogue from the Torridon Group sandstone, Moine Thrust Belt, NW Scotland. J. Struct. Geol. 108, 180–197.
Watkinson, A.J., 1976. Fold propagation and interference in a single multilayer unit. Tectonophysics 34, T37–T42.
Weeks, J.R., 2001. The Shape of Space. CRC Press.
Weijermars, R., 1982. Vergence boundaries: an extension of the vergence concept. J. Struct. Geol. 4, 407–409.
Welker, A.J., Hogan, J.P., Eckert, A., Tindall, S., Liu, C., 2019. Conical folds – an artefact of using simple geometric shapes to describe a complex geologic structure. J. Struct. Geol. 123, 96–104.
Whitten, E.H.T., 1966. Structural Geology of Folded Rocks. Rand McNally, Chicago.
Wiest, J.D., Osmundsen, P.T., Jacobs, J., Fossen, H., 2019. Deep crustal flow within postorogenic metamorphic core complexes: insights from the Western Gneiss Region of Norway. Tectonics 38, 4267–4289.
Wilcox, R.E., Harding, T.P., Seely, D.R., 1973. Basic wrench tectonics. Am. Assoc. Petrol. Geolog. Bull. 57, 74–96.
Williams, J.R., 1980. Similar and chevron folds in multilayers using finite-element and geometrical models. Tectonophysics 65, 323–338.
Williams, G.D., Chapman, T.J., 1979. The geometrical classification of noncylindrical folds. J. Struct. Geol. 1, 181–185.
Willis, B., 1894. The mechanics of Appalachian structure. In: Powell, J.W. (Ed.), Thirteenth Annual report of the United States Geological Survey to the Secretary of the Interior, 1891-1892: Part 2. USGS, pp. 211–282.
Willis, B., 1923. Geologic Structures. McGraw-Hill Book Company.
Willis, B., Willis, R., 1934. Geologic Structures, Third edition. McGraw-Hill, New York.
Wilson, G., 1967. The geometry of cylindrical and conical folds. Proc. Geol. Assoc. 78, 179–209.
Wilson, P.I.R., McCaffrey, K.J.W., Wilson, R.W., Jervis, I., Holdsworth, R.E., 2016. Deformation structures associated with the Trachyte Mesa intrusion, Henry Mountains, Utah: implications for sill and laccolith emplacement mechanisms. J. Struct. Geol. 87, 30–46.
Withjack, M.O., Schlische, R.W., 2006. Geometric and experimental models of extensional fault-bend folds. In: Buiter, S.J.H., Schreurs, G. (Eds.), Analogue and Numerical Modelling of Crustal-Scale Processes, Geological Society of London, Special Publications, 253, pp. 285–305.
Withjack, M.O., Olson, J., Peterson, E., 1990. Experimental models of extensional forced folds. Am. Assoc. Pet. Geol. Bull. 74, 1038–1054.
Wiltschko, D.V., Chapple, W.M., 1977. Flow of weak rocks in Appalachian Plateau folds. AAPG Bull. 61 (5), 653–670.
Withjack, M.O., Islam, Q., Lapointe, P., 1995. Normal faults and their hanging-wall deformation – an experimental study. Am. Assoc. Petrol. Geolog. Bull. 79, 1–18.
Wu, Y., Eckert, A., Liu, X., Obrist-Farner, J., 2019. The role of flexural slip during the development of multilayer chevron folds. Tectonophysics 753, 124–145.

Xiao, H., Suppe, J., 1992. Origin of rollover. Am. Assoc. Petrol. Geolog. Bull. 76, 509–529.
Xypolias, P., Alsop, G.I., 2014. Regional flow perturbation folding within an exhumation channel: a case study from the Cycladic Blueschists. J. Struct. Geol. 62, 141–155.
Yakovlev, F.L., 2008. Quantitative methods of analysis of natural formations mechanisms for folds and for systems of linear folding. In: Problems of tectonophysics, 40th anniversary of the foundation of the Tectonophysics laboratory at the institute of physics of the Earth by M. Gzovsky. Publishing of IPE RAS, Moscow, pp. 149–188 (In Russian).
Yakovlev, F.L., 2012a. Methods for detecting formation mechanisms and determining a final strain value for different scales of folded structures. Compt. Rendus Geosci. 344, 125–137.
Yakovlev, F.L., 2012b. Identification of geodynamic setting and of folding formation mechanisms using of strain ellipsoid concept for multi-scale structures of Greater Caucasus. Tectonophysics 581, 93–113.
Yamato, P., Kaus, B.J.P., Mouthereau, F., Castellort, S., 2011. Dynamic constraints on the crustal-scale rheology of the Zagros fold belt, Iran. Geology 39, 815–818.
Yarbuh, I., Contreras, J., 2015. The interplay between deformation, erosion and sedimentation in the deep-water Mexican Ridge foldbelt, western Gulf of Mexico basin. Basin Res. 29, 446–464.
Zagorčev, I., 1974. Some problems of classification and terminology of folds. Rev. Bulgar. Geol. Soc. Sofia 35, 338–343 (In Bulgarian).
Zagorčev, I., 1993. The geometrical classification of folds and distribution of fold types in natural rocks. J. Struct. Geol. 15, 243–251.
Ziesch, J., Tanner, D.C., Krawczyk, C.M., 2014. Strain associated with the fault-parallel flow algorithm during kinematic fault displacement. Math. Geosci. 46, 59–73.
Zulauf, G., Zulauf, J., Maul, H., 2017. Quantification of the geometrical parameters of non-cylindrical folds. J. Struct. Geol. 100, 120–129.
Zulauf, J., Zulauf, G., Hattingen, E., 2020. Boundinage and two-stage folding of oblique single layers under coaxial plane strain: layer rotation around the axis of no change (Y). J. Struct. Geol. 135 https://doi.org/10.1016/j.jsg.2020.104023.
Zulauf, G., Zulauf, J., Hattingen, E., 2021. From parasitic via non-cylindrical to extension-parallel folding of oblique single layers under coaxial plane strain: Layer rotation around the shortening axis (Z). J. Struct. Geol. 145 https://doi.org/10.1016/j.jsg.2021.104303.
Zuluaga, L.F., Fossen, H., Rotevatn, A., 2014. Progressive evolution of deformation band populations during Laramide fault-propagation folding: Navajo Sandstone, San Rafael monocline, Utah, U.S.a. J. Struct. Geol. 68, 66–81.
Zuluaga, L.F., Rotevatn, A., Keilegavlen, E., Fossen, H., 2016. The effect of deformation bands on simulated fluid flow within fault-propagation fold trap types: Lessons from the San Rafael monocline, Utah. Am. Assoc. Pet. Geol. Bull. 100, 1523–1540.